Developing Carbon Tolerant Ni/ScCeSZ cells via Aqueous Tape Casting for Direct Biogas fed Solid Oxide Fuel Cells (SOFC)

by

Nor Anisa Arifin

A thesis submitted to
University of Birmingham
for the degree of

DOCTOR OF PHILOSOPHY

Centre of Fuel Cell and Hydrogen Research
School of Chemical Engineering
College of Engineering and Physical Science
University of Birmingham
October 2018

إِنَّ مَعَ الْعُسْرِ يُسْرًا

INDEED WITH HARDSHIP
COMES EASE

15:85

I dedicate this thesis to my beautiful family ….

ABSTRACT

Solid Oxide Fuel cell (SOFC) is a promising solution to energy independence, greener energy, with high electrical efficiency and theoretically compatible to operate with gaseous carbonaceous fuel. The problem arises when the benchmark materials (Ni/YSZ) performance drop with operation with carbon fuels. Hence, this thesis aims to develop SOFC cell with alternative materials that have high electrochemical performance with dry carbon fuels for intermediate temperature SOFC.

This thesis demonstrates the successful manufacturing of the anode supported cells of Ni/YSZ, Ni/ScCeSZ and Sn-Ni/ScCeSZ via reverse aqueous tape casting method. With this method, SOFC half cells with dense thin electrolyte and porous thick anode produced using multi-layered tape casting and single co-sintering stage. Ni/ScCeSZ was chosen as the base anode substrate material due to the 10ScCeSZ's high conductivity property and better ability to tolerate carbon-based fuels. Despite the long history of Ni/ScCeSZ cell, this thesis shows the first work that compare Ni/YSZ and Ni/ScCeSZ cells for IT-SOFC with hydrogen and dry carbon fuels. Tin (Sn) introduced as dopant in the final stage to further enhanced the performance in dry carbon operation. for Sn-Ni/ScCeSZ cell. To author's knowledge, this thesis reported the first work on the electrochemical performance in dry biogas

Comparative study of the electrochemical performance in hydrogen and dry biogas reveals that the maximum power density of Ni/YSZ cell instantly dropped by an average of 80.6% when switched from hydrogen to biogas, 0.37 W/cm^2 to 0.05W/cm^2, respectively. Ni/ScCeSZ showed better performance in both fuels, with maximum power densities of 0.42 W/cm^2 in hydrogen and 0.28 W/cm^2 biogas (37.5 % drop). Ni/YSZ and Ni/ScCeSZ show significant differences in the ASR value in biogas operation with values of 2.52 $\Omega.cm^2$ and 0.72 $\Omega.cm^2$ respectively. With Sn-Ni/ScCeSZ, the OCV increased with the fuel swap from 0.99 V to 1.04 V and the performance in biogas lowered only by an average of 8.3% with a maximum power density of 0.314 W/cm^2 in biogas.

Contradict to the literature, this thesis provides a new insight to the cause of performances drop with the fuel switch which was mainly affected by the reforming ability of Ni/ScCeSZ and Ni/YSZ anode. Small amount of amorphous carbon deposited on the Ni/YSZ anode while higher amount of graphitic carbon found on the Ni/ScCeSZ and Sn-NiScCeSZ anodes. Sn increased the catalytic activity reforming and methane cracking accompanied by increase amount of graphitic carbon on the anode.

ACKNOWLEDGEMENT

CONFERENCE/PUBLICATIONS

Oral presentation

SOFC-XV: 15th International Symposium on Solid Oxide Fuel Cells (2017) FLORIDA

FCH2: Fuel Cell and Hydrogen Technology conference (2017) BIRMINGHAM

ICFCHT: International Conference of Fuel Cell and Hydrogen Technology (2017) KUALA LUMPUR

EFCF: 12th European SOFC and SOE Forum (2016) LUCERNE

Publication

ECS (The Electrochemical Society) Transaction: Electrochemical performance and carbon resistance comparison between Tin, Copper and Silver-doped Nickel/Yttria-Stabilized Zirconia anodes SOFCs operated with biogas (Co-Author - Journal)

ECS (The Electrochemical Society) Transaction: Carbon-Tolerant Ni/ScCeSZ via Aqueous Tape Casting for IT-SOFCs (Main Author- peer reviewed conference paper)

Ceramics International: Electrochemical and Thermal characterisation of Doped Ceria Electrolyte with Lanthanum and Zirconium (Co-author - Journal)

12th EFCF Conference Proceeding: Multilayer and Co-sintering Ni/8YSZ for SOFC by Aqueous Tape casting (Main Author- conference paper)

NOMENCLATURE

Abbreviation	Definitions
AFL	Anode functional layer
AS	Anode substrate
ASC	Anode supported cell
ASR	Area specific resistance
BSE	Back-scattered electron
CD_{max}	Maximum current density
cermets	Ceramic and metal materials
CTE or TEC	Coefficient of thermal expansion
E_a	Activation energy in kJ/mol
EDX	Energy dispersive X-ray analysis
EIS	Electrochemical impedance spectroscopy
ESC	Electrolyte supported cell
GDC	Gadolinium doped ceria (also known as ceria doped gadolinium oxide)
IT-SOFC	Intermediate temperature SOFC
iV-PV	Current- voltage and power densities curve
Ni/ScSZ	Nickel-scandia stabilised zirconia
Ni/ScSZ or NiScCeSZ	Nickel-(ceria doped) scandia stabilised zirconia
Ni/YSZ	Nickel-yttrium stabilised zirconia
OCV	Open circuit voltage in Voltage
PC	Pre-calcined
PD_{max}	Maximum power density in W/cm^2
PF	Pore former
PV	Power density
Q_{fuel}	Volumetric flowrate
R_{ct}	Charge transfer resistance
R_{diff}	Mass diffusion resistance

R_s/R_{ohm}	Ohmic resistance
R_{tot}	Total resistance
ScSZ or ScCeSZ	(Ceria doped) scandia stabilised zirconia
SE	Secondary electron
SEM	Scanning electron microscopy
SOFC	Solid oxide fuel cell
TEM	Transmission electron microscopy
TGA	Thermo-gravimetric analysis
TPB	Triple phase boundary
TPO	Temperature programme oxidation
U_f	Fuel utilisation
XPS	X-Ray photoelectron spectroscopy
XRD	X-Ray diffraction
YSZ	Yttrium stabilised zirconia

TABLE OF CONTENTS

LIST OF FIGURES

LIST OF TABLES

CHAPTER 1: INTRODUCTION

1.1 Solid Oxide Fuel Cell (SOFC)

A fuel cell is an electrochemical device that can directly convert the chemical energy in a fuel feed into electricity without going through a combustion process to produce electricity with significantly lower net release of pollutants compared to other power generation processes. A fuel cell is similar with a battery in terms of direct conversion of the chemical compound to electricity, but different in terms of fuel supply. A battery contained the fuel inside the system while in a fuel cell, the fuel is supplied continuously, which potentially increases the operating time of the fuel cell indefinitely.

A solid oxide fuel cell (SOFC) is a high temperature fuel cell that operates between 600-1000°C with an efficiency of 60% to 92% if coupled in a combined heat and power (CHP) system [30]. SOFC is the only fuel cell that uses solid oxide (ceramic) as its electrolyte, which alleviates corrosion and leakage problems faced in high temperature fuel cells with liquid electrolytes such as the Molten Carbonate Fuel Cell (MCFC).

The significant advantage of the SOFC compared to other fuel cells is its fuel flexibility. Besides pure hydrogen, various fuels such as ethanol, kerosene, methane and biogas can fuel SOFCs [32, 33]. SOFC offer on-site uninterruptable electricity supply thus independent from power cuts and distribution problems. This makes this technology easily adaptable to server – based companies that require high levels of energy security such as Microsoft, Google, Apple, and AT&T. The ability to produce energy on-site is particularly useful for countries with isolated islands and difficult terrains such as Japan and South Korea. The success of the CHP-SOFC residential application of ENE-FARM (Japan) especially in terms of environmental effect has guided the government's decision to support the installation of 2.5 million units by the year 2030.

1.1.1 SOFC working principle

In SOFC, redox (reduction and oxidation) reactions take place at high temperature as prescribed by the solid electrolyte materials. Figure 1-1 summarises the working principle of an SOFC with air and hydrogen as fuel. The air is fed at the cathode side and oxygen is reduced with electrons from the external electrical circuit when the oxygen molecules reach the cathode/electrolyte interface.
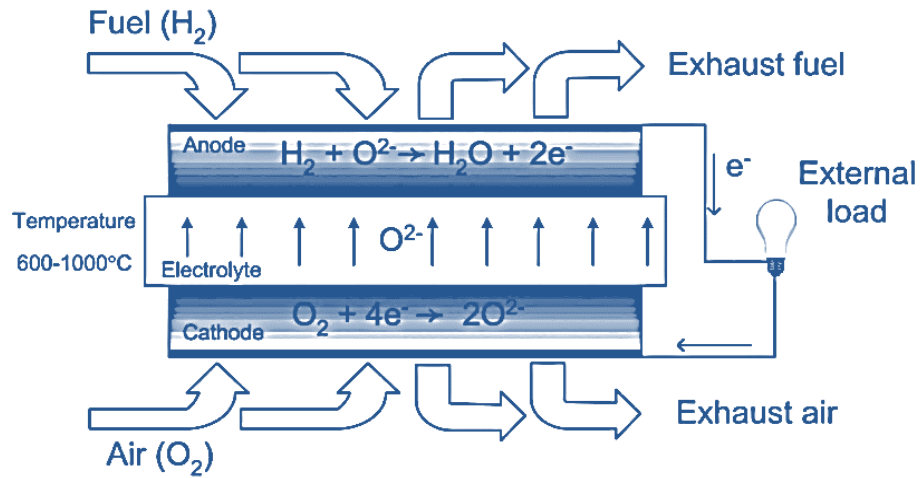
Figure 1-1: Schematic of an SOFC with hydrogen as fuel [5].

The half-cell reaction at the cathode side may be expressed as:

$$O_2 + 4e^- \rightarrow 2O^{2-} \qquad \text{[Eq. 1.1]}$$

The oxygen ions are then incorporated into the solid electrolyte and migrate to the anode side. At the anode/electrolyte interface, a catalyst (usually Ni) oxidizes the fuel gas that is fed to the anode with the help of oxide ions. The half-cell reaction at the anode side is:

$$H_2 + O^{2-} \rightarrow H_2O + 2e^- \qquad \text{[Eq. 1.2]}$$

Thus, the overall reaction then is:

$$H_2 + {}^1/_2 O_2 \rightarrow H_2O \qquad \text{[Eq. 1.3]}$$

Only water, heat and electrons are produced from the reaction. The electrons flow through the external circuit delivering electricity, and the heat generated has to be removed or can be used for combined heat and power (CHP) application which gives a higher total efficiency of up to 92% [34].

The electrochemical potential of the SOFC with hydrogen as fuel can be expressed by the Nernst equation:

$$E = E^0 + \frac{RT}{2F} ln \left(\frac{p_{H_2} p_{O_2}^{1/2}}{p_{H_2O}} \right) \qquad \text{[Eq. 1.4]}$$

Where,

$$E^0 = -\Delta G^0_{rxn}/2F \qquad \text{[Eq. 1.5]}$$

E is the Nernst potential which represents the ideal standard potential for the cell reaction, E^0 is the reversible potential, and $-\Delta G^0_{rxn}$ is the Gibbs free energy of the reaction Eq. 1.3 both at temperature T, R is the universal gas constant with value of 8.314 J/mol.K, and F is the Faraday constant with value of 96485 C/mol. p_{H_2}, p_{O_2} and p_{H_2O} present the partial pressures of hydrogen, oxygen and water vapour, respectively. The reversible potential, E^0 is also known as electromotive force (EMF) or open circuit voltage(OCV) [35]. Substituting the ΔG^0_{rxn} value of -188.6 kJ/mol and the Faraday constant of 96485 C/mol in Eq. 1.5 gives an OCV value of 0.99 V at 800°C (1073K). As the enthalpy is energy dependent, at 1000°C (1273K), the OCV reduces to 0.91V [1].

In real fuel cell operation, the measured open circuit voltage (OCV) value is usually less than the theoretical value as the theoretical value is the reversible potential. The OCV is the first indicator for the quality of the SOFC's cell electrolyte. Low OCV values and an OCV drop

usually indicate not fully dense electrolyte, cracked electrolytes or leakage from sealing of the cell to the holder, as would follow from Eq. 1.4 when the partial pressures deviate from the ideal.

1.1.2   SOFC Design

Because of the all solid parts, the SOFC is the only fuel cell that can possibly exist in two different geometries; planar and tubular fuel cell. Planar SOFC has the advantages in terms of the power produced and ease of manufacture while tubular fuel cells are said to be more stable in operation, having no thermal mismatch problem with the support structure and better at thermo-cycling. Due to the higher power density and the ease of fabrication of planar fuel cells, more focus is given to planar fuel cells.
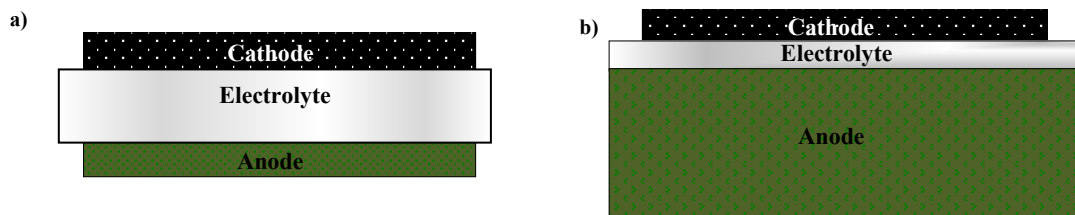
Figure 1-2: Different SOFC structures; a) electrolyte supported cell (ESC), and b) anode supported cell (ASC).

The most common configuraton in planar fuel cells is either the anode supported cell or the electrolyte supported cell. Figure 1-2 shows the configuration for both setups. Previously, cathode supported fuel cells were considered to have a potential as they exhibited the least degradation, however due to high materials and manufacturing cost, this design has been abandoned [36].

Electrolyte supported cells are suitable for high temperature SOFC (1000°C); as a high temperature is needed to reach satisfactory conductivity due to high ohmic resistance originating from the thick electrolyte [37]. The thickness of the electrolyte, anode, and cathode

are usually around 100 to 200μm, 50 μm, and 50 μm, respectively [38]. The advantages of a thick electrolyte layer are; higher mechanical strength due to high density of the ceramic materials and better sealing properties that prevents reactant cross-over [38].

In recent years, more focus has been laid on reducing the degradation of SOFC by reducing the operating temperature. For this reason, in the intermediate temperature SOFC (650-800°C), anode supported cells are preferred due to higher performance as it has a thin electrolyte; hence low ohmic resistance [36, 39]. For anode supported cells, the thickness of the anode substrate is between 500 to 1500 μm, with thin anode functional layer, electrolyte, and cathode layer[38]. The optimum thickness of the anode functional layer is between 5 to 10 μm, electrolyte is between 5 to 10 μm, and cathode 50 μm [38].
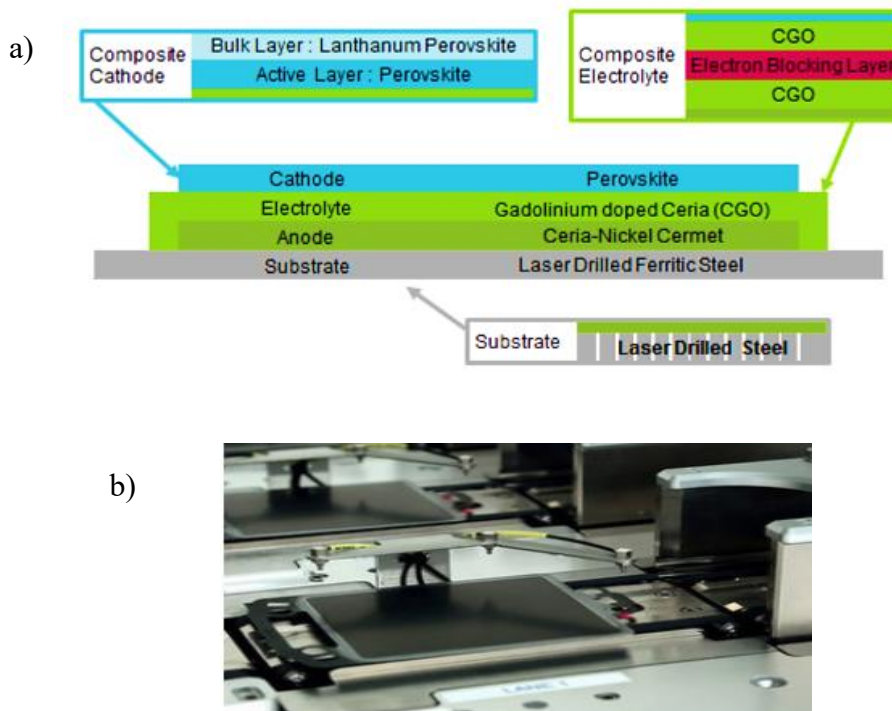
*Steel-cell dimensions are not disclosed by CERES power

Figure 1-3: CERES Power Steel-Cell a) component and structure [6] b) in manufacture.

Another approach in the planar cell is using inert metal or ceramic as support to emphasize the mechanical strength, hence achieving better cell durability as seen with by Rolls-Royce in their flat ceramic tube introduced in 2003 with a durability of 40, 000 hours. The famous steel-cell by CERES power uses an inert drilled steel metal support with multilayer active composite electrodes screen-printed on top as shown in Figure 1-3.

1.1.3 SOFC Components

The three basic components of the SOFC are anode, electrolyte, and cathode as shown in Figure 1-4. As our research is working with manufacturing anode supported cells, the discussion onwards will be narrowed to the anode supported cell configuration due to the reasosn explained in previous sub-section (Section 1.1.2).
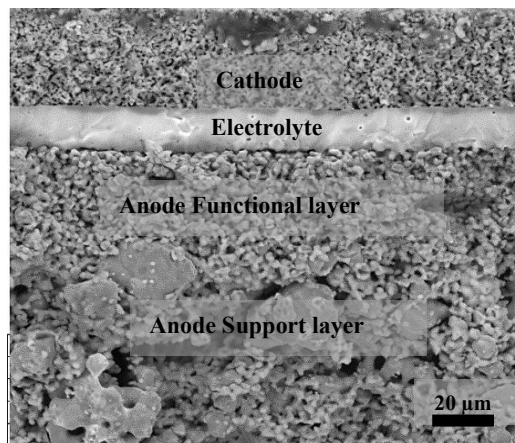
Figure 1-4: Microstructure of SOFC cell with bi-layer anode.

1.1.3.1 Anode

The function of the anode is to provide reaction sites for the electrochemical oxidation of the fuels. For anode supported cells (ASC), the function of the thick anode support is to provide mechanical strength to the cell and extended reaction sites. Coarse nickel oxide powders with additional pore former are used in manufacturing to develop pores for mass diffusion of the

fuel. Another thin anode layer (~10 μm) which is called the 'anode functional layer' or AFL made from finer nickel oxide powders is applied on top of the anode support as the anode reaction zone. The reaction will only take place in the triple-phase-boundary region (TPB) which is defined as the sites where the electron-conducting phase (metal), oxide ion conductor (electrolyte) and gas phase (fuel that fills the pores) all meet together as shown in Figure 1-5 [22]. If the TPB is not connected to the electrolyte, the anode and the anode electrical connection, the electrochemical reaction will not occur. An increase in TPB length is critical in improving the SOFC performance.
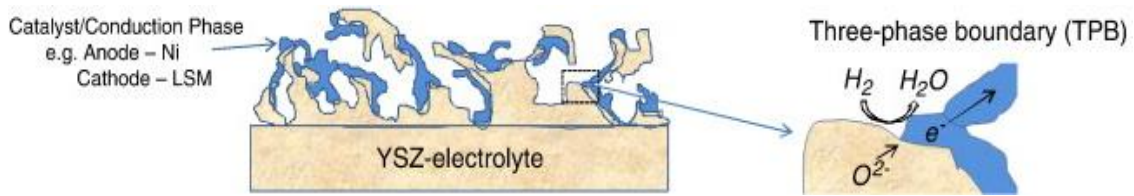
Figure 1-5: Triple phase boundary (TPB) where reactions occur in the SOFC [22].

The state-of-the-art material for SOFC anodes is a Ni/YSZ cermet (mixture of ceramic and metal material). The ceramic material, yttrium stabilised zirconia (YSZ), provides high oxygen ion conductivity above 700°C. The electrolyte material role in the anode is 1) to increase the anode performance by providing more extension to the TPB, 2) to control the thermal expansion mismatch between electrolyte and Ni based anode, 3) to avoid Ni agglomeration, and 4) to improve the mechanical stability. To complement the high temperature requirement, Ni has been widely used with regards to its promising high electronic conductivity, providing the required catalytic activity for electrochemical reaction, a high stability under chemically reducing conditions, low cost and thermal stability at high SOFC operating temperature [26,

40]. Nickel is also commonly used as a catalyst for methane reforming reaction for SOFC fed with hydrocarbon fuels.

The ratio of the cermet components, the starting material size, and the processing conditions greatly affect the electrical conductivity and electrochemical performance of the anode. Higher nickel content leads to higher electrical conductivity as shown by Figure 1-6, with 40 vol% of nickel found to have the lowest anode polarisation resistance [26]. Koide et. al [41] suggest that the optimum composition of bi-layer anodes is 61:39 by volume ratio of Ni:YSZ on the thin anode functional layer (AFL) and 40:60 by volume ratio for the thick anode substrate (AS). The volume ratio of 40:60 of Ni:YSZ in the anode substrate (AS) was also adopted by Forschungszentrum Jülich (FZJ) and Pacific Northwest National Laboratory (PNNL) [26].
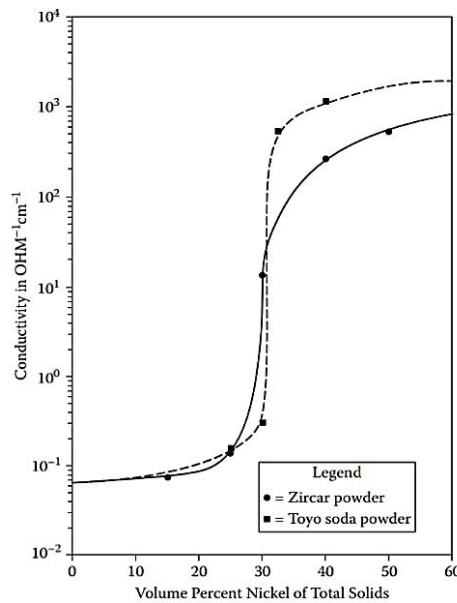
Figure 1-6: Electrical conductivity with respect to Ni content [16].

1.1.3.2   Electrolyte

The function of the electrolyte is to conduct oxide ions between the cathode and anode. The electrolyte must have high ionic conductivity at the cell operating temperature and little or no

electronic conduction to minimise leakage currents [4]. The electrolyte needs to be dense, thin, and leak-proof to avoid fuel cross-over and to reduce ohmic resistance.

The state-of-the-art material for SOFC is the 8 mol% yttrium stabilised zirconia (8YSZ) with regards to the material stability, high ionic conductivity, mechanical strength, and cost, despite the higher ionic conductivity of scandium stabilised zirconia (ScSZ). Figure 1-7 and 1-8 shows the conductivity of YSZ at different molar concentration of Y_2O_3, which shows the 8 mol% has the highest conductivity value. At lower molar concentration, 2 to 2.5 mol% will produce a tetragonal ZrO_2 which has high mechanical strength, but lower conductivity. With a molar concentration of 3-7 mol% of Y_2O_3 will produce a mixture of cubic and tetragonal phase will be produced which also has a low conductivity value [42].
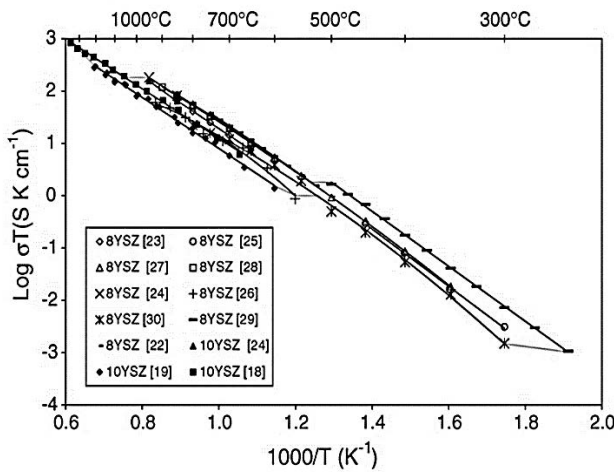
Figure 1-7: 8YSZ and 10YSZ conductivity across several references [4].
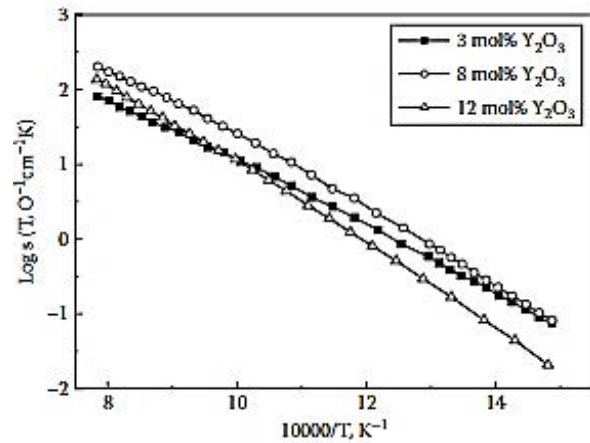
Figure 1-8: YSZ conductivity at different mol% concentration [10].

1.1.3.3   Cathode

The cathode layer provides reaction sites for the electrochemical reaction for reduction of the oxidant. The cathode layer needs to have a high electronic conductivity, thermal and chemical compatibility with the electrolyte, and high catalytic activity for the oxygen reduction reaction.

For high operating temperature (800-1000°C), strontium-doped lanthanum manganese (LSM), offers an excellent thermal expansion match with zirconia and provides good performance. For intermediate temperature, IT-SOFC (600-800°C), strontium-doped lanthanum cobalt ferrite (LSCF) is more suitable. A gadolinium doped cerium (GDC or CGO) interlayer is needed between the electrolyte and the LSCF cathode to avoid reaction between cobalt and zirconia forming resistive phases of $La_2Zr_2O_7$ and $SrZrO_3$.

1.1.4   SOFC Performance Characterisation

The standard representation of a fuel cell electrochemical performance is illustrated by the polarisation curve with voltage and current density relationship (*i*-V curve) as shown by Figure 1-9. Real fuel cell operation potential is less than the ideal potential as there are potential losses during fuel cell operation which are activation losses, ohmic losses, and mass –transport related losses. Note that the term overpotential, overvoltage, polarisation, voltage drop, losses, and irreversibility are interchangeable [43].
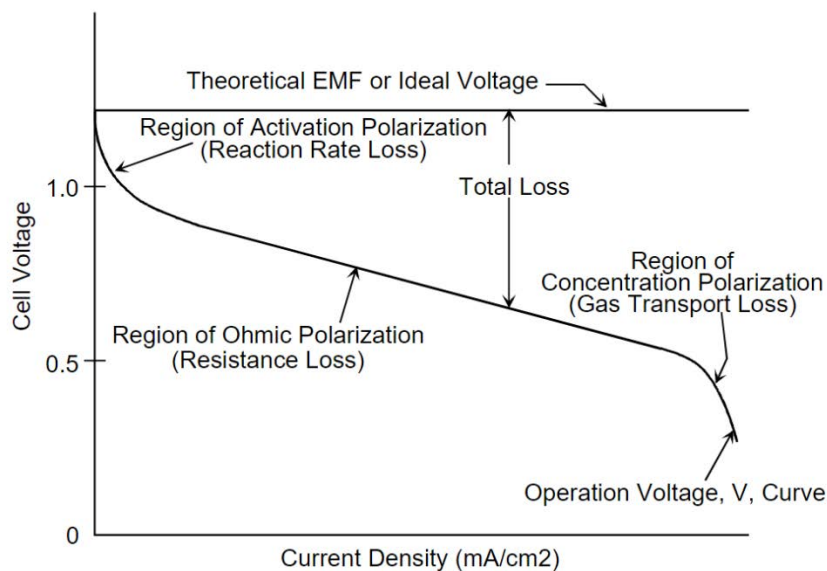
Figure 1-9: Typical polarisation losses in fuel cell system [1].

Activation losses are caused by the slow reaction at the electrode-electrolyte interface especially on the cathode surfaces as LSM has low ionic conductivity [44]. However, as SOFC operates at very high temperature, the non-linear region at low currents that indicate the activation losses is insignificant [43]. Ohmic polarisation is caused by the resistance of the ion flow in the electrolytes as well as electron flow in the electrodes and interconnects [43]. The contribution of each component depends on the geometry of the fuel cell. In planar SOFC, the ohmic resistance contribution for the electrolyte supported cell (ESC) mainly originates from the electrolyte while for anode supported cell (ASC) with thin electrolyte, the ohmic resistance is largely contributed by the interconnects and current-collection as the contribution from the electrolyte becomes insignificant because of the thin layer [45]. Ohmic resistance (R_{ohm}) represents the resistance in electrolyte and interconnects;

$$R_{ohm} = R_{electrolyte} + R_{interconnect}$$

Mass-transfer polarisation or concentration polarisation is due to resistance to mass transport to the electrodes and interfaces. A large voltage drop shows at higher current density when the electrolyte/electrode interface experiences shortage of reactant species, amongst others due to slow diffusion through the electrodes [44].

The area specific resistance (ASR) represents the resistance value of the whole cell which can be calculated from the slope of the iV-curve. The highest ASR will be calculated near the OCV while a low ASR will be derived at a lower point in the iV-curve. Although it is very tempting to calculate the ASR at low current densities (0.5 A/cm^2 and below), it will not represent the actual resistance value of the cells. Based on Hauch et al [46], if the gradient is fairly constant, the ASR value can be calculated from the iV curve by;

$$ASR = \frac{OCV - V}{I_v} \qquad\qquad \text{[Eq. 1.6]}$$

However, as the polarization curve has changing slope due to it's shape, the best way to calculate the ASR is from the gradient of the precise operating points in question. The ASR value will be more accurate with in-situ measurement using Electrochemical Impedance Spectroscopy (EIS). In-depth EIS study can identify each components contribution towards the total ASR. This process is very lengthy and time-consuming. Besides the data from the single-cell test, data from a symmetrical cell for each component is essential to analyse the impedance completely. The EIS response (Nyquist plot) usually consists of two or more semicircles. In an electrode-supported thin-film electrolyte system, polarisation dominated by the electrode process as the contribution from the electrolyte is insignificant. The resistance from the electrode process consists of; the mass diffusion resistance (R_{diff}) which usually relates to changes of fuel flow rate, or partial pressure reflected by the semi-circles at a lower frequency range whereas the charge transfer resistance (R_{ct}) indicated by the semi-circles at higher frequency range as shown in Figure 1-10 [47].
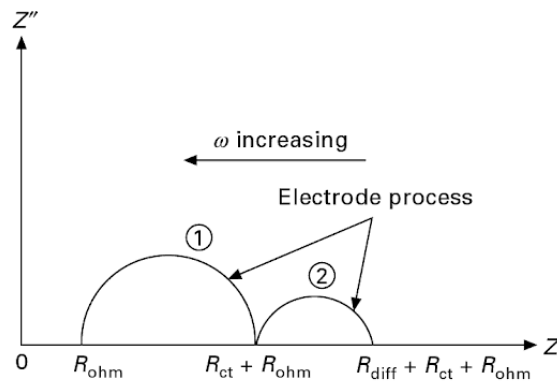
Figure 1-10: A typical impedance spectrum for an electrode-supported thin film electrolyte system [11].

In some cell testing setup, very low fuel utilisation (i.e very high fuel flowrate) are used to obtain high electrochemical performance. As this will not be portrayed in the ASR value, it is

necessary to supply the fuel utilisation value in the report. In practice, maximum power density value plotted on the *iV*-curve graph are often used for electrochemical performance comparison. With additional information on the ASR value and fuel utilisation value and temperature, the electrochemical test comparison will be more accurate [46].

1.1.5   Hydrocarbon Fuel SOFC

The most significant advantage of the SOFC is that it can operate with various types of fuel other than hydrogen. Pure hydrogen is expensive as the route of producing hydrogen can be very long and costly even if the energy source originates from renewable material. Using biogas, and other carbonaceous bio-fuels for SOFC operation without converting this to pure hydrogen is an extremely more efficient way to reduce the carbon footprint. This is deemed possible as since 2011 BloomEnergy$^{®}$ has implemented the use of natural gas and biogas with their patented SOFC based server (BloomEnergy Server $^{®}$) delivering 200kW of power [48].

Typically, for an SOFC power plant using a hydrocarbon fuel, the plant is equipped with hydrogen sulphide (H_2S) scrubber and fuel reformer chamber prior to feeding the SOFC. Theoretically, direct utilisation of hydrocarbons as fuel for SOFC is possible as Ni is also a catalyst for the dry reforming reaction. One of the interesting carbon fuels high in interest is biogas since abundant amounts of biogas are readily available from wastewater treatment, or originating from various agricultural activities, especially in developing countries. Utilising biogas directly as fuel is highly desirable in terms of environment and cost.

Biogas consists of methane, carbon dioxide, and traces of impurities. With direct use of biogas fuel, the possible reactions between methane and carbon dioxide that may take place are shown in Eq. 1.7 and 1.8.

Carbon dioxide (dry) reforming [49, 50]:

$$CH_4 + CO_2 \rightarrow 2H_2 + 2CO \qquad \Delta G_{f\ 700°C} = -23.82\ kJ/mol \qquad \text{[Eq. 1.7]}$$
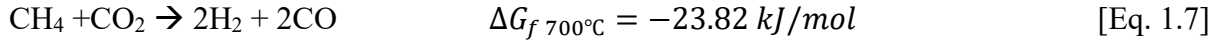
Reverse water-gas shift reaction [49, 50]:

$$CO_2 + H_2 \leftrightharpoons H_2O + CO \qquad \Delta G_{f\ 700°C} = -3.24\ kJ/mol \qquad \text{[Eq. 1.8]}$$
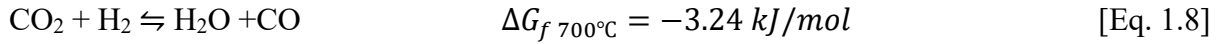
Unlike steam reforming, internal reforming usually accompanied with carbon deposition which leads to the anode deactivation. The possible reactions for carbon deposition are by methane cracking (Eq. 1.9), the Boudouard reaction (Eq. 1.10) and the reverse carbon gasification reaction (Eq. 1.11) [49, 50].

$$CH_4 \leftrightharpoons C(s) + 2H_2 \qquad \Delta G_{f\ 700°C} = -16.34\ kJ/mol \qquad \text{[Eq. 1.9]}$$

$$2CO \leftrightharpoons C(s) + CO_2 \qquad \Delta G_{f\ 700°C} = 0.76\ kJ/mol \qquad \text{[Eq. 1.10]}$$

$$H_2 + CO \leftrightharpoons C(s) + H_2O \qquad \Delta G_{f\ 700°C} = 4.00\ kJ/mol \qquad \text{[Eq. 1.11]}$$
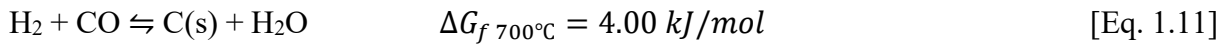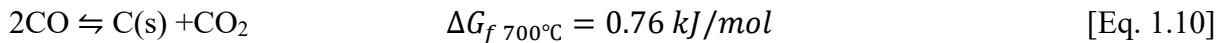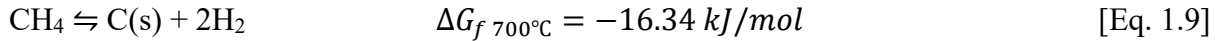
For SOFC operation above 700°C, carbon formation via Boudouard reaction (Eq. 1.10) and reverse carbon gasification reaction (Eq 1.11) are not favourable as their Gibbs free energy value are positive. Hence, the source of carbon deposition for an SOFC operating at this temperature will be only by methane cracking.

The product from the reforming reaction, CO and C then will be electrochemically oxidized at the TPB. Even though the carbon on the anode can be oxidized into CO, it depends on the catalytic activity of the materials. If there is a carbon buildup, the carbon deposition will lower the volume of triple phase boundary (TPBs) resulting from the deactivation of Ni catalyst and inhibition of fuel diffusion in the anode. After some time, this will deactivate the entire SOFC anode. Example of this phenomenon can be referred to Figure 1-11 which shows carbon growth

on Ni/YSZ anode after 4 hours of exposure to humidified methane. Figure 1-12 [51] shows severe carbon deposition on Cu-CeO$_2$-ScSZ after exposed in ethanol for 300 hours at 800°C. Note that in Figure 1-12, anode pellets exposed to ethanol in a quartz chamber, not in SOFC mode. In the SOFC mode, the carbon deposited on anode surface (especially near the TPB area) can be electrochemically oxidised into CO or CO$_2$ depending on the catalyst ability and rate of reaction, but the effect will not be as severe.
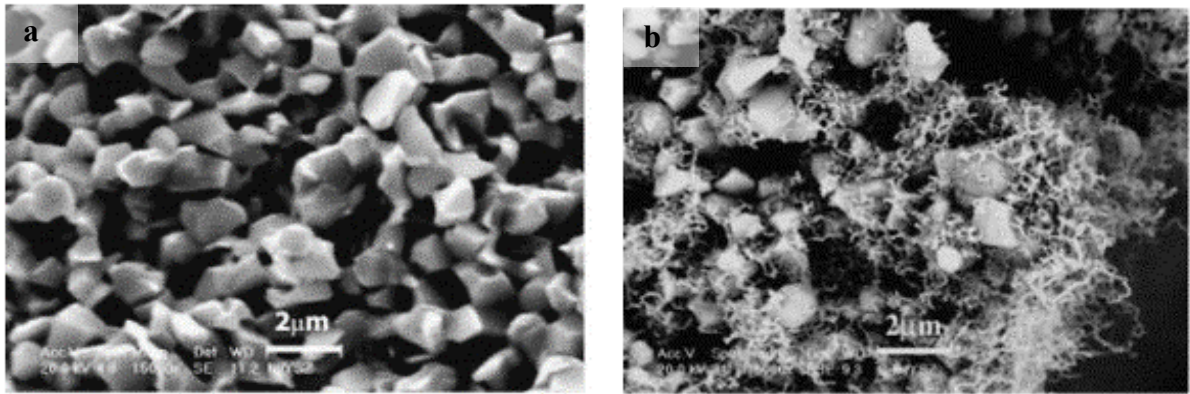
Figure 1-11: Microstructure of Ni/YSZ anode a) before, and b) after exposed to humidified methane at 600°C [52].
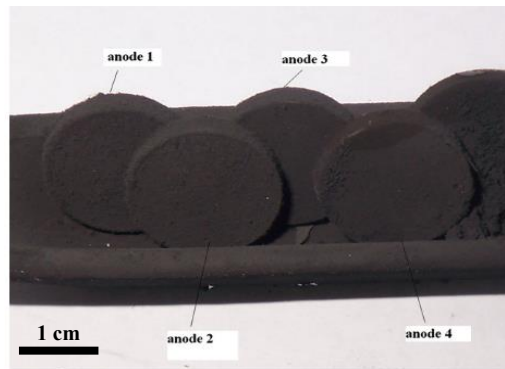
Figure 1-12: Cu-CeO$_2$-ScSZ anode pellets after 300 hour exposure to pure ethanol at 800°C [51].

Carbon can form in different morphology; amorphous, filamentous and graphitic. The carbon morphology depends on the carbon interaction with metal catalyst [50], the influence of the crystal structure [51, 52], thermodynamic condition and SOFC reduction condition [53, 54].

For SOFC operating in the range of 750-800 °C with high catalyst surface area in the anode, the most likely type of carbon form is amorphous carbon that can be in two different form, either as film or filamentous. Several reports also found graphitic carbon in SOFC operating at 700-800°C [53, 54]. For carbon filaments, Alstrup [55] suggested; initially, carbon filament growth starts from carbide, causing the re-construction of the metal particle. The carbide later decomposes into carbon filament and metal. After decomposition, the surface carbide still present in which, at the steady state growth period the carbon atoms produced by the surface reaction diffuse rapidly through the surface carbide, maintaining a constant carbon concentration below the edges.

According to Boldrin et al. [24], there are several situations where carbon can lead to anode deactivation: 1) multi-layers of carbon chemisorbed or attached by physical adsorption on metal surfaces, 2) encapsulation by carbon particles, that deactivates the metal completely, 3) growth of carbon filaments (whisker carbon) that can stress and fracture the support or push the metal particles of the support, 4) pore blockage, and 5) dissolution of carbon atoms into the metal causing a volume expansion. In SOFC, situation 3 and 5 can destroy the whole cell structure [24]. Figure 1-13 [24] shows the illustration some of these different carbon deposition behaviour.
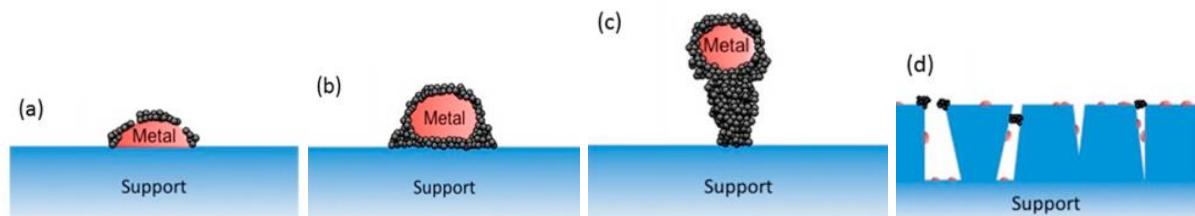
Figure 1-13: Different carbon deposition behaviour that leads to anode deactivation [24].

Nevertheless, not all carbon growth gave a negative impact on the SOFC cell operation as in several cases, a small amount of graphitic carbon growth enhanced the electrochemical performance [15, 53, 54]. Mallon and Kendall [54] suggest that the enhancement with a small amount of graphitic carbon deposited was due to improved nickel anode conductivity from the network growth.

1.2 Motivation

The advantage of SOFC with direct fuel utilisation is compromised when degradation of the anode due to carbon deposition and sulphur poisoning becomes a major problem. Even though a lot of research has been going on to avoid anode degradation, the development of alternative anode materials that can offer high power performance with less carbon deposited at acceptable cost has not yet been achieved. Either the electronic conductivity is too low, or the cost is too high when using precious metals as additional catalyst.

Despite the low attention that has been given to Ni/ScCeSZ cermets in the last decade, this material actually holds advantages over the benchmark material Ni/YSZ and other alternative anode materials. It exhibits less carbon deposition [14, 15], better tolerance to sulphur poisoning[55] and higher ionic conductivity [4]. To the author's knowledge, only electrolyte supported Ni/ScCeSZ SOFC cells are available in the market, while anode supported Ni/ScCeSZ SOFC cells have not been widely commercialised. Furthermore, it is interesting to use the Ni/ScCeSZ as anode support material as the anode substrate layer is the region where the reforming reaction expected to occur to transform the hydrocarbon fuel into hydrogen and carbon monoxide as the reactant.

Another present challenge for developers is to produce robust and high performance SOFC cells using low cost materials and fabrication methods [1]. Different strategies are being explored either through alternative materials or at cell manufacturing level. For cell manufacturing, typically SOFC companies such as Versa Power and IdealCell produce SOFC cells via solvent tape casting as it is possible to produce at a large scale at low cost. Current enhancement in research in the tape casting process has shifted interest to more environmental friendly processes using aqueous based and multi-layer tape casting that also leads to single step co-sintering.

In the past, research using Ni/ScCeSZ has been carried out using other preparation procedures but work done via aqueous tape casting has been very limited with a lot of parameters left undefined. Furthermore, despite of extensive efforts on optimising the manufacturing parameters, previous work by our research group using a pellet pressing method was not entirely successful to produce an anode supported Ni/ScCeSZ cell that met the requirements of an SOFC cell.

1.3   Research Context/Focus

This thesis focuses on producing an anode supported SOFC cells with Ni/10ScCeSz anode substrate via aqueous tape casting for direct utilisation of carbonaceous fuel. Prior to producing the Ni/ScCeSZ cells, the aqueous tape casting method was perfected first for Ni/YSZ anode supported cells. To compare the suitability of both Ni/YSZ and Ni/ScCeSZ with carbon fuel, SOFC cell tests were carried out using hydrogen and simulated biogas. Electrochemical performance was monitored to evaluate and understand the differences in both materials with regard to both fuels. The final part of this work is to further enhance the Ni/ScCeSZ cell by introducing tin (Sn) as dopant to achieve the goal of improving the tolerance with hydrocarbon

fuels (biogas in this case study). Tin was chosen as dopant as continuation of the previous work done in the research group [50, 56].

1.3.1 Aim/Objectives

- Fabricate anode supported in-house cells using two different materials; NiO/YSZ and NiO/ScCeSZ using the aqueous tape casting method. Make adjustments needed to adapt to different material properties.

- Evaluate the performances of Ni/ScCeSZ cells compared to Ni/YSZ cells in hydrogen and biogas, with the aim to prove Ni/ScCeSZ will show better performance in biogas.

- Produce an improvised high performance SOFC anode using Sn-Ni/ScCeSZ with better tolerance to hydrocarbon fuels.

CHAPTER 2: ALTERNATIVE MATERIALS AND MANUFACTURING

2.1 Overview

Originally, fuel cell technologies were expected to significantly reduce the dependencies on oil and resulting environmental impacts. However, the capital cost of SOFC itself and the operation cost associated with hydrogen as fuel make it almost impossible for developing countries to invest in this technology. To bridge the gap, using more readily available hydrocarbon fuels than hydrogen would reduce the operating costs for electricity generation. This can be achieved through a cleaner process than the combustion engine, resulting in less pollution. Hence, the development of SOFC cell that can tolerate hydrocarbon fuels is highly important.

This literature review chapter will be divided into two main sections. The first part introduces alternative electrolyte and anode materials for hydrocarbon operation, focusing on scandia stabilised zirconia (ScSZ) and up-to-date research on Ni/ScSZ as one of the promising material for hydrocarbon fuels. The second part will cover the manufacturing process focusing on aqueous tape casting for SOFC and multilayer tape casting processes.

2.2   10Sc1CeSZ as alternative electrolyte materials

Electrolyte materials can be divided into four categories; zirconia based, ceria based, lanthanum based, and other materials [57]. Based on Figure 2-1 [9], five electrolyte materials with the highest conductivities and hence suitable for intermediate SOFCs are; YSB (bismuth oxide based electrolytes), followed by LSGMC and LSGM (lanthanum gallate electrolytes), GDC (gadolinium doped ceria), and ScSZ (scandium stabilised zirconia). Compared to zirconia, other oxides may have higher conductivity, but they have their disadvantages such as high electronic conductivity, high cost, and manufacturing difficulty [9].
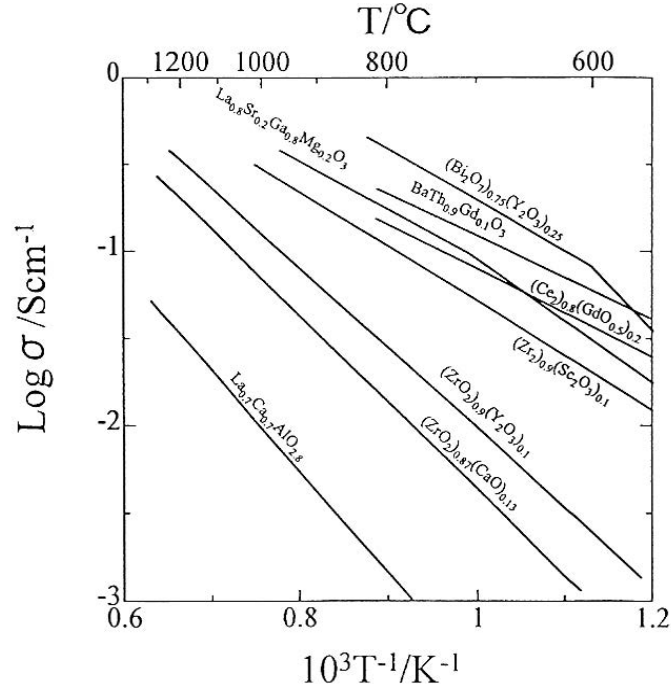
Figure 2-1: Conductivity of different ionic conductors [9].

Bismuth-based electrolytes have the highest conductivity compared to other oxides. Yet, it has not been widely researched as SOFC material as it has phase transformation and structural stability problems [58]. Ceria based electrolytes have purely ionic conductivity at high oxygen partial pressure but becomes partially reduced on the anode side of the SOFC which is undesirable as this increases the electrical conductivity, leading to short circuit [9, 57]. Lanthanum gallates electrolyte have shown higher ionic conductivities compared to zirconia based electrolytes but faced gallium evaporation at low oxygen partial pressure reducing atmosphere, mechanical instability, issues with the production of thin films, and higher cost as previewed by Wincewicz and Cooper [57].

Zirconia on the other hand, is commonly used because of several attributes: availability of the material, chemical stability, non-toxicity, and relatively cheap raw materials [40]. Among the zirconia based electrolyte, ScSZ is a very promising alternative electrolyte material based on the high conductivity. Conductivity of ScSZ at 850°C is approximately 1.5 higher compared to

YSZ. However, certain doping ratios of scandia doping can result in phase transition and aging. Onward discussion of this point will focus on the background of ScSZ electrolyte.

2.2.1 Phase structure and conductivity of 10Sc1CeSZ

High temperature zirconia (ZrO_2) exists in cubic fluorite structure between 2680°C and 2370°C, and transforms to tetragonal below 2370°C and monoclinic below 1170°C [42]. The cubic phase is desirable as it has the largest oxygen-vacancy conduction ($\sigma_{v\ddot{o}}$), which leads to high conductivity values. The size of the Zr^{4+} ion is too small to sustain the fluorite structure at room temperature; hence it has to be substituted by larger cations of lower valence, which also introduces oxygen vacancies [2]. Doping zirconia with 8-9 mol% of yttrium oxide (Y_2O_3) or scandium oxide (Sc_2O_3) stabilises the cubic phase of zirconia at room temperature. Figure 2-2 shows the substitution of the ions in the sublattice to stabilize the cubic phase. When the Y^{3+} or Sc^{3+} cations replace Zr^{4+}, a vacancy is created in the sublattice as three O^{2-} ions replace four O^{2-} ions in the structure[9, 26]. The vacancy causes electron movements which creates energy potential.
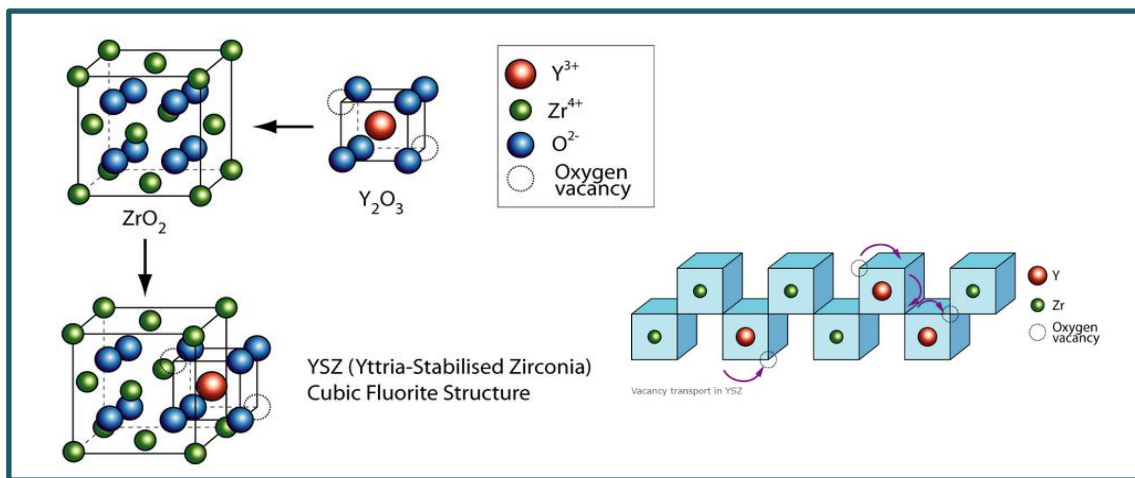
Figure 2-2: Substitution of Zr^{4+} with Y^{3+} in the ZrO_2 sublattice [2].

Kroger-Vink notation is a standard notation for defects for ionic crystal. For ScSZ, the Kroger-Vink notation for the association of Sc_2O_3 and ZrO_2 can be written as:

$$Sc_2O_3(ZrO_2) \rightarrow 2Sc'_{Zr} + 3O_0^x + V_O^{\cdot\cdot} \qquad \text{[Eq 2.1]}$$
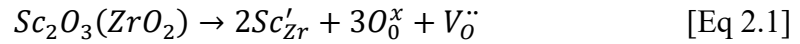
Scandia stabilised zirconia (ScSZ) has the highest ionic conductivity because of the smaller size mismatch between Zr^{4+} and Sc^{3+} ions compared to Zr^{4+} and Y^{3+} that leads to lower activation energy requirement for oxygen migration. Figure 2-3 and 2-4 shows the phase diagrams of doped zirconia systems at different molar concentration of Y_2O_3 and Sc_2O_3 respectively.
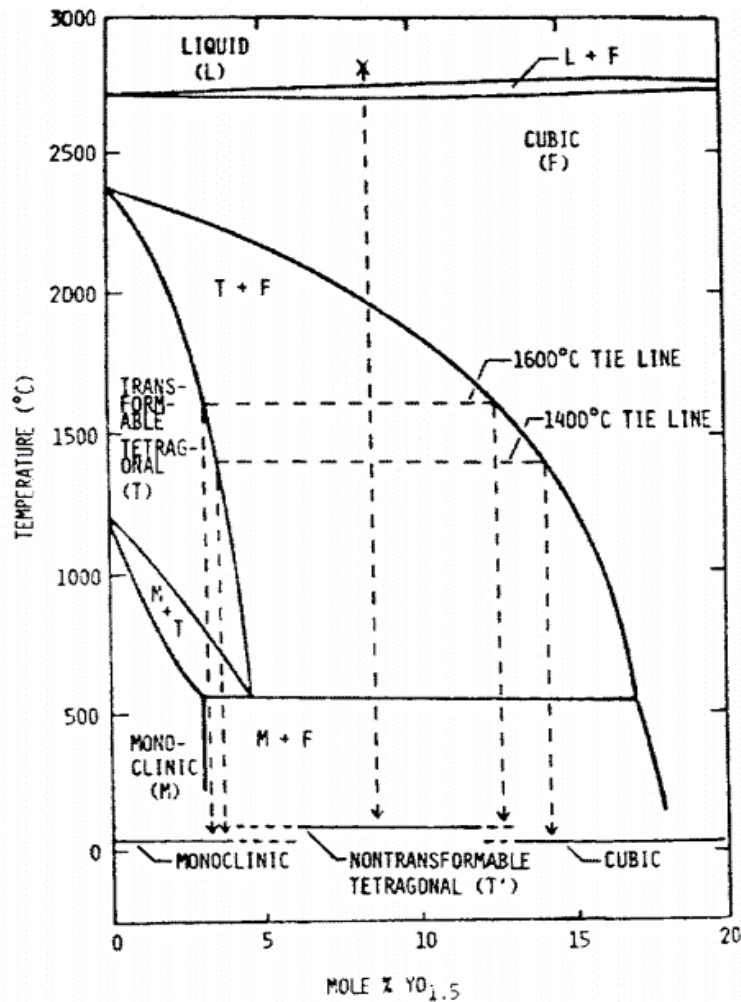
Figure 2-3: Phase diagram of YSZ [21].
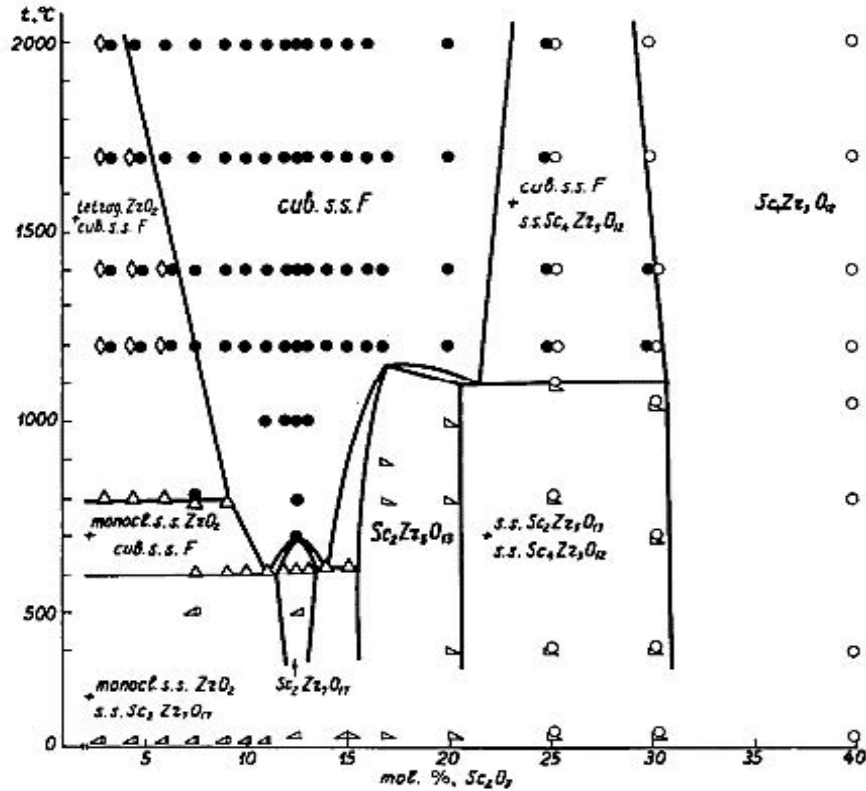
Figure 2-4: Phase diagram of ScSZ [17].

Fergus et al.[4] compared the conductivity values of YSZ and ScSZ at different molar concentration produced either by cold pressing/sintering sample or hot pressing. Their results on Figure 2-5 clearly display the superior conductivity of ScSZ compared to YSZ in all samples regardless off the fabrication method and molar concentration of the dopants. The maximum conductivity value achieved was with 8 mol% Y_2O_3 for YSZ and 10 mol% of Sc_2O_3 for ScSZ. This is in agreement with the report from Hearing et al. [29] as shown in Figure 2-6. At high temperature (950°C) the conductivity of 10ScSZ reached 0.275 Scm^{-1} while the lowest conductivity showed by 7ScSZ with value of 0.160 Scm^{-1}. The differences in conductivity were smaller at lower temperature (750°C) which were 0.075 Scm^{-1} and 0.025 Scm^{-1} for 10ScSZ and 7ScSZ respectively [29]. As the conductivity of 10ScSZ is the highest at most temperature, 10ScSZ is the most common form of ScSZ powder that is commercially available.
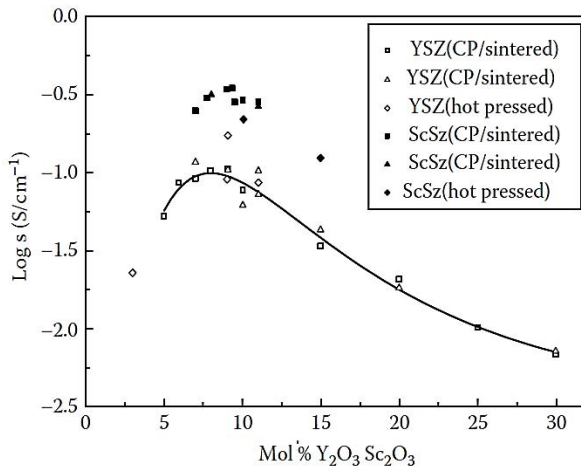
Figure 2-5: Conductivity of YSZ and ScSZ [4, 26].
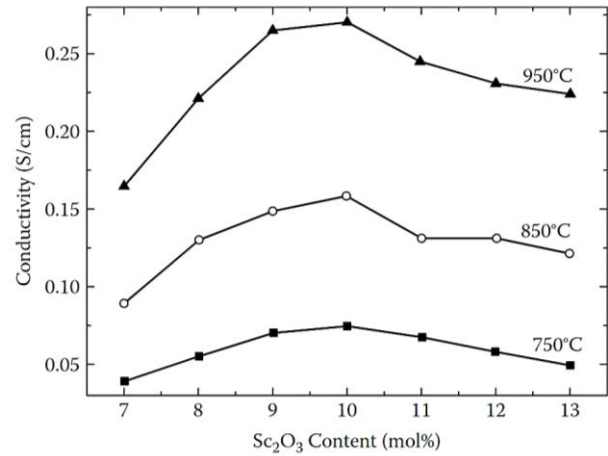
Figure 2-6: Conductivity of ScSZ with different mol% at different test temperature [29].

2.2.2 Aging effect on ScSZ

The effect of aging and structural changes on ScSZ with different dopant contents were studied by several authors. Sumi et al. [15] reported that high temperature annealing (1000°C), 8YSZ degrades by 16% per 1000 hour while ScSZ electrolytes show a steady conductivity at the annealed temperature as in Figure 2-7. Ukai et al. [59] reported that no significant decrease was observed with 10ScSZ samples after 2500 hours annealed at 1000°C. This is in agreement with one of several studies by Badwal et al. [23] for 10ScSZ and 11ScSZ at 1000°C. However, at 850°C, the resistivity increased and the aging effect were more significant due to the existence of different phase structure; cubic phase at high temperature and mixture of cubic and rhombohedral structures at lower temperature. The effect of phase changes was described as a 'jump' in the conductivity measurement during heating and cooling as shown in Figure 2-8 [23].
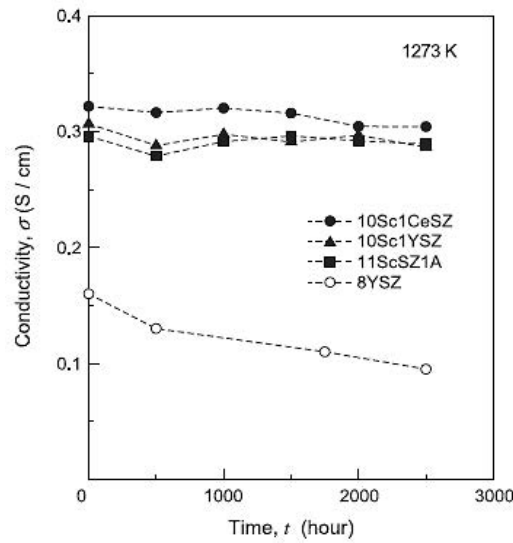
Figure 2-7: Electrical conductivity changes with annealing time of 10Sc1CeS, 10Sc1YSZ, 11ScSZ1A and 8YSZ at 1273 K (1000°C) [15].
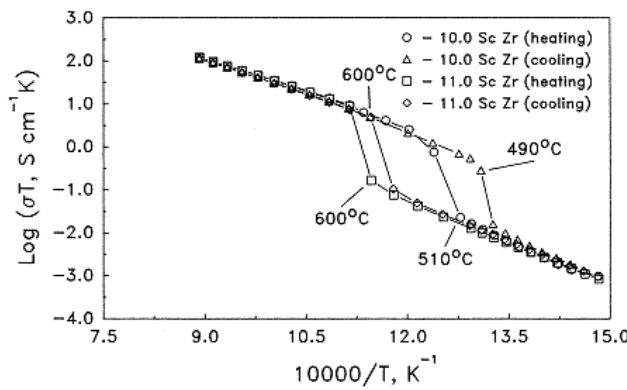
Figure 2-8: Conductivity 'jump' in 10ScSZ and 11ScSZ [23].
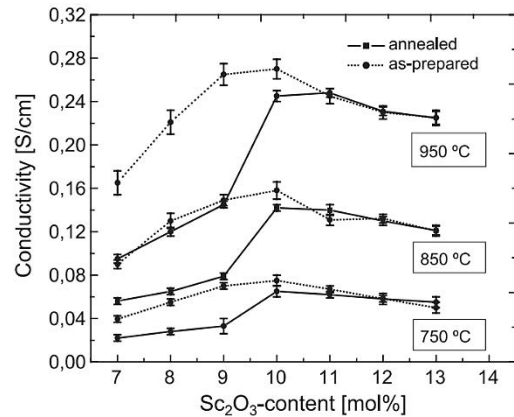
Figure 2-9: Conductivity at different temperature bas-prepared and annealed for ScSZ [29].

Haering et al. [29] also reported that at high temperature annealing (1000°C for 1000 hours), the phase structure of 10ScSZ consists of 90% cubic and 10% rhombohedral. Figure 2-9 shows the effect of annealing time at different temperatures on the conductivity of different zirconia-scandia systems as reported by Haering et al. [29]. Figure 2-7 also shows that 11ScSZ1A (alumina doped scandia stabilised zirconia) has lower conductivity compared to 10ScSZ but has the least degradation, which makes it suitable for long term operation. Nevertheless, because 10ScSZ has a higher conductivity, it is readily available compared to 11ScSZ.

26

2.2.3 Co-doping ScSZ

Figure 2-4 shows the structure diagram of ScSZ [17]. Co-doping 10ScSZ with other oxides such as Ce, Yb, Bi, Al and Gd prevents the phase changes from cubic to rhombohedral phase [4, 27]. The phase changes are undesirable as it shows significant decrease in conductivity due to less oxygen vacancy.

Haering et al. [22] shows that co-doping with small amount of alumina actually transforms the 10ScSZ cubic phase to rhombohedral instead of stabilising the cubic phase. It was observed that increasing the amount of alumina (Al_2O_3) to 5.5% increases the cubic phase structure. However, increasing the alumina amount is not of interest in SOFC as higher amount of alumina leads to a decrease in conductivity of ScSZ system [22]. This is important to note as Al_2O_3 is sometimes added as sintering aids to lower the co-sintering temperature of the electrolyte.
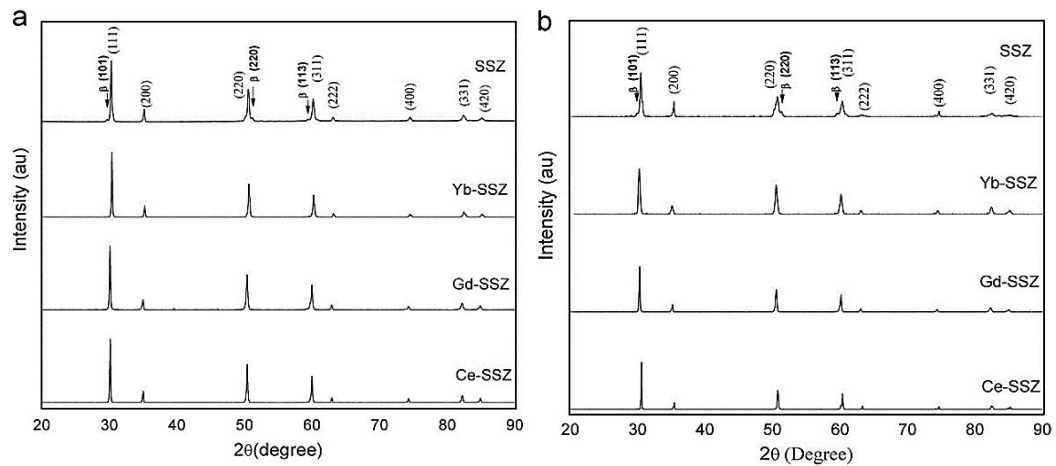
Figure 2-10: XRD patterns of ScSZ pellet with different dopant a) before aging, and b) after aging [27].

Kumar et al. [27] investigated the effect of co-doping with trivalent rare earth elements including ceria (Ce), ytterbium(Yb) and gadolinium (Gd) to ScSZ phase stability and conductivity after annealed at high temperature. The authors show that Ce gives the best result in improving the phase stability and preventing high temperature ageing as no secondary phases

reflected in the XRD patterns in Figure 2-10. Besides that, from the bulk conductivity shown in Figure 2-11, they concluded that 10ScSZ doped with Ce exhibits the least degradation after the high temperature annealing. Hence, most of the 10ScSZ commercial powders are doped with 1 mol% of CeO_2.
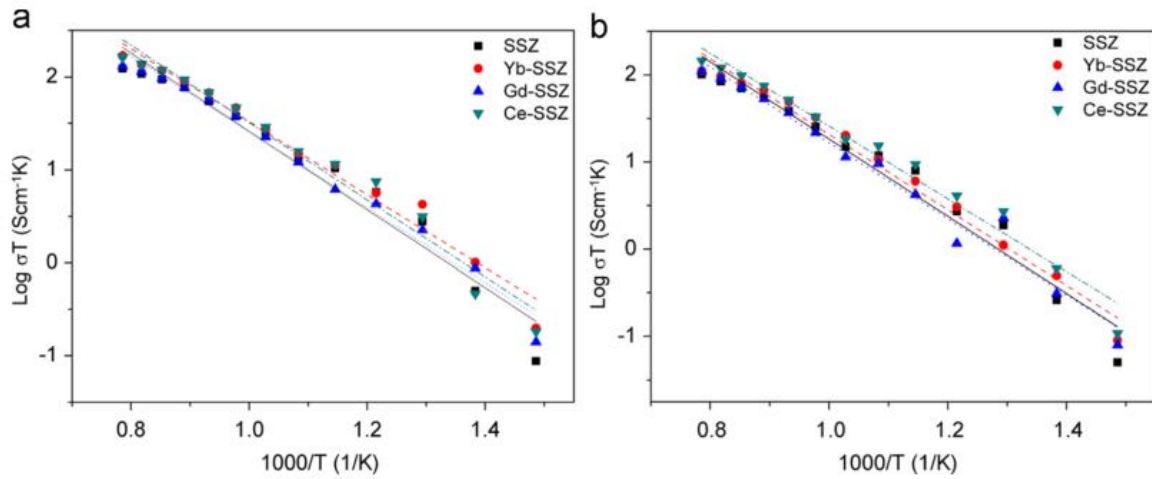
Figure 2-11: Arrhenius plot of ScSZ with different dopant a) before aging, and b) after aging [27].

Using XRD analysis, raman spectroscopy and conductivity data of the synthesised powder, Dasari et al. [60] suggested that 0.5 mol% of CeO_2 is sufficient to stabilise the cubic phase. 0.5 mol% CeO_2 gave even higher conductivity compared to 1 mol% and 5mol% of CeO_2 content. Recent studies reported successful doping of ScSZ with 1 mol% europium sexquioxide [61] and 0.5 mol% niobia [62].

2.3   Developing Ni/10ScCeSZ as carbon tolerant anode

SOFC exposure to hydrocarbon fuels may lead to anode deactivation if carbon produced by either methane cracking or boudouard reaction inhibits the triple phase boundary (TPB) area. Cu-base and Ce-based anodes have been considered as alternative anode material to replace Ni anode for hydrocarbon operations. Although Cu-based anodes reported to have higher tolerance to carbon deposition, Cu-based anodes have less reforming activity compared to Ni-based

anodes. Ceria-based anodes especially gladolinium-cerium oxide (GDC) is usually paired with ceria-based electrolyte which has issues with electrical conductivity at low oxygen partial pressure. Despite the fact Ni is a catalyst for methane cracking (Eq. 1.9) which produces carbon, it also has good reforming ability for hydrocarbon fuels. This point onwards will cover the comparison between Ni/YSZ and Ni/ScSZ used both in hydrogen and hydrocarbon fuels.

2.3.1 Electrochemical performance

With electrolyte supported cells tested at 1000°C with hydrogen, Sumi et al. [15] showed a higher performance of Ni/ScCeSZ cells compared to Ni/YSZ cells with highest power density of 2.5 W/cm^2 and 2.3 W/cm^2 respectively. Yoon et al. [63] reported that there was no significant performance difference with thin ScSZ electrolyte (with Ni/YSZ substrate), compared with Ni/YSZ cell with YSZ electrolyte at at 800°C (0.58 vs 0.55 W/cm^2). The ohmic resistance due to the ScSZ electrolyte was significantly low compared to YSZ electrolyte but the polarisation due to the electrodes was very high [63]. The influence of the thin electrolyte layer was too insignificant, showing that to improve the performance, it is not adequate to change only the electrolyte layer in the anode supported cells, but need to substitute all the ceramic components (YSZ) in Ni/YSZ with ScSZ.
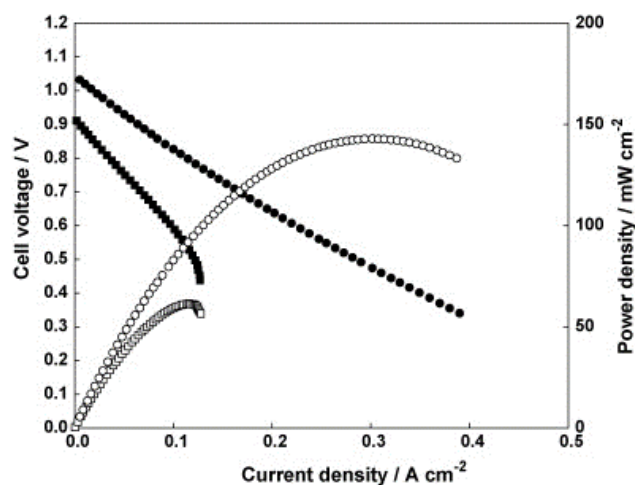
Figure 2-12: *i*V-PV curve at 850°C for NiYSZ/YSZ/PT SOFC cell operating in hydrogen and methane a) electrolyte supported cell with 50 ml/min of hydrogen(circle), and 25 ml/min of methane [30].

29

Several reports show drop of performance with Ni/YSZ cells when the fuel switched from hydrogen to biogas. Troskialina [64] showed drastic performance drop from maximum power density of 0.35 W/cm^2 to 0.05 W/cm^2 accompanied by OCV drop from to 1.05V to 0.93V with the fuel swap. Buccheri et al [30] observed similar trend with Ni/YSZ electrolyte supported cells as shown in Figure 2-12.
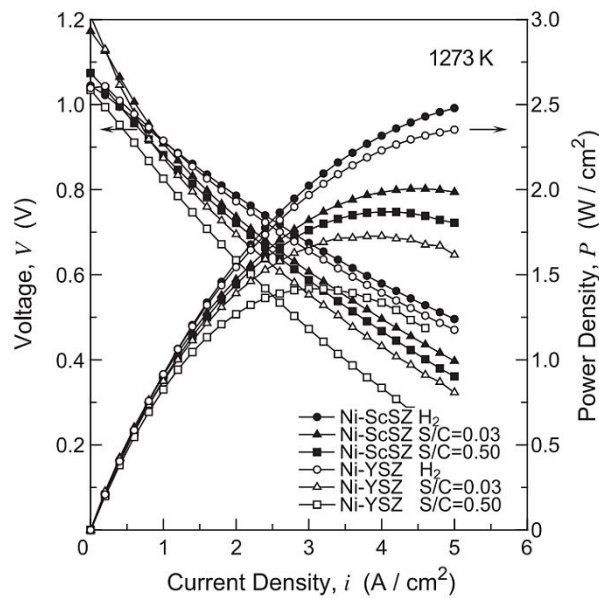
Figure 2-13: Performance of Ni/YSZ and Ni/ScSZ with hydrogen and methane at different S/C content [15].

Sumi et al [15] compared the effect of the fuel swap from hydrogen to methane on electrolyte supported Ni/YSZ and Ni/ScSZ cells. At 1000°C, the maximum power density of Ni/ScSZ supplied with humidified methane (3% water content) was 2.0 W/cm^2 compared to 1.7 W/cm^2 shown by Ni/YSZ as showed in Figure 2-13. Next section will show the difference in carbon deposition behaviour found by Sumi et al [65] between these two cells that was speculated to be the main reason of the differences response to hydrocarbon fuels. Their observation also showed that the S/C ratio affected Ni/YSZ cells more than Ni/ScSZ cells.

Figure 2-14 from Huang et al. [66] showed the performance result of Ni/ScCeSZ in-house cells in humidified hydrogen and methane at different temperatures. At 850°C, the maximum power density was almost unchanged with the fuel swap, while at 800°C and 700°C the effect of using methane as fuel was more obvious. The fuel swap greatly influenced the performance at 750°C; where the maximum power density drop from 0.35 W/cm^2 in hydrogen to 0.25 W/cm^2 in humidified methane [66]. Huang et al. [66] suggested that this may be due to slower gas-phase diffusion reaction of methane as fuel. This was in agreement with the temperature dependency of carbon deposition rate behaviour of Ni/ScCeSZ observed by Sumi et al. [65] mentioned in previous section.
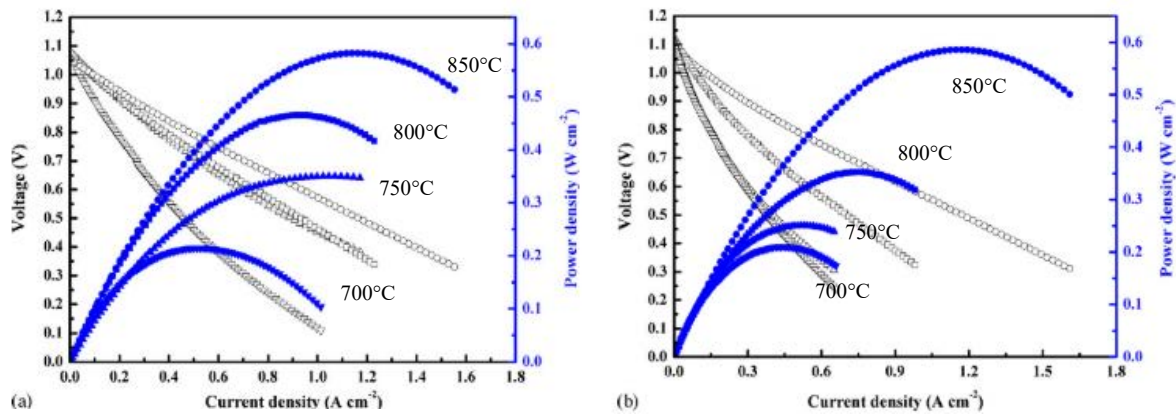
Figure 2-14: Power density curves for Ni/ScCeSZ in a)humidified hydrogen, and b) humidified methane [66].

Kishimoto et al. [67] has successfully shown the possibility of using liquid kerosene with a Ni/ScCSZ without any degradation and no carbon trace on the cell. High steam-to-carbon (S/C) ratio influenced the performance and the carbon deposition amount. The average current density at 0.75V was 0.14 A/cm^2 with a fuel utilisation value (U_f) of 55%. Kishimoto et al [67] suggested that high U_f protect nickel from carbon deposition because a lot of water produced by electrochemical reaction adsorbed on the nickel surface. An interesting work by Zhou et al [68] who explored the possibility of using carbon black particle as fuel as opposed to having

fuel in gaseous form using a microtubular SOFC Ni/ScSZ cell. Their in-house microtubular cell used a cathode supported design. The water vapour and nitrogen were blown to give a gasification effect to feed the carbon to the anode side. The SOFC cell successfully generated maximum power density of 0.173 W/cm^2 at 900°C. Shiratori et. al [33] had attempted to run actual biogas and simulated biogas from municipal organic waste using Ni/ScSZ cell. From their observation, with CH$_4$/CO ratio of 1.5, stable performance at 800°C for 800hr was achieved with simulated biogas with no obvious carbon deposition using simulated biogas. On the other hand, severe coking was observed using the actual biogas. Shiratori et. al [33] suggested that this was due to high presence of H$_2$S in the actual biogas. It can be speculated that Ni/ScSZ cells still can tolerate hydrocarbon gasses without the presence of sulphur. The stability test showed stable cell voltage above 0.8V for 800 hours at 0.2 A/cm^2. Up to this point there were already several evidence showing the capability of Ni/ScCeSZ to work with hydrocarbon fuels.

Other works using Ni/ScSZ cells were focusing on the improvement on Ni/ScSZ cells by introducing ceria in different forms. From the same group, Huang et al [66, 69] and Ye et al.[51, 70] explored the enhancement by thin layer deposition of Cu-LSCM-ScSZ on Ni/ScSZ support, Ni-free Cu-Ce-ScSZ anode and GDC impregnation. Impregnation of 2.0 wt% GDC with Ni/ScSZ showed highest enhancement to the performance even in hydrogen with maximum power densities value from 0.584 W/cm^2 in Ni/ScSZ to 0.825 W/cm^2 (Ni/ScSZ with GDC) at 850°C. Using humidified methane (with 3% H$_2$O), the maximum power density produced was increased to 0.848 W/cm^2 from originaly 0.825 W/cm^2. These authors also tested their modified ScSZ anode substrate with steam ethanol with highest power density of 0.669 W/cm^2 at 850°C which experienced only 4% drop from operation in humidified hydrogen. Table 2-1

summarised the performance result for SOFCs using ScSZ electrolyte operated with alternative fuels.

Table 2-1: Performances of ScSZ SOFC electrolytes with alternative fuel

Source	Design	T (°C)	Anode/Cathode	Fuel	Performance
Sumi et al. [15]	ESC	1000	Ni-ScCeSZ/LSM+Pt mesh	Humidified methane 3% H_2O-CH_4	2.5 W/cm^2 in H_2, 2.0 W/cm^2 in CH4
Huang et al.[66]	ASC	700-850	Ni-GDC-ScSZ/PCM	Humidified methane (3% H_2O-CH_4)	0.238-0.825 W/cm^2 in H_2 0.244-0.848 W/cm^2 in CH_4
Huang et al.[66]	ASC	700-850	Ni-ScSZ/PCM	Humidified methane (3% H_2O-CH_4)	0.212-0.584 W/cm^2 in H_2 0.205-0.586 W/cm^2 in CH_4
Huang et al.[69]	ASC	850	Ni-ScSZ+ LSCM-CeO_2	Steam ethanol	0.700 W/cm^2 in H_2 0.669 W/cm^2 in C_2H_5OH,
Ye et al. [51]	ASC	700-800	Cu-Ce-ScSZ	Steam ethanol	0.372- 0.130 W/cm^2 in H_2 0.222- 0.094 W/cm^2 in C_2H_5OH
Ye et al. [70]	ASC	850	Cu-LSCM-ScSZ	Steam ethanol	114 W/cm^2 in H_2 158 W/cm^2 in C_2H_5OH
Kishimoto et al. [67]	ESC	800	Ni-ScSZ/Pt	n-dodecane /kerosene	0.14 A/cm^2 at 0.75V
Zhou et al. [68]	ASC	850	Ni-ScSZ tube/ LSM-ScSZ	Carbon black	0.173 W/cm^2
Shiratori et al. [33]	ASC	800	Ni-ScCeSZ/LSM-ScSZ	Simulated and actual biogas	Above 0.8V @ 200mA/cm^2 over 800 hours on simulated biogas

  **ASC –anode supported cells, ESC-electrolyte supported cells, CSC=cathode supported cell

2.3.2 Carbon deposition behaviour

Somalu et al. [14] reported higher amount of carbon deposited on Ni/YSZ compared to Ni/ScCeSZ cells exposed to gaseous mixtures of 82% N_2, 10% CH_4 and 8% H_2O in quartz tube reactor at 700°C. This was in agreement with work by Eguchi et al. [71] who made similar observation on these two cell materials. Note that both authors carried out the carbon deposition observation on SOFC cell but not in SOFC mode; meaning there was only a catalytic reaction, but no electrochemical reaction happening in the quartz tube reactor. Interestingly, Somalu et

al. [14] also observed that the amount of carbon deposited was not affected by the addition of 1 mol% of the cerium oxide in the ScSZ powder, as both Ni/10Sc1CeSZ and Ni/ScCeSZ have the same carbon ratio. Their result is re-tabulated and presented in Table 2-2 [14].

Table 2-2: The ratio of carbon deposited for Ni/10Sc1CeSz, Ni/10ScSZ and Ni/8YSZ , re-tabulated from Ref [14].

Anode	Deposited carbon ratio at 700°C (mg-carbon/mg catalyst x 100) %		
	40% Ni (S/C = 0.8 for 1 hr)	20% Ni (S/C = 0.6 for 5 hr)	10% Ni (S/C = 0.6 for 5 hr)
Reference	[14]	[71]	[71]
Ni/10ScCeSZ	0.28	11.7	15.8
Ni/10ScSZ	0.28	-	-
Ni/8YSZ	0.35	33.4	39.6

Sumi et al. [20, 65] found that the carbon deposition ratio on Ni/YSZ and Ni/ScCeSZ actually depended on the temperature, where at 1273 K (1000°C), the ratio of carbon deposited on Ni/YSZ was higher than in Ni/ScCeSZ and vice versa at 1123 K (850°C). This observation is shown in Figure 2-15. Ke et al. [72] found similar observation with test temperature at 800°C and 900°C. Ke et al. [72] suggested that with increasing temperature, the carbon deposition seems to be inhibited in Ni/ScCeSz anode due to different H_2O_{ad} behaviour in Ni/ScCeSZ which influenced by the affinity of Ni and ScCeSZ. Both observation by Sumi et al. [20, 65] and Ke et al.[72] were using actual tested SOFC cell, which gave opposite observation compared to Eguchi et al. [71] and Somalu et al. [14]. For carbon deposited amount for SOFC anode, the observation of Sumi et al. [20, 65] and Ke et al. [72] considered to be more relevant the sample used actual tested SOFC cell rather than anode pellet tested in a quartz chamber. To compare the rate of carbon deposition on the SOFC material, work by Eguchi et al. [71] and Somalu et al. [14] were significant.
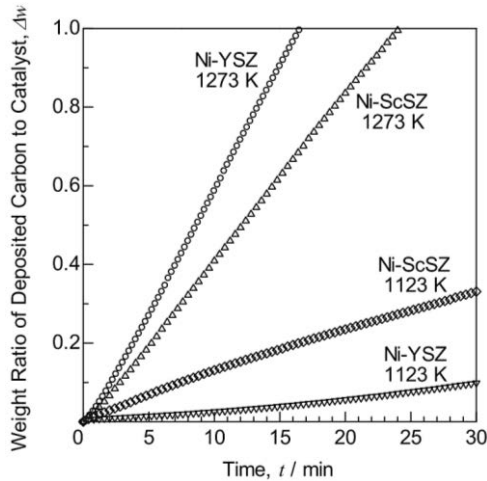
Figure 2-15: Weight ratio of carbon deposited to catalyst on Ni/YSZ and Ni/ScSZ at different temperature [20].
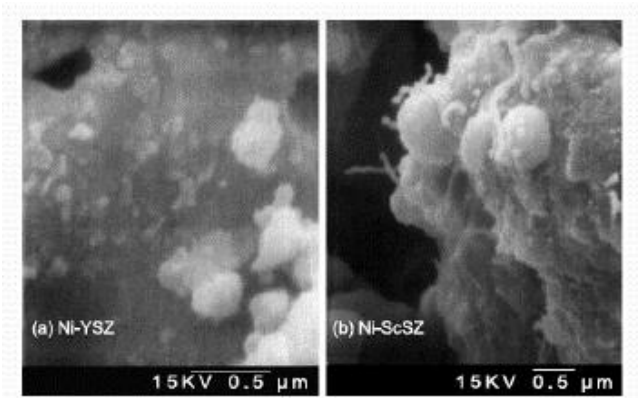
Figure 2-16: SEM images of a) Ni/YSZ and b)Ni/ScCeSZ anode after being exposed to CH4 for 5 mins at 1000°C [15].

Sumi et al. [15] also found that Ni/ScCeSZ exhibits different carbon morphology; filamentous carbon formed on Ni/ScCeSZ and amorphous carbon formed on Ni/YSZ as shown by Figure 2-16. Using Raman Spectroscopy, the ratio of graphitic to amorphous to on carbon formed on Ni/ScCeSZ was found to be higher compared to Ni/YSZ [65].

Eguchi et al. [71] found that the initial rate of methane reforming was higher for Ni/YSZ cells compared to Ni/ScSZ cells at 500 and 700°C. However, after 600 minutes, the rate of methane conversion in Ni/YSZ cells rapidly dropped, which was speculated to be due to anode deactivation, while Ni/ScCeSZ cells showed steady operation until the end of the 900 minutes test in humidified methane. Hence showing that Ni/ScCeSZ has higher tolerance for long term operation in methane.

From the literature, the carbon tolerance behaviour shown by the Ni cermet with different oxide (YSZ and ScCeSZ) influenced from two factors:

1) Different stability of zirconia phase; when doped with either yttria or scandia. Where ScCeSZ phase is more sensitive towards treatment conditions. Under reduction-

35

oxidation (redox) treatment, the crystallinity phase structure of ScCeSZ reported to change from cubic to rhombohedral [73, 74]. Sumi et al. [65] found that the lattice parameter of Ni/ScSZ increase under reduction treatment that suggest the decrease in Ni solubility by a partial changes of crystal structure. The side effect of the phase changes was likely influenced the type of carbon growth.

2) Stronger interaction between Ni and ScSZ compared to Ni and YSZ [15, 72]. Using Temperature Programme Reduction (TPR), Ke et al. [72] found the reduction temperature of Ni/YSZ to be lower (377°C) compared to that of Ni/ScCeSZ (507°C). The reduction temperature of Ni/YSZ system was closer to pure NiO reduction temperature, which indicates less influence from YSZ and vice versa for ScSZ. Ke et al [72] suggested the stronger interaction in Ni/ScCeSZ caused higher H_2O_{ad} enrichment by anodic current on Ni surface, which leads to higher local O/C ratio than supplied in bulk fuel. Hence, making Ni/ScCeSZ becomes more effective in carbon inhibitions under high temperature than Ni/YSZ when current flows.

According to Baker [75], carbon filaments have amorphous core, surrounded by graphitic skin and have a metal component either on the filament's tip or as dispersion along the body of the filament. Carbon filament can exist as whisker-like structure, branched structure, bi-directional and multi-directional structure [75]. Because of the duplex structure (amorphous and graphitic), the surface area increased; hence increased the electrical conductivity. The carbon filaments observed by the author under SEM and TEM observation can be referred to Figure 2-17.
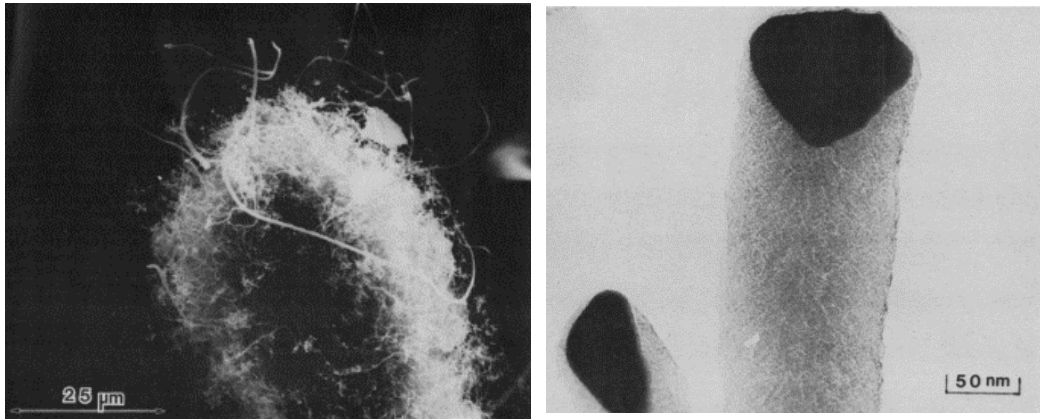
Figure 2-17: Growth of carbon filaments a) under SEM; near the edges of carbon fiber b) under TEM; showing their metal particle heads.

Generally, growth of carbon filament always linked to degradation of SOFC performance. For example, Lanzini et. al [28] reported excessive carbon filament networks as shown in Figure 2-18 that were found on the Ni/YSZ cells tested with methane at 800°C led to performance deterioration. The observation by Sumi et al [15] with Ni/ScSZ cells was opposite to this observation. Perhaps besides different crystalline structure, the test temperature and duration also contribute to the difference effect of carbon filament growth.
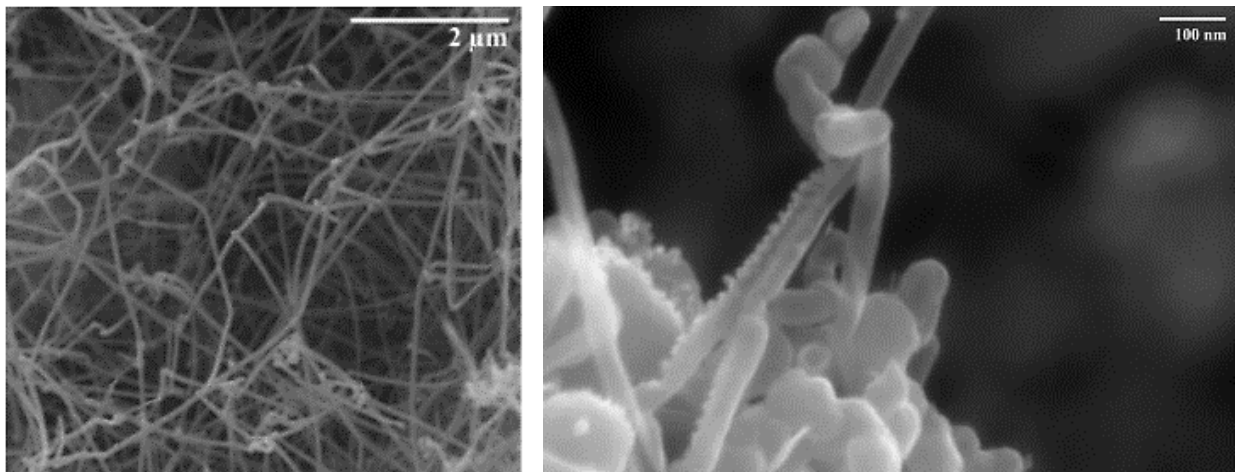
Figure 2-18: Carbon fibres formation on the anode substrate surface near the fuel inlet [28].

2.3.3 Doping/Surface alloying

Some of the works presented in Section 2.2.1 show how the introduction of ceria based materials has successfully enhanced the performance and ability to operate the SOFC using hydrocarbon fuels. Another method that has widely been used to improve carbon tolerance of SOFC cells is surface alloying or doping. Through this method, doped-Ni preferentially oxidises C atoms rather than forming C-C bonds [25]. Reportedly, alloying Ni with small amount of precious metals (such as Au, Ru, Rh, Pt and Pd) enhances the steam reforming ability of the Ni and the electrochemical performance [76]. Using the surface impregnation method, Niakolas et al. [77] showed no carbon deposition in the internal steam reforming of methane after 200 hours at 850°C. Recent work by the same author [77] explores the possibility of using Au as catalyst on the cathode side for solid oxide electrolysis cell (SOEC) [78]. Takeguchi et al [76] showed that doping with any of the precious metal (Ru, Rh, Pt or Pd) promoted CH_4 decomposition reaction and H_2 production. In terms of electrochemical performance, doping with either Ru or Pt enhanced electrochemical performance in humidified methane, with Pt-doped cells showing lowest cell resistance [76]. Despite the promising performance showed by precious metals, they remain very costly, hence alloying with other metals with the same effects are favoured.

Alloying with base metals such as Cu, Fe, Co, Sn, and Ag has successfully proven to give quite the same effect as precious metals. Nikolla et al [25] linked density functional theory (DFT) studies to lab based temperature-programme-reduction (TPR) and methane conversion study on Sn-Ni/YSZ cells. The amount of methane converted to hydrogen by 1 wt% Sn shows the highest conversion which shown in Figure 2-19.
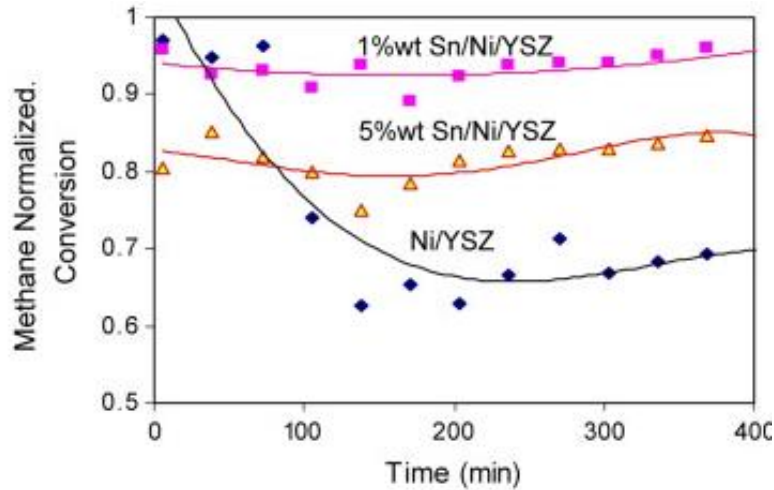
Figure 2-19: Normalised methane conversion as a function of time [25].

By using XPS and XRD analysis, Andarini [56] confirmed the formation of Sn/Ni alloy after high temperature sintering the doped cells. In further work by Nikolla et al [79], the author suggested that; (i) the Sn/Ni catalyst is more efficient than Ni in forming C-O bonds rather than C-C bonds which implies a higher rate of oxidation of carbon atoms rather than the development of solid carbon, (ii) Sn atoms displace low coordinated sites for nucleation and growth for carbon fibres (iii) Sn/Ni active sites are more abundant, while the Ni (with no dopant) active sites were under-coordinated; i.e Sn atoms improved the Ni coordination sites, (iv) weakens the binding of carbon atoms to low-coordinated sites.
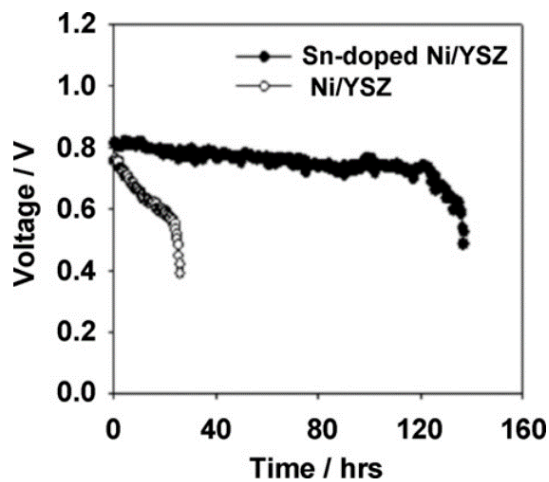
Figure 2-20: Long term stability test at 650°C in humidified methane at 0.3 A/cm² [8].

39

In work by Troskialina et al [50], the Sn-Ni/YSZ cells maintained the performance when the fuel was switched from hydrogen to dry biogas whilst the Ni/YSZ cells performance dropped significantly. The same result was observed with Kan et al.[8] who also reported a longer stability in humidified methane with Sn-Ni/YSZ than that of undoped Ni/YSZ as shown in Figure 2-20. In terms of carbon deposition, less amount of carbon deposited reported on the Sn-Ni/YSZ cells reported by the literature [8]. Using ethanol as fuel, Farrell et al.[80] observed structural and electrochemical degradation on undoped cells opposed to Sn-Ni/YSZ cells. Hence, Farrell et al.[80] suggested that Sn/Ni alloys inhibit carbon-induced degradation, resulting more stabilised operation in hydrocarbon fuels and less carbon deposition.

With these positive remarks on surface alloying with Sn, this work attempts to further improve the performance of biogas internal reforming on Ni/ScCeSZ by introducing Sn. To date, the effect of Sn/Ni alloying was only tested on Ni/YSZ cells. Therefore, it is interesting to see either similar or any deviation behaviour of Sn-Ni/ScCeSZ from what has been reported for Sn-Ni/YSZ.

2.4 Manufacturing via Aqueous Tape Casting

The three main methods mainly used for thick substrate processing for SOFC planar cell are tape casting, pressing and calendaring. Die-pressing is a technique of pressing powders with high pressure by either cold, warm, cold-isostatic or hot isostatic pressing. This technique is useful for a small batch production. In large scale production, this technique is not as popular as tape casting in producing SOFC cells as it is discontinuous process [19]. Calendaring is a process of combining two tapes (produced by tape casting) by using two or more rollers. The limitation in this method is, it cannot be used to combine very thick anode tapes and a very thin electrolyte films or thin anode films. However, thin anode substrate (<500 µm) and thick functional layers (>20 µm) can be combined together [38]. Table 2-3 shows the differences in

the thickness of the substrate produced and slip characteristic for the three method, re-tabulated

from [38].

Table 2-3: SOFC susbstrate manufacturing for planar cells

Technique	Thickness (final fired states) μm	Slip/paste/suspension characteristics
Tape casting	100-800	Low viscosity (Pa s); azeotropic solvents, various organics
Pressing	500-2000	High viscosity or simple powder mixture; pressing agent, fewer organics
Calendering	100-2000	Same as tape casting

Tape casting has been used in ceramic manufacturing over 5 decades as it is a continuous

process and very cost effective; hence suitable for mass production. For the planar SOFC that

uses ceramic materials for the main components, this technology has become very useful and

has been adopted by a lot of SOFC cell manufacturers. Tape casting is a process that involves

spreading the slurry at desired thickness (~10-1000 μm) on a carrier film at certain speed using

a spreader called 'doctor blade' as shown in Figure 2-21 [3].
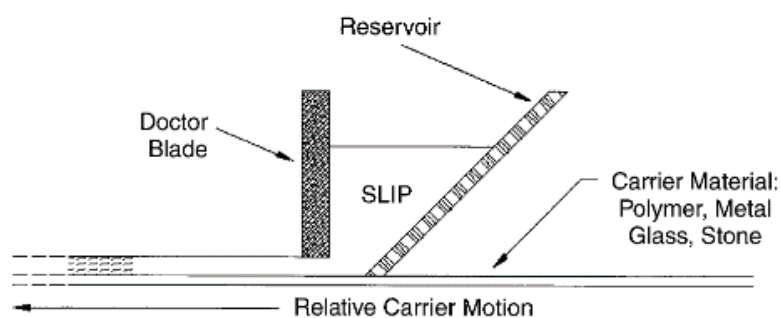
Figure 2-21: The basic principles in tape casting [3].

The thickness will be determined by the gap height, shape of the blade, casting speed and slurry

viscosity[3]. Although the process seemed to be simple, the design, the formulation and the

setting to make the process work is not as simple [3]. The tape casting slurry must be adjusted

to produce tapes with 1) no defects during drying, 2) cohesion to allow the manipulation of died tape, 3) microstructural homogeneity, 4)good thermo-compression ability (for laminating /calendaring), 5) easy pyrolysis, and 6) high mechanical strength after sintering[31].

2.4.1   Aqueous vs solvent tape casting

Tape casting originated as an aqueous processing method but due to practicality, highly volatile solvents are widely used. Solvent tape casting holds advantages compared to aqueous tape casting in terms of ease of manufacturing [3] and higher quality green tape [7], despite of its harmful effects to environment, health, and fire hazards. In most solvent based tape casting, either Butanone, Methyl ethyl ketone (MEK), or Toluene is used [7, 81-84], which all have relatively low flaming points, are highly irritant, cause prolonged health effects, are hazardous to expecting mothers, and harmful to the environment. Thus, attention has started to revert back to aqueous tape casting that uses harmless distilled water instead.

Major problems linked to the water based system include: bubbles from ball milling and de-airing which leads to pinholes, cracking, brittleness, dewetting, high slip viscosity and curdling in the green tape [3]. According to Nahass et al [85], the major difference in solvent tape casting and water based tape casting is the sensitivity to process perturbation. Despite of these complexities, currently an SOFC manufacturing company, SOLID Power produces its cells via aqueous based tape casting and screen printing [86], with other manufacturing companies working towards this route as well.

In SOFC cell fabrication, there is quite a number of literature available on successfully fabricating electrolyte supported cell using water based tape casting but very limited on anode substrate. Among these, the papers discuss the method, parameters and characterisation of the successfully made green tape, but limited information is available that compares up to the

electrochemical performance. Because of lack of other research resources to support this work, it is difficult to judge the usefulness of the SOFC cells produced by aqueous tape casting.

Mistler et al. [3] provide a very good start on the whole tape casting process but more focusing on the solvent based route. Hotza et al [31] provide a good review on aqueous tape casting focusing on the organic's role and composition for water based systems. The most recent review by Nishihora et al. [87] on manufacturing porous ceramic materials via tape casting process was highly beneficial for producing anode support for SOFC. This chapter will be focusing specifically on aqueous tape casting concerning SOFC cell fabrication.

2.4.2   Slurry preparation

Preparation of the slurry prior to tape casting consists of two ball milling. Basically the solvent, dispersant and cermet powders are mixed in the first ball milling step for 19-24 hours to ensure complete deagglomeration. In the second ball milling step, the binder and plasticizer are mixed into the slurry for at least 4 hours with lower rpm. The order of mixing is significant as the interactions of the organics are affected [88].

Because bubbles will form excessively in the ball milling step at high ball milling speed, the ball milling rpm must be just adequate to mix the materials. The optimum rpm can be calculated using [89]:

$$Nc = \ 0.6 \ x \ 54.2/R^{0.5} \hspace{4cm} \text{[Eq. 2.1]}$$

where R is the mill inside radius in feet

The second ball milling stage set to be lower rpm than the first stage to avoid bubbles forming. The ball milling media and the slurry should fill around ¾ of the jar [88].

Basically, the procedures are similar for both aqueous and tape casting system, except for additional two steps below for the water based system:

i.   Zeta potential and sedimentation test prior to tape casting to find out the optimum amount of dispersant and optimum pH [90, 91]. The highest potential (in the negative value) is favourable.

ii.   Longer de-airing time [91].

Compared to the solvent system, optimising the water-based system is more challenging as the optimum conditions are quite narrow. The slurry must be well dispersed, wet the carrier film and have the right viscosity. Based on ternary plot in Figure 2-22 [31], where extensive research was made based on aqueous tape casting, the amount of the solid loading lies in between 25-80 mass % , while the organics, where usually aimed to be as low as possible, with a maximum of 18 mass% and water content at range of 25-70%.
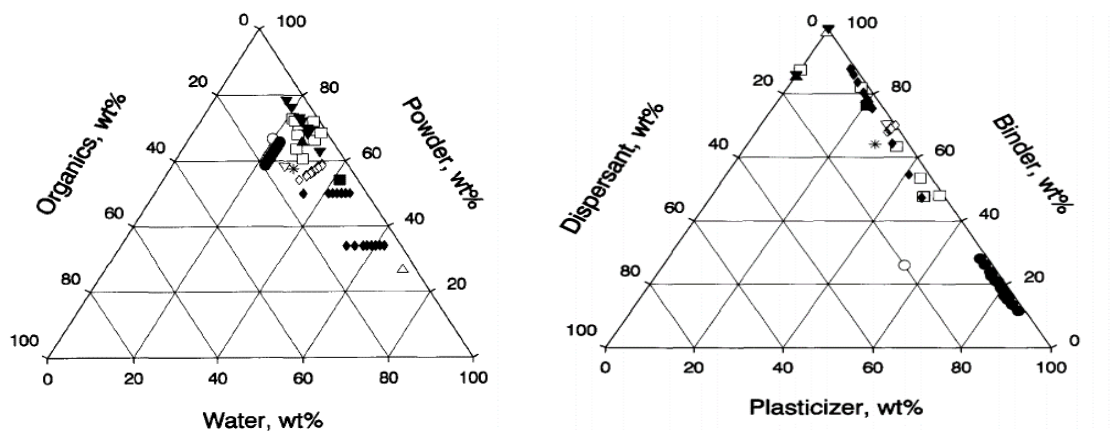
Figure 2-22: Optimised slurry composition for aqueous based tape casting from several literatures , as reviewed by Hotza [31].

In SOFC system, the organics should be minimised in the electrolyte system where the aim is to obtain a dense layer. However, for the anode substrate system with 30-40% porosity needed to achieve the reaction for the triple phase boundary, the void spaces from the organics burnout are beneficial for the fuel channelling. Table 2-4 summarise the optimised slurry composition from different papers based on aqueous tape casting for SOFC. Only two literature articles were found that gave the composition used for anode substrate, which mark with red bold in Table 2-4. For a slurry with materials with different density, as faced for formulating the SOFC anode slurry, the organics need to be specially tailored to make sure both the metal and ceramic in suspension [3].

Table 2-4: Optimised slurry composition based on Aqueous Tape Casting in SOFC cell fabrication.

Source	Solid loading (wt %)	Dispersant (wt %)	Binder (wt %)	Plasticiser (wt %)	Surfactant (wt %)	Anti-Foam (wt %)	Distilled water (wt %)	Other organics (wt %)	Type
[91]	55.0	1	25	-	0.5	0.5	16.5	-	Electrolyte
[91]	50.0	2	25	-	0.5	0.5	20.5	-	Electrolyte
[92]	44.6	0.8	5.0	8.1	0.1	0.1	41.2	-	Electrolyte
[93]	55.0	1.5	4.5	4.5	-	-	34.5	-	Electrolyte
[94]	55.0	1.5	4.5	4.5	0.1	0.1	34.3	-	Electrolyte
[95]	**55.0**	**1.5**	**4.5**	**1.35**	**0.1**	**0.1**	**36.1**	**1.35**	**Substrate**
[96]	**44.5**	**0.9**	**4.8**	**12.8**	**0.3**	**0.5**	**34.1**	**1.1 (PF)**	**Substrate**
[96]	40.9	0.8	1.2	2.0	1.5	0.3	53.3	-	Electrolyte

*PF = Pore former

4.1.1.1   2.3.2.1   Dispersant

The main roles of the dispersant are as follow; 1) to separate the particles in the solvent, 2) to reduce viscosity hence increase the solids loading, and 3) to decrease amount of solvent [3]. In the aqueous based system, prior to the slurry development, the optimum colloidal stability needs to be determined by zeta potential measurement [7] as in Figure 2-23. The zeta potential test is very useful to check the optimum amount of dispersant as well as the best pH required. The effect of dispersant addition can be seen in Figure 2-23 where the maximum zeta

potential value increased to 45mV (absolute) when using dispersant at 1.5 wt%, compared to an initial value below 30mV (absolute) [92, 97].

With regards to SOFC, two types of dispersant that are quite popular are PAA (polyacrilic acid) and Darvan C-N (ammonium polymethylacrylate). Based on these, an excellent zeta potential for GDC is in between 1.0-1.5 wt% at pH 9-10 with value of 45mV (absolute value) [91, 92, 94]. It is interesting that for YSZ with different surface area and particle size distribution, a very different set of zeta potential values reported by Baquero et al [91]. YSZ systems were also reported to be stable at basic region, pH> 8 with 1-2 wt% dispersant with maximum zeta potential more than 60 mV (absolute) [7, 90]. For larger particle size of YSZ, the zeta potential values are even higher after 24 hours as it need more time for stabilisation [90] as shown in Figure 2-23 b.
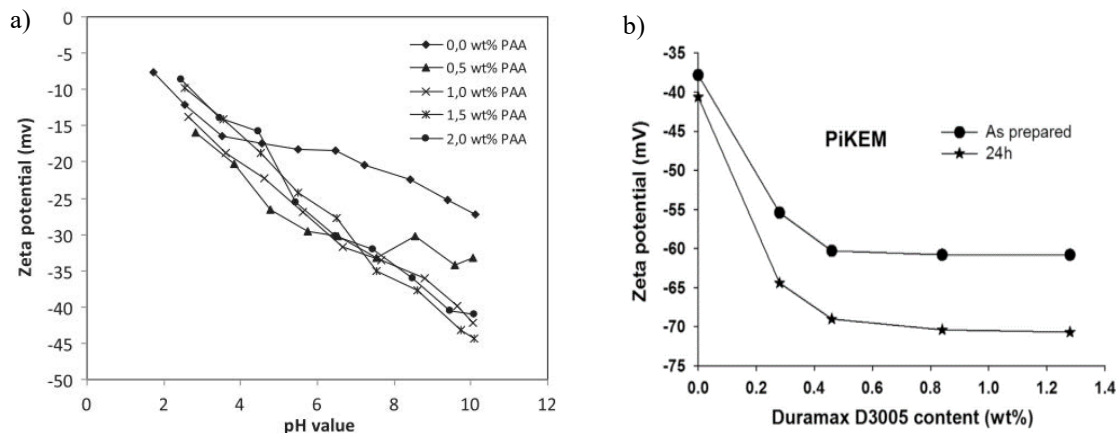
Figure 2-23 : Zeta potential in a) GDC with respect to pH and dispersant content[92] b) YSZ with different ultrasonic treatment durations [90].

Typically, sedimentation test complementing the zeta potential test to re-emphasize on the effect of operating pH and the composition result obtained previously, which normally agrees at pH 8.0 -9.0 for GDC [92, 94]. No reports were found for ScSZ system with respect to

sedimentation test. It is worth mentioning that increasing the amount of dispersant makes the slurry becomes less viscous [98] which is desirable. But according to the zeta potential, dispersant amount beyond 2 wt% is not desirable in terms of colloidal stability.

To select between different dispersant Schafbauer et al. [81] carried out sedimentation test and measure the slurry's rheology. A well dispersed slurry is desired otherwise the aggregation can lead to poor packing thus weak green material [99].

4.1.1.2   2.3.2.2   Binder

According to Mistler [3] binder is a very important additive as it supplies the network that holds the entire chemical system together in the green tape state. In aqueous based tape casting, there are two approaches based on the type of binders, either water-soluble binder or water-based emulsion binders [3]. A detailed comparison between the two binders is covered by Mistler [3]. In SOFC both binders are widely used, PVA is an example for the water-soluble binder while Mowilith LDM 6138 (Clariant) [91, 100, 101] is quite famous as a water-based emulsion binder. Other types of emulsion binders are Duramax B1000 from Rohm & Haas [102] and WB4101 from Polymer Incorporated [103]. WB4101 has been used by Wang et al [103] and reported to produce a good quality and dense electrolyte tape even compared to the solvent based tape.

For PVA, the amount of binders used among the literatures was in total agreement which was found to be in between 4.5-5 wt % [92-95]. Using latex-emulsion type binders, the binder content is quite high, which is around 25-30 wt% but using less water (less than 20%) and no plasticiser added in the system as the latex acts both as the binder and plasticiser[91, 100-102].

It has been reported by Schafbauer et al. [81] that slurry with low binder content gives a brittle green tape which cracks when bent. On the other hand, high binder content will make the slurry very viscous that make it very hard to tape cast and cause low de-airing effect with a large number of pinholes in the dried green tape [81]. For solid binder like PVA, it is more practical to dissolve the binder prior to binder addition to the slurry mixture for complete dissolution as practised by Akbari et al.[92]. Since the binder is perfectly mixed, no excessive shaking needed to dissolve the PVA, hence reduce the bubble formation during the mixing stage.

4.1.1.3   2.3.2.3   Plasticiser

Plasticisers are organics with low molecular weight, used to reduce the glass transition temperature, (T_g) of binder, soften the tape so that the tape can be rolled, and as an anti-adhesive [95]. As mentioned before, for water-based emulsion binder, the latex acts both as binder and plasticiser. Thus, no additional plasticiser is added to the system.

Glycerol is a common plasticiser used in the tape casting process in earlier processes [3]. Recently PEG is used, based on the compatibility and effectiveness to reduce the glass transition temperature for PVA [3]. Degree of plasticization depends on the molecular size of the plasticizer with lower molecular weight PEG gives better plasticising effect. In most cases, PEG 400 are used [92, 95, 96]. The suggested ratio of binder to plasticiser was 1:1 by volume [81]. Interestingly using the same plasticizer, the ratio of plasticiser to binder used varied quite a lot, from 0.5: 1 to 1.6:1 by weight.

In solvent tape casting, two different type of plasticiser usually used, usually assigned to Type I and Type II plasticiser [3]. Type I plasticiser role is to reduce the T_g of binders while Type II plasticiser acts as internal lubricant of the system. In Aqueous tape casting, usually only one

type of plasticiser is used. The only report that used two type of plasticiser was by Fu et al [95] which use glycerol as the anti-adhesive and PEG as the internal lubricant.

2.3.2.4   Other organics

As surface tension in water is very high, wetting agent are sometimes used in water based tape casting. By adding a wetting agent, the water retention should be lowered and spread evenly on the mylar film. However, a wetting agent can also stabilise bubbles, hence a de-foamer must be added [104]. Both of this additive should be at minimum quantity. An excess amount of anti-foam will cause crater or fish eye defect while an excess of surfactant will cause an excessive amount of bubbles [104]. Table 2-5 summarised the different organics used from different sources in aqueous tape casting in respect to SOFC.

Table 2-5: Different organics used in aqueous tape casting by several authors.

Type	Chemical name/Brand code and Supplier	Source
Dispersant	PAA (several suppliers)	[92, 95, 96]
	PAA polyeletrolyte: Duramax D3005 (Rohm & Haas Co. PA)	[90]
	Ammonium poly (methacrylate): Darvan C-N, Darvan 812 A (Vanderbilt Minerals)	[91, 101]
Binder	Mowilith LDM 6138 (Clariant)	[91, 100, 101]
	WB4101 Polymer Innovations	[12]
	Duramax B1070 Rohm & Haas	[102]
	Duramax B1000 Rohm & Haas	[90]
	PVA	[92, 95, 96]
Plasticiser	PEG 400	[92, 95, 96]
	Glycerol	[92, 95, 96]
Wetting agent	2,4,7,9,-Tetramethyl-5-decyne-4,7-diol ethoxylate (Sigma Aldrich)	[92, 95, 96]
De-foamer	Octanol	[92, 95, 96]
	DF002 (Polymer Innovations Inc)	[102]
	Antifoam (Sigma Aldrich)	[101]

2.4.3 Tape drying

Most of the work mentioned up to this point dried the slurry either at room temperature or in a built-in heating bed at 25°C for 12-24 hours. An alternative drying method used in tape casting is using freeze-casting which are beneficial for porous material. This method will not be covered in this thesis as the green tape consist of dense electrolyte and porous anode layer.

2.4.4 Tape Quality

Comparing the water based tape quality to solvent based tape quality; it is still debatable as more reports become available now on successful fabrication of the tape via aqueous tape casting. Michalek et al [7] present a very detailed steps with both of the systems in an attempt to compare aqueous based and solvent based tape casting. From the report, by using the same powders with different solvent and organics, solvent based gave higher density electrolyte than the water based with 99% and 94% dense, respectively. Their results are shown by Figure 2-24. Nevertheless, Wang et al [103] reported higher density of electrolyte achieved by the aqueous tape casting than that of solvent-based; using water based emulsion binder WB4101 by Polymer Innovations, USA.
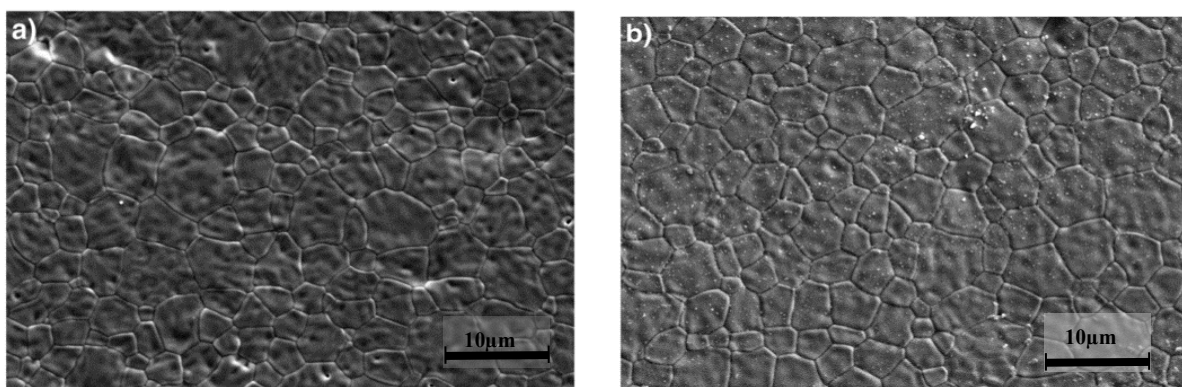
Figure 2-24: Comparison between tape quality, a) solvent based b) aqueous based [7].

2.4.5   Multilayer Tape Casting

SOFC production via multi-layered tape casting and single co-sintering has been reported several times. These two steps significantly reduce the manufacturing time and cost as separate sintering steps excessively time and energy consuming. Furthermore, multilayer tape casting (tape cast on top of each layer and co-sintered together) produces excellent interfaces and good control of microstructures [12, 83, 84, 105]. The example of the conventional process can be seen in Figure 2-25 where five sintering steps were used in standard cell fabrication.

There are two routes for multilayer tape casting; the one that is quite popular recently is by tape casting/laminating/co-firing (TLC) by laminating several layers of thin green tapes using iso-static press at certain pressure, typically at 3500 N/cm^2 and 75°C for 10 min [82, 105, 106]. The other way is by reverse multilayer tape casting as in Figure 2-26 where the electrolyte is tape cast on silicone coated PET film first, followed by the anode functional layer and finally the anode substrate layer [12, 19, 69], which also known as co-casting. This is in the opposite sequence to what usually practised where electrolyte and anode functional layer were screen printed on pre-sintered anode substrate. From five sintering step, the sintering reduced to only two sintering steps.

Figure 2-27 illustrates the advantage of using reverse multilayer tape casting as shown by Schafbauer et al [19]. With the conventional cell fabrication method, the anode structure governs the thickness and microstructure of all consecutive layers. With reverse tape casting process, homogeneity layer of the thin electrolyte and anode functional layer can be achieved as there will be less thickness deviation originated from the previous anode layer [19].

Among the limited literature on reverse multilayer aqueous tape casting, Wang et al [12] successfully made an SOFC using multilayer tape casting with maximum power density of 0.8 W/m^2 at 800°C with an OCV value near 1.1V.
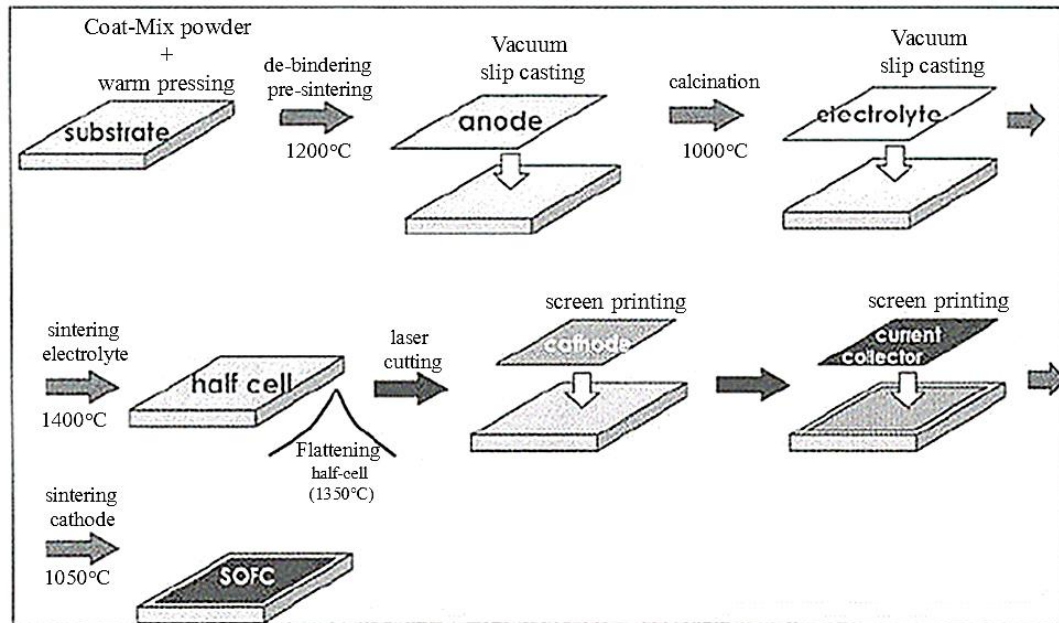
Figure 2-25: Conventional cell production for SOFC in Forschungszentrum Jülich before 2005 [19].
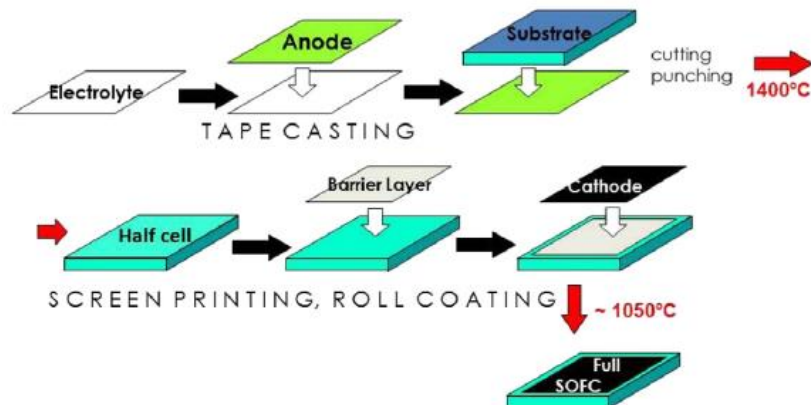
Figure 2-26: Reverse tape casting reduced sintering step in Forschungszentrum Jülich [13].
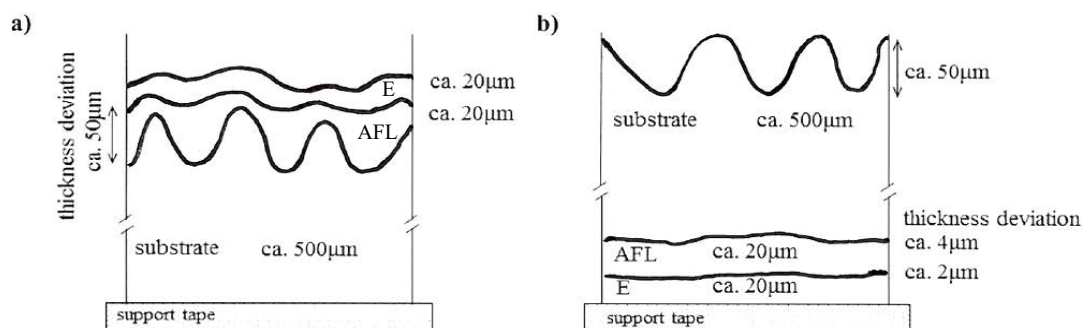
Figure 2-27: Schematic diagram of problem on a) conventional manufacturing system, vs b) reverse multilayer tape casting. Redraw from [19].
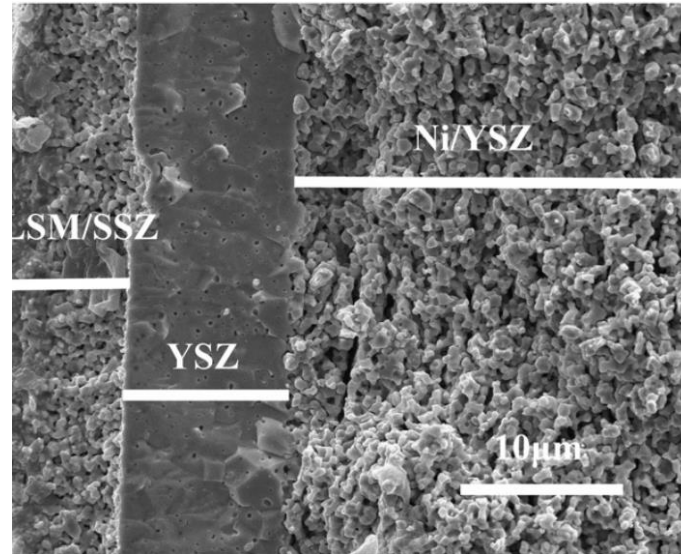
Figure 2-28: Cross-section image of SOFC cell manufactured using reverse multi-layer aqueous tape casting [12].

Figure 2-28 shows the cross-section of the produced cell with dense electrolyte and porous anode using reverse multilayer aqueous tape casting reported by Wang et al [12]. Another report was by Zhou et. al.[107], that successfully fabricated large Ni/YSZ cells (10 cm x 10 cm) using this method for stack testing. Highly dense electrolyte produced reflected by high OCV value of 1.1V. For Ni/YSZ cell with LSCF cathode, the maximum power density produced at 850°C was 0.534 W/cm^2 [96]. With the large Ni/YSZ cells, the maximum power density achieved was 0.266 W/cm^2 at 800°C [107]. The main difference in the performance by the two authors was speculated to be due to porosity. The amount of pore former used in Zhou et. al [96] was 1.1 wt% compared to 15 wt% used by Wang et. al. [12]. On top of that, Zhou et al. [107] used higher co-sintering temperature (1450°C compared to 1400°C) that was beneficial to achieve dense electrolyte, but it also caused the anode to be less porous.

As this method shorten the SOFC cell-manufacturing step and was capable to meet the requirement needed by each layer, manufacturing method using this route will be attempted to produce Ni/YSZ and Ni/ScCeSZ anode supported cells.

CHAPTER 3: MATERIALS AND METHODOLOGY

3.1 Overview

This chapter will discuss the methodology and materials used in this thesis. The material section will cover the materials characterisation such as particle size, sintered ceramics microstructure and list of other materials used in this work. The methodology section includes full cell manufacturing via reverse aqueous tape casting, preparation for cell testing, electrochemical test procedure and characterisation analysis. The characterisation analysis carried out for optimisation were zeta potential, sedimentation test, rheology test, thermogravimetric analysis (TGA), and dilatometer analysis. SEM-EDX were carried out both for optimisation and during post test analysis. As tape casting and full cell optimisation represent a large part of this thesis, more elaborated optimisation will be reported in the following chapter.

3.2 Materials

3.2.1   Starting powder (ceramic and metal)

For anode substrate (AS), as-received nickel oxide (Type A Novamet supplied by Hart Materials Ltd. Staffordshire UK) with average particle size of 9.101±0.085 μm was used. Finer particle size of as-received nickel oxide (Type F) from Pi-Kem Ltd. Tamworth UK with average particle size of 0.637±0.145 μm was used instead for the anode functional layer (AFL). The ceramics used for the electrolyte materials were fully stabilised commercial 8YSZ $(Y_2O_3)_{0.08}(ZrO_2)_{0.92}$) from TOSOH Corp, Tokyo Japan with average particle size of 0.855±0.103 μm, and 10ScCeSZ $((Sc_2O_3)_{0.1}–(CeO_2)_{0.01}–(ZrO_2)_{0.89})$; from Daiichi Kigenso Kagaku Kogyo Ltd (DKKK) Osaka, Japan with average particle size of 0.514± 0.053 μm.

In the anode substrate and the functional layer, the ratio of NiO to ceramic used was 65:35 wt%. In the anode substrate, electrolyte powders pre-calcined at different temperatures were used.

For the cathode, as-received lanthanum strontium manganese, $La_{0.80}Sr_{0.20}MnO_3$ (will be addressed as LSM) from Praxair, Connecticut USA with an average particle size of 0.90 μm were used. The sizes were measured using a Malvern Mastersizer 2000. All the size measurements are summarised in Table 3.1. Throughout this thesis, three different batches of 10ScCeSZ were used in manufacturing stages. Hence, there were slight variations in the electrochemical performance.

Table 3-1: SOFC materials size and purpose

Materials	Size (d_{50}) (μm)	Component	Brand/supplier
Coarse NiO (AS)	8.101 ± 0.185	Anode support (AS)	Type A/Novamet
Fine NiO (AFL)	0.637 ± 0.145	AFL	Type F/Pi-Kem
Fine NiO (AS in Section 5.4.2)	1.0-2.0 μm (supplier's specification)	Anode support (AS) for Section 5.4.2	Grade F/Hart materials
8YSZ as-received	0.855 ± 0.103	Electrolyte layer, AFL	TZ-8YSZ/TOSOH
8YSZ PC 750	0.701 ± 0.003	Anode support (AS)	TZ-8YSZ/TOSOH
8YSZ PC 800	0.612 ± 0.001	Anode support (AS)	TZ-8YSZ/TOSOH
8YSZ PC 850	0.606 ± 0.001	Anode support (AS)	TZ-8YSZ/TOSOH
10Sc1CeSZ as-received	0.514 ± 0.053	Electrolyte layer, AFL	DKKK
10Sc1CeSZ PC 850	0.418 ± 0.001	Anode support (AS)	DKKK
10Sc1CeSZ PC 900	0.372 ± 0.001	Anode support (AS)	DKKK
10Sc1CeSZ PC 950	0.347 ± 0.005	Anode support (AS)	DKKK
LSM	0.901 (supplier specification)	Cathode	Praxair

*PC = Pre-calcined, AFL= Anode functional layer

3.2.1.1 Ceramics sintered structure

YSZ and ScCeSZ discs were prepared by mixing the as-received powders with 3 wt% PVA solutions and pressed by isostatic pressing at 4 bar. The PVA solution prepared by mixing the PVA solution by 4:1 ratio of water/PVA with poly(vynil) alcohol 87-90% hydrolysed (with average MW~30,000-70,000) supplied by Sigma. The discs were sintered at 1350 to 1450°C to

compare the microstructures of the ceramics accordingly, which presented in Figure 3-1. Generally, the discs sintered at 1400°C and 1450°C have dense structures with some entrapped
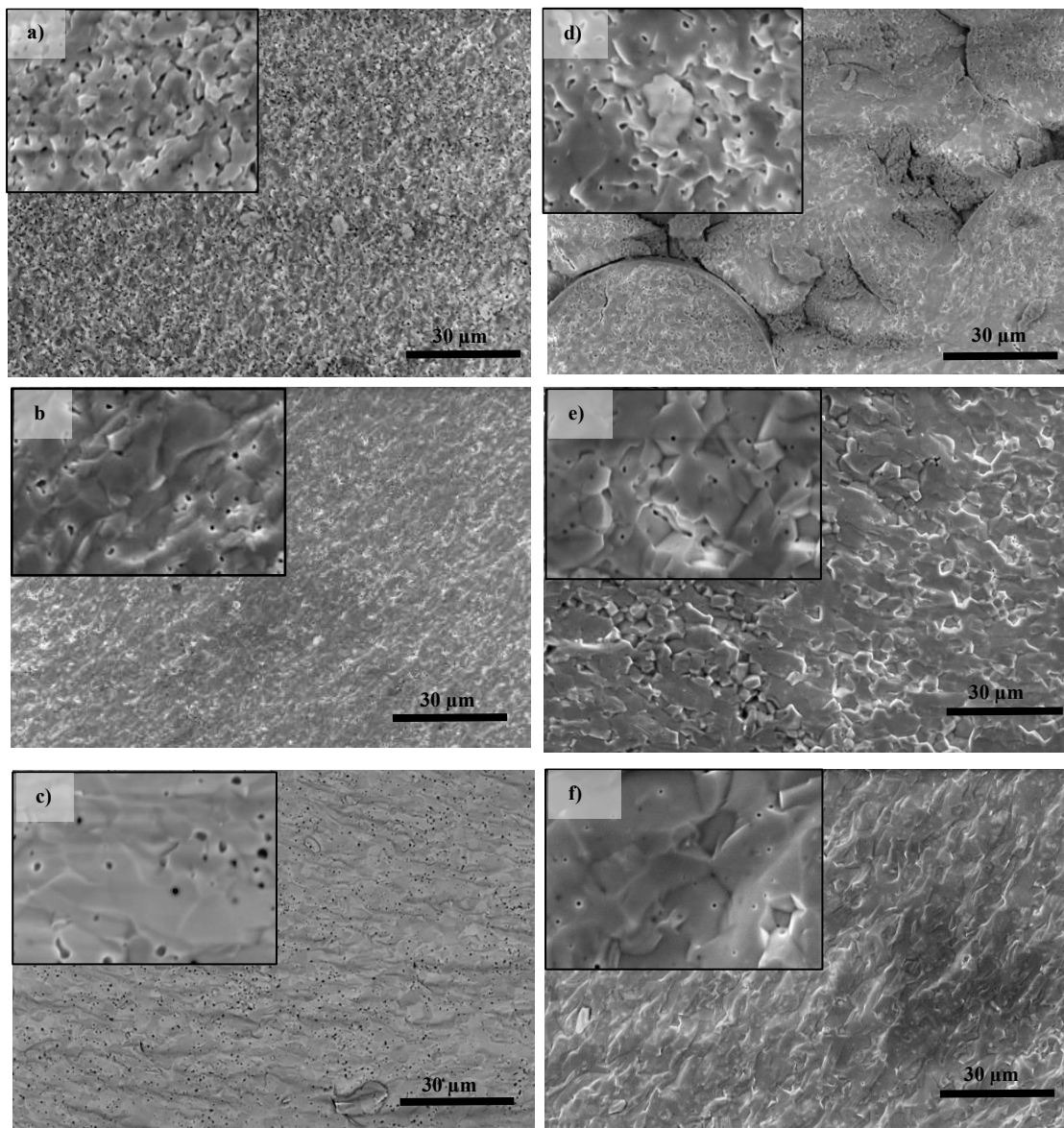
Figure 3-1: SEM Microstructure of the fracture surfaces of the ceramics sintered at different temperatures; a) YSZ (1350°C), b) YSZ (1400°C), c) YSZ (1450°C), d) ScSZ (1350°C), e) ScSZ (1400°C), and f) ScSZ (1450°C).

pores. ScCeSZ disc has a denser structure at 1450°C compared to YSZ sintered at the same temperature which shows that ScSZ is a good candidate for electrolyte material in term of the dense structure. Discs of both of the materials were less dense when sintered at 1350°C.

Furthermore, at 1350°C, the ScCeSZ disc showed big circular structures that speculated to be originating from the mixing action using pellet and mortar. The preparation method affected the ScCeSZ but not YSZ. Besides the 'circular pattern' at 1350°C, the microstructure of the ScCeSZ disc was less porous compared to YSZ and the fracture structure of ScCeSZ was more obvious compared to YSZ. The size of the pores in the dense structure of ScCeSZ were smaller than that of YSZ. Optimisation for sintering temperature was done separately on tape cast sample.

3.2.2 Other materials

Originally the organics used were based on anode substrate tape casting formulation by Fu et al [95]. For anode layers, the organics used for tape casting procedures were:

- Poly(vinyl) alcohol 87-90% hydrolysed (average MW~30,000-70,000) as binder,

- Poly(ethylene) glycol (average MW 400) as plasticizer I,

- Glycerol (Fisher BioReagents) as plasticizer II and anti-adhesive,

- Antifoam 204-mixture of polyether dispersions (Sigma Aldrich) as de-foamer

- Distilled water as solvent.

- Selections of the dispersants; salt of poly acrylic acid salt by BASF Dispex Ultra 4404, salt of phosphonic acid (Acros) and ammonium poly methyl acrylate (Darvan C-N). These dispersants were tested for stabilisation before slurry optimisation which will be elaborated in later in this chapter.

- Tapioca starch as pore former in the anode substrate layer. No pore former used in the anode functional layer (AFL).

For the electrolyte layer, the organics supplied by Polymer Innovations Inc. consisted of WB4101 (water-based binder), DS001 (dispersant), PL005 (plasticizer) and DF002 (antifoam). Table 3-2 summarises the organics and other materials used in this thesis.

Table 3-2: Organics and other materials used in this thesis

Material name	Function	Supplier
Dispex Ultra 4404	Dispersant (Anode)	BASF, USA
PVA MW 30K-70K	Binder (Anode)	Sigma Aldrich,UK
Antifoam 204	De-foamer (Anode)	
PEG MW 400	Plasticiser 1 (Anode)	
Glycerol	Plasticiser 2 (Anode)	
Tapioca starch	Pore former (Anode substrate)	Retail shop
WB4101	Water based binder (electrolyte)	Polymer Innovations Inc, USA
DS001	Dispersant for WB4101 system (electrolyte)	
DF002	Defoamer for WB4101 system (electrolyte)	
PL005	Plasticiser for WB4101 system (electrolyte)	
DAD-87 (dense silver paste)	Conductive paste and sealant	Shanghai Research Institute, Shanghai China
V-737 (Terpineol based)	Ink vehicle for three roll mills	Haraeus, Harau Germany
Darvan C-N	Dispersant	Vanderbilt Materials, USA
0.25mm 99.99% silver wire	Wire Connectors	Scientific wires, Essex, UK
Alumina tube	Cell holder/ cell mount	ALMATH Crucibles Ltd, Newmarket UK
Macor	Cell holder (Fuel End)	Precision ceramics, Birmingham UK
Hydrogen (H_2) gas	Fuel at anode	BOC, Birmingham UK
Helium (He) gas	Inert gas for dilution and carrier	
Carbon dioxide (CO_2) gas	Fuel at anode (simulated biogas)	
Methane (CH_4) gas	Fuel at anode (simulated biogas)	

3.3 Methodology

3.3.1   Particle characterisation

The materials in Section 3.1 were characterised using a Malvern Zetasizer 2000 which uses a light scattering technique to determine the size of particles. According to the user manual [108], the software applied *'Mie theory'* to calculate the distribution of particle sizes and the specific surface area. Mie theory was developed to predict the way light is scattered by spherical particles and monitored the light passes through or adsorbed by the particles. This theory considered to be accurate with spherical particles, with assumption that the user input in the right refractive index and absorption data. Each size of the particle will have its own scattering pattern, like a fingerprint that is unique and unlike any other sizes.

Sample preparation was done by preparing suspensions of 0.1 wt% of the powders and 1 drop of PMMA dispersant- Darvan C-N. The suspensions were agitated using an ultrasonic bath for 30 minutes prior to insertion in the machine's dispersing unit.

3.3.2   Thermogravimetric analysis (TGA)

Thermogravimetric analysis continuously records the changes of weight of the solid sample as a function of time and temperature. The purpose of TGA in this study was to find out the burnout and sintering stage of the Ni/YSZ/Ni/ScCeSZ tape cast samples. The analysis was carried out using a TG 207 (NETZSCH) with fragments of the green tapes used as the samples. The system heated up to a maximum temparture of 900°C with a ramp rate of 5°C /minute.

3.3.3   Dilatometer analysis

Shrinkage and expansion of the materials with respect to temperature was measured using a dilatometer machine - DIL 402C (NETZSCH) shown in Figure 3-2. The sample was placed in

an alumina holder and sandwiched by alumina spacers. Two types of samples were used. With tape cast samples, green tapes were pressed together to produce 1cm x 1cm x 2cm samples.

Figure 3-2: Dilatometer analysis machine - DIL 402C (NETZSCH).

Electrolyte and anode powders were pressed using a 1 cm diameter metal die to produce 2 cm thick pellets for dilatometer analysis. As-received and pre-calcined 10ScCeSZ, YSZ and cermet powders were mixed with 3 wt% pre-mixed PVA solution and cold pressed using an iso-static pressing machine. To solidify the pellet, the pressed sample was sintered at 900°C with organic burnout stages at 350°C and 550°C. The analysis on the green tape and the pellet followed the temperature profile set up as shown in Figure 3-3 without any gas purge.
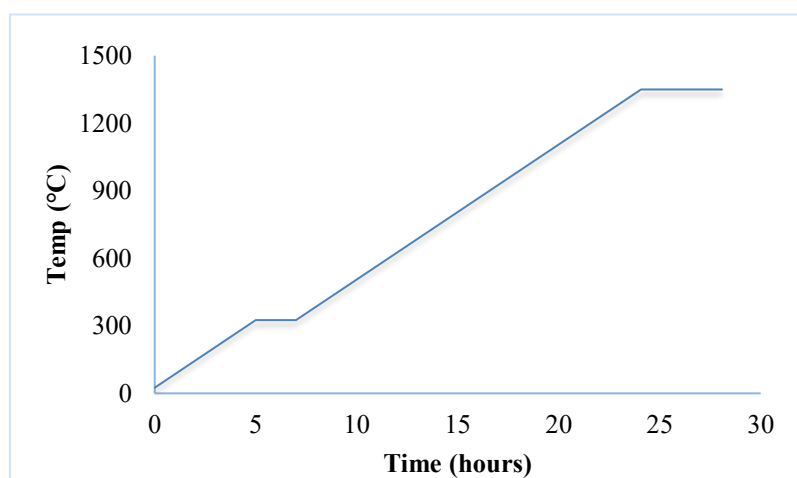
Figure 3-3: Temperature profile for dilatometer analysis.

3.3.4 Conductivity test

A conductivity test was carried out to compare the conductivity of 8YSZ and 10Sc1CeSZ from 550°C to 800°C. To measure conductivity of a bulk sample, a four-probe method with setup shown in Figure 3-4 was used. To prepare a 3cm x 1cm x 1cm samples; the electrolyte materials (either 8YSZ or 10Sc1CeSZ) were combined with pre-mixed 3 wt% PVA solutions and cold-pressed using a SGS hydraulic press at 5 tonnes. The pressed bars were sintered at 1450°C for 4-hours with 1-hour dwelling for organic burnout at 350°C.

Silver paste (DAD-87) was used to attach 0.7 mm diameter pure silver wires (99.99 %) to the sintered sample. Both voltage and current wires were connected to a Solartron 1470E for measurement. As the conductivity test was carried out at high temperature, a vertical high temperature furnace (VECSTAR) shown in Figure 3-5 was used. The conductivity measurement followed the temperature profile in Figure 3-6 with no oxygen flow employed. Galvanostatic setup was used with constant current to measure the voltage produced. The conductivity of the materials, σ (S/cm), was calculated using the relation shown in Figure 3-4.

$$R = \frac{V}{I} = \frac{\rho l}{A} = \frac{l}{\sigma A}$$

$$\sigma = \frac{I \ x \ l}{V \ x \ A}$$
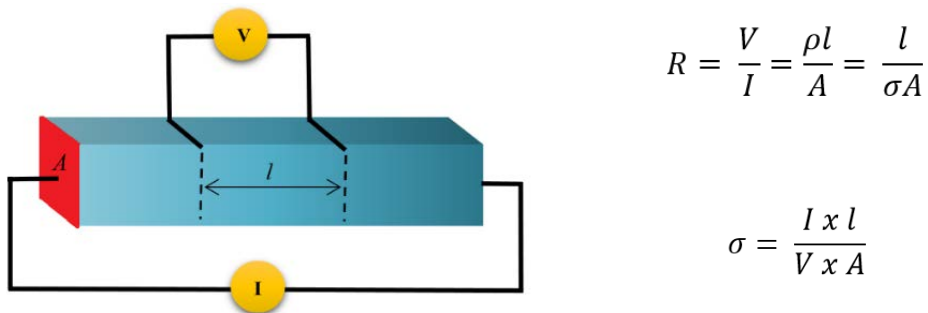
Figure 3-4: Four probe method for measurement of conductivity, where R is resistance of the conductance, V is the voltage, I is the current, ρ is the resistivity in Ω.cm, σ is the total conductivity in S/cm, *l* is the equal distance between the points, and A is the cross-section area

The reading were taken from 800°C to 550°C for three times for each sample. The thermocouple used was Type K, which were placed near the sample (within 0.5 cm) in the middle of the furnace. The accuracy of the temperature could be improved gin the future experiment by placing two or more thermocouple with proximity of 1-2 mm.
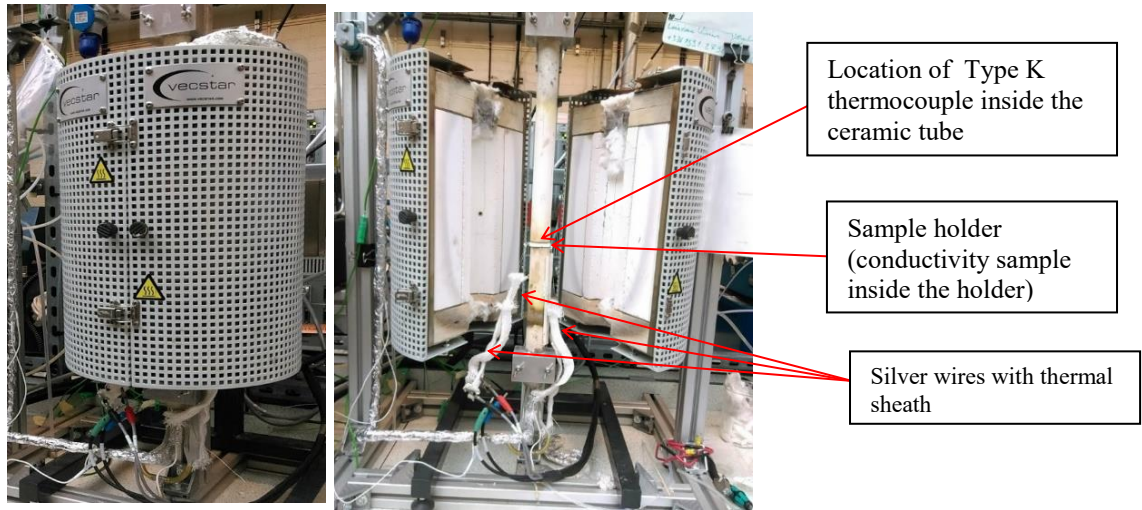
Figure 3-5: Vecstar high temperature vertical furnace.
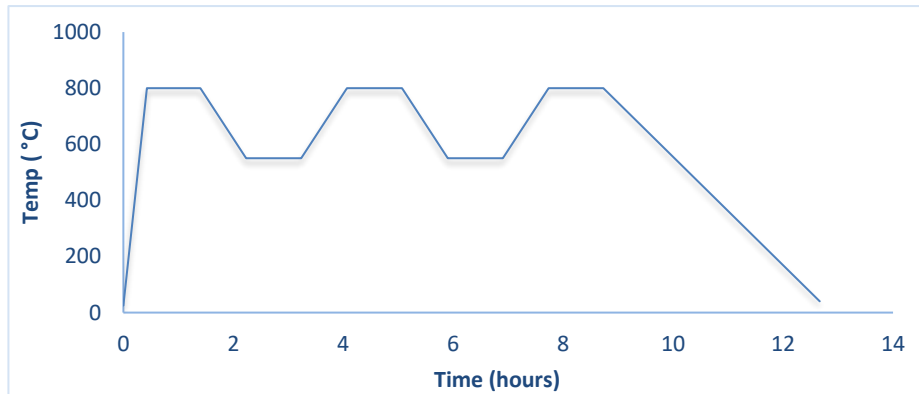
Figure 3-6: Temperature profile for conductivity test.

3.3.5 Rheology Test

Rheology is the study of behaviour of liquid or soft solid flow. In this thesis, the test was carried out to observe rheology behaviour of the tape casting slurry with different dispersant using an AR-G2 Magnetic Bearing Rheometer (TA Instrument). To measure the rheology behaviour, a

small amount of tape casting slurry was introduced to the shear plate. The cone rotated according to the shear rate that had been setup. The measurements were performed at 20°C with a shear rate of 0.1 cm/sec to 20 cm /sec with a cone size of 20 mm and cone angle of 2°. The viscosity with respect to the shear rate was recorded.

3.3.6   SOFC Full cell preparation

The full cell preparation description in this section is the final SOFC fabrication process. Tests carried out to optimise tape casting parameters will be covered in Chapter 4.

3.3.6.1 Tape casting

Ball milling and de-gassing

For the electrolyte slurry, a water-based emulsion binder system (WB4101) supplied by Polymer Innovations Inc. (USA) was used with the composition as shown in Table 3-3. For both anode layers, the cermet powders were mixed with distilled water, dispersant and anti-foaming agent by ball milling for 24 hours at 120 rpm for complete dispersion of the powders. Mixtures of different sizes of zirconia grinding media were used to ensure uniform homogeneity. 3 wt% tapioca starch was added to the anode substrate slurry as pore former. The plasticizers and binder were added, followed by further 4 hours of ball milling at 70 rpm. Prior to ball milling, the PVA solution was prepared using distilled water at 80°C with the weight ratio of 1:4 to ensure complete solubility of the solid PVA.

A 5 to12 hours de-gassing process using vacuum de-gassing was used to eliminate all bubbles, followed by 1 to 2 hours of slow rolling using a ball milling machine at low rpm. The organics and optimum compositions for the anode substrate (AS) and anode functional layer (AFL) are shown in Table 3-4. The solids loading used was 55 wt% (35 vol %), the amount of organics was 15.1 wt%, with water as solvent at 29.9 wt%. The binder-to-plasticiser ratio was 1:1.

Table 3-3: Electrolyte tape casting formula

Chemicals	Function	wt %
8YSZ/10ScCeSZ	Ionic conducting phase	49.8
WB4101	Binder	19.3
DS001	Dispersant	2.0
DF002	Anti-foam	0.4
PL005	Plasticiser	0.5

Table 3-4: Anode tape casting formula

Chemicals	Function	Wt %		
		AFL	AS (NiOYSZ)	AS (NiOScCeSZ)
Nickel Oxide	Metal phase	35.75	35.75	35.75
8YSZ/10ScCeSZ	Ion conducting phase	19.25	19.25	19.25
Tapioca Starch	Pore former	-	3.00	3.00
BASF Dispex Ultra 4404®	Dispersant	1.00	1.00	1.00
Water	Solvent	35.40	30.0	30.0
Antifoam 204	Antifoam	0.20	0.20	0.20
PVA	Binder	4.10	5.40	5.40
PEG 400	Plasticiser I	2.70	4.00	2.70
Glycerol	Plasticiser II	1.40	1.40	2.70

Slurry tape casting

The slurries were tape cast onto a silicone coated PET film using a single blade laboratory tape casting machine with vacuum bed (L800 by MTI Corp). The machine uses a vacuum to hold the PET film. The gap height can be set using a built-in micrometer as shown in Figure 3-7. The blade's gap height and speed were adjusted for each layer accordingly as indicated by Table 3-5. A thin electrolyte layer was tape cast first with a gap height of 0.10 mm, followed by the AFL layer with gap height of 0.15 mm and finally the thick anode substrate layer with gap height of 2.00 mm. This method was adapted from Schaufbauer et al. [81] and Wang et al. [12]. Each layer was dried in an oven before tape casting another layer on top of it. The drying was done at 70°C for the electrolyte and AFL, and 33°C for the thick anode substrate layer.
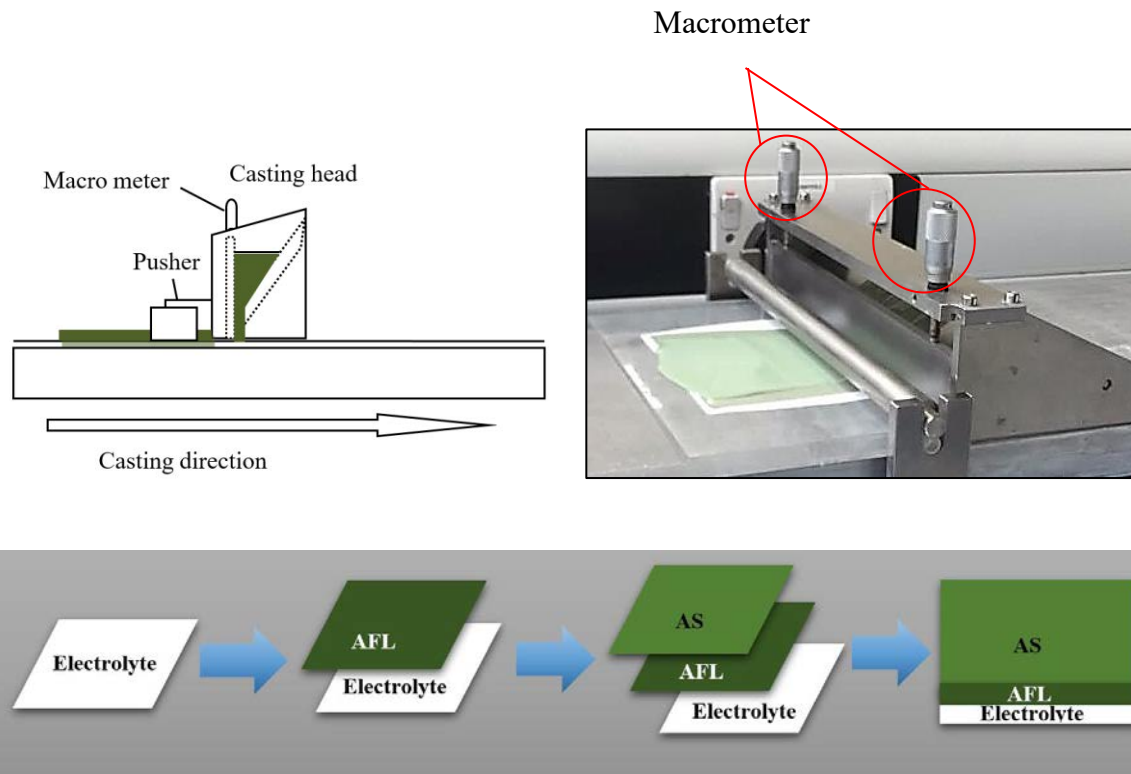
Figure 3-7: Multilayer tape casting with vacuum bed tape casting machine MTI Corp L800.

Table 3-5: Settings for different tape casting layers

	Electrolyte	AFL	AS
Tape cast speed	3.33 mm/s	6.33 mm/s	6.3 mm/s
Gap Height (µm)	10-12	15	200
Drying temp/duration	70°C / 10-15 minutes	70°C/ 10-15 minutes	33°C/Overnight

Co-Sintering

Button cells (3 cm diameter) were produced from the green tapes using a metal punch cutter and co-sintered according to the temperature profile in Figure 3-8. The cells were co-sintered at 1350°C for Ni/8YSZ and 1300°C for Ni/10ScCeSZ for 4 hours with 1°C/minute heating rate and organic burnout stage at 550°C. Only between the burnout stage and the temperature the material started to sinter, the heating rate used was 3°C/minute. Several dwelling stages were used to minimise the effect of expansion and contraction of the cell layers relative to each other.

65

Prior to co-sintering, the cut-tapes were further dried at 100°C for 1 hour with a 5 gram weight on top to emphasize the cell flatness. The final co-sintering temperature was the optimised temperature, balancing between the densification of the electrolyte and cell flatness. The further enhance the cell flatness, a 1gram alumina plate was placed on top of the cell during the co-sintering process.
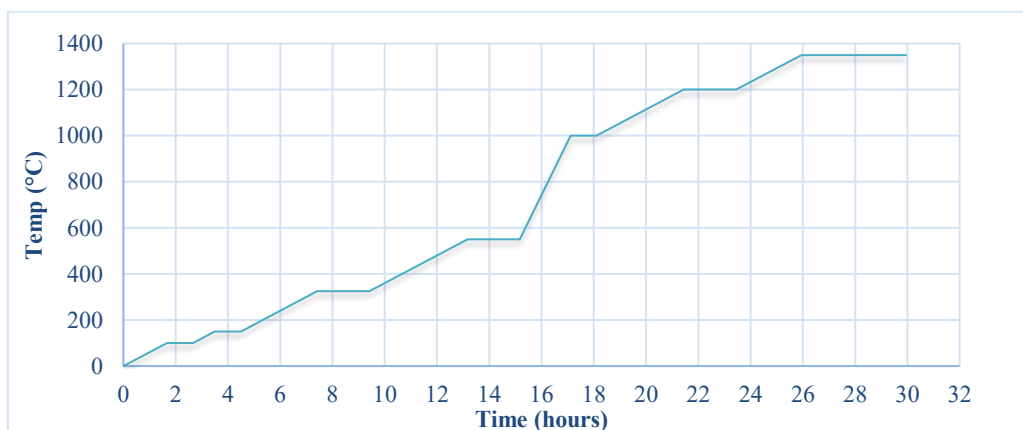
Figure 3-8: Half-cell co-sintering temperature profile.

Cathode layer- thin layer deposition
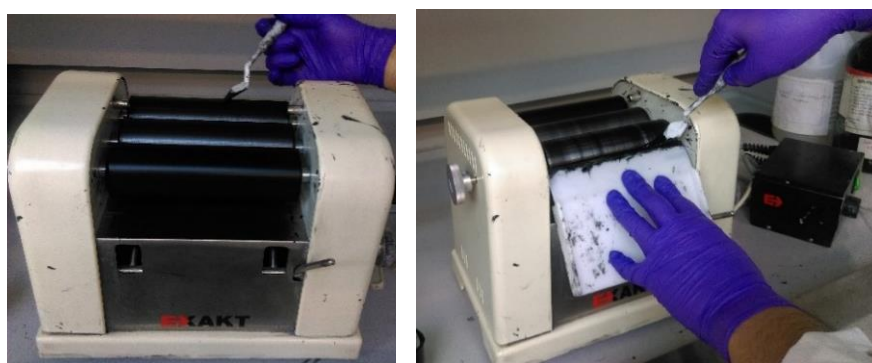
Figure 3-9: Cathode ink production using three roll mill machine (EXAKT USA).

The sintered cells were hand painted with two 15µm thick layers of cathode ink with 2 cm diameter and further sintered at 1100°C with a heating rate of 1°C/minute and organic burnout

stage at 550°C. The first cathode ink layer (cathode active layer) was made from 50:50 vol% LSM and YSZ (with 26.0 vol% solid content) while the second layer consisted of only LSM (with 23.1% solid content). Figure 3-9 shows the dispersion process of the LSM cathode powder with ink vehicle V-737 (Hareus) using EXAKT Three Roll Mill machine. The SOFC full cell preparation used in this thesis is summarised in Figure 3-10.

Powder pre-calcination

Ball milling 1st stage (24 hours @ 120rpm): Powders, water, dispersant, anti-foam

Ball milling 2nd stage (4 hours @ 70rpm):

De-gassing (5-12 hours) + slow rolling

Tape casting (in sequence, drying in between): Electrolyte, AFL, AS

Multilayer green tape

Co-sintering half cells at 1350°C/1280 °C

LSM Cathode painting

Cathode sintering at 1100°C
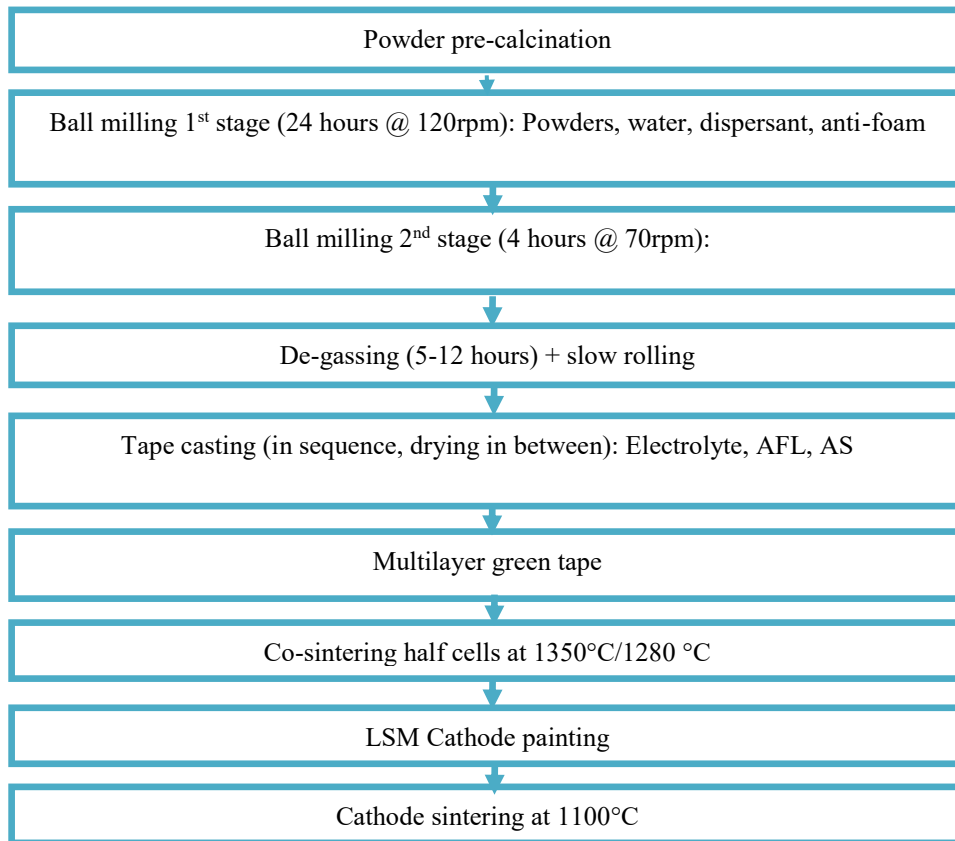
Figure 3-10: SOFC full cell manufacturing.

3.3.7   Cell testing and Performance

After cell manufacturing, the cells needed to be prepared for electrochemical testing. Figure 3-11 shows the summary of the process.

Full cell manufacturing → Current collectors → Cell Mounting → Cell testing → Characterisation

Figure 3-11: SOFC Cell testing preparation and characterisation.

3.3.7.1 SOFC Cell Testing Preparation

The attachment of the current collectors at both of the electrode surfaces was achieved using dense silver paste (DAD 87) with a minimum coverage area as shown in Figure 3-12a. Active area calculations were based on the exposed cathode surface which was $1.68cm^2$. The same coverage areas were assumed on all tests. 0.25mm diameter of silver wires (Scientific Wires Company) 99.99% pure were used as the current collectors. For the current measurements, 6 strands were used while for voltage, 4 strands of wires were used.
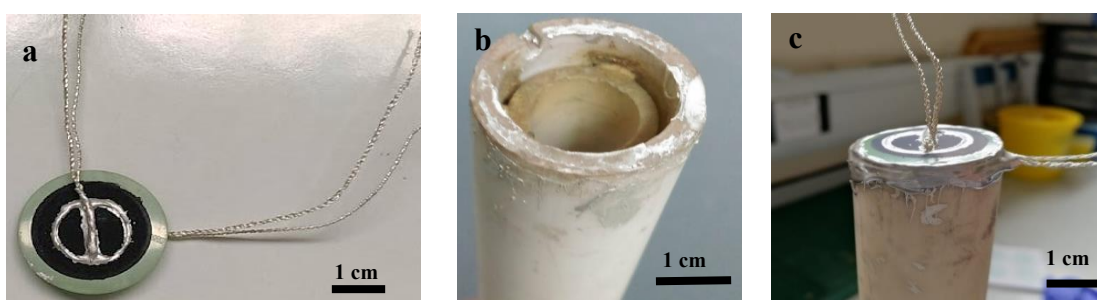
Figure 3-12: Attachment of a) SOFC cell and current collectors b) Double layer alumina holder c) SOFC cell mounting to cell holder.

A double layer alumina cylinder tube; with tube length of 300 mm was used as shown in Figure 3-12b. The outer/inner diameter of the cylinders were 30 mm and 20 mm respectively. The SOFC cell was mounted on the larger diameter alumina cylinder using dense silver paste (DAD-87) with the cathode side facing outwards and the anode side facing downwards towards the direction of fuel as depicted in Figure 3-12c. The mounted cell together with the cell holder was dried at 120°C overnight and re-patched again with silver paste the next day.

Figure 3-13 and 3-14 represent how the cell testing setup in the horizontal furnace (brand LENTON). The other end of the mounted cylinder was connected to the fuel mixer that provided the fuel from individual gas lines. The fuel flowed in the inner tube while the spaces in between the two cylinders channelled the excess fuel and gaseous products. The cathode was exposed to ambient air as the oxygen was used in the reaction.

	Furnace
	Alumina cell holder - outer tube
	Alumina cell holder – inner tube
	Anode
	Cathode
	Electrolyte
	Ag wire
(v)	Potentiostat - Solartron
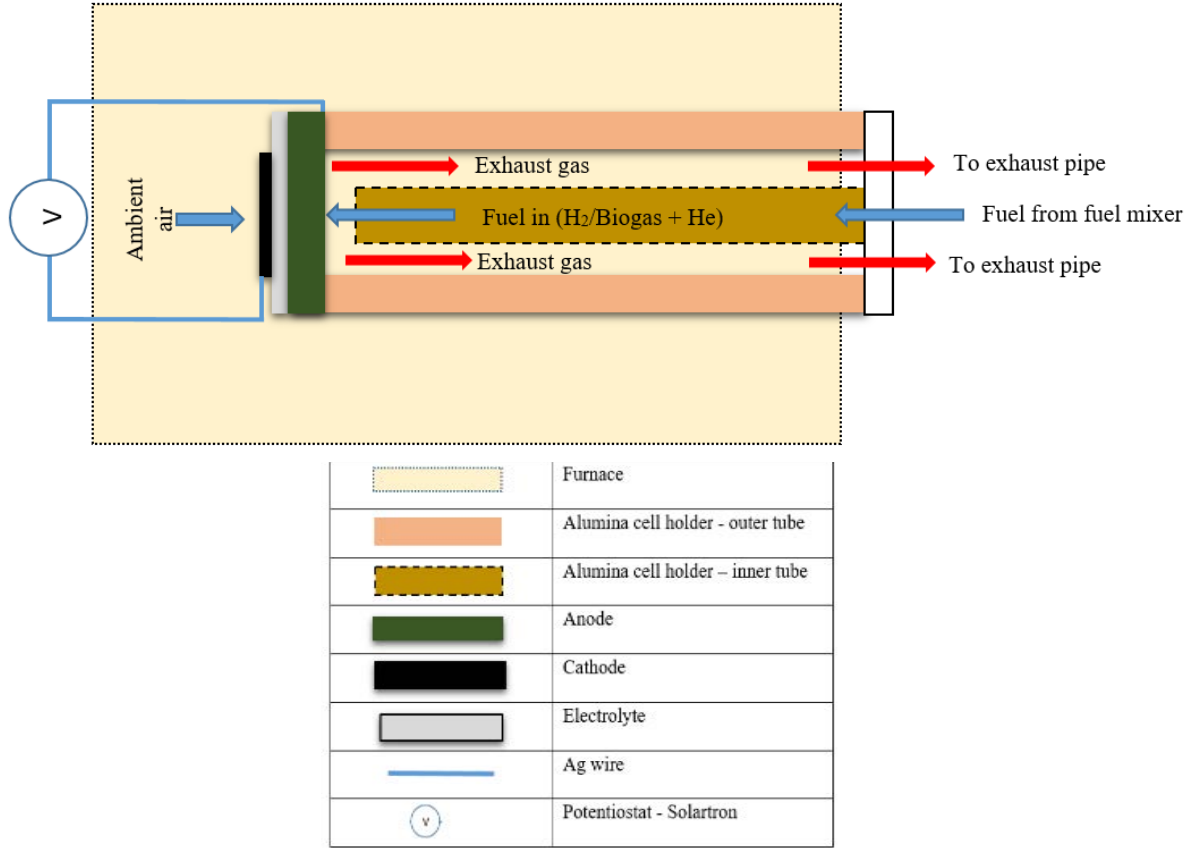
Figure 3-13: Cell mounting and test rig setup.
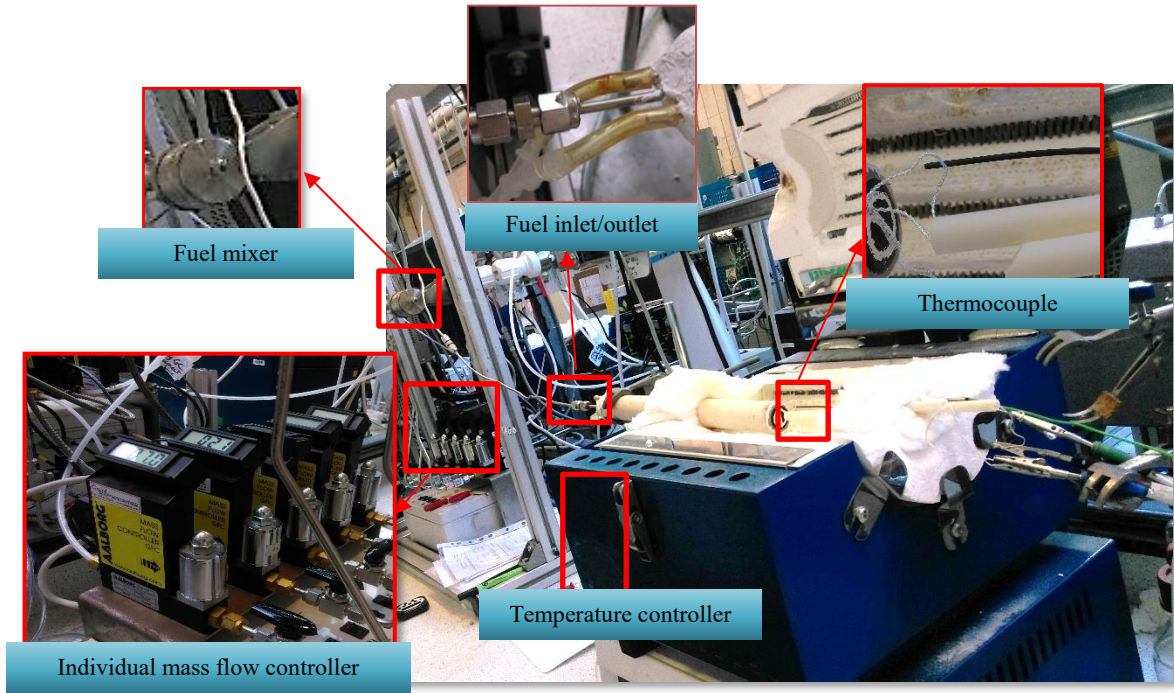
Figure 3-14: Laboratory SOFC horizontal test rig set-up.

The rig was connected to four individual gas feeds which were; methane, hydrogen, helium and carbon monoxide with independent mass flow controllers as shown in Figure 3-14. The gas purity and supplier for each gaseous can be referred to Table 3-2. The test rig was connected to a Solartron 1470 E and 1455 FRA analyser for recording the electrochemical performance and impedance measurement.

3.3.7.2 Cell testing procedure

The SOFC testing furnace was heated up to 750°C at 5°C/minute with no gas flow at the inlet. To ensure the gas line as well as the mounting was leak-proof, a leak test was carried out prior to the heating up and after the furnace reached 750°C. The leak tests were also a quick way to find out if the density of the electrolyte was acceptable. Reduction of the cell carried out at 6 hours with hydrogen introduction at 750°C at a flow rate of 21 ml/minute with additional Helium at 7 ml/min. The reduction was considered to be completed when the OCV value stabilised.

Optimum and high flowrates were used in the electrochemical test in hydrogen. The optimum flowrate was 21 ml/min H_2 and 7 ml/minute He while at higher flowrate setup, 60 ml/minute H_2 was used. The test at 60 ml/minute was carried out at 750 and 800°C to obtain the maximum power density values. Overnight SOFC electrochemical tests used the low temperature and low flowrate setting. Total 24 hours of test in hydrogen were completed before swapping to biogas fuel.

In the biogas setup, simulated biogas was mixed from methane and carbon dioxide with a ratio of 2:1. This composition was chosen according to the C-H-O ternary diagram (Figure 3-15) that indicates carbon build up is most likely with this composition for temperatures from 750°C to

800°C. The gas flowrate used for biogas fuel was 14ml/min CH_4, 7 ml/min CO_2, and 7 ml/minute He.
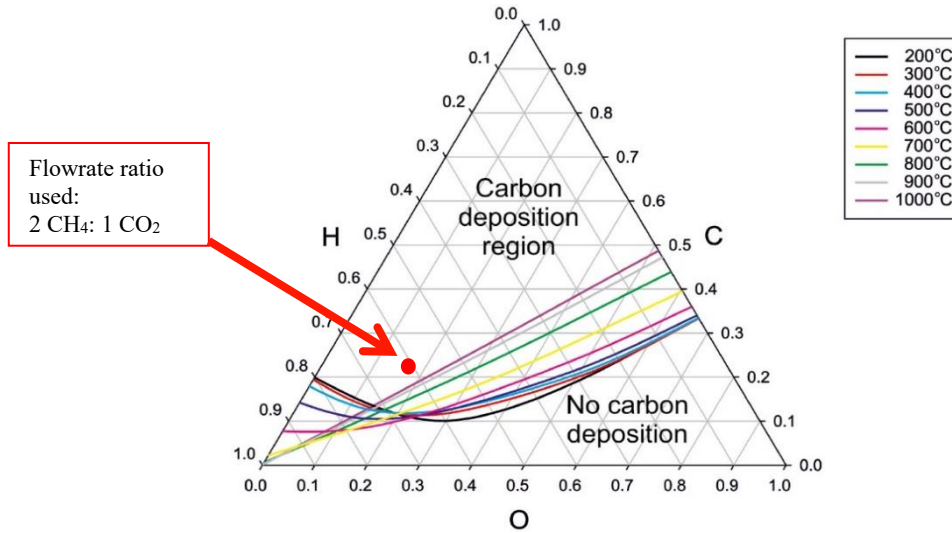
Figure 3-15: C-H-O ternary diagram for carbon deposition region (all type of carbon) at P=1 bar [18].

A post biogas test was carried out to compare with the initial test in hydrogen and to detect any obvious post-effect of running biogas on the cell. The cells' performances were analysed alternately for 48 hours in using OCV readings, current density-voltage (*iV*) curves, potentiostatic, and impedance (EIS) analysis. For the electrochemical tests presented in Chapter 7 for evaluation of the tin-doped Ni/ScCeSZ cells; a slightly longer duration of test was applied.

3.3.7.3 Electrochemical Impedance Spectra (EIS) Analysis

Electrochemical impedance spectroscopy (EIS) is a very powerful tool to determine the source and quantify the resistance inside the whole SOFC cell. The principle in EIS technique is to perturb the electrochemical cell with an AC signal of small amplitude and to observe the ways in which the system follows the perturbation at steady state [47]. In this thesis, the EIS analysis

measured at 0.5 V, 0.7 V and at OCV from frequency range of 0.1 Hz to 1M Hz with signal amplitude of 10 mV.

3.3.8 Microstructure analysis

3.3.8.1 Scanning Electron Microscopy with Energy Dispersive Xray Spectroscopy (SEM-EDX)

SEM of the microstructure of the cell sample was performed using a table top microscope SEM Hitachi TM3030 with a magnification range of 250-5k with an acceleration of 15kV. As the samples are already conductive, no coating is required for microstructure analysis. The samples used were unpolished fragments from SOFC cells. For carbon deposition analysis, the cells were coated with Pd/Pt as the electron beam passed through the carbon sample if uncoated. Both back-scattered electrons (BSE) and secondary electrons (SE) were employed to inspect the cross-sectional and surface morphology, to analyse the distribution of the cermet and the microstructure of each layer. EDX elemental mapping with mixed BSE and SE mode was used to identify the elemental distribution in the samples.

3.3.8.2 XRD-analysis

In this work, X-Ray diffraction analysis carried out to identify the different phase structure in a Ni/ScCeSZ sample. The Ni/ScCeSZ was prepared using pellet and mortar with ratio of 65:35 wt% and addition of 3 wt% of PVA. The mixture was pressed using SGS hydraulic press machine at 4-5 tonne. The sample sintered at 1400°C for 4 hours to solidify the pellet. The sample then exposed to reducing atmosphere in a quartz tube with 20 ml/min hydrogen at 750°C for 24 hours prior to XRD scanning analysis. The crystalline structure of the sample determined by using XRD with Cobalt K-alpha radiation.

3.3.8.3 Porosity measurement

The Archimedes method was used to analyse the porosity of the anode substrate using dry, wet, and immersed weight. The technique is suitable as the anode substrate is porous throughout and has been used widely in literature in measuring the SOFC cell's porosity. The same balance was used throughout the measurement to minimise error. To measure the porosity, anode substrate without electrolyte layer was sintered using the temperature profile in Figure 3-8. The porosity reported is the average porosity value of three samples.

3.3.9   Catalytic activity test

Catalytic activity tests were carried out to identify the catalytic reaction of the different materials with dry simulated biogas. Ni/YSZ and Ni/ScCeSZ pellets were prepared using the same preparation method in the XRD analysis in Section 3.2.8.2. The pellets were placed in a quartz chamber in a horizontal furnace. Simulated biogas which consist of 14ml/min of CH_4, 7 ml/min CO_2 and 7 ml/min of He was purged for 3 hours at 750°C. The outlet gasses were connected to mass spectrometer analysis to evaluate the amount of gases presents in the outlet stream.

3.2.10 Temperature Programme Oxidation (TPO)

Temperature programme oxidation tests were carried out to quantify the amount of carbon in tested SOFC cells (Ni/YSZ, Ni/ScCeSZ and Sn-Ni/ScCeSZ). Prior to the actual test, callibration using three known amount of carbon graphite were carried out. Approximately 200gram of samples from SOFC tested cell were placed in the middle of the quartz chamber in a horizontal furnace with compressed air flow of 50ml/min for oxidation of carbon. The furnace was heated to 600°C at 5°C/minute and annealed for 1 hour to allow complete carbon burn-off. The exhaust gasses were annalysed by the response from connected mass spectrometer. Calculation of the deposited carbon will be discussed in Section 6.3.2.

CHAPTER 4: SOFC FULL CELL FABRICATION OPTIMISATION via REVERSE AQUEOUS TAPE CASTING

4.1 Overview

Tape casting is a well-known technique used to produce large scale ceramic substrates [31, 93]. Major problems in aqueous tape casting includes pinholes, cracking, brittleness, dewetting, high slip viscosity, and curdling as mentioned in Section 2.4.1. This chapter provides insight into the cell manufacturing optimisation for both Ni/YSZ and Ni/ScCeSZ cells used in this research. It presents the challenges, the attempts taken, and optimum conditions found for manufacturing using aqueous tape casting in SOFC full cell production. The manufacturing method was perfected for the benchmark materials Ni/YSZ and used as the standard method to produce Ni/ScCeSZ following several adjustments.
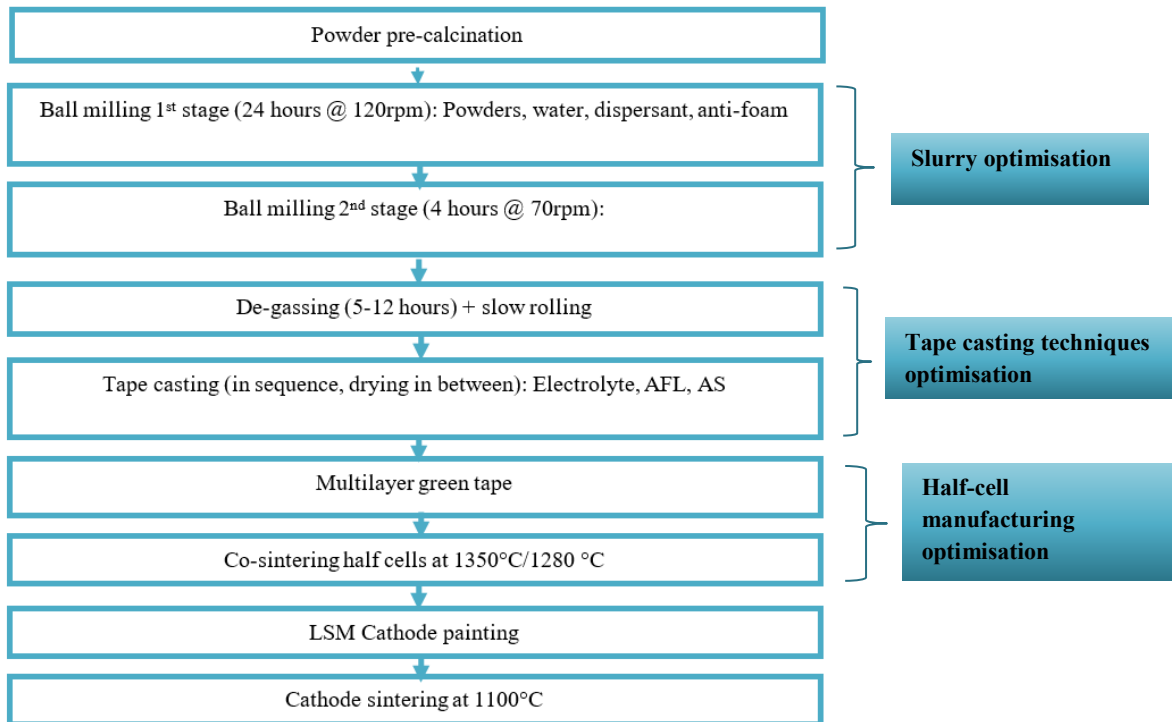
Figure 4-1: Full cell manufacturing process with optimisation focus.

During optimisation, each stage in Figure 4-1 was iterated until satisfying conditions were achieved. Figure 4-1 is the replication of Figure 3-10 with a focus on the main optimisation area. In the end of the fabrication optimisation, the SOFC cells manufactured met the structure requirements of all three components: dense electrolyte, thick porous anode substrate and thin porous cathode. The chapter is divided into two sections. The first part is on tape casting optimisation and the second part on the full cell manufacturing. A summary of these processes was already reported in Chapter 3.

4.2 Aqueous tape casting techniques optimisation

In the preliminary work using the same composition and parameters on electrolyte (13YSZ) powder, flexible flawless green tape that can be bend with no pinholes produced as shown in Figure 4-2. However, using the same composition for thick anode substrate produce tapes with several defects.

Figure 4-2: Flexible and defect-free thick green tape using 13YSZ powder obtained during preliminary trial.

For thick anode substrate, it was observed that when slurry optimisation was carried out focusing only on the composition of the slurry, a high degree of imperfections of dried green tape were seen. Wavy structure, mud-cracking defects, crow feet cracks, and pinholes formed on every sample despite any changes in the formulation. Figure 4-3 shows examples of defects on sub-optimal samples dried at room temperature. Optimisation was focused on the thick

anode tape as this is where the main problems occurred, compared to the thin electrolyte and anode functional layers. The term 'green tape' used in this chapter denotes a dried tape that has yet to be sintered, not the colour of the dried tape cast sample.

It was found that besides the formulation, additional parameters have high impact on manufacturing thick anode tapes:

a) De-airing or de-gassing method and duration,

b) Drying rate and temperature: Low drying rate is preferable.
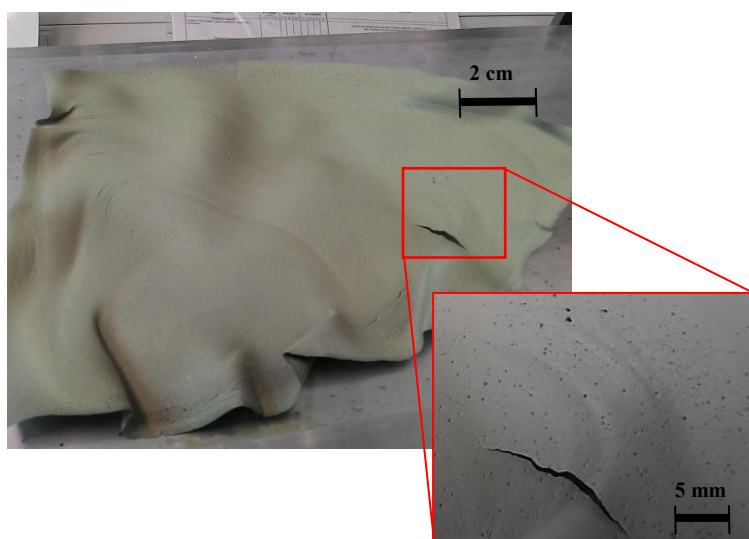
Figure 4-3: Defects on green tape, wavy structure, cracks and pinholes.

4.2.1 De-gassing

Filtering the slurry with a 50 μm fine net for paint filter or food filter worked well for apparent bubbles. Yet, there were small size bubbles inside the slurry, which were not visible in the slurry before casting. Figure 4-4 shows a green tape full of pinholes that originated from a filtered slurry with no apparent bubbles. Immediately after tape casting, the bubbles appeared on the tape casting bed, hence causing pinholes in the dried green tape. De-gassing for 5-12 hours using a vacuum desiccator with additional slow rolling was adequate for all the bubbles to

disappear. A long de-gassing duration was also applied in work done by Baquero et al. [91] which used a de-gassing duration of 24 hours. Figure 4-5 shows the condition of the slurry during and after the de-gassing process.
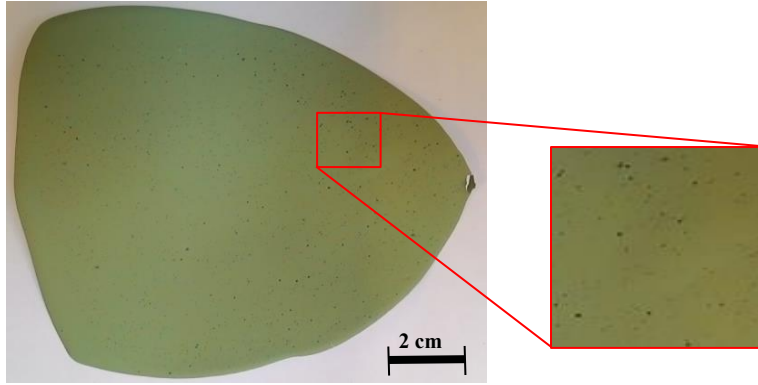
Figure 4-4: Dried tape fabricated without the de-gassing process.
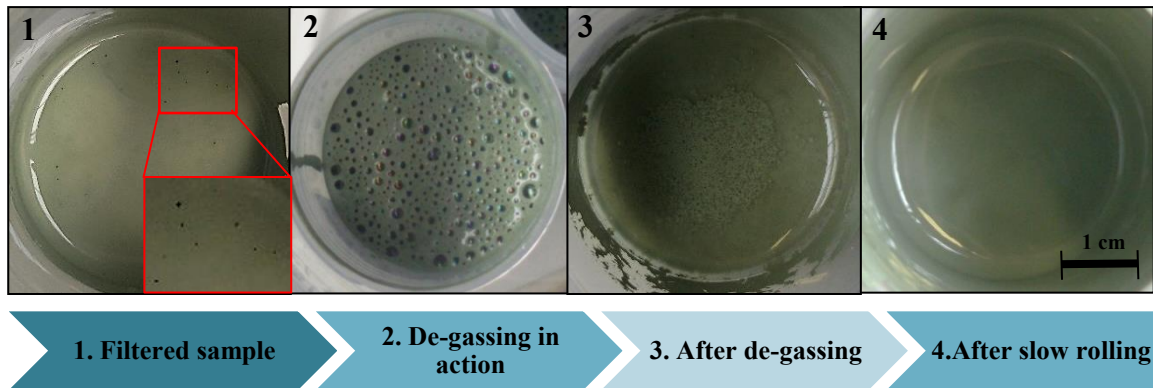
Figure 4-5: Degassing process of anode substrate slurry.

4.2.2 Drying rate

Through several trials, the drying rate was found to be crucial and a slow drying rate was preferable. The sensitivity towards high drying rates was only observed when drying anode substrates with thicknesses before sintering around 500-600 μm. No such problem arose when the slurry was cast as a thin layer (of approximately 50 μm) as shown in Figure 4-6. This is supported by a theory in literature that suggested there is a critical cracking thickness (CCT)

where a tape with a given in-plane stress will spontaneously crack during drying due to shrinkage stresses [109]. The CCT is expressed by;

$$CCT = \left(\frac{K_c}{1.4\sigma}\right)^2 \qquad \text{[Eq. 4.1]}$$

where K_c is the fracture toughness and σ is the in-plane stress.

This problem exists primarily in water-based systems as the capillary forces during drying are higher than solvent-based system, as a result from the high surface tension of water [110]. This explains why the cracks only appear in thick tapes of anode substrate.

Figure 4-6: Crack-free thin tape (~50μm), dried at room temperature with the exact thick tape slurry as in Figure 4-7.

When the thicker tapes were dried at room temperature, the tape showed mud-cracking drying problems as shown in Figure 4-7a. Drying in an oven at 50°C resulted in larger cracks across the tape and produced stiff tapes as shown in Figure 4-7b. At 30°C in the low temperature oven, a crack-free green tape was produced as shown in Figure 4-7d. Using another low temperature oven fitted with a blower greatly reduced the drying time but produced mud-cracking defects as shown in Figure 4-7c.
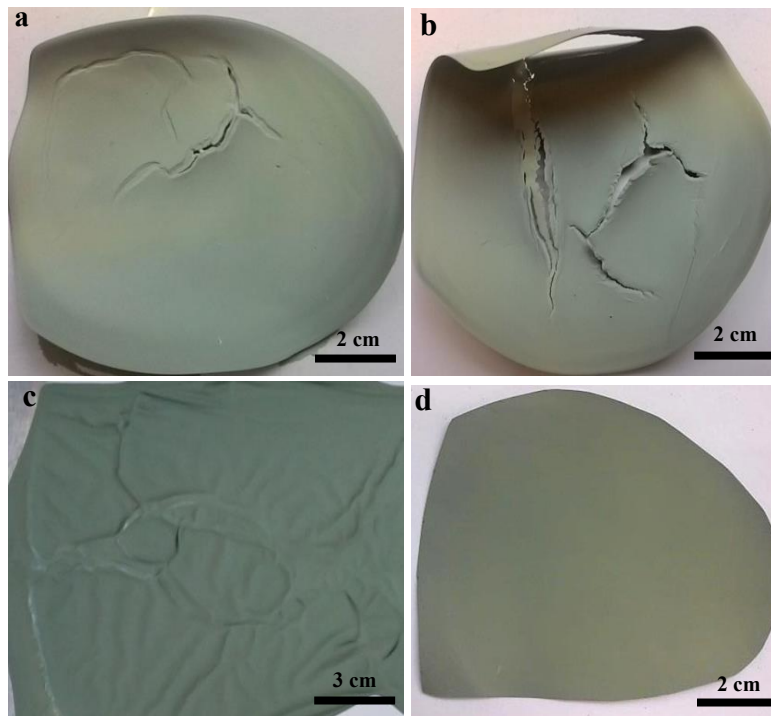
Figure 4-7: Cracking defects with a) drying at room temperature, b) drying at 50°C c) drying at 30°C with air blown, and d) drying at 30°C.

The cracks in Figure 4-7a) to c) may be speculated to be due to non-uniform drying between the skin and the body of the tape. With a high drying rate, the outer layer of the thick tape dried first, forming a semi-dry skin whilst the middle of the tape was still wet. Stresses on these two layers of skin and slurry caused the drying skin to stretch to the point where it causing a large drying crack [111]. With slow drying rates, as in the low temperature oven without any air blown, the drying rate on the skin matches the drying rate on the bulk of the slurry, hence reducing the stresses between the two layers. Comparing the drying condition observed with work done by Fu et al [95]; which dried their thick anode tape at room temperature, it is in agreement as the temperature in those geographical locations is approximately 33°C with high humidity content in the atmosphere. Other works dried their tapes in low temperature oven, at 25°C.

4.3   Slurry Optimisation

Tape casting mixed ceramic oxide and metal oxide powder (cermet) was found to be trickier compared to tape casting thick electrolyte tape as shown in Figure 4-2. The reasons may lie in the differences in the powder properties. In all aspects, the NiO and ceramics powder (8YSZ and 10ScCeSZ) used and resulting slurries were extremely different; particle size, rheology behaviour and stability. The particle size influenced the arrangement of the particles in the tape cast slurry, hence affected the rate of drying as well. The effect of the parameter (drying rate and de-gassing method) and composition was more apparent in formulating the composition for the thick anode substrate. The optimisation of the organics was carried out using 55 wt% solid loading content with a ratio of NiO:YSZ of 65:35 wt%. Before going into the optimization process, the summary of role of organics can be referred to Table 4-1, which was reviewed on Chapter 2 based on Mistler [3] and Hotza [31].

Table 4-1: Roles of organics in tape casting [3, 31]

Organic type	Role
Binder	1) Provide the network to holds the entire chemical system together in a tape 2) Provide strength in the green tape
Plasticiser	1) To increase the flexibility of the tape, so that the tape can be rolled 2) To soften the tape 3) Decrease the glass transition temperature of a binder
Dispersant	1) to separate the primary particles in the solvent so that the binder can coat them individually, 2) reduce viscosity hence increase the solids loading, and 3) to decrease amount of solvent
Wetting agent	To decrease the high surface tension of the water so that the slurry can be spread evenly on the carrier film.

Slurry optimization was carried out based on the formulation reported by Fu et. al [95] , but with different types of dispersant, de-foamer and surfactant. Table 4-2 shows the attempts used

in producing flexible Ni/YSZ tapes as shown in Figure 4-8. Briefly, in optimising the slurry, the amounts of the three organics in the formulation; binder, plasticiser and anti-foam, were varied. In the actual optimisation stage, a lot more efforts have been made with almost 20 formulations tested (supplied in Appendix). However, for simplification, only 9 compositions are reported here to show the effect of the key variables.
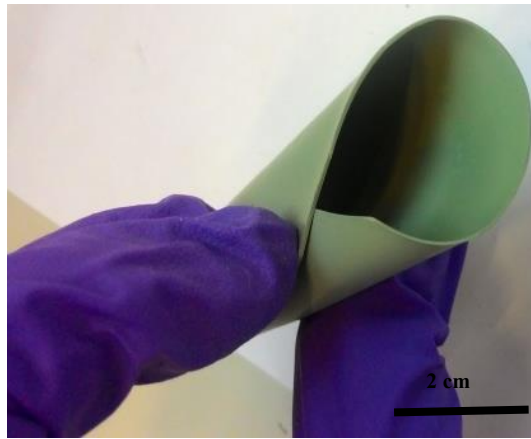
Figure 4-8: Flawless and flexible green tape anode.

Table 4-2: Optimisation stage for anode substrate

	Wt%								
	Vary binder				**Vary de-foamer**		**Vary plasticiser**		
	A1	**A2**	**A3**	**A4**	**B1**	**B2**	**C1**	**C2**	**C3**
Ceramics	55	55.0	55.0	55.0	55.0	55.0	55.0	55.0	55.0
BASF Dispex	1.0	1.0	1.0	1.0	1.0	1.0	1.0	1.0	1.0
PVA	4.5	5.0	5.5	6	5.5	5.5	5.5	5.5	5.5
PEG 400	1.35	1.35	1.35	1.35	1.35	1.35	2.75	4.13	5.5
Glycerol	1.2	1.2	1.2	1.2	1.2	1.2	1.2	1.2	1.2
Wetting agent	0.1	0.1	0.1	0.1	0.1	0.1	0.1	0.1	0.1
Anti-foam	0.1	0.1	0.1	0.1	0.2	0.5	0.2	0.2	0.1
Water	-balance the 100% composition-								

Optimisation of the amount of dispersant was based on the sedimentation test and zeta potential value. Slurry with 6.0 wt% of binder (composition A4 in Table 4-2) was too thick which made it impossible to pour out from the mixing bottle. Binder amount of less than 5.5 wt% produced

cracked tapes, hence composition A3 chosen to continue for next optimisation. As composition A3 produced a high amount of bubbles, increasing the anti-foam from 0.1 to 0.2% (B2) reduced the amount of bubbles. Nevertheless, de-gassing was still needed to completely remove all the bubbles. Varying the amount of PEG change the drying time and the flexibility of the tape. Composition C2 gave an acceptable tape that was flexible with no defects and which was used as the first starting point for tape casting in this work. As the work progressed, slight adjustments were made with the addition of pore former and no wetting agent used in the final slurry as presented by Table 3-4 in Chapter 3. Note that in section 4-3, the composition used for the parameter was following composition in Table 3-4 without the pore former. Pore former was added on later stage.

This section onwards presents more detail elaboration on the effect of organics based on the final slurry formulation in Table 3-4, with only one parameter deviates while other parameters were kept constant. Dispersant selection was based on the pre-stability test as described in the next section.

4.3.1 Dispersant

Two sedimentation tests were carried out to select the dispersant from a choice of 1) phosphonate salt (BASF Dispex Ultra 4404, 2) polyacrylic acid (PAA) 500g/mol (Acros Organics), and 3) ammonium poly methyl acrylate (Darvan C-N by Vanderbilt). The first sedimentation tests were carried out with 1.0 wt% of dispersant in a suspension of 0.01 vol% of YSZ. Suspensions with phosphonate salt (BASF) and PMMA (Darvan C-N) used distilled water while in PAA the tests were carried out at pH 9. The pH was adjusted using 0.1 mol% ammonium solution. The pH used followed recommendation of the supplier and literature [93, 95]. Figure 4-9 shows the sedimentation test results which portrayed that PAA as the best candidate in which there was no settling of the suspension for a maximum of four days. Luo et

al [94] also reported that the maximum holding time for PAA was four days. PMMA and phosphonate salt (BASF Dispex FA 4404) last only for two days and one day maximum, respectively. The PAA dispersant had excellent properties confirmed by the rheology test as in Figure 4-10 where PAA shows the lowest viscosity compared to the others. The slurry shows shear-thinning behaviours, which means the viscosity of the slurry decreases with increasing shear rate. The final composition slurry's viscosity was 3544 mPa s. at shear rate of $10s^{-1}$.
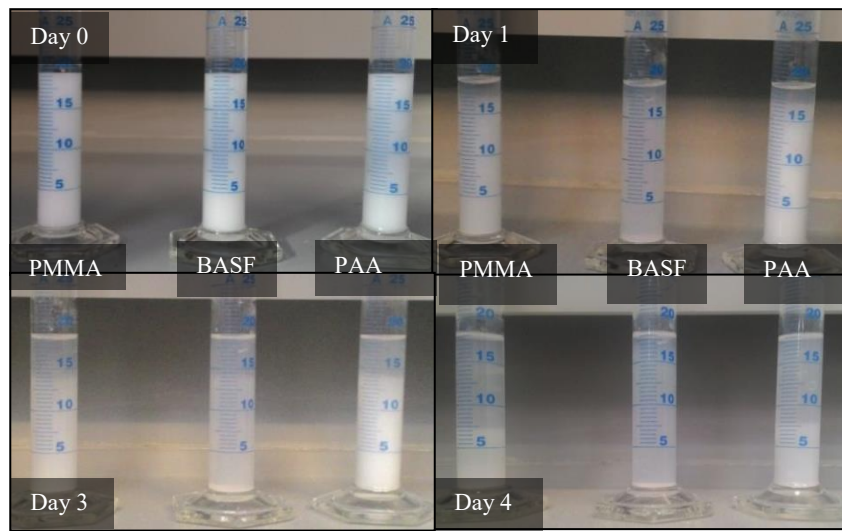
Figure 4-9: Sedimentation test using suspension of powder in water with 1.0% dispersants.
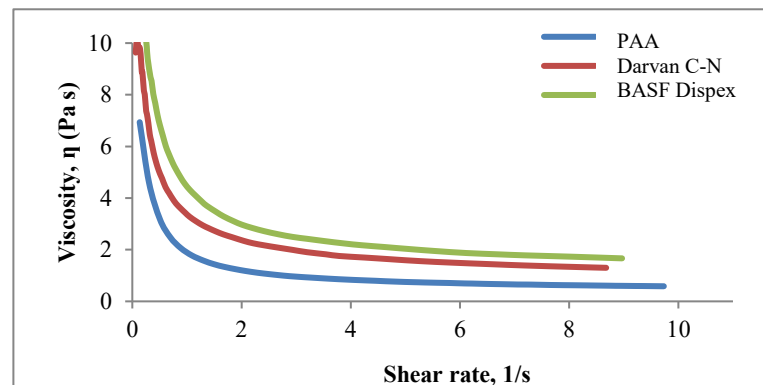
Figure 4-10: Rheology behaviour of different type of dispersant.

The second sedimentation test was carried out with the actual tape cast slurries with two different dispersants; one with BASF Dispex FA 4404 and another one with PAA. The same

method was practised by Schafbauer [81]. After one week of sedimentation test using the actual slurry, the settling of both systems was similar as shown in Figure 4-11. The settling may not have been affected too much by the degree of dispersion in the high viscosity slurry with the presence of other organics, despite the superiority previously shown by PAA.
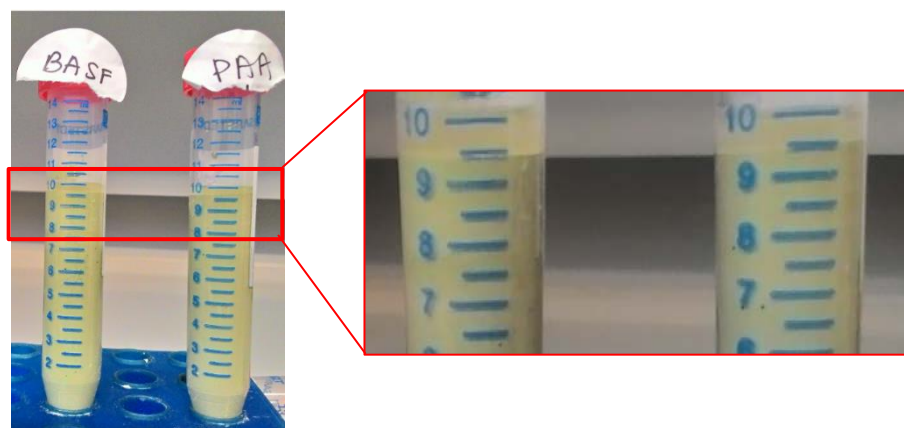
Figure 4-11: After 1 week of sedimentation test using actual tape casting slurry.
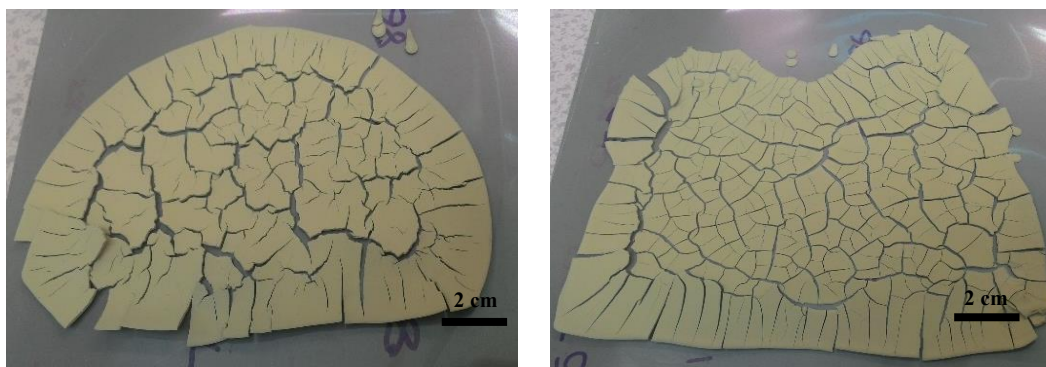
Figure 4-12: Cracked tape with attempt of using PMMA (Darvan C-N) as dispersant.

Despite the better stability of the PAA and PMMA (Darvan C-N) dispersants, phosphonate salt (BASF Dispex Ultra) was chosen for the work reported in this thesis. For PAA, the pH needed to be adjusted to pH 9 prior to mixing and needed to be maintained at this value. This value may change with the addition of other organics, hence after first and second stage of mixing, the pH of the slurry would require to be monitored and adjusted. This added difficulties to the manufacturing process. Darvan C-N (PMMA) was tried as the second-best candidate. However,

constant cracking in the tape produced as shown in Figure 4-12 due to lower slurry's viscosity as reflected by Figure 4-10. The slurry's viscosity at shear rate of 10 s⁻¹ with Darvan C-N was 1344 mPa.s opposed to final slurry viscosity 3544 mPa s. Hence, phosphonate salt (BASF Dispex Ultra FA 4405) was finally selected.

Zeta potential measurements were attempted several times but the readings were not consistent and no conclusive result can be made from it. Hence, the result is not reported here. The only consistency from the reading was higher than -40mV with dispersant amount higher than 1.0 wt%. The 1.0 wt% of dispersant used in the formulation was based on the dispersant amount used for 8YSZ in previous literature [91, 100].

4.3.2 Binder

By referring to Schafbauer et al [81], a ratio of 8% binder to solids loading (4.5wt% of slurry) was tested. Figure 4-13 shows as-dried green tape that had large cracks both perpendicular and in line with the casting direction. It was brittle and cracked when bent. A tape with 10% binder to solid loading ratio (5.5 wt% in slurry) had sufficient strength and could be rolled as in Figure 4-14. Increasing the binder amount more than 10% increased the viscosity too much and it was not possible to cast the slurry.
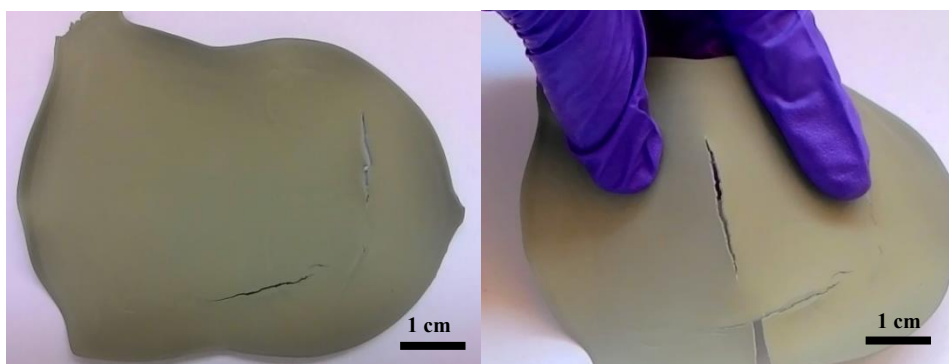
Figure 4-13: As-dried green tape at 8% of binder to solid loading.
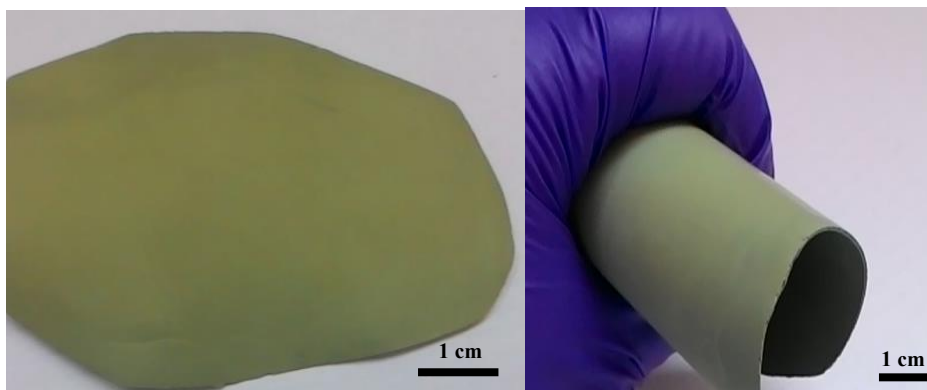
Figure 4-14: As-dried green tape at 10% of binder to solid loading.

In the report by Schafbauer et al.[81], as the amount of binders increased, more pinholes formed as there was a low de-airing effect. As this slurry was filtered, de-aired and slow ball-milled prior to casting, this correlation was not observed here.

4.3.3 Plasticiser

As the organics used were adapted from the work by Fu et al. [95], two types of plasticiser were used. In [95], glycerol was used as anti-adhesive and PEG 400 as the plasticiser. The optimised amount of plasticiser found was with a 1:1 ratio of plasticiser to binder wt% ratio. Increasing this by 20% increase the flexibility of the tape, when decreasing by 20% and more, the dried tape was cracked, curled and not flexible. Negative effect of using too much plasticiser has not been observed, however. Figure 4-15 shows the result of the dried tape with different plasticiser content.
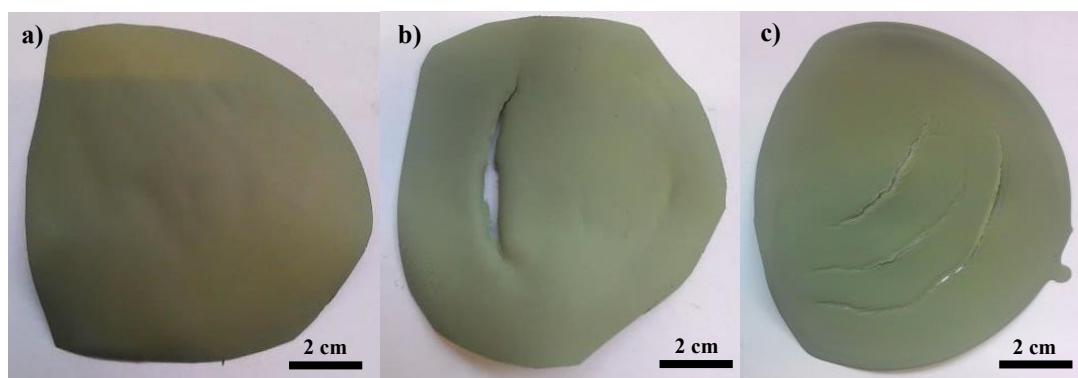
Figure 4-15: Different plasticiser content with wt% of plasticiser of binder a) 120 wt%, b) 80%, and c) 60%.

In the tapes obtained in Figure 4-15, only a small amount of glycerol was used following the formulation from [95]. The plasticiser used in the formulation was 25 wt% glycerol and 75 wt% PEG 400. Another short test that was carried out was to observe the individual effect of PEG 400 and Glycerol, and the combined effect (1:1 ratio) of the two plasticisers. However, there was a slight difference in the drying parameter (due to technical error) where the tape was dried at 35°C compared to the drying temperature of 30°C that was previously used in the cell manufacturing.

The plasticiser's role in the slurry is to lower the glass transition temperature (T_g) of the binder and to soften the binder so it is bendable. Using only PEG 400 leads to a hard and stiff tape with cracks at several places as shown in Figure 4-16. Glycerol on the other hand, gave a remarkably flawless and flexible tape. However, the tape that was using glycerol as the plasticiser had a higher amount of humidity in the tape compared to the other two compositions and needed more time to completely dry. From this result, it can be concluded that PEG 400 is very effective in lowering the T_g of PVA which makes the tape very hard while glycerol is very effective as internal lubricant. If a temperature lower than 35°C was used, maybe the tape could dry with lower drying rate thus avoiding cracks. This experiment was unfortunately not concluded due to limited time and space.

The tape with mixtures of PEG 400 and glycerol at 1:1 ratio was completely dry and gave a better consistency than the one with PEG 400 only. In the optimised composition in the cell manufacturing, a PEG:Glycerol ratio of 3:1 was used, resulting in crack-free tapes. The drying temperature was 30°C.
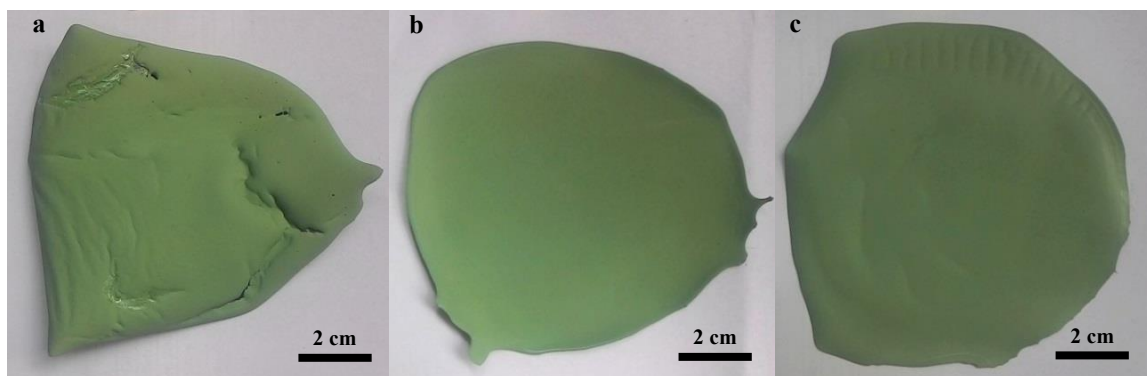
Figure 4-16: Different plasticiser effect with a) using PEG only b)using Glycerol only, c) using PEG and Glycerol (1:1 ratio).

4.3.4   Wetting agent

Using a wetting agent (2,4,7,9-Tetramethyl-5-decyne-4,7-diol ethoxylate, Sigma Aldrich) gave negative impact on multilayer tape casting as shown in Figure 4-17. Initially the wetting agent was essential to aid the spread of the slurry on the silicone coated PET film, however the wetting agent may have changed the surface properties of the previously tape cast layer as well. Hence, no wetting agent was used in the final slurry formulation.
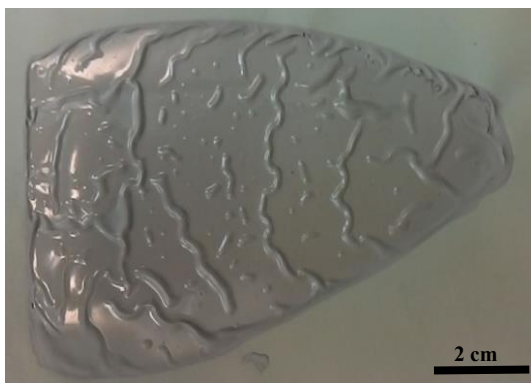
Figure 4-17: Effect of wetting agent in multilayer tape casting.

4.3.5   Pore former

Tapioca starch was used in this work as pore former referring to work by McDonald et al [112]. Figure 4-18 shows the microstructure of the anode substrate without pore former after sintering at 1350°C. For mass transport of fuel and increasing the triple phase boundary (TPB)

area, 30-40 vol% porosity is desired. Figure 4-19 shows a porous anode microstructure with 5 wt% of pore former in the slurry that produced an anode substrate porosity of 45.6%. As this was above recommendation value, the final composition used 3wt% of pore former which gave the anode porosity value of 35.7%. The microstructure of the anode substrate shows that there were microsize pores and macrosize pores originated from the organic burn-off. The micro-pores originated from the burn-off of the plasticiser, binder, and dispersant while the macro-pores stemmed from tapioca starch that was used specifically as the pore former.
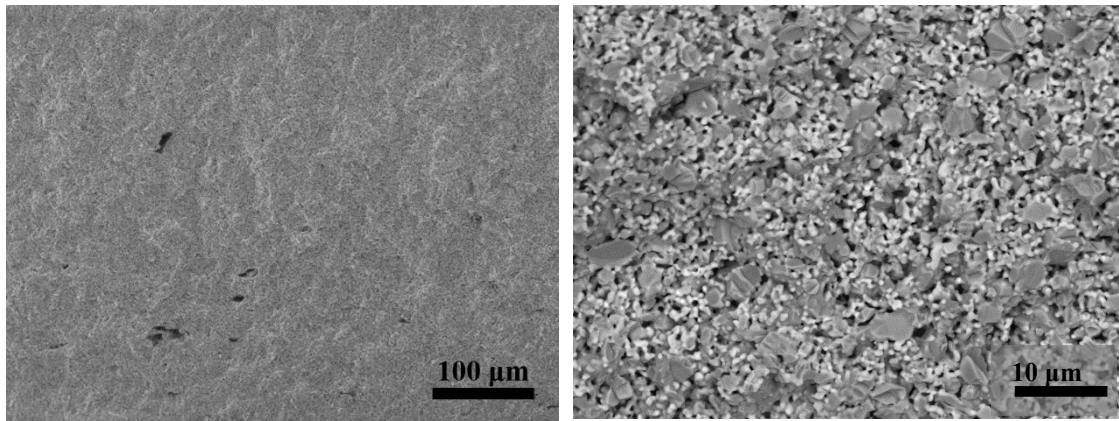
Figure 4-18: Anode substrate microstructure with 0 wt% pore former after sintering.
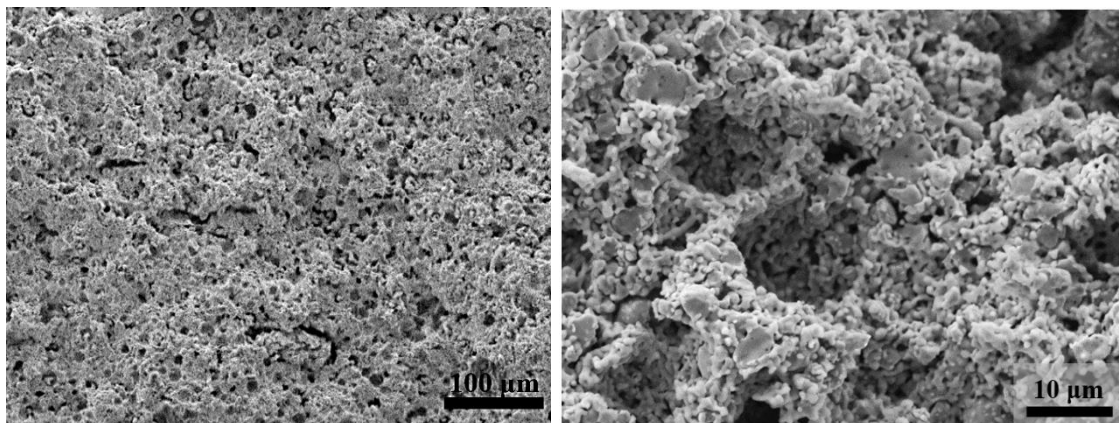
Figure 4-19: Anode substrate microstructure with 5 wt% pore former after sintering.

4.3.6 Final composition for Ni/YSZ and Ni/ScCeSZ

Up to this point, the optimisation was focused on the Ni/YSZ anode substrate. Substituting ScCeSZ as the ceramic material in the formulation of the Ni/YSZ anode substrate resulted in cracked tape shown in Figure 4-20a. By maintaining roughly the same formulation, same amount of organics with 1:1 ratio of PEG 400: Glycerol, the crack-free green tape shown in Figure 4-20b was obtained. Increasing the amount of glycerol increased the internal lubricant for the Ni/ScCeSZ anode. Decreasing the PEG amount increased the T_g of the binder, hence resulted in slower drying rate.
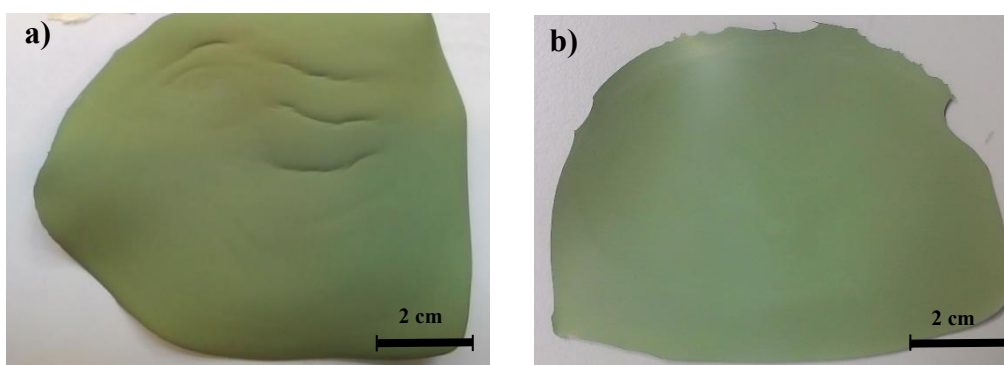
Figure 4-20: Ni/ScCeSZ dried green tape with different PEG/glycerol wt % ratio) a) using 3:1, and b) 1:1.

Figure 4-21: Cracked cell with 50 wt% solid loading.

The final formulations for the anode substrate for Ni/YSZ and Ni/ScCeSZ can be referred in Table 3-4. As mentioned, the optimised composition was made based on 55 wt% of solid

loading. Using 50 wt% leads to cracked cells when sintered as there was not enough solid material in the slurry as shown in Figure 4-21.

The optimised composition in this work lie in between the wide ranges of composition reported by D Hotza et al.[31] which is shown in Figure 4-22. The anode functional layer and anode substrate composition fit perfectly with the graph in Figure 4-22 (shown by the green circle and red triangle) despite none of the references were using pore former. The anode functional (active) layer formulation used similar composition without the addition of pore former. The powder size in AFL was fine NiO (0.6.37±0.145) to increase the triple phase boundaries (TPB) area.
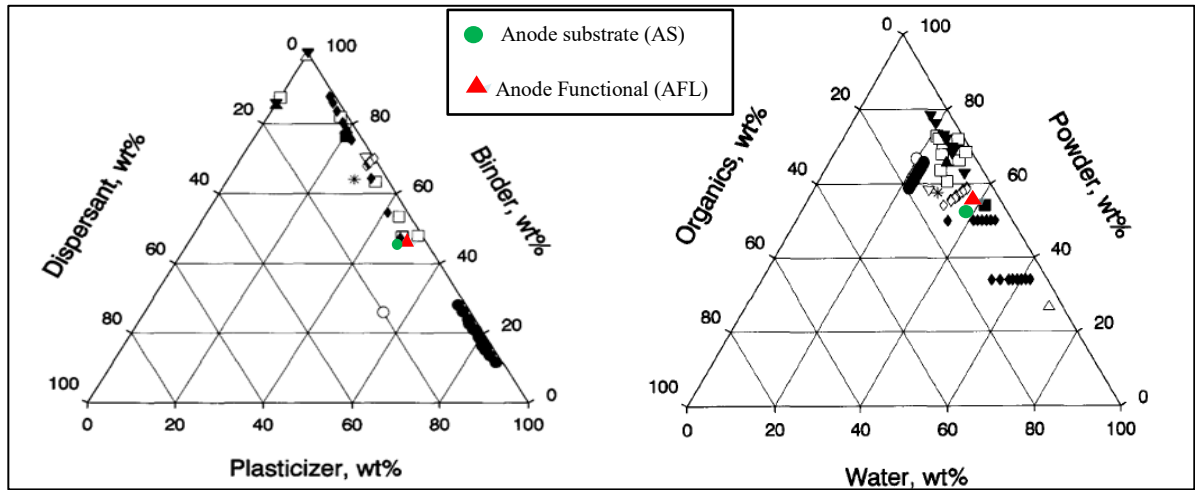
Figure 4-22: Comparing the obtained formulation to the literature, literature data from Hotza [31].

4.4   Half-cell manufacturing optimization

4.4.1   Multilayer tape casting

Reverse multilayer tape casting as described by Schafbauer et al [81] and Wang et al [113] was adapted for manufacturing half-cells as elaborated in Chapter 3. The electrolyte layer was tape cast first to get a thin and flat electrolyte layer, followed by a thin anode functional layer, and finally the thick anode substrate layer. The final compositions for the anode substrate, anode

functional layer and electrolyte for Ni/YSZ and Ni/ScCeSZ can be found in section 3.3.6.

Figure 4-23 shows the sample of successful multilayer green tape produced in this thesis.
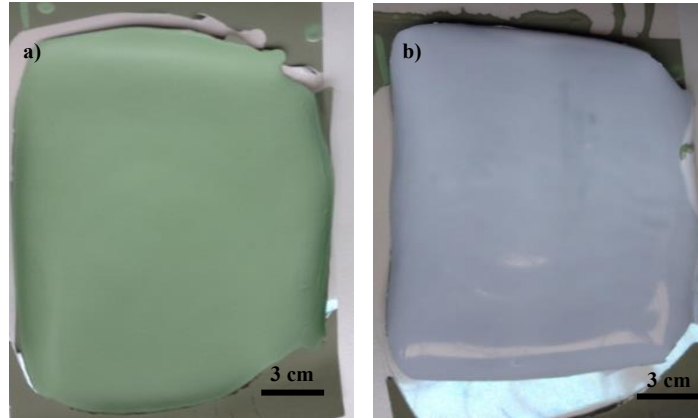
Figure 4-23: Multilayer green tape produced on a silicone coated PET film with a) anode layer side up, and b) electrolyte layer side up.

4.4.2   Co-sintering

For optimisation of the co-sintering temperature, only electrolyte layer and anode substrate layer were used in this sub-section. The co-sintering temperature influenced the microstructure of the anode and electrolyte, the mechanical strength, and the flatness of the SOFC cell produced. This section mainly focuses on the challenge to produce flat SOFC half-cells with dense electrolyte and porous anode. To do that, the behaviour of the sample during heating up was monitored using thermo-gravimetric (TGA) and dilatometer analysis. The samples used were from the actual dried tape of anode substrate (Ni/YSZ) and electrolyte (YSZ).

4.4.2.1   TGA Analysis

From the TGA analysis presented in Figure 4-24, there were four main contributions to mass losses in the sample. The first part, which was from room temperature to 100°C, presented the mass loss due to water evaporation. Evaporation was higher in the anode substrate as the tape was previously dried at low temperature, 33°C, while the electrolyte was dried at 70°C. The

drastic mass losses in the second part from 100°C to 500°C were due to rapid burn-off of the organics; while the third part showed insignificant mass losses as all the organics and water were eliminated.

The mass loss value in each section of Figure 4-24 are presented by Table 4-3 with total mass losses of 21.2% and 17.7% for anode substrate and electrolyte, respectively. The anode substrate contained slightly more organic amount since tapioca starch used as pore former. The mass of the samples remains constant after 500°C as the organics already burn-off at Part II. If the mass loss of the anode substrate in part I is eliminated, the two graphs will be closer together and coincide at some points. Based on this result, prior to co-sintering at high temperature, the cut green tape sample was dried at 100°C in the low temperature furnace with approximately 150g of dead-weight on top.
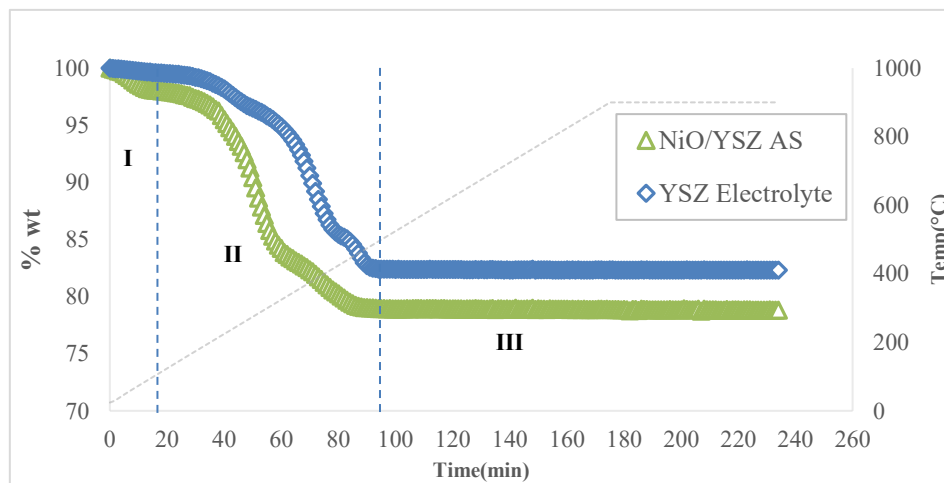
Figure 4-24: TGA analysis for anode substrate (Ni/YSZ) and electrolyte (YSZ) and using tape cast sample.

Table 4-3: Mass loss according to the TGA for anode and electrolyte tape

	Mass loss (% wt)		
	Part I **(20-100°C)**	**Part II** **(100-500°C)**	**Part III** **(500-900°C)**
NiO/YSZ	1.94	19.10	0.13
YSZ electrolyte	0.39	17.19	0.10

4.4.2.2 Dilatometer analysis

Figure 4-25 shows the plot of sample length changes with respect to temperature. The first section (Part I) in the TGA analysis shows higher mass loss in the anode while in the dilatometer, the length changes were the opposite of the mass changes. The second section (Part II) shows the length changes occurred only at the beginning of the second section and remain relatively constant for the anode tape. In the electrolyte tape, the small decrease in length observed from 350°C to 500°C indicates different burn-off stages in the electrolyte and anode. The third section (Part III) shows a linear increase of length for both samples, while the materials expand without any influence of water and organics. If the sample has been sintered previously, the gradient can be used to calculate the thermal expansion coefficient (TEC or CTE) of the material. In literature, the TEC values reported to be 11×10^{-6}/K for 8YSZ, 17×10^{-6}/K for Ni and 15.1×10^{-6}/K [114] for Ni/YSZ with 50wt% Ni. Note that the TEC value reported here is for reduced Ni opposed to the sample used in this dilatometer analysis which the sample was in NiO unreduced state.

The sample was not previously sintered in this work as the objective was to monitor how the tape changes in length during sintering. Hence, we will express the gradient in term of the length changes with respect to temperature only. The anode substrate's gradient was 1.11×10^{-5}/°C while the gradient for the electrolyte was slightly higher; 2.49×10^{-5}/°C, reflecting greater rate of length changes in the electrolyte layer. Table 4-4 shows the summary of the sample length changes from the dilatometer analysis. In previous work on multi-layer sintering, similar dilatometer profile was found between electrolyte and anode substrate with more significant differences towards Part IV [106].

The fourth section (Part IV) indicates the point where the materials starts to sinter; in which, in the anode mixture, the sintering starts at 1000°C while in the electrolyte the sintering

temperature was slightly higher, at 1069°C. Rapid sintering starts at 1050°C for the anode substrate and at 1100°C for the electrolyte. The rate of sintering of the electrolyte were higher than the anode and closes the gap between the anode and electrolyte total shrinkage. At the end of the measurement, the differences in length of the samples was found to be only 2.8%; with shrinkage of 18.9% and 16.1% for the anode substrate and the electrolyte, respectively. The overall dilatometer observation trend observed here agrees with the work reported by Jin et al. [130] in the fabrication of multilayer tape casting with different anode gradients.
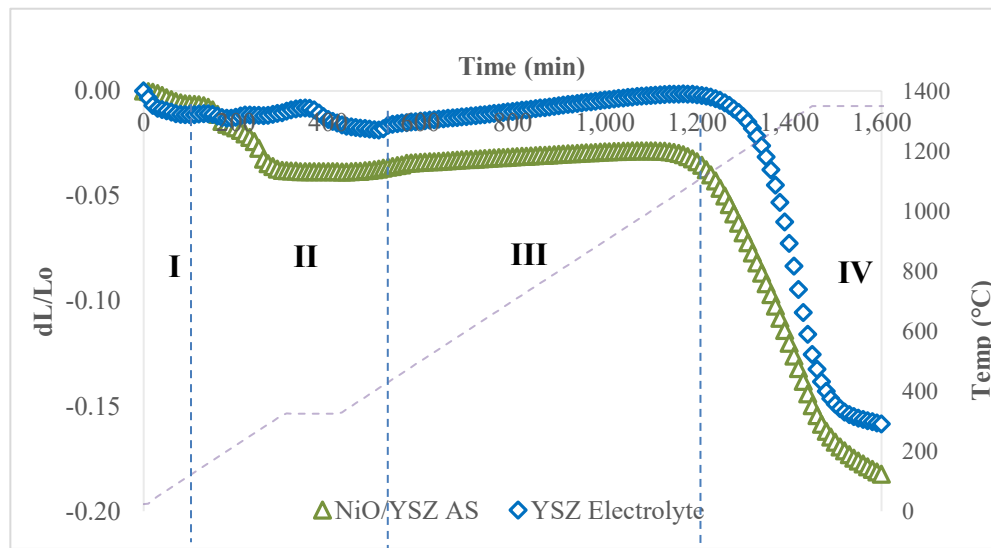
Figure 4-25: Sample length changes differences between anode substrate (NiO/YSZ) and electrolyte (YSZ) using green tape sample.

Table 4-4: Sample length changes dL/L$_0$ (%) for anode and electrolyte

	dL/L$_0$ (%)			
	Part I	Part II	Part III	Part IV
Ni/YSZ	-0.6	-2.8	+0.6	-16.1
YSZ	-1.1	-0.7	+1.6	-15.9

**length reduction in negative sign, length increment in positive sign

However as the anode thickness was far greater than the electrolyte, the effect of 2.8% shrinkage difference was emphasised. The dilatometer analysis analyse the changes of

individual sample length, whilst in the real half-cell (consist of anode and electrolyte), the shrinkage and expansion as well as the thickness of each individual layer will have an impact on the subsequent layer. Hence, there was deviation from the observation from the dilatometer analysis.
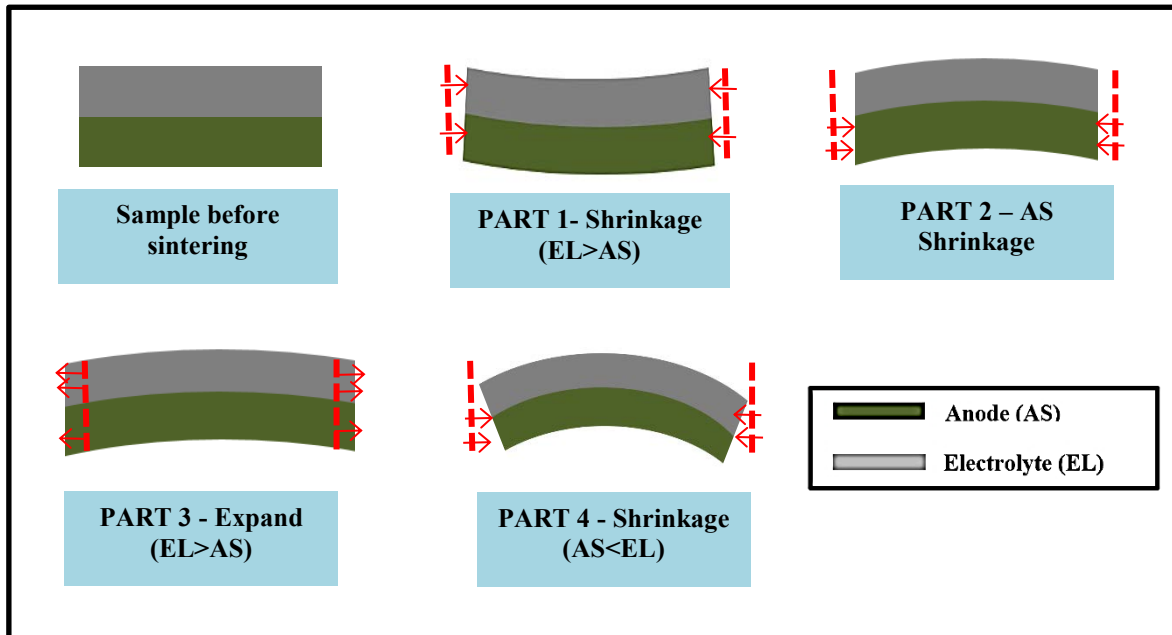
Figure 4-26: Shrinkage and expansion behaviour of the SOFC tape cast sample in anode/electrolyte co-sintering.

Figure 4-26 attempted to link the actual co-sintering behaviour of the half-cells with the observed result in dilatometer measurement. In Part-I, the shrinkage of the electrolyte was slightly higher than the anode. At this stage, the cell should bend towards the electrolyte as there was a greater force at the electrolyte-side. In Part-II, both of the layers shrink, but the anode substrate shrinks first as the anode's organics burn-off at a lower temperature. The higher degree of anode shrinkage in this part overturn the direction of the curvature towards the anode, which also emphasises by the thickness. In Part-III, both of the layers expands with slightly higher expansion by the electrolyte layer. In Part-IV, the degree of shrinkage of the electrolyte was higher, but due to the thickness and previous shrinkages, the effect of this may not be

observed. If the degree of cell curvature in Part-II was small, perhaps it can be neutralised by the higher expansion rate of the electrolyte in Part-III.

Rapid expansion and shrinkage showed by Part-III and Part-IV may lead to cracked cells, which can be controlled using a slow heating rate. The lowest heating ramp rate setting in the furnace was 1°C/minute, which was the same heating rate used in the dilatometer analysis. As this could not be reduced further, several dwelling stages were used to minimise the stresses between the two layers during co-sintering from room temperature to 1350°C.

4.4.2.3 Improving cell flatness by pre-calcination

Cell curvature is a typical problem during SOFC cell fabrication as the full cell has three layers with different materials, thicknesses, and porosity levels. The cell needs to be as flat as possible to increase the contact angle of the cell with the current collectors and fit the geometry of the cell holder. Despite of the co-sintering setting to reduce the mismatch of shrinkage and expansion behaviour, it still produced curved SOFC cells. The SOFC cell curved towards the anode (concave) for Ni/YSZ cells, whilst for Ni/ScCeSZ the cells were curved and cracked as shown in Figure 4-27. The co-sintering was done with a 10 g weight placed on top of the tape sample to improve the cell flatness following a common practice of ceramic tape manufacturing.

In the previous dilatometer analysis, the sample dimension used was similar for both anode and electrolyte sample. The sample thickness for both NiO/YSZ and YSZ tape used in the dilatometer analysis needed to be at least 2 mm, which did not represent the real thickness dimension in the SOFC cell. In a real SOFC, the thickness of the anode was approximately 600 to 700 μm while the electrolyte layer were only 10 to15 μm. Hence, by the curved cell produced,

it showed that the influence of the anode shrinkage was emphasized by the thickness of the anode.
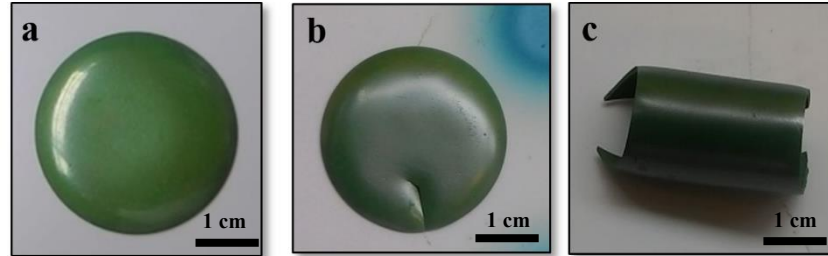
Figure 4-27: SOFC half-cell; before and after sintering at 1350°C a) NiO/YSZ, b) NiO/ScSZ, c) NiO/ScSZ without dead-weight.

This problem may have been emphasised more in this work as the half-cell was co-sintered together without pre-sintering the anode layer. Based on McDonald's work [112] with pre-sintered anode, the SOFC curved the opposite way. Referring to previous works on curved samples, the cell flatness can be improved in several ways; which are 1) increase the electrolyte layer thickness, 2) reduce the anode substrate thickness, 3) alter the material's property, and 4) use a lower sintering temperature.

Considering all the options, option 1 and 2 seemed to be the easiest but a thicker electrolyte increases the ohmic resistance, while reducing the anode thickness will reduce the mechanical strength of the cell.

One method practiced by Hong et al. [115] was by pre-calcination carried out on the cermet powder to alter the sintering property of the materials. NiO coarsened with temperature, hence the heat treatment was not carried out on NiO powder as the NiO starting powder size was already large; 9.10 μm (d_{50}). Table 4-5 presents the effect of pre-calcination temperature on the particle size of the ceramics (8YSZ and 10Sc1CeSZ). Interestingly, the ceramics particles reduce slightly in size when pre-calcined at high temperature. The distribution of the particles

of the ceramic powders are presented in Figure 4-28. After pre-calcination (heat treatment), the distribution of the powders have sharper peak compared to the as received powders.

Table 4-5: Ceramic particle sizes after heat treatment at different temperature

	Pre-calcined Temp (°C)	Size (d_{50}) (µm)
8YSZ	As-received	0.855 ± 0.103
	700	0.701 ± 0.003
	800	0.612 ± 0.001
	850	0.606 ± 0.001
10Sc1CeSZ	As-received	0.514 ± 0.053
	850	0.418 ± 0.001
	900	0.372 ± 0.001
	950	0.347 ± 0.005
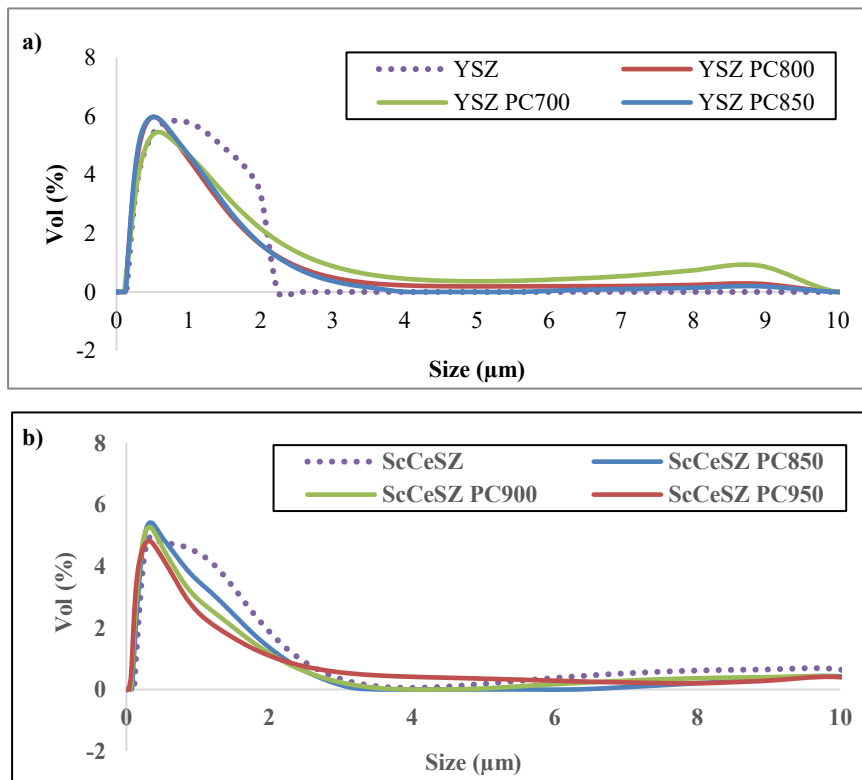
Figure 4-28: Particle size distribution of a) YSZ powders b) ScCeSZ powders with different heat treatment temperature.

Ni/YSZ

The 8YSZ powder pre-calcined at 800°C produced flat cells, with a porous anode and dense electrolyte. Figure 4-29a shows Ni/YSZ cell with YSZ powder pre-calcined at 700°C. Despite having a weight placed on top, the cell still curved towards the anode. Figure 4-29c shows that with a pre-calcined temperature of 850°C, the cell curved towards the opposite direction, which was towards the electrolyte. The shades of green of the anode substrate relates to the porosity of the cells, with darker green indicating a dense cell and vice versa. The insight of the impact of pre-calcination on the SOFC layers is presented by the SEM microstructure in Figure 4-30. As the flatness improves with the increase of pre-calcination temperature, the anode becomes more porous and the electrolyte becomes less dense. From the increased porosity of the anode and thicker electrolyte layer indicated by the SEM images, it can be concluded that less shrinkage is experienced with higher pre-calcined powders. From the electrolyte microstructure of the SOFC cells in Figure 4-30, the cell curved towards the anode direction is still suitable for electrochemical testing but with the cell produced curved towards the electrolyte, the electrolyte was not dense. The repeated experiment with higher co-sintering temperature (1400°C) carried out showed a denser electrolyte, however it compromised with the cell flatness.
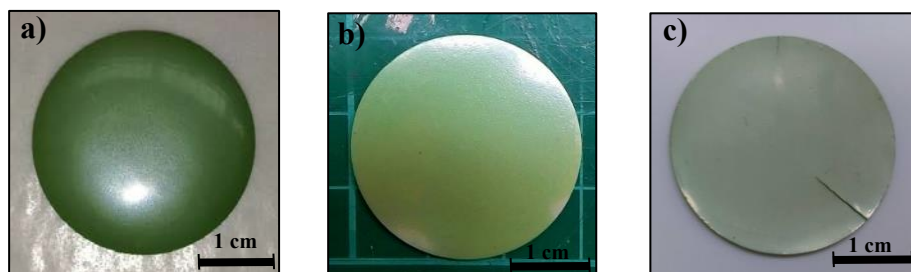
Figure 4-29: NiO/YSZ half-cells co-sintered at 1350°C with different YSZ pre-calcination temperature a) 700°C, b) 800°C, and c) 850°C.
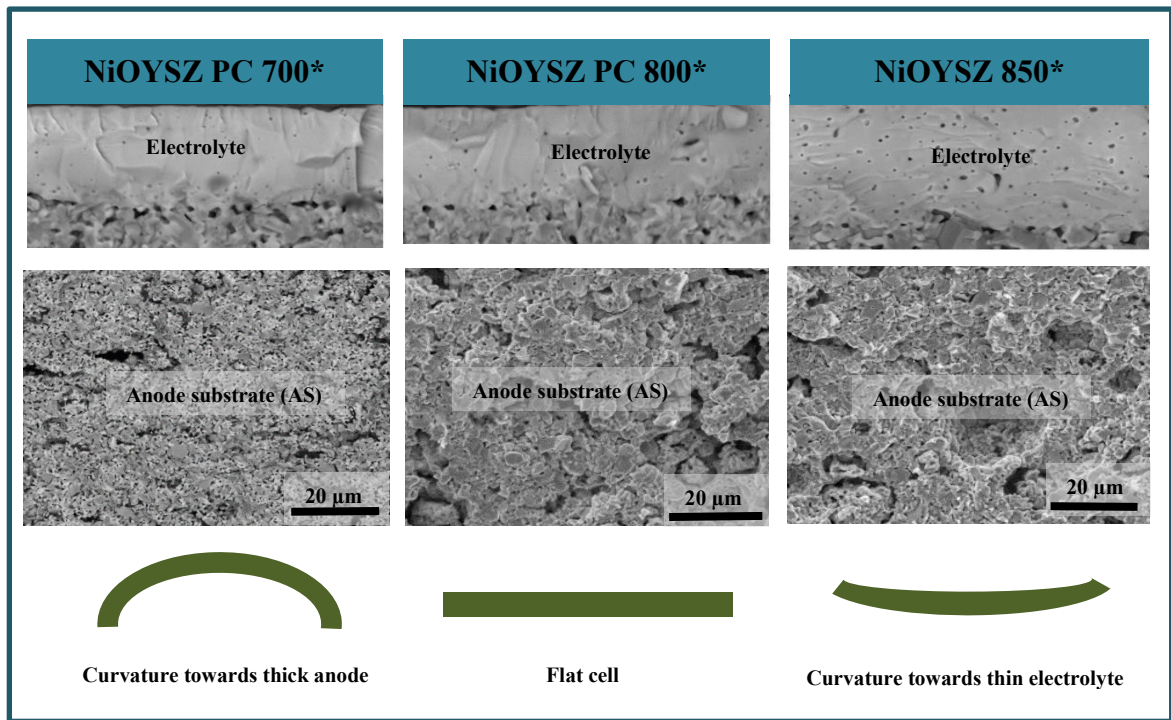
*PC = pre-calcined temperature

Figure 4-30: Microstructure analysis and different direction of curvature in the NiO/YSZ half-cells with different powder pre-calcination temperatures.

Ni/ScCeSZ

As the half-cells for Ni/ScCeSZ were badly curved caused by over-sintering of the anode as shown previously with a co-sintering temperature of 1350°C, dilatometer analysis on the ceramic powder was performed using pellet pressed samples. The results shown in Figure 4-31 show that ScCeSz powder sintered 100°C earlier than the YSZ electrolyte, but the net shrinkages were almost similar; 19.26% and 20.61% for 8YSZ and 10ScCeSZ, respectively. Dilatometer analysis was also carried out with all the pre-calcined powder and as-received powders for each layer, however as the results were inconclusive, the dilatometer analysis results are not included in this report.

Using powders pre-calcined at different temperatures with several co-sintering temperatures, the optimum match was found using powder pre-calcined at 900°C and co-sintering at 1300°C. With 10ScCeSZ powder pre-calcined at 900°C, when co-sintered at 1250°C, a flat cell with porous electrolyte structure was obtained which implies inadequate sintering, while with a sintering temperature of 1350°C a curved cell with dense electrolyte was obtained. At 1300°C, a reasonably flat cell was obtained with the desired microstructure. The observations on the microstructure and cell flatness are summarised in Figure 4-32.
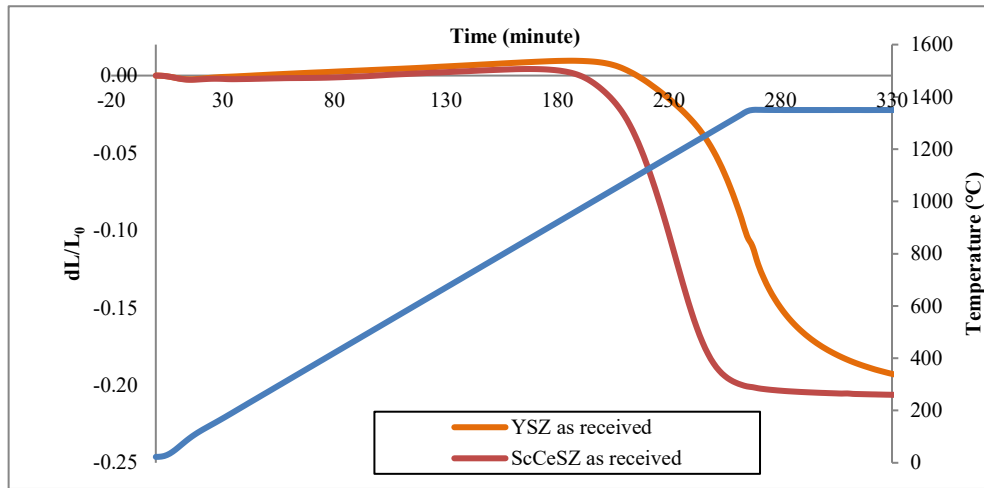
Figure 4-31: Dilatometer analysis of as received electrolyte powders of 8YSZ and 10ScCeSZ (powder pressed sample).

Figure 4-33 shows some of the observations on the optimisation attempt by using different pre-calcined ceramic powders in the anode substrate to produce flat NiO/ScCeSZ cells that fulfil basic SOFC requirements.

All the results suggests that pre-calcination of the ceramic powder for the anode substrate alter the response of the material to sintering. Beyond the optimum limit, a fragile cell with highly porous anode and less dense electrolyte will be produced. Higher sintering temperature will give the desired dense electrolyte, however it will also over-sinter the anode, making the anode dense as well which leads to a curved cell.
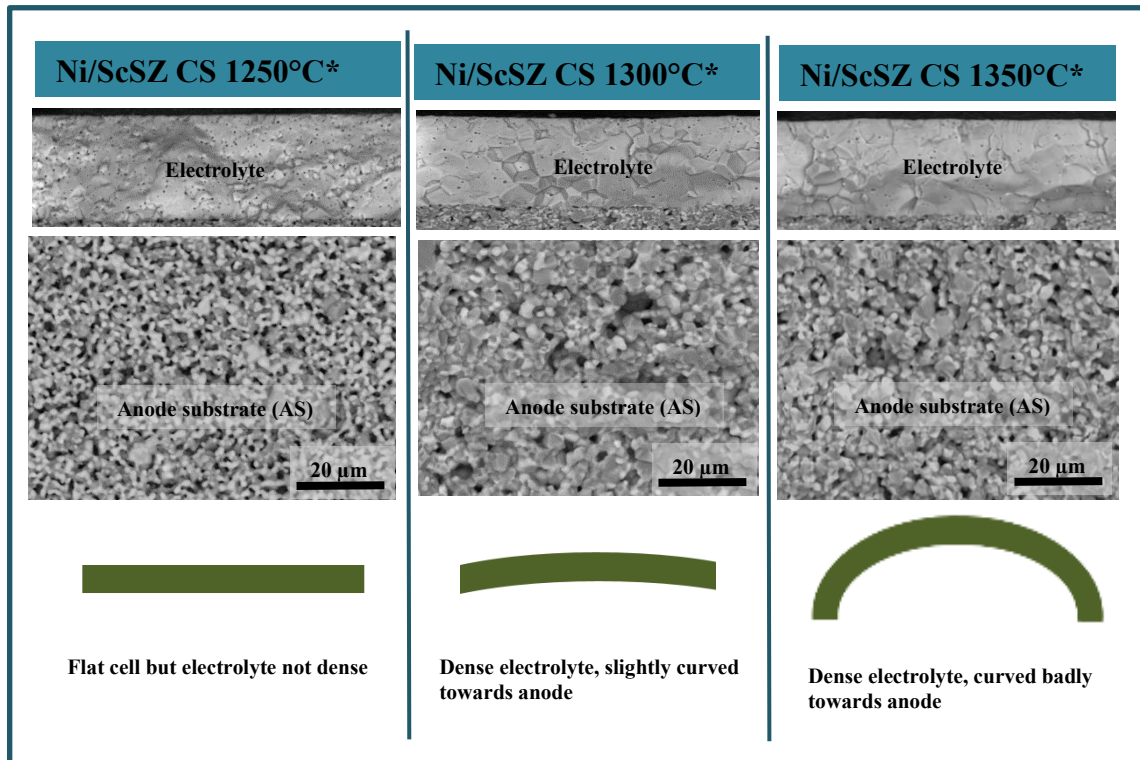
*CS = co-sintering temperature

Figure 4-32: Effect of sintering temperature on the microstructure of a NiO/ScCeSZ cell with ScCeSZ powder pre-calcined at 900°C.
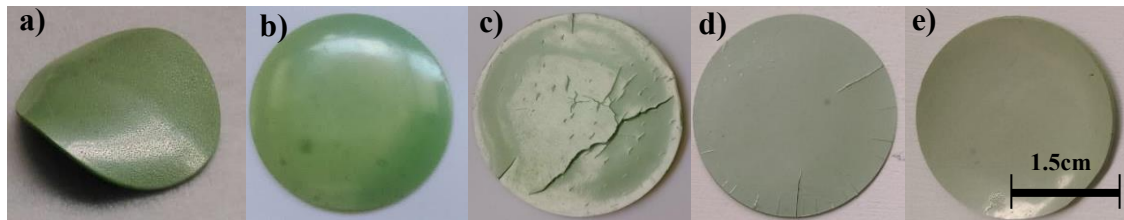
Figure 4-33: NiO/ScCeSZ half-cells with different pre-calcination temperatures at; a) 850°C, b) 900°C, c) 950°C, d) 950°C with dead-weight, and e) 1000°C.

4.5   Final SOFC cells

Figure 4-34 shows the full-cells with silver wires attached, while Figure 4-35 shows the cross-section of the bi-layer anode supported cells obtained in this thesis with no delamination between any of the interfaces of the layers. The electrolyte thickness on the Ni/YSZ and Ni/ScCeSZ cells produced were 10 to 12μm and 16 to 18μm respectively. Using 10 to 12μm of electrolyte for Ni/ScCeSZ cells, the open-circuit voltages obtained were around 0.86 V, which indicates there was fuel cross-over. Hence, thicker electrolytes were used.
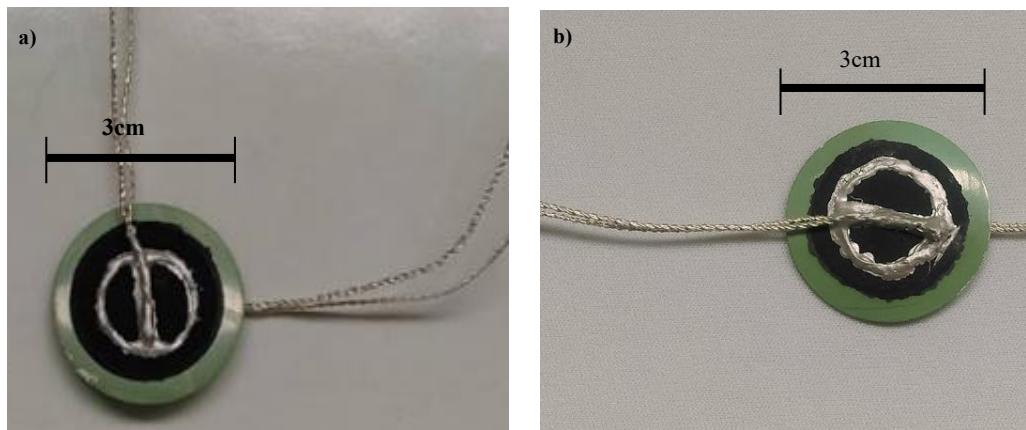
Figure 4-34: SOFC full cell with different ceramic material a) Ni/YSZ, and b) Ni/ScCeSZ.
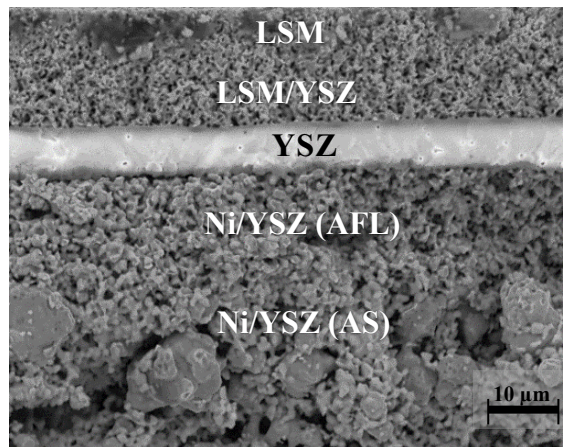
Figure 4-35: Cross-section image of Ni/YSZanode supported cell with bi-layer anode.

4.5.1 Electrolyte grain-boundary/fracture structure

Figure 4-36 shows the comparison of electrolyte cross-section images from Ni/YSZ and Ni/ScCeSZ cells. The major differences that can be seen from both cell types was the electrolyte microstructure. In most SEM images obtained from Ni/ScCeSZ samples, the grain boundaries of the electrolyte can be clearly seen from the cross-sectional image unlike Ni/YSZ samples, no matter whether the electrolyte was dense or less dense. Araki et al [116] and Orlovskoya et al [117] shows the same structure when investigating the fracture surfaces of ScSZ pellets. According to Orlovskoya et al. [117], the fracture structure as on Figure 4-36d was only observed for samples sintered at higher temperature, where the amount of vacancies increased greatly, which produced more repulsive forces between cations, which in turn puts the grain under compressive stresses. This force a crack to move along the grain boundaries as it is easier propagate compared to across the grain. The expansion and shrinkage during co-sintering influenced the appearance of the fracture structure as well, as the ScCeSZ pellet in Figure 3-1 (Section 3.1.1) shows less obvious grain boundaries.
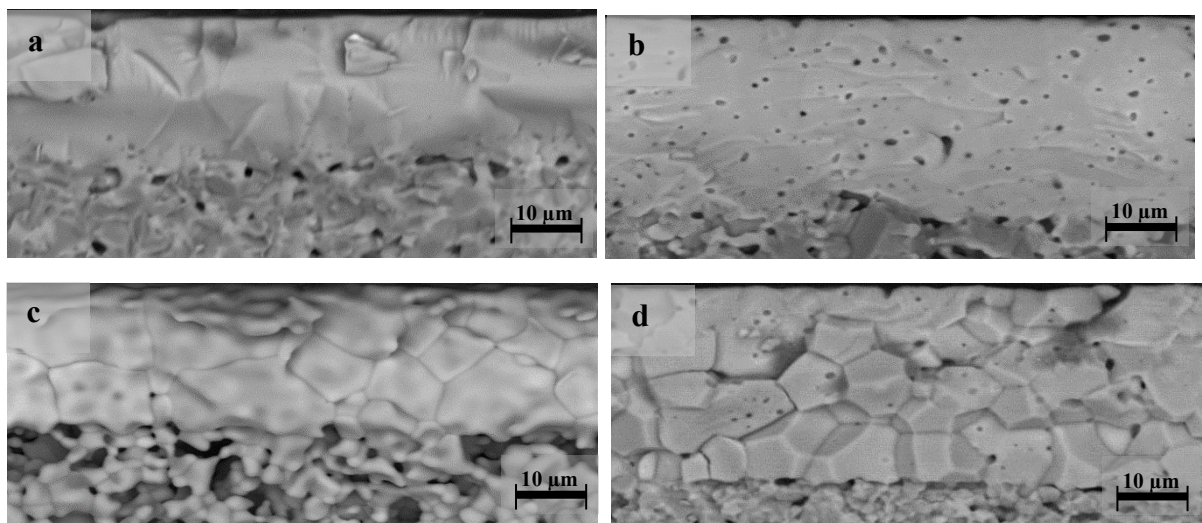
Figure 4-36: Microstructure of electrolyte for a) dense Ni/OYSZ cell, b) less dense electrolyte NiO/YSZ cell, c) dense NiO/ScCeSZ cell, and d) less dense NiO/ScCeSZ (all samples were not reduced).

The smooth and flat surface of the fracture of ScCeSZ in Figure 4.36c-d indicates the electrolyte was cubic phase opposed to rhombohedral and tetragonal phase which has rough structure on the fracture surface as referred to description by Orlovskaya et al. [117]. This fracture structure may be the reason why the electrolyte layer of ScSZ needed to be thicker. With thin layer 10ScCeSz electrolyte, it was found that the electrolyte layer cracked and exposed the anode layer underneath, which was not observed in the Ni/YSZ cells. The observation was found on Ni/ScCeSZ cell pre-calcined at 950°C with co-sintering temperature of 1300°C which has been shown previously in Figure 4-33c. Figure 4-37 shows this observation on the electrolyte surface of NiO/ScCeSZ half cells.
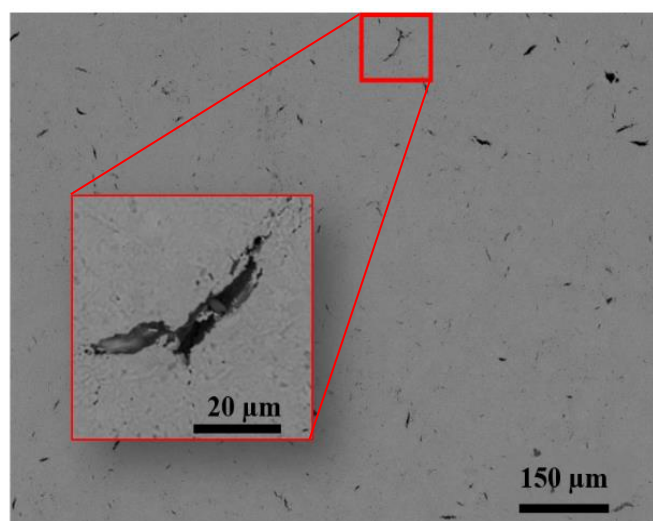
Figure 4-37: Cracks on thin electrolyte layer (10-12 μm) of NiO/ScCeSZ half-cell after co-sintering.

4.5.2   Anode Porosity

Another difference observed was the porosity of the anode substrate where the porosity of the Ni/ScCeSZ were higher than with the Ni/YSZ cell as reflected by Figure 4-38. With the Ni/ScCeSZ cells, the porosity was 39.8% while the Ni/YSZ cell's porosity was 35.7% based on the Archimedes method. This might be due to the lower co-sintering temperature used

(1300°C vs 1350°C) to improve cell flatness. Inevitably, this will also influence the electrochemical performance.
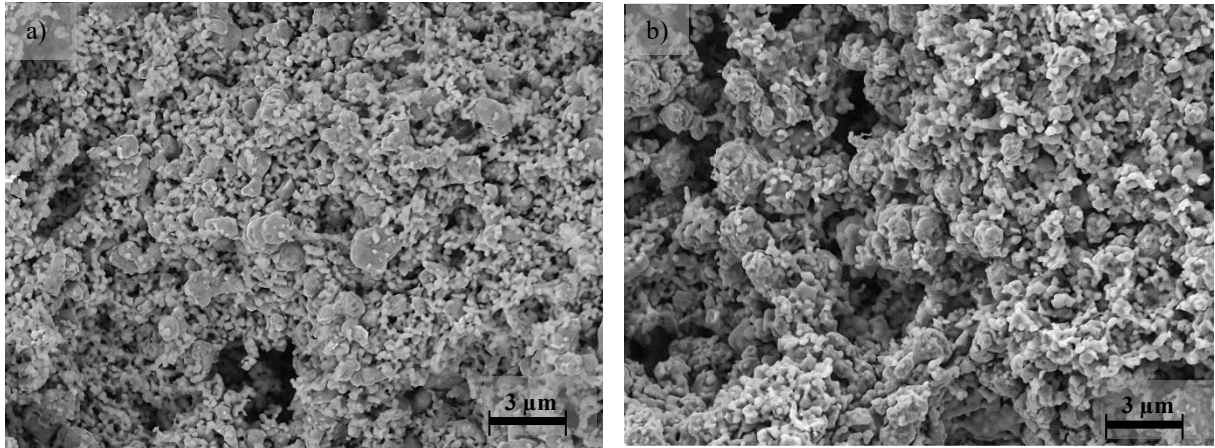
Figure 4-38 : Anode substrate microstructure a) Ni/YSZ, and b) Ni/ScCeSZ.

4.6 Additional discussion

4.6.1 Tape casting

In this work, multilayer tape casting was successfully demonstrated to produce SOFC cells that meets the high quality cells' criteria. Besides the advantage of this method (reducing the manufacturing steps and more homogenous thickness layer achieved), the multilayer tape casting method used due to unsuccessful previous attempts in our research group in obtaining dense electrolyte layer for Ni/ScCeSZ with screen printing method regardless much higher sintering temperature (1500°C) used. By this method, dense electrolyte with minimum OCV value of 1.0 V and high electrochemical performance achieved, with comparison to commercial Ni/YSZ cells (refer to Table 5.4 in Section 5.3.2).

Tape casting itself appears to be simple. However, to achieve formulation that works, a lot of parameters need to be considered [3]. The interactions with the organics and powder properties need to be considered. The tape casting machine and drying setting needed to be

optimised to minimise stresses in the tape. In early attempts with anode thick tape casting, the author encountered problems which was not experienced in tape casting thick electrolyte layer. In the thick anode, more efforts needed to adjust to two different materials' rheological properties which affected by surface area, density, particle size and particle distribution [3]. The biggest challenge was on drying the thick anode tapes which was later found to be solved by controlling the drying rate (low drying rate preferred) with sufficient binders and plasticisers.

In addition to co-casting, TLC (tape-casting, laminating and co-sintering) method [82, 105, 106] covered in Section 2.3.4 was attempted as an alternative solution to tape thick drying problem. Laminating several thin layers of anode and electrolyte at 3500 N/cm^2 and 75°C for 10 min was not successful as the layers detached in green state. These layers were further delaminated after co-sintering. To author's knowledge, this method has not been reported to be successful using aqueous based tape casting in any work. As binder (PVA) is the organic that affects the attachment of the layers, future attempts with TLC method should be made with other water based binder.

4.6.2   Manufacturing differences on Ni/YSZ and Ni/ScCeSZ cells

The main goal in manufacturing is to produce flat SOFC cells that meet all the requirement for a high-quality performance. In producing a flat cell, powder pre-calcination and co-sintering altered accordingly to balance with the desired microstructure; thick porous anode and thin dense electrolyte. All the optimisation was perfected on Ni/YSZ cells and adjusted to Ni/ScCeSZ manufacturing requirement. Ideally for performance comparison purpose, all parameters must be the same. Despite the effort, this chapter shows that it was impossible to do so as different materials had different requirements. This surely will have some impact on

the electrochemical performance. In this work, the differences in manufacturing parameters and the possible effects on the cell performances were:

1) Starting powder size

    a. Pre-calcination temperature of electrolyte powder in anode substrate: 800°C vs 900°C for YSZ and ScCeSZ, respectively. After annealing at high temperature, the ScCeSZ particle size reduced to almost half the original size, from 0.514 to 0.372 µm while YSZ size reduced from 0.855 to 0.612 µm. For anode, larger YSZ/ScCeSZ size was desired as it increases anode effective electrical conductivity.

2) Tape casting stage

    a. The plasticiser ratio, in which Ni/ScCeSZ cells use 1:1 ratio of PEG:Glycerol. This small change had no effects on the performance as all the organics burnt off during sintering.

    b. The thickness of electrolyte tape cast. As thicker electrolyte layer will give more ohmic resistance, it will less performance with the same thickness.

    c. Co-sintering temperature: 1350°C vs 1300°C for NiYSZ and Ni/ScCeSZ, respectively. Higher co-sintering benefits the densification of the electrolyte while with lower co-sintering temperature, anode porosity in Ni/ScCeSZ cells were higher.

Besides the manufacturing differences, different electrolyte microstructure observed within the two cells. Ni/ScCeSZ had obvious grain boundary and fracture structure in the electrolyte layer than that of Ni/YSZ. Because of this, thicker electrolyte layer was fabricated for Ni/ScCeSZ cell.

CHAPTER 5: CONDUCTIVITY AND ELECTROCHEMICAL PERFORMANCE OF NI/10SCCESZ VS NI/8YSZ SOFC IN HYDROGEN

5.1 Overview

Scandia stabilised zirconia (ScSZ) has been tested as an SOFC electrolyte material for more than 20 years. Nevertheless, only electrolyte supported Ni/ScSZ cells (ESC) are available commercially. The application of Ni/ScSZ as the material for anode supported cells (ASC) is presumed to give better performance, with a significantly thinner electrolyte layer. Electrochemical performance comparisons between anode supported cells (ASC) using Ni/YSZ and Ni/ScSZ manufactured from approximately the same specification for intermediate temperature (IT) SOFC has been very rare despite ScCeSZ's known superior conductivity. Previously, Sumi et al [15] and Ukai et al [59] had elaborated the comparison of performances for electrolyte supported cell at high temperature (1000°C). This chapter reports the electrochemical performance evaluation of Ni/10ScCeSZ and Ni/8YSZ ASC in SOFCs operating with hydrogen at intermediate temperatures using in-house cells produced by multilayer aqueous tape casting. Continuous electrochemical tests was carried out at different temperature and flowrates for 24 hours total duration in hydrogen. Prior to the electrochemical performance, conductivity tests were carried out separately on the electrolyte sample to compare the conductivity of the two different materials. In this chapter, the performance comparison will be mainly focused on the maximum power densities and EIS.

5.2 Conductivity of 10ScCeSZ vs 8YSZ

The superior electrical conductivity of ScSZ has been widely reported in literature [4, 9]. A conductivity test was carried out prior to electrochemical testing to re-confim that this trend was achievable using the commercial powder purchased. Table 5-1 displays the resistivity and conductivity of the sintered sample of the ceramic powders used in the Arrhenius plot in Figure

5-1. The conductivity values given at 750°C for 8YSZ and 10ScCeSz were 8.5x10^{-3} S/cm and 1.6x10^{-2} S/cm respectively. Compared to the literature, the 10ScCeSZ conductivity values obtained were slightly lower than the literature while the YSZ values were quite similar with values across the literature [9, 26]. Higher 10ScCeSZ conductivities have been reported based on enhanced powder synthesis method and nano-powders as the ionic conductivity highly dependent on the powder synthesis method as well as the size of the particles [26].

Table 5-1: Conductivity and resistivity of 10Sc1CeSZ and 8YSZ.

T (°C)	Resistivity (ohm.cm)		Conductivity (S/cm)	
	10ScCeSZ	8YSZ	10ScCeSZ	8YSZ
550	584.104	1647.614	0.0017	0.0006
600	364.436	642.700	0.0027	0.0016
650	158.362	265.366	0.0063	0.0038
700	89.171	202.084	0.0112	0.0049
750	62.708	117.125	0.0159	0.0085
800	44.635	66.691	0.0224	0.0150
850	33.977	45.714	0.0294	0.0219

The activation energy, E$_a$ can be obtained from a plot of the natural logarithm form of the Arrhenius equation;

$$\ln k = -\frac{E_a}{RT} + \ln A \qquad \text{[Eq. 5.1]}$$

Where, k is the reaction rate constant, R is the gas constant, and A is the pre-exponential factor which relates to the amount of times molecules will collide in the orientation necessary for a reaction to happen.

The activation energy reported in the literature for YSZ was in the range of 91 to 95 kJ/mol [26, 102], which is close to what we obtained in our result, 90kJ/mol as in Table 5-2. For 10ScCeSZ, the closest temperature range reported was from 597 to 727°C by Kazlauskas et al.

[118], where the temperature used in this thesis were slightly higher (550-850°C). The activation energy for 10ScCeSZ produced by Kazlauskas et al. [118] was 84 kJ/mol, while in this work E_a was slightly lower; 76 kJ/mol. The activation energy obtained were similar to the 7.8ScSZ powder obtained by Badwal et. al [10] at higher temperature range (78 kJ/mol for 850-1000°C). On the other hand, the measured conductivity of 10ScCeSZ at each point (as in Table 5-1) was still lower than the values from the literature.
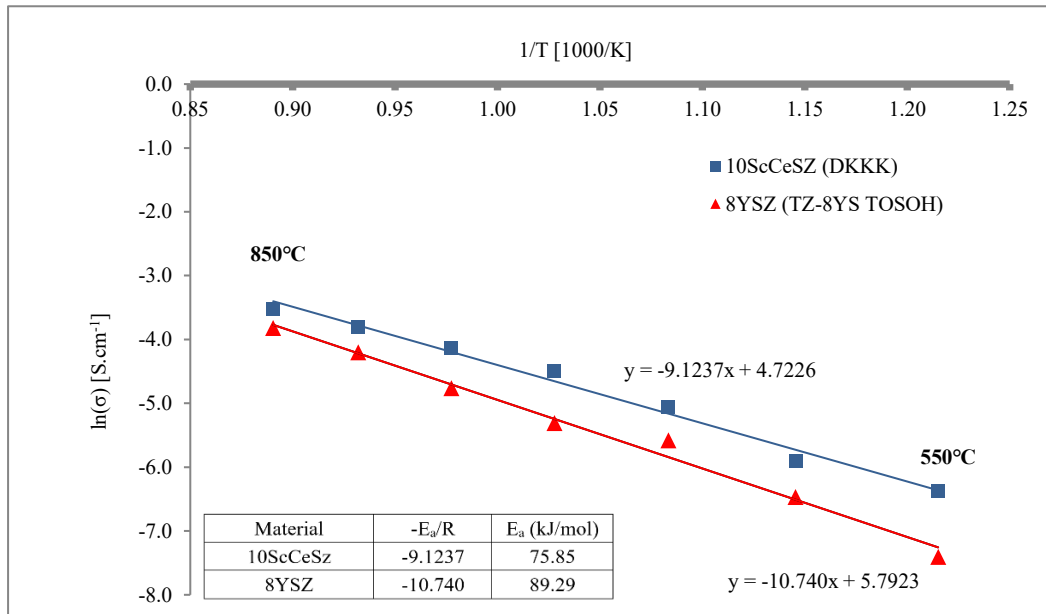
Figure 5-1: Conductivity of 8YSZ (TZ-8YS TOSOH) and 10ScCeSZ (DKKK).

Table 5-2: Comparison of activation energy (Ea) for 8YSZ and 10ScCeSZ

Material	E_a (kJ/mol)	Temperature range (°C)	source
8YSZ	89	550-850	*This study*
8YSZ	91	850-1000	[26]
8YSZ	95	500-700	[9]
8YSZ	94	300-690	[112]
10ScCeSZ	76	550-850	*This study*
10ScCeSZ	84	597-727	[118]
10ScCeSZ	156	350-500	[119]
10ScSZ	87	850-1000	[23]
10ScCeSZ	69	300-690	[112]
7.8ScSZ	135	400-500	[10]
7.8ScSZ	78	850-1000	[10]

A wide range of electrical conductivity values reported from literature is logical due to the setup of the conductivity test carried out, either by four-probe method or by two-probe method as compiled by Kazlauskas et al [118] in their work. Using nano-sized 10ScCeSZ powder, lowest activation energy was reported by McDonald et al [112] with only 69 kJ/mol, yet a lower conductivity value at 700°C with a value of 0.0013 Scm^{-1} reported; which was unexpected.

5.3 Electrochemical Performance

Three setups were used in the electrochemical tests; Setup A with a low flowrate at 750°C, which had the highest fuel utilisation value, Setup B with higher flowrate which gave higher OCV value and a slight increase of performance; and Setup C with the same high flowrate at higher temperature, 800°C which gave the best result. Performance comparison with the three setup will be elaborated in Section 5.3.2 and 5.3.3 only to simplify the discussion and avoid redundancy.

Table 5-3: Electrochemical Test Setting/Parameter

Setup	Temp(°C)	Gas Flowrate (ml/minute)
A	750	28 (H_2: He, 3:1)
B	750	60 H_2
C	800	60 H_2

5.3.1 Open Circuit Voltage (OCV or EMF)

The cell measured for OCV with Setup A for 6 hours as the first sequence of the cell testing with hydrogen to allow complete reduction of NiO to Ni in the anode. The non-linear part of the OCV graph in Figure 5-2 indicates the reduction of the SOFC cells; in which the cell microstructure may shift and re-arrange until the structure stabilised and produced a constant

OCV. With reduction of the NiO to Ni, the anodes (AS and AFL) becomes more porous and channel the fuel to reach the electrode/electrolyte interface.

The OCV in both cells were stabilised at 0.99 V and 1.05 V after 1-hour of hydrogen introduction into the test chamber for the Ni/YSZ and Ni/ScCeSZ cells, respectively. At 750°C, the OCV calculated from Eq. 1.5 with a Gibbs free energy value of -191.35 kJ/mol [11] is 0.99 V. Other literature has reported higher OCV values for hydrogen operation, maybe due to different Gibbs free energy value used. Even though the OCV value of Ni/YSZ was slightly lower, the value perfectly fit the calculated value. The OCV value of Ni/ScCeSZ was slightly higher compared to the Ni/YSZ as the Ni/ScCeSZ has a thicker electrolyte layer due to manufacturing process limitation. Thicker electrolyte gave a better seal towards any defects in the electrolyte dense structure.
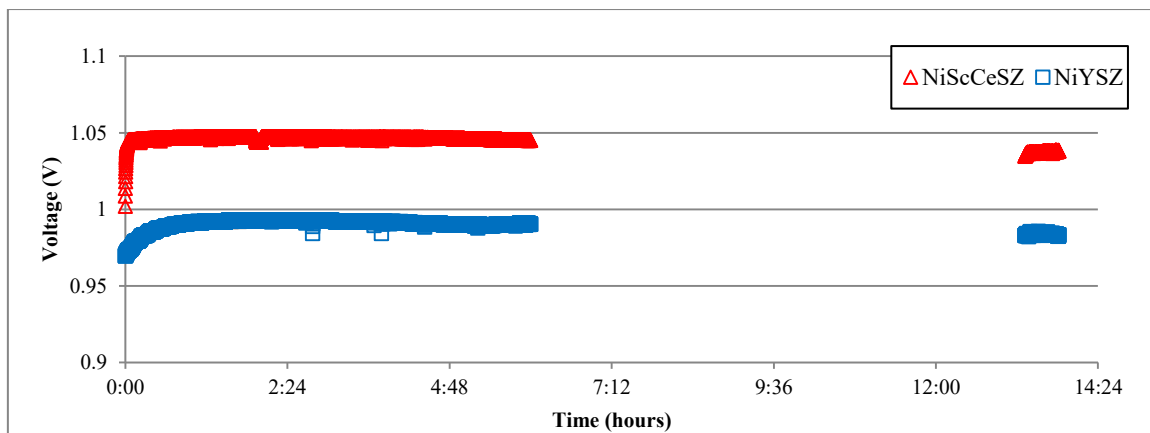
Figure 5-2: OCV reading of Ni/ScCeSZ and Ni/YSZ at 750°C with 21ml/minute hydrogen (Setup A)

From Figure 5-2, the OCV value obtained at approximately 13-hours slightly decreased to 0.98V and 1.04V for Ni/YSZ and Ni/ScCeSZ respectively. As both of the cells show the same OCV degradation pattern, the decrease may have originated from degradation of the dense silver paste that was used as the sealing material.

5.3.2 *i*-V curve and Maximum Power Density, PD$_{max}$

To obtain the *i*-V curve, a potentio-dynamic mode was selected with the current density measured continuously at different voltages from OCV down to 0.4V and vice versa. Figures 5-3 and 5-4 show *i*-V curves measured at 750°C for both Ni/YSZ and Ni/ScCeSZ cells after 6-hours and 20-hours of operation. In Ni/YSZ there was an insignificant drop in the current density between these two measurement. The maximum current density value at 6-hours was 0.95A/cm^2, which reduced to 0.92A/cm^2 at 20-hours.

With increasing cell testing time, Troskialina [64] found a performance improvement in the commercial cells used due to increasing contact time. With increasing contact time, porosity volume increased as well due to further reduction of NiO to Ni. The porosity of the in-house fabricated cells was nearly beyond the porosity limit recommended (40% maximum). Thus, in this case, an increased in contact time gave no further NiO reduction. Hence, no performance improvement with time.
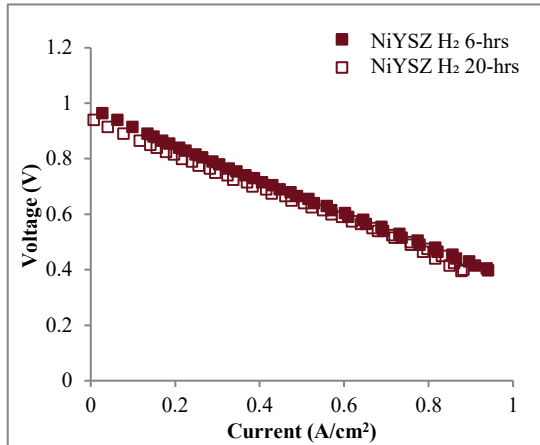
Figure 5-3: *i*V-curve for Ni/YSZ in hydrogen at 750°C (setup A).
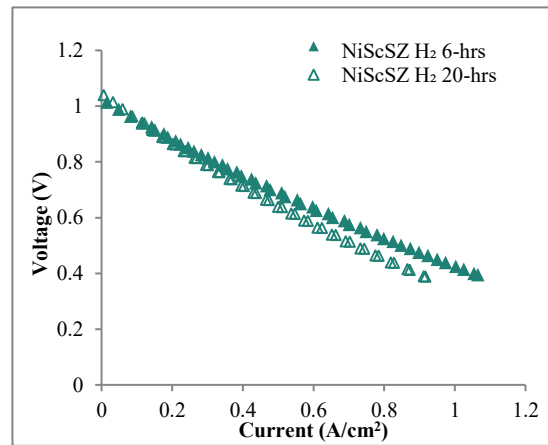
Figure 5-4: *i*V-curve for Ni/ScCeSZ in hydrogen at 750°C (setup A).

The small reduction of the performance in Ni/YSZ cells may originate from either coarsening, agglomeration or depletion of the nickel with operation time as explained by long term –

evaluations of nickel anodes by Zekri et al [120]. A larger drop of performance observed in Ni/ScCeSZ indicates initial instability of the cells over longer operation that may be due to the phase structure changes of 10ScCeSZ, which will be discussed in Section 5.3.4. The maximum power densities (PD$_{max}$) were calculated using the current density value and voltage applied. Figures 5-5, 5-6 and 5-7 show iV-PV (combined current-voltage and power density) curve produced at the three different setups specified previously which are also presented in Table 5-4.
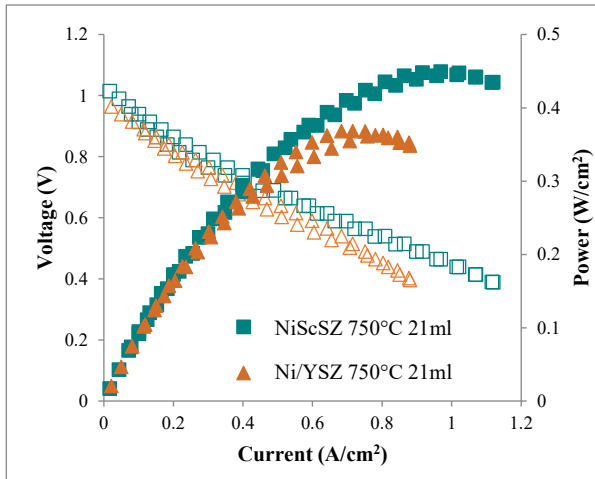
Figure 5-5: Maximum power density of Ni/YSZ and Ni/ScCeSZ with setup A.
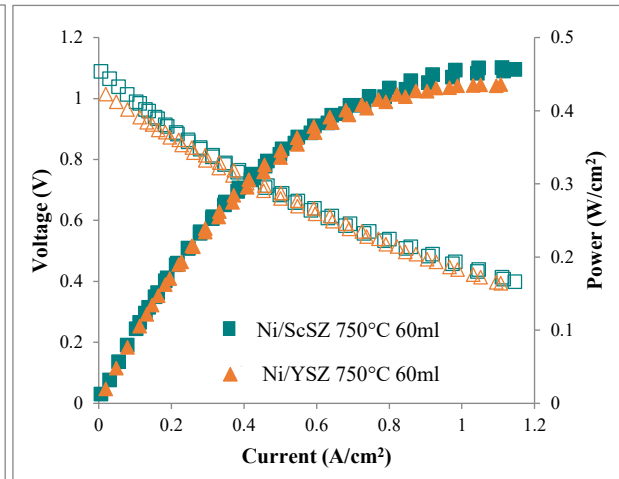
Figure 5-6: Maximum power density of Ni/YSZ and Ni/ScCeSZ with setup B.
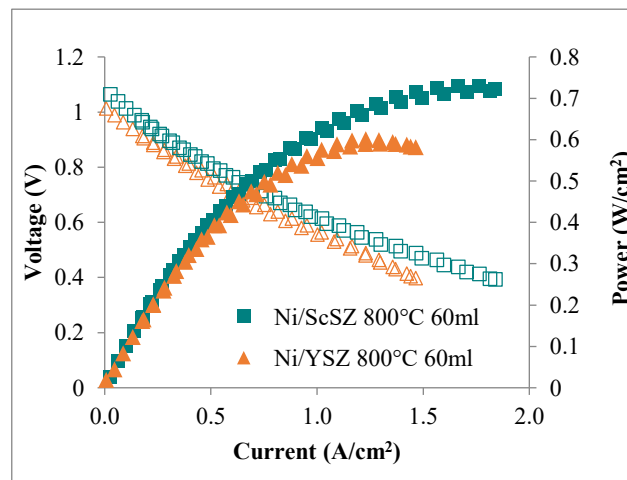
Figure 5-7: Maximum power density of Ni/YSZ and Ni/ScCeSZ with setup C.

Table 5-4: Maximum power densities and OCV in hydrogen for Ni/YSZ and Ni/ScCeSZ cells.

	Temp (°C)	Q_{fuel} (ml/min)	OCV	PD_{max} (W/cm^2)	CD_{max} (A/cm^2)	CD at 0.7V (A/cm^2)	*U_f at $CD_{0.7V}$ %
Ni/ScCeSZ	750	21 H$_2$ 7 He	1.02	0.42	1.02	0.46	90.5
		60 H$_2$	1.09	0.48	1.14	0.50	37.0
	800	60 H$_2$	1.06	0.73	1.85	0.75	52.8
Ni/YSZ	750	21 H$_2$ 7 He	0.99	0.37	0.88	0.39	82.4
		60 H$_2$	1.01	0.44	1.12	0.50	37.0
	800	60 H$_2$	1.01	0.60	1.46	0.66	48.9
Commercial Ni/YSZ [64]	800	60 H$_2$	1.04	0.47			
Commercial Ni/YSZ [112]	750	21 H$_2$ 7 He	1.02	0.33-0.42			

CD=current density, PD$_{max}$=maximum power density. Calculation based on active area=1.68 cm^2
*U_f calculator= refer to Appendix II
**reference [64, 112] were using an active area of 2 cm^2

Setup A: The maximum power densities obtained for Ni/YSZ and Ni/ScCeSZ were 0.37 W/cm^2 and 0.42W/cm^2, respectively. Referring to Figure 5-5, the current density value from OCV down to 0.64 V produced by the cells were similar, with 5% lower produced by Ni/YSZ cells. At the minimum voltage applied, 0.4 V, the differences increased to 13.7% with current density values of 0.88A/cm^2 and 1.02 A/cm^2 for Ni/YSZ and Ni/ScCeSZ respectively. The fuel utilization values in this setup were the highest; with 90.5% and 82.4% for Ni/ScCeSZ and Ni/YSZ, respectively. Comparing the maximum density values obtained by Troskialina [64] with Ni/YSZ commercial cells, the values obtained in this work are in the range reported. Hence, this shows that a good quality cell successfully fabricated by the manufacturing method elaborated in Chapter 4.

Setup B: Figure 5-6 shows the performance by both cells were similar throughout the measurement even though the measured electrical conductivity (Table 5-1) at 750°C for 10ScCeSZ was twofold. The obvious differences on the plot were the OCV and the maximum

power density obtained for Ni/YSZ and Ni/ScCeSZ. The OCV values obtained were 1.01V and 1.09V, while the maximum power densities values were 0.44 W/cm^2 and 0.48W/cm^2, respectively. At the operational voltage (0.7V), the current density produced for both cells were the same; 0.50A/cm^2. Comparing the fuel utilisation value in Setup A and B, even though a higher power density was achieved compare to Setup A, the fuel utilisation value drop to 37% in both cells; showing less economical operation due to excess of fuel supply.

Setup C: The small increase in temperature greatly influenced the performance of both cells. As predicted, the power density and fuel utilisation value increased compared to setup B as shown by Figure 5-7 and Table 5-4. The maximum power densities of the cells were 0.60 W/cm^2 and 0.73 W/cm^2 for Ni/YSZ and Ni/ScCeSZ, respectively. The current densities produced at 0.4 V were 1.46 A/cm^2 and 1.85 A/cm^2; with the Ni/ScCeSZ offering the higher value. Despite the increase of performance with this setup, lower operation temperature is desired due to materials stability factor. Comparing the maximum power density achieved with the same setting; the values obtained in this work was slightly higher than the commercial Ni/YSZ ASC that reported by McDonald [112]. Sumi et al. [65] found 15% of difference of performance in hydrogen operation using electrolyte supported cells between these two materials when tested at 1000°C. This is similar to what we obtained in this setup with a difference of maximum power density of 17%.

The difference of performance between Ni/YSZ and Ni/ScCeSZ in hydrogen was similar as obtained by Sumi et al [15] in their electrolyte supported cells. From the two-fold conductivity value shown, higher difference of performance was expected. In the conductivity test, the samples were prepared using same co-sintering temperature (1450°C), while in the

manufacturing stage, higher co-sintering temperature was used for Ni/YSZ cell compared to Ni/ScCeSZ (1350°C vs 1300°C). Hence, the superior conductivity value obtained in the conductivity was not reflected by the electrochemical performance evaluation.

Low temperature characterization for Ni/ScCeSZ cells

Figure 5-8 and Table 5-5 summarise the results of potentio-dynamic tests carried out on Ni/ScCeSZ cells to observe the electrochemical performance across 800-600°C. At temperature below 700°C, the power density obtained was still too low, which reflected by the previous conductivity measurement. Besides lower electrochemical activity on the anode side, the cathode material used, LSM, is not suitable for low temperature operation and should be replaced with strontium-doped lanthanum cobalt ferrite (LSCF) for lower temperature operation. However, it was not implemented here as it was outside the scope for this thesis and would have required to have a barrier layer (usually Gadolinium-Doped-Ceria or GDC) in between the LSCF cathode and zirconia electrolyte.
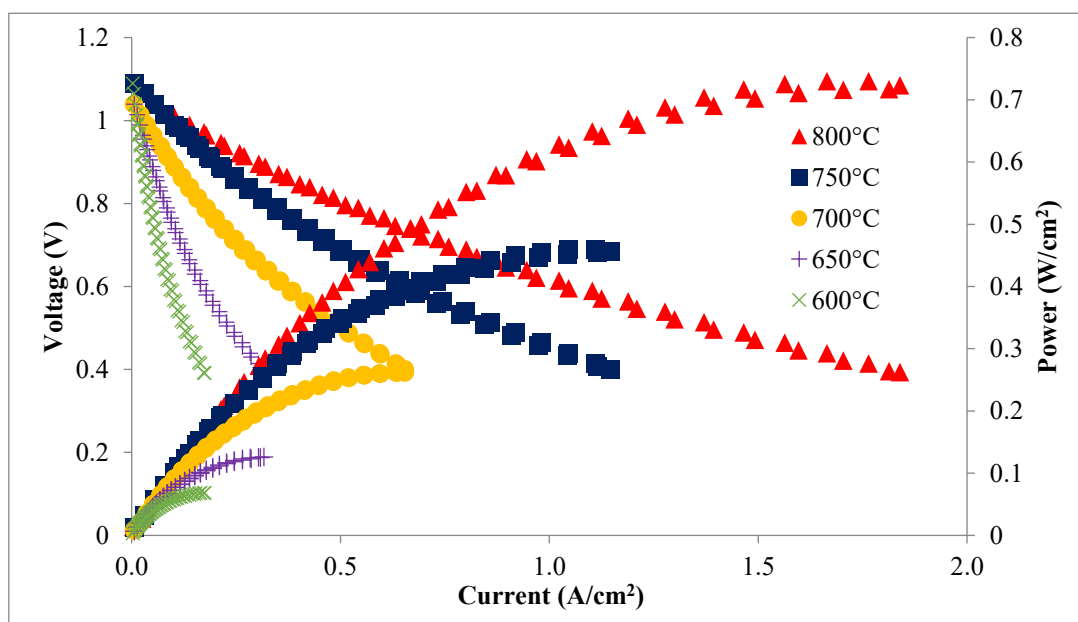
Figure 5-8: Maximum power density of Ni/ScCeSZ across 600-800°C with 60 ml/min hydrogen.

Table 5-5: Performance of Ni/ScCeSZ anode supported cell with 60 ml/minute hydrogen.

Temp (°C)	OCV	PD_{max} (W/cm2)	CD_{max} (A/cm^2)	CD at 0.7 V (A/cm^2)	U_f at $CD_{0.7V}$ %	ASR at 0.7 V (Ω.cm^2)
600	1.1	0.07	0.18	0.08	5.6	4.78
650	1.05	0.12	0.32	0.13	9.2	2.55
700	1.03	0.26	0.65	0.28	19.7	1.02
750	1.09	0.48	1.14	0.50	37.0	0.60
800	1.06	0.73	1.85	0.75	52.8	0.37

*ASR measured using EIS analysis; Nyquist plot supplied in Appendix II
**CD=current density, CDmax= maximum current density, PDmax=maximum power density

The maximum power densities for Ni/ScCeSZ at 700°C, 650°C and 600°C were 0.26, 0.12, and 0.07 W/cm^2 respectively. Table 5-5 shows that the ASR increased slightly more than 10 fold, while the maximum power density reduced by a factor of 10 at 600°C compared to 800°C. This was in complete agreement with the conductivity data presented in Table 5-1 where the conductivity decreased by a factor of 10 with the temperature reduction in this range. It is best to conclude that Ni/ScCeSZ cells with LSM cathode are not suitable for low temperature SOFC operation.

5.3.3 Electrochemical Impedance Spectroscopy (EIS)

Impedance spectroscopy analysis was carried out at 0.5V, 0.7 V and at 1.05V (near OCV) to evaluate the resistance in each cell. However, to simplify the discussion, only impedance analysis of 0.7V will be elaborated here.

A complete area-specific-resistance (ASR) studies on individual electrode with symmetrical cells is needed along with exaggerated repeating experiments with single cells need to be carried out to re-confirm the exact contribution of the resistance sources. According to Mogensen [121], impedance spectra obtained from a single cell in general are difficult to interpret due to the many processes involved. Nevertheless, practically the EIS spectra presented on the Nyquist

plot can generally be broken down into ohmic resistance (losses due to electrolyte and interconnects) and polarisation resistance (losses due to chemical, electrochemical, and transport processes) [121]; which will be used on this point onwards.
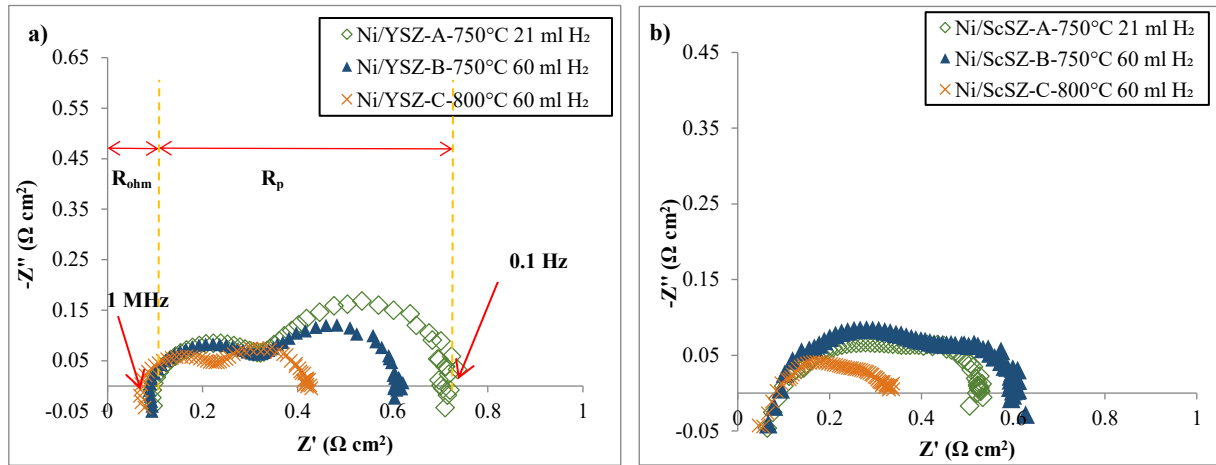
Figure 5-9: Nyquist plot at 0.7V for a)Ni/YSZ, and b) Ni/ScCeSZ.

Despite the superior conductivity of 10ScCeSZ, Figure 5-9 shows similar ohmic resistance (approximately 0.09 Ω cm^2) for both cells, as opposed to the expected lower ohmic resistance by the Ni/ScCeSZ. This was due to thicker electrolyte layer in Ni/ScCeSZ compared to Ni/YSZ; 17 μm and 10 μm respectively). This speculation was confirmed when the resistivity values from Section 5.2 used to calculate the ohmic area specific resistance. From Section 5.2, the bulk resistivity values obtained at 750°C was 62.7 Ω.cm for ScCeSZ and 117.3 Ω.cm for YSZ. Using these values and the thickness of the electrolyte, the area specific resistance calculated was similar between the cells; 0.107 cm^2 in Ni/ScCeSZ cells and 0.117 Ω cm^2 in Ni/YSZ cell. The value measured using EIS (Table 5.6) and the calculated value (from resistivity value) may origin from different length of silver wires used in the two experiment. Besides that, different furnace was used for the conductivity test and the SOFC electrochemical test. To improve the measurement accuracy especially when different furnace used, minimum two thermocouple should be use in all experiment with maximum distance of 1mm from the sample.

Table 5-6: ASR value evaluates with EIS for Ni/YSZ and Ni/ScCeSZ at 0.7 V

	Ni/YSZ			Ni/ScCeSZ		
	Setup A 750°C 21ml/min H_2+7 ml/min He	Setup B 750°C 60ml/min H_2	Setup C 800°C 60ml/min H_2	Setup A 750°C 21ml/min H_2 +7 ml/min He	Setup B 750°C 60ml/min H_2	Setup C 800°C 60ml/min H_2
R_{ohm} (Ω cm^2)	0.094	0.090	0.0690	0.087	0.093	0.085
R_p (Ω cm^2)	0.626	0.530	0.360	0.443	0.507	0.254
R_{total} (Ω cm^2) (Measured ASR)	0.720	0.620	0.429	0.530	0.600	0.339
Calculated ASR at 0.7V (Ω/cm^2)	0.743	0.685	0.462	0.582	0.588	0.362

In all setups, the ASR measured in the impedance spectra for Ni/ScCeSZ cells were only slightly lower than the values in Ni/YSZ; which in agreement with the performance of both cells. The highest difference was in Setup A with approximately 27% higher ASR in Ni/YSZ compared to that of Ni/ScCeSZ. In the Ni/YSZ cells, increasing the flowrate of the fuel reduced the electrode polarisation (R_p) as expected. When the flowrate increased, more fuel can access the triple phase boundary; hence more electrochemical reaction. A reduce in polarisation value in Ni/YSZ cell indicates that the Ni/YSZ cell was limited by mass diffusion resistance, which usually showed by the changes in the semi-circle at higher frequency, as in Figure 5-9.

Ni/ScCeSZ was not limited by mass diffusion resistance as the porosity was already high. However, the ASR behaviour towards the increased flowrate was confusing as a lower ASR was expected with higher flowrate. This observation has been double checked. In this test, only one measurement was obtained for ASR from EIS because of faulty EIS cable was attached initially. Nevertheless, the changes of ASR at 0.7 V at 6-hours and 20-hours can be calculated from the iV-PV curve in Figure 5-4. After the first 6 hours, the calculated ASR value was 0.582 Ω.cm^2 (as in Table 5-6). The ASR value increased to 0.773 Ω.cm^2 at 20 hours of operation.

Hence, if compared to the calculated ASR at Setup B with this ASR value, the ASR value actually lowered with the increased of the flowrate. The possibility of the cause of increase in ASR value, i.e the degradation reflected by the Ni/ScCeSZ cell will be discussed in Section 5.5.

Setup C has significantly lowest ASR as expected as the ceramics have higher conductivity. The ASR value for Ni/YSZ was 0.429 Ωcm^2, which was even lower than the one reported by Wang et al [12] and Zhou et al [96] that also used reverse multilayer tape casting method. Ni/ScCeSZ cell has lower ASR (0.339 Ωcm^2) than that of Ni/YSZ, which the difference was contributed by less polarisation resistance value. Theoretically, as the temperature increase, the ohmic resistance should decrease as the electrolyte conductivity increase, which observed in Ni/YSZ cell when changed from 750°C to 800°C. However, the ohmic resistance in Ni/ScCeSZ shows only a slight drop in setup C with the temperature increase (0.093 Ωcm^2 at 750°C vs 0.085 Ωcm^2 at 800°C).

Comparing the calculated value of total ASR and the value measured using EIS, both results were similar. The ASR values were calculated using the gradient at a point in the linear part of the *i*-V curve, which in this case it was based on the gradient at 0.7 V.

5.3.4   Current density at 0.7V

Potentiostatic values at 0.7 V were measured for 3 hours in Setup A with the *i*V measurement, OCV, and impedance measured in between, represented by the spaces shown in Figures 5-10 and 5-11. Ni/YSZ cells produce a steady current density with slight increase in each run while Ni/ScCeSZ cells show a gradual deteriorating pattern. The net decrease in Ni/ScCeSZ cells for the 12 hours' duration was 11.6%. Within the first loop of measurements with 3 hours

duration, the largest current density decrease was 5%; which reduced to 1.2% in the next loop. The measured current density at 18 hours in hydrogen was 0.343 A/cm^2 and 0.380 A/cm^2 for Ni/YSZ and Ni/ScCeSZ, respectively. The gradual degradation found of Ni/ScCeSZ cell performance will be covered on Section 5.4 and 5.5.
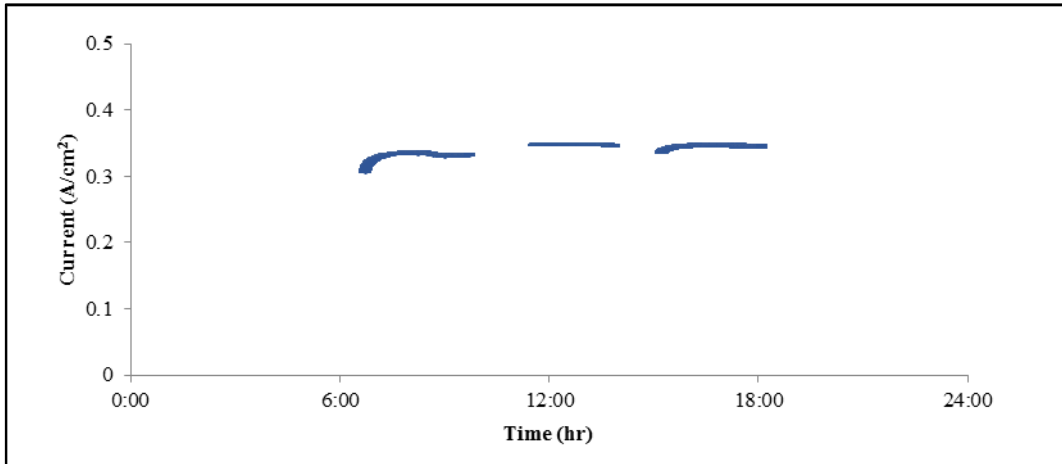
Figure 5-10: Current density of Ni/YSZ at 0.7 V at 750°C.
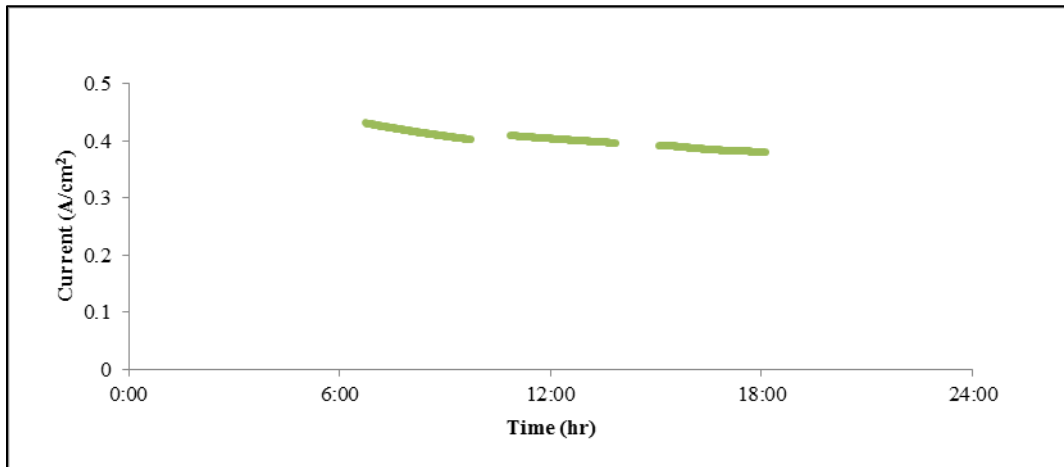
Figure 5-11: Current density of Ni/ScCeSZ at 0.7 V at 750°C.

5.4 Degradation

The constant gradual degradation with Ni/ScCeSZ cells in Section 5.3 shows instability in the Ni/ScCeSZ cell. Degradation was not initially the focus of this thesis. However, as it is essential to understand the origin of the degradation problem and find ways to solve it. This degradation study was carried out at the very end of the research. Hence, the result of this

observation was not implemented towards the other chapters but it will be useful for future works in manufacturing Ni/ScCeSZ as SOFC anode material.

5.4.1   XRD analysis

Speculation on the phase structure changes led to this additional analysis. XRD analysis carried out on electrolyte (ScCeSZ) pellets with different pre-treatment condition, one sample was prepared from as-received ScCeSZ powder and another one with ScCeSZ powder pre-calcined at 900°C. The pellet sintered at 1280°C for four hours and cooled down to room temperature. After the XRD analysis, the pellet from as-received ScCeSZ exposed to reducing environment with 30ml/min H_2 at 750°C for 24 hours to monitor the effect on the phase structure.
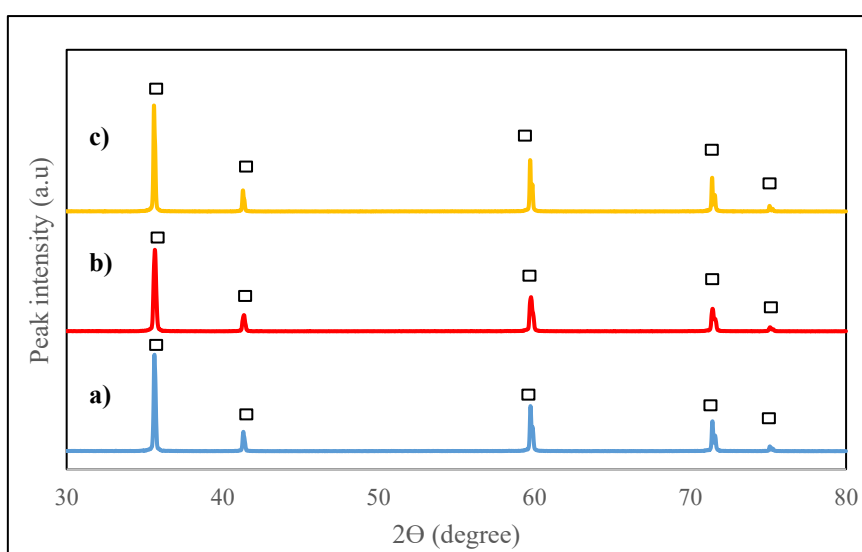
Figure 5-12: XRD analysis on ScCeSZ sintered pellet with different pre (and post treatment) condition; a) ScCeSZ b) ScCeSZ pre-calcined powder at 900°C and c) ScCeSZ pre-calcined powder at 900°C, annealed at 750°C in reducing environment (in 30 ml/minute H_2).

The XRD analysis on ScCeSZ pellets (Figure 5-12) showed there was no other structure exist besides pure cubic ScSZ. If there was phase changes from cubic to rhombohedral (or tetragonal), new peaks should be detected from the XRD patterns.This is in agreement with Kishimoto et al [74] which found no structural changes using XRD or Raman Spectra on

10ScCeSZ electrolyte discs after the sample annealed at high temperature or in reduced

environment [74]. Yarmolenko et al [122] observed pure cubic phases at room temperature

using sintering temperature higher than 1300°C, while at 1200°C (and lower) mixture of cubic

and rhombohedral phases exist. As the sintering temperature used was near to 1300°C, only

pure cubic phase structure detected in this thesis. At lower sintering temperature, other

structures were detected in [122] observation. Upon heating up, reversible cubic to

rhombohedral and rhombohedral to cubic phase transition were found in the 300-500°C

temperature range [122]. Regardless the sintering temperature used, above 600°C, only cubic

phase found using XRD Rietveld multiphase analysis [122]. Hence, at SOFC operating

temperature, the cubic phase is stable.
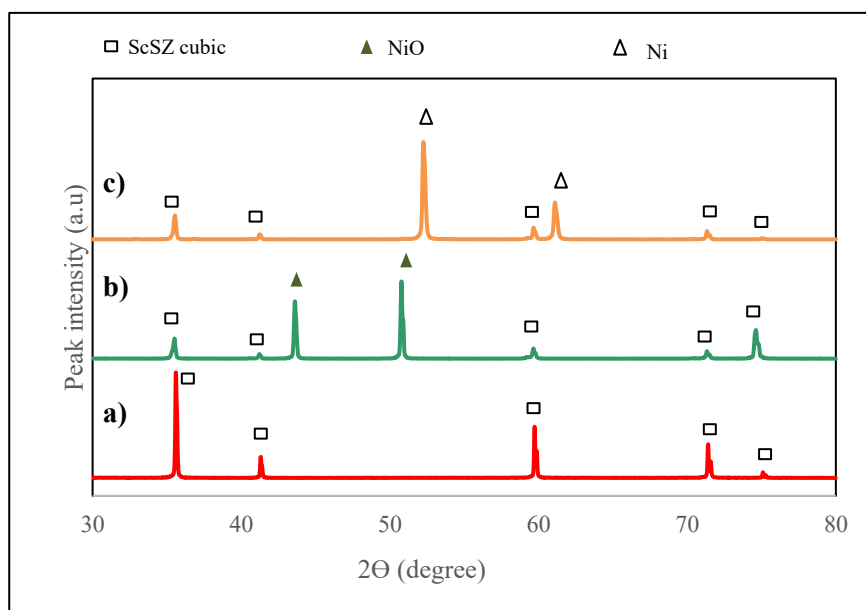
Figure 5-13: XRD analysis sintered pellet using PC900 ScCeSZ; a) ScCeSZ, b) NiO/ScCeSZ, and c) Ni/ScCeSZ annealed at 750°C in reducing environment (in 30 ml/minute H_2).
***PC900 =using pre-calcined powder at 900°C.**

To monitor the effect of mixing with NiO and under reducing environment on ScCeSZ, XRD

analysis on anode pellet (NiO/ScCeSZ), and reduced anode cermet (Ni/ScCeSZ) was carried

out. The XRD result reported in this analysis has been repeated three times to ensure the reliability of the analysis. As the author used 10ScCeSZ powder calcinated at 900°C in the SOFC cell in this work, the same powder used to produce pellet for XRD analysis. The 24 hours reduction with 30 ml/min H_2 flow carried out ensured all NiO reduced to Ni as shown in 5-13b and 5-13c. The XRD analysis result shown by Figure 5-13 indicates that despite the speculation that gradual degradation caused by phase structure changes, there was no apparent new peaks of ScCeSZ detected. If there was any phase transition in the sample, the space group symmetries in the unit cell for one crystal system to another (cubic to rhombohedral or tetragonal) will change [129]. According to reference [129], given the structure of one phase involved in a second-order type transition, the first step in the analysis of the second phase will be to relate to the unit cells between the two phases. If the unit cells are related, then the lines in the powder diffraction pattern are also related.

Opposed to this work observation, using Raman Spectra, Kishimoto et al [74] suggest that annealing with NiO changed the cubic phase of 10ScCeSz (from the same ScCeSZ supplier used in this work) to a mixture of cubic and rombohedral phases. After short exposure under reducing atmosphere at 900°C, the cubic and rhombohedral 10ScCeSZ structure in the anode disc further changed to tetragonal phase. Additional analysis using Raman Spectroscopy could help to verify this in the future work. As the result on the phase structure analysis using XRD shows no new peaks detected, it is safe to rule out the degradation caused by this factor. Analysis using Raman spectra analysis could be used in future work.

Opposed to gradual degradation observation in our work on Section 5.3, Shiratori et al [33] reported no degradation was observed with simulated humidified biogas operation. It shows that the degradation of Ni/ScCeSZ performance could also affected by the testing parameter or the manufacturing parameter used.

5.4.2   Influence of particle size to performance stability

Previously, the effects of changing manufacturing parameters to the cell performance by changing porosity volume, sintering temperature and pre-calcination temperature were carried out in optimising Ni/ScCeSZ cell. However, with the objective to produce Ni/ScCeSZ cell with similar manufacturing parameters with Ni/YSZ and understanding at that time, results in this section were previously omitted as they were not deemed conclusive. Now, as more XRD analysis revealed that the source of degradation was not because of phase structure changes as expected, they obtain new significance.

Next assumption to phase transition was the high porosity in Ni/ScCeSZ that speculated to be the cause of degradation due to percolation break-up. Ni/ScCeSZ cell with reduced porosity (SC05) was investigated. No pore former used in this test and the porosity in this cell from the organics burnt off. The porosity value calculated from Archimedes method was 26.5 vol %.
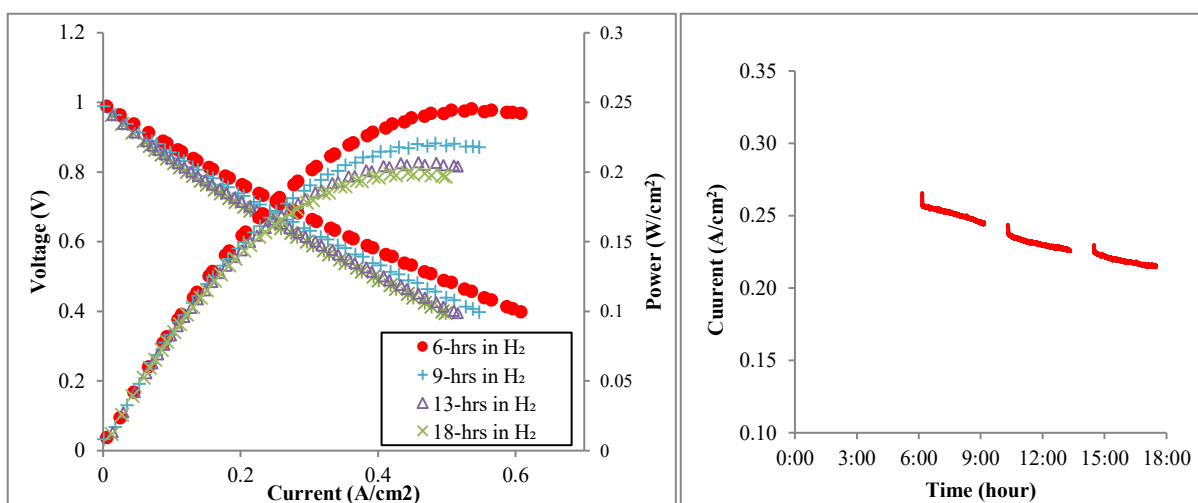
Figure 5-14: Electrochemical performance with Setup A of reduced porosity Ni/ScCeSZ cell (SC05): Showing a) *i*V-PV curve and b) current density obtained at 0.7 V.

As displayed in Figure 5-14, with reduced porosity, there were still gradual degradation in SC05. The power maximum power density measured at the first 6 hour were much higher than measure after 18 hours of test. The current density curve clearly showed degradation in each test loop. Hence, the assumption that degradation caused by excessive porosity could be eliminated. The electrochemical performance was much lower than that from any other Ni/ScCeSZ cell tested due to less anode porosity.

Another assumption was that the degradation caused by incompatibility of NiO and ScCeSZ particle size. NiO size used in anode substrate were 8.101µm (d50) while the ScCeSZ in the anode cermet size after pre-calcined was 0.372µm. The large gap in NiO size and the 10ScCeSZ size might hit the critical point of the percolation threshold. Hence, Ni/ScCeSZ cell with finer NiO powder (cell SC06) were fabricated with absence of pore former as in SC05. In this test, NiO powder with particle size of 1-2µm (Grade F) were supplied from Hart Materials, Wolverhampton, UK. The cell tested for 24 hours using Setup A.
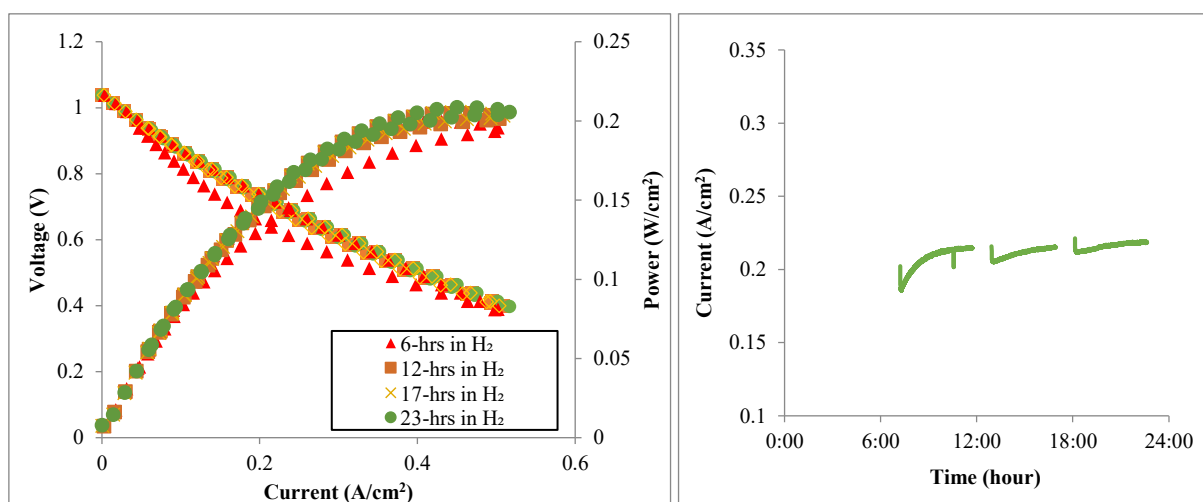
Figure 5-15: Electrochemical performance of Ni/ScCeSZ cell (SC06) with fine NiO starting powder. Showing a) *i*V-PV curve and b) current density obtained at 0.7 V.

As one can see from the result in Figure 5-15, the performance increases with SOFC test duration opposed to observation on Section 5.3.4. The power density curve (*i*V-PV) shows improving performance from the first 6 hours to the *i*V measurement and stabilised without degradation. The long current density measurement shows gradual increase and stabilization which was not seen on Ni/ScCeSZ cell previously. Up to this point, it is assumed that the particle size of the NiO and ScCeSZ powder pre-calcined at 900°C was not compatible. Compared to the standard electrochemical performance in Section 5.3, reducing the size of the starting powder in Ni/8YSZ while other parameters kept constant shows slight degradation in the cell performance as shown in Figure 5-16. Standard coarse NiO (Novamet type A with average particle size of 8.101 µm) used in the anode for this test. From the result, it shows that with finer YSZ particle size, gradual degradation also reflected by the Ni/YSZ electrochemical cell performance. The highest PD_{max} was shown by the first electrochemical test and slightly degrade with time. The pre-calcined YSZ powder at 850°C used in this work was 0.606 µm while the one used in standard formulation (pre-calcined at 900°C) was 0.612 µm. This re-confirm that the degradation was caused by the incompatibility of the powders starting size.
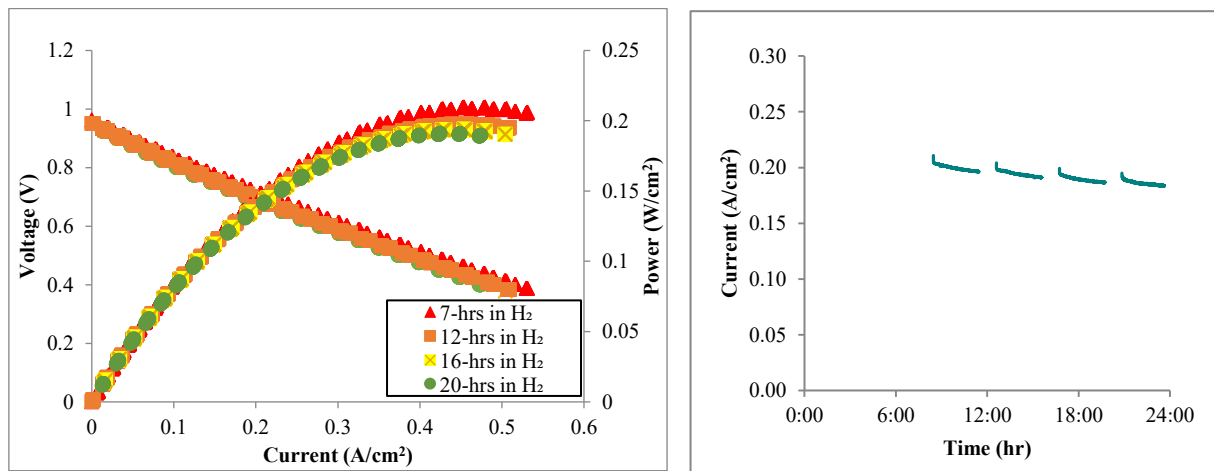
Figure 5-16: Electrochemical performance of Ni/YSZ cell (YSZ05) with coarse NiO starting powder. Showing a) *i*V-PV curve and b) current density obtained at 0.7 V.

5.5 Additional discussion

5.5.1 Electrochemical Performance

Although the conductivity values of ScCeSZ and YSZ reported higher in literature, the conductivity values measured in this work were validated when the calculated ohmic resistance (R_{ohm}) using the conductivity/resistivity data at 750°C were within the same range as the ohmic resistance obtained from the EIS measurement.

At 750°C, the conductivity value of 10ScCeSZ measured was almost twice that of the 8YSZ with values of 0.016 S/cm and 0.009 S/cm. Despite the higher conductivity of the 10ScCeSZ electrolyte, the difference of performance of Ni/ScCeSZ and Ni/YSZ cells was only 17%. The polarisation resistance value of Ni/ScCeSZ was much lower than that of Ni/YSZ cell, but the ohmic resistance was similar. If the same electrolyte thickness used, 10 μm for both cells, the ohmic resistance in Ni/ScCeSZ cell would be 0.063 $\Omega.cm^2$ (calculated from the resistivity data), opposed to the calculated ASR value of Ni/YSZ. This value will be approximately 58% lower than the ohmic resistance in the Ni/YSZ cell. If the polarisation resistance were kept constant, and the ohmic resistance adjusted with the new predicted EIS value, the total ASR for Ni/ScCeSZ would be 0.494 $\Omega.cm^2$, compared to the current measured ASR, 0.530 $\Omega.cm^2$. With lower ASR, the performance of the Ni/ScCeSZ with thinner layer electrolyte should be higher than observed here.

Despite the concern on the small difference of the performance, the only literature that compares Ni/ScCeSZ and Ni/YSZ carried out on high-temperature SOFC (1000°C) showed similar differences (17%) in the maximum power maximum density. The limitation of the changes may be limited by the contribution by other materials as well, as Ni contributes to 60

131

vol% in anode while LSM contributes 50% in cathode active layer and 100% in the second cathode layer. Nevertheless, the difference in the current density produced by the cells was more substantial only towards the lower voltage applied. In other words, the Ni/ScCeSZ cells showed higher limiting current compared to Ni/YSZ.

5.5.2 Degradation

From the XRD scan of several ScCeSZ, NiO/ScCeSZ and Ni/ScCeSZ (reduced), it is safe to eliminate the assumption that the degradation due to phase structure changes as no new peaks from other phase structure besides cubic were detected.

Comparing the microstructure of the Ni/ScCeSZ and Ni/YSZ cells, the difference was in porosity and the starting powder size of the electrolyte in the anode substrate. The effect of porosity had been eliminated while the relationship between the degradation and starting particle size was established in Section 5.4.2. Although the degradation can be solved with changing the NiO starting powder size, the explanation of why the degradation taken place only in Ni/ScCeSZ with coarse NiO has not been thoroughly discussed. Comparing the coarse NiO to fine NiO, the former has lower surface area available, hence less TPB reaction site. Then the performance with Ni/ScCeSZ cells should be low from the beginning, not gradually degrading as observed.

Fergus et al. [26] compiled observations of several works on the effect of NiO size and YSZ towards anode effective conductivity with the conclusion that the electrical conductivity increases with electrolyte's particle size. The anode electrical conductivity greatly influenced the tendency of NiO clustering (or coarsening) and downshifted the percolation threshold.

Which also means, larger electrolyte's particle size can reduce Ni coarsening. Initially, degradation due to Ni coarsening was ruled out as there was no degradation observed in Ni/YSZ cell. Nevertheless, with reference from [26], it can be deduced that degradation observed in Section 5.3 was due to Ni coarsening which caused by incompatibility of the starting materials sizes in Ni/ScCeSZ. Ni coarsening further leads to isolation of Ni particle, hence decreasing active anode fraction, causing percolation break-up and decreasing triple phase boundary [123].

CHAPTER 6: NI/10SCCESZ VS NI/8YSZ SOFC IN SIMULATED DRY BIOGAS

6.1 Introduction

SOFC has the ability to convert carbonaceous fuels in direct internal reforming with no or little pre-processing. For internal reforming systems with carbon fuels, the fuel is assumed to undergo reforming reaction on the surface of coarse Ni particles in the anode substrate region while the final electrochemical reaction takes place in the anode functional layer region, which has finer Ni particles. In this work, when dry simulated biogas consisting of CH_4 and CO_2 in contact with the Ni surface, a dry reforming reaction (Eq. 1.7) is expected to occur; releasing 2 mol of H_2 and 2 mol of CO. The molar flow rate of biogas used was two-fold compared to hydrogen as shown by Figure 6-1. With double molar flow, the electrochemical performance may be doubled if 100% of the biogas fed converted to CO_2 and H_2 following Eq. 1.7. However, methane cracking that lead to carbon deposition may also occur at the operating temperature.
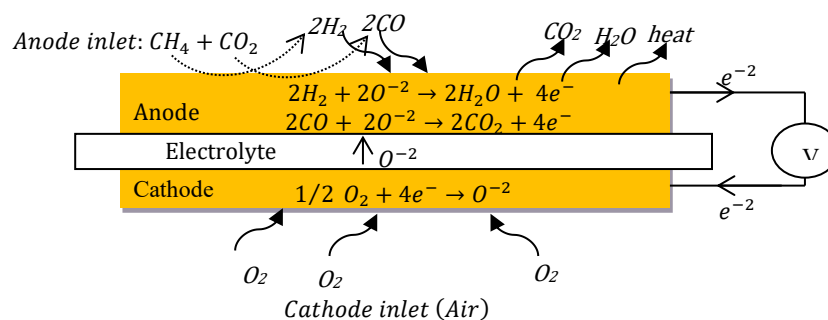
Figure 6-1: Desired reaction in the SOFC cell fed with dry simulated biogas with internal reforming reaction.

This chapter reports comparative studies of using Ni/ScCeSZ as a replacement for Ni/YSZ anodes in SOFCs operating with dry simulated biogas using in-house fabricated cells as reported in Chapter 4. The electrochemical characterisation reported in this chapter is a continuation after 24-hours test in hydrogen reported in Chapter 5. The tests carried out at

750°C with a dry simulated biogas flowrate of 14 ml/minute methane (CH_4), 7 ml/minute carbon dioxide (CO_2) and 7 ml/minute helium (He); which was the same flowrate as in setup A for hydrogen. The comparison was made using OCV, polarisation curve, maximum power densities, constant current potential, and electrochemical impedance spectroscopy. Four different cells were tested for each electrochemical performance with the same parameter but only the one that presents the best result is plotted, with other results presented in a table or bar chart where necessary. To understand more about the effect of operation under biogas, carbon deposition test were evaluated using SEM-EDX and a mass spectrometer.

6.2 Electrochemical Performance Characterisation

6.2.1   Open Circuit Voltage (OCV)

Unlike in the hydrogen tests, the OCV test for biogas operation was carried out only for 90 minutes in order to avoid carbon deposition. In OCV mode, the system is in thermodynamic equilibrium. While in operation, carbon undergo preferential electrochemical oxidation and convert into CO near the triple phase boundary (TPB). The duration applied for OCV under biogas setup is a balance of the time needed to replace H_2 and minimum time for minimizing carbon deposition build up in OCV mode. Figure 6-2 shows the first 90 minutes of OCV in hydrogen and the whole duration of OCV in biogas setting. As seen in previous chapter, the OCV in hydrogen stabilised at 0.99 V for Ni/YSZ cell and 1.05 V for Ni/ScCeSZ cells as depicted by Figure 6-2. In biogas, the OCV values dropped from 0.99 V to 0.89 V for Ni/YSZ cell. A less significant drop from 1.05 V to 1.00 V was seen for Ni/ScCeSZ cell. The gradual drop shown by the first part in the OCV measurement for Ni/YSZ cells was the transition from hydrogen to biogas which was more obvious than the trend shown by the Ni/ScCeSZ cells. Consistent results observed in all cells tested as presented by Figure 6-3. The same drop in

Ni/YSZ cells was previously observed Troskialina [50] using Ni/YSZ cells and Yin et al. [124] when using Ni/YSZ/ScSZ cells. The OCV measurements, in this case, may not reflect the electrolyte quality but rather the effect of partial pressure of the reactants. With decreasing reactant partial pressure, OCV was also affected as it decreases the Nernst voltage. Chapter 5 sub-section 5.3.2 shows that, increasing amount of reactant by increasing the hydrogen flowrate from 28 ml/minute to 60 ml/minute increase the OCV as the higher number of electrons passes as well as the system pressure. As the system pressure remains, it is speculated that the OCV drop portrayed lower reactant amount compared to previous feed in hydrogen. This speculation can be supported by the high OCV obtained in Chapter 7 with Tin-doped Ni/ScCeSZ cell.
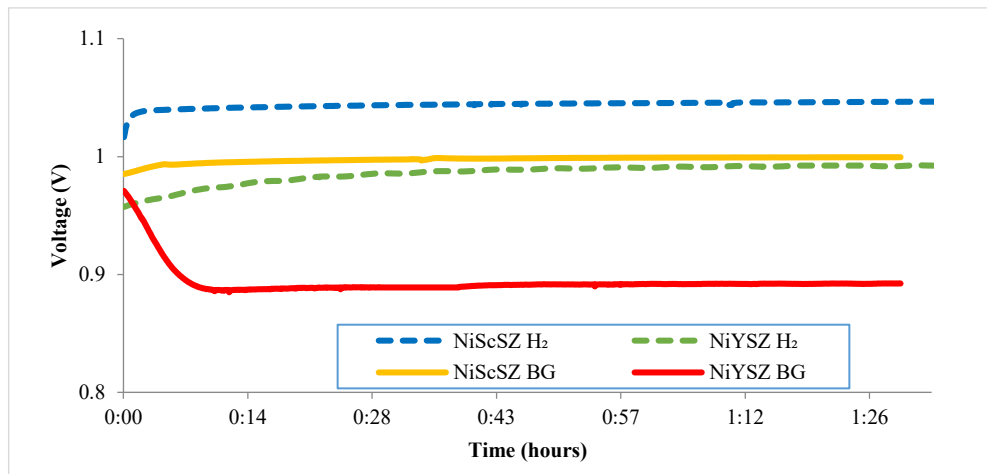
Figure 6-2: Initial OCV for Ni/ScCeSZ and Ni/YSZ at 750°C with 28 ml/min total gas feed in hydrogen and biogas.
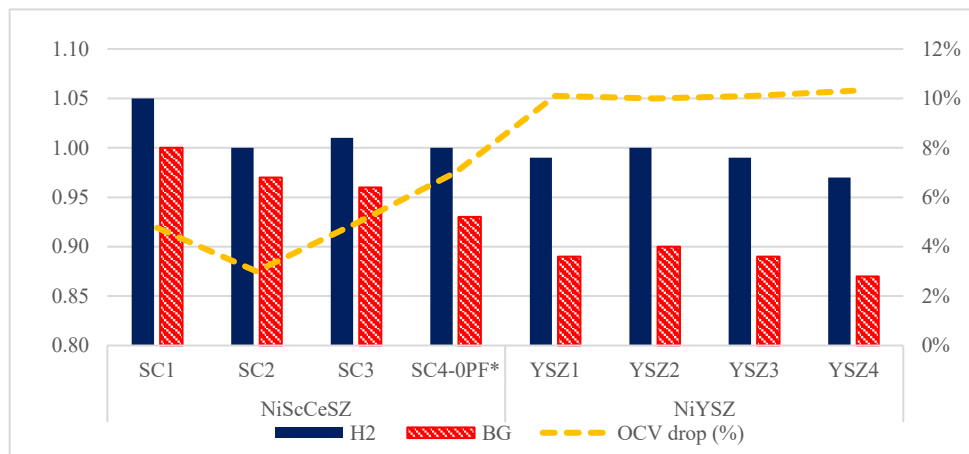
Figure 6-3: OCV drop bar chart across four different samples for Ni/YSZ and Ni/ScCeSZ.

6.2.2 *i*-V/ Polarisation curve

Figure 6-4 shows the comparison of polarisation curves of the cells in hydrogen and simulated biogas. The input were taken from the first measurement of the *i*-V curve at 6 hours in hydrogen and at the 1.5-hours after swap to biogas for Ni/ScCeSZ (SC1) and Ni/YSZ (YSZ1). In hydrogen, both cells showed a large linear portion on the *i*-V curve with no obvious activation loss region in the low current density region and no obvious concentration polarization as indicated by the curve at higher current density region.
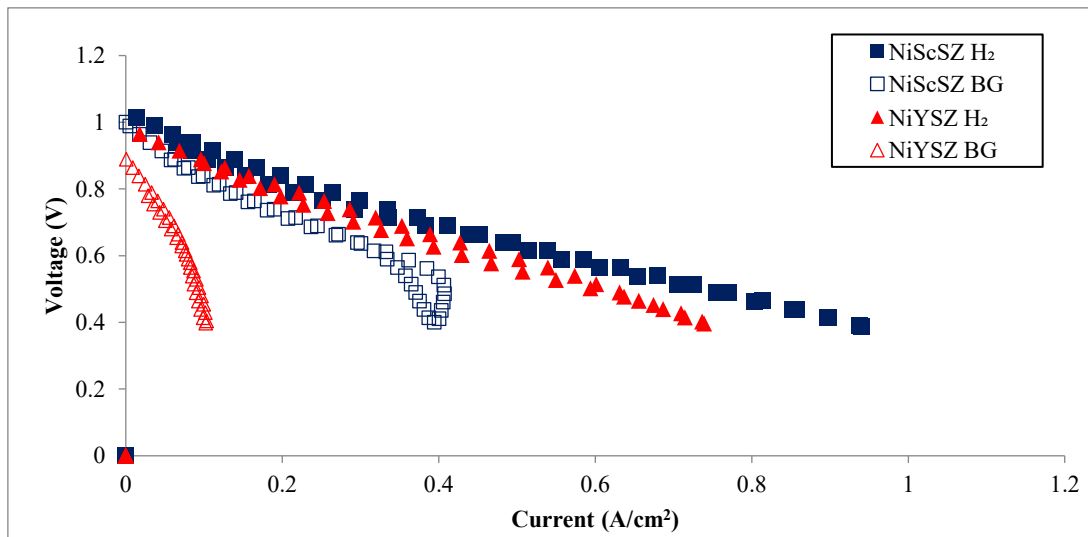
Figure 6-4: IV-curve under hydrogen and biogas operation.

The amount of current produced at each potential step reduced when swapped to biogas; in another words, with increasing current the potential drop for both cells in biogas was more rapid compared than in hydrogen. The maximum current density values were less in biogas than in hydrogen. In biogas, Ni/ScCeSZ shows the quadruple current density values than Ni/YSZ, which were 0.51 A/cm^2 and 0.12 A/cm^2 respectively. For Ni/ScCeSZ cells in biogas, the trend of the curve up to 0.43A/cm^2 was similar to the one in hydrogen but reduced rapidly beyond that.

The concave curves at higher current density shown by the Ni/ScCeSZ cells with biogas indicate that polarisation due to concentration polarisation was more obvious than it was on hydrogen. As previously covered in Chapter 1, the large voltage drop may originate from shortage of reactant species or due to slow diffusion through the electrodes [44]. Out of four cells tested, two of the Ni/ScCeSZ cells showed this shape of *i*-V curve which can be seen from Figure 6-8. In Ni/YSZ cell tests with biogas, the obtained *i*-V curve gave the impression that the reactant supply was insufficient as significant differences showed as compared to the performance in hydrogen. The shape of the *i*-V curve for Ni/YSZ cell (YSZ1) under biogas operation was not too clear in Figure 6-4 because of the effect of other plots, but it can be clearly seen from Figure 6-7 that the polarisation due to the mass-transfer was obvious. In addition to insufficient reactant supply, a higher mass-transfer polarisation in biogas was also suspected due to a larger molecular weight of CO (and higher hydrocarbons chain) and longer times required for CO to reach the reaction site at the interface of the electrolyte and anode [1].

6.2.3 *i*-V and Maximum Power Density, PDmax

The plots in Figures 6-5 and 6-6 present the comparison of the maximum power density in hydrogen and biogas. Switching the fuel from hydrogen to biogas shows a drastic reduction of the performance of the Ni/YSZ cell – YSZ1 as displayed by Figure 6-5. YSZ1 showed the highest performance drop of the Ni/YSZ cells, 86.5%; from 0.37 W/cm^2 to 0.05 W/cm^2. Initial speculation was that this was due to carbon deposition that blocked the Ni/YSZ anode instantly when the fuel swap took place. The same pattern of a drastic drop in performance of commercial Ni/YSZ cells in biogas was observed in previous work in our group by Troskialina [50]. Koh et al. [125] tested with Ni/YSZ cells with lower Ni content (50:50 vol%) in diluted methane; shows a less severe effect of the fuel swap.

On the other hand, the maximum power density drop in the Ni/ScCeSZ cell - SC1 was only 33.3% (0.42 W/cm^2 to 0.28 W/cm^2) as displayed in Figure 6-6. Up to this point, from the maximum power density value and OCV obtained, it appeared that Ni/ScCeSZ cells can tolerate more biogas operation. The average drop of performance in Ni/ScCeSZ cells was 42.0±6.48 % while the performance drop in Ni/YSZ cells was consistently higher with an average drop of 80.6±4.05%. All *i*-V/PV curves for performance in biogas for Ni/YSZ cells and Ni/ScCeSZ cells are displayed in Figures 6-6 and 6-7, respectively. It can be seen that the power density result from the Ni/YSZ were more consistent compared to that generated by the Ni/ScCeSZ cells. This may have impacted from different batches of 10ScCeSZ starting powders used. Individual performance in biogas are presented and summarised in Table 6-1 and Figure 6-9. An attempt to produce a Ni/ScCeSZ cell with lower porosity which used no pore former (as Ni/ScCeSZ has slightly higher porosity) resulting in lower performance in hydrogen and biogas, but the behaviour towards the fuel swap was equally low (43% drop). The electrochemical result presented as SC4-0PF in Table 6-1 will be used as a base result in Chapter 7 to compare with the Sn doped cells which were manufactured without pore former.

Table 6-1: Maximum power density (PD$_{max}$) values in hydrogen and biogas for Ni/YSZ and Ni/ScCeSZ cells

Sample	PD$_{max}$ (W/cm^2)			PD$_{max}$ drop (%)	CD$_{max}$ (BG) A/cm^2
	H$_2$ in*	H$_2$ out*	BG*		
YSZ1	0.32	0.37	0.05	86.5	0.10
YSZ2	0.29	0.30	0.06	79.9	0.12
YSZ3	0.33	0.37	0.08	78.3	0.15
YSZ4	0.27	0.27	0.06	77.6	0.13
SC1	0.44	0.42	0.28	32.7	0.51
SC2	0.33	0.27	0.14	47.8	0.31
SC3	0.45	0.38	0.21	44.2	0.53
SC4-0PF**	0.25	0.21	0.12	43.1	0.29

*H$_2$ in – based on the first measurement in hydrogen, H$_2$ out based on the last measurement before the swap, BG-first measurement in biogas
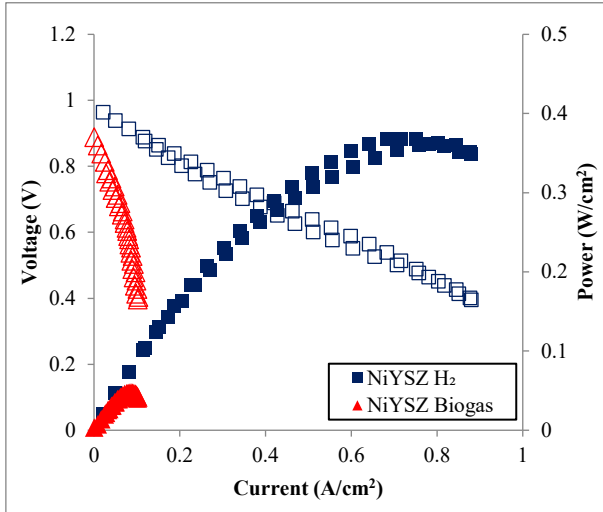
Figure 6-5: Ni/YSZ performance in H₂ and biogas (YSZ1).
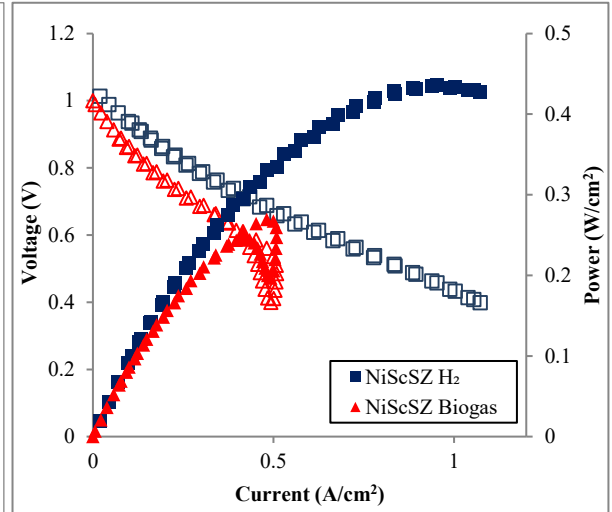
Figure 6-6: Ni/ScSZ performance in H₂ and biogas (SC1).
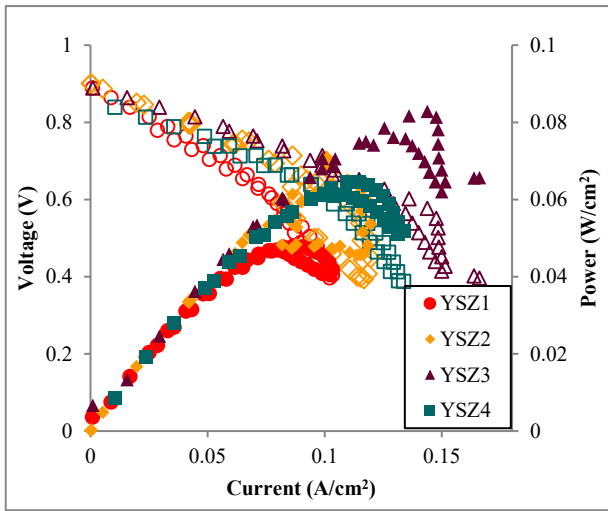
Figure 6-7: Ni/YSZ performance in simulated biogas.
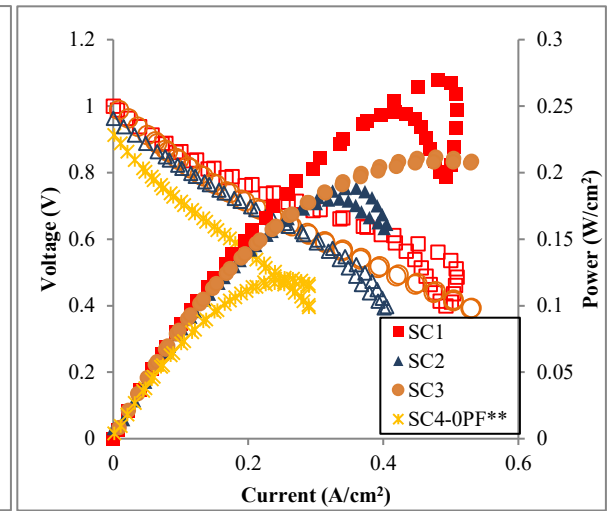
Figure 6-8: Ni/ScCeSZ performance in simulated biogas.
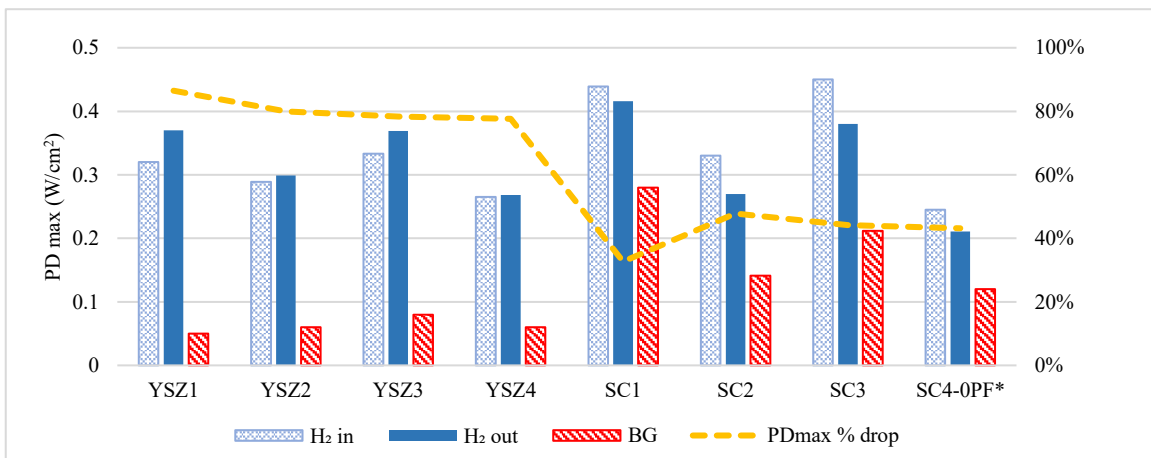
*H₂ in – based on the first measurement in hydrogen, H₂ out based on the last measurement before the swap, BG-first measurement in biogas

Figure 6-9: Summary of performance in hydrogen and biogas for Ni/YSZ and Ni/ScCeSZ cells.

6.2.4 Post biogas hydrogen test

In post biogas *i*-V measurements that were made after 1.5 hours of swapping back to hydrogen, both cells recovered from the drop in performance instantly as depicted in Figures 6-10 and 6-11. Ni/YSZ showed a better degree of recovering than the Ni/ScCeSZ despite the assumption that carbon had already been severely deposited on the anode surface, that hindering the electrochemical reactions. The maximum power densities in hydrogen after biogas operation for both cells were quite similar with values of 0.32 W/cm^2 and 0.33 W/cm^2 for Ni/YSZ and Ni/ScCeSZ cells, respectively. The pattern of the *i*-V curve also returns back to normal when swapping back to hydrogen.

The recovery of both cells (especially the Ni/YSZ cell), in post-biogas hydrogen test leads to two possible speculations;

1) the low performance in biogas may not largely affected by carbon deposition, but more due to lack of catalyst activity; hence less amount of reactant produced, or

2) most of the carbon formed near the TPB sites is already electrochemically oxidized, hence unblocking the active TPB sites for electrochemical reaction by hydrogen.
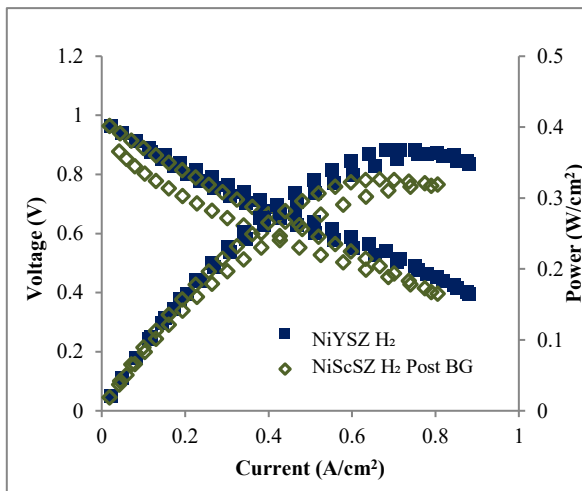
Figure 6-10: *i*V-PV of Ni/YSZ before and after biogas feed.
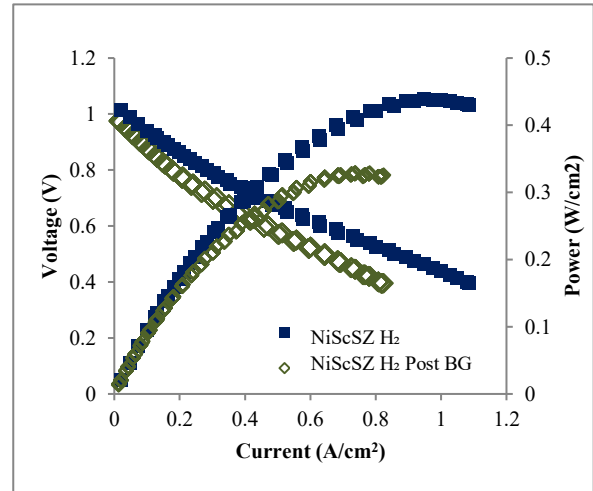
Figure 6-11: *i*V-PV curve of Ni/ScCeSZ before and after biogas feed.

6.2.5   Impedance spectroscopy analysis

Figure 6-12 and Table 6-2 shows how the fuel swap affected the impedance in Ni/YSZ cells and Ni/ScCeSZ cells measured at 0.7 V. The impedance was measured at 0.5 V, 0.7 V and OCV but only impedance data at 0.7 V are presented to simplify the comparison between the two materials. The ohmic resistance in an electrode supported cell with thin electrolyte layer mainly regards the interconnects or current collectors for thin electrolyte with thick anode supported cells [44, 45]. Hence, the ohmic resistances of the Ni/YSZ and Ni/ScCeSZ cells in biogas were unchanged despite of the drop in performance.

Table 6-2: Measured Area Specific Resistance (ASR) for Ni/YSZ and Ni/ScCeSZ in biogas

	Ni/YSZ		Ni/ScCeSZ	
	H_2	BG	H_2	BG
R_{ohmic} (Ωcm^2)	0.09	0.09	0.09	0.10
$R_{p, polarisation}$ (Ωcm^2)	0.63	2.66	0.44	0.63
R_{total} (Ωcm^2) - Total ASR	0.72	2.75	0.53	0.73
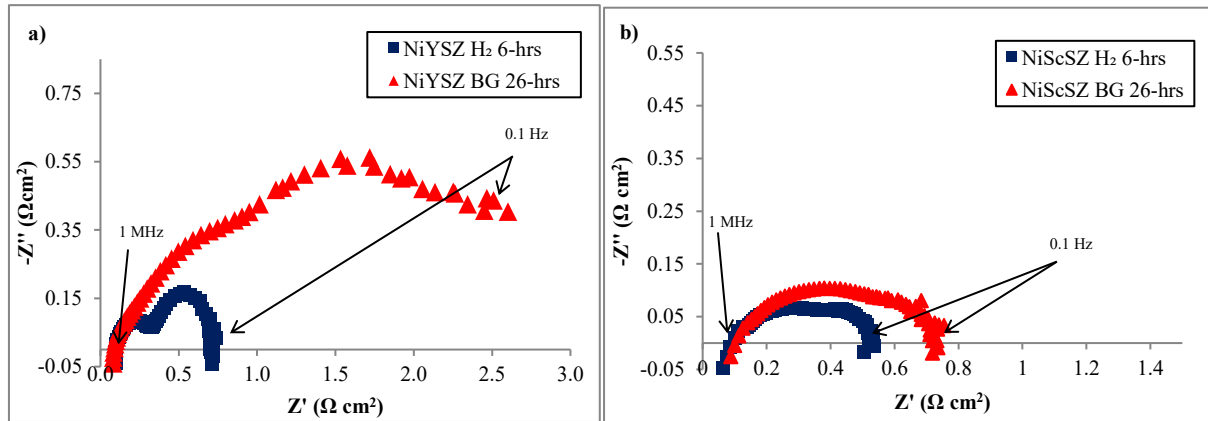
Figure 6-12: Nyquist plot showing the impact of changing from hydrogen to biogas on impedance at 0.7V for a) Ni/YSZ, and b) Ni/ScCeSZ.

Figure 6-12a shows the Nyquist plot for Ni/YSZ cells under hydrogen and biogas operation. The impedance plot shape changed and the size quadruple when the fuel switched from hydrogen to biogas. Fuel changes on the anode side will affect mass diffusion resistance (R_{diff})

and charge transfer resistance(R_{ct}), which reflected at lower frequency region and higher frequency region, respectively. The total ASR value considerably increased from 0.72 Ωcm^2 to 2.75 Ωcm^2. In biogas, the shape of the Ni/YSZ impedance plots suggested that there were four semi-circles contributing to polarisation, compared to the prior to two semi-circles in the hydrogen test. This is in agreement to [46] which uses multilayer tape casting with Ni/YSZ/LSCF cells. Because predicting and fitting the semi-circle impedance analysis is beyond the scope of this thesis, analysis will only based on what has been established up to this point. As the polarisation resistance was too high in biogas for Ni/YSZ cell, the plot did not cross the real axis under biogas operation, the value reported here is the approximation value based on a calculated ASR value (calculated at the gradient at 0.7V). Due to a significantly lower amount of reactants available in the anode of the Ni/YSZ cell, the charge transfer resistance and mass diffusion resistance increased greatly. From the extremely high ASR, it can be speculated that only a minimum amount of electrochemical reaction took place.

Figure 6-12b shows the Nyquist plot for Ni/ScCeSZ cells under hydrogen and biogas operation. The total ASR resistance increased to 0.73 Ω cm^2 from originally 0.53 Ω cm^2 in hydrogen. With Ni/ScCeSZ cells, the size of semi-circle in high frequency increased with the fuel swap which clearly indicates an increase of charge transfer resistance. Overall, this section shows that the ASR changes in Ni/ScCeSZ cells were lower than in Ni/YSZ cells; dominated by the increase of charge transfer resistance. Hence, this shows that Ni/ScCeSZ cells performance was more robust in biogas than with Ni/YSZ cells.

6.2.6   Current density at 0.7 V

Figures 6-13 and 6-14 show the overall current density value at 0.7 V for the cells for 48 hours of operation time. The 24 hours test under biogas was started after completion of 24

hours test in hydrogen. As shown in Chapter 5, the current density in hydrogen was stable in Ni/YSZ cells operation with 3% on average increase in each run; while Ni/ScCeSZ cells showed a decrease of 11.2% over 12 hours duration.

The last current density recordings in hydrogen before the fuel swap were 0.343 A/cm^2 and 0.380 A/cm^2 for Ni/YSZ and Ni/ScCeSZ cells respectively. These values dropped to 0.104 A/cm^2 for Ni/YSZ and 0.286 A/cm^2 for Ni/ScCeSZ at the first potentiostatic reading after the swap. For Ni/YSZ, the value stabilised around the same reading throughout the cell testing but the current density in Ni/ScCeSZ cells further dropped to 0.255 A/cm^2 at the end of the first run of potentiostatic measurement. After overnight testing with biogas, indicated at the 40-hour mark in Figure 6-14, the current density reduced to 0.236 A/cm^2. Even with the decrease, the reading in Ni/ScCeSZ cells under biogas was still higher compared to the last reading generated in Ni/YSZ cells.

As reflected by the iV-PV analysis on post-biogas, the current density restored to almost the same value as previously when the system swapped back to hydrogen. In the post-biogas current density, Ni/YSZ shows slightly higher and more stable current density value of 0.320 A/cm^2 while in Ni/ScCeSZ, the reading shows 0.315 A/cm^2. The iV-PV curve of post-biogas test in Figures 6-10 and 6-11 also shows higher current density of Ni/YSZ cells value at 0.7V.
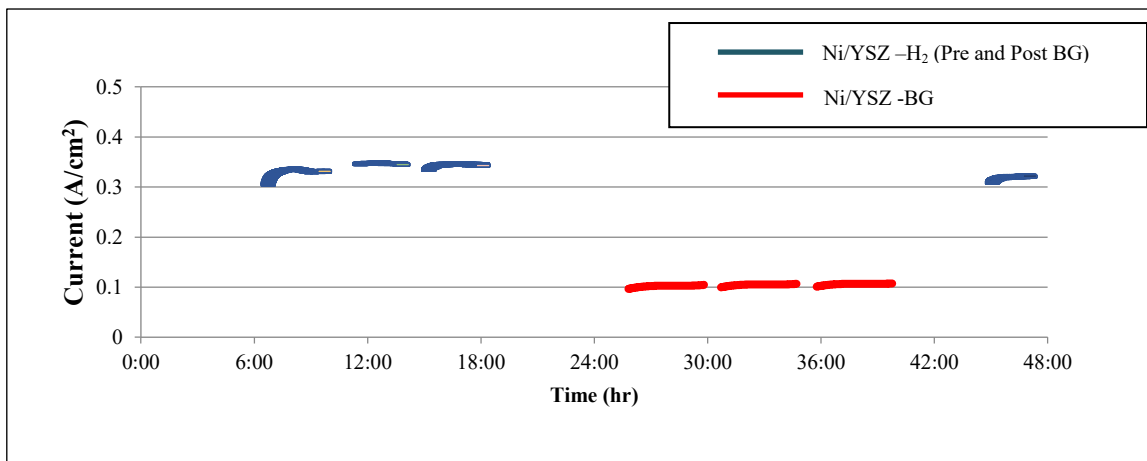
Figure 6-13: Current density of Ni/YSZ at 0.7V at 750°C with alternate hydrogen and biogas setup
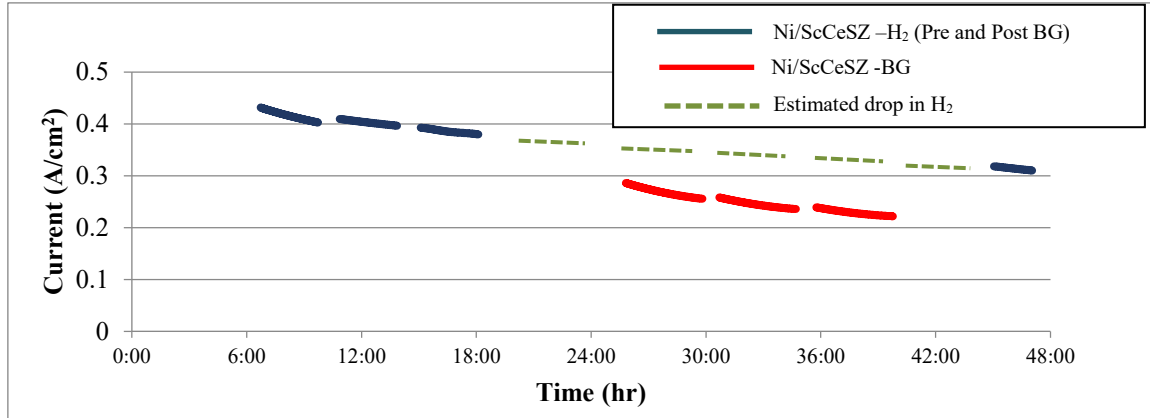
Figure 6-14: Current density of Ni/ScCeSZ at 0.7 V at 750°C with alternate hydrogen and biogas setup

The maximum power density of Ni/ScCeSZ in the *i*V-PV curve was still slightly higher because the drop of potential at higher current density of Ni/YSZ was greater. Using the gradient from the second current density measurement (that shows the least drop), the drop of current density of the system run continuously in hydrogen was estimated, shown by the green-dotted line in Figure 6-14. The current density from the post-biogas analysis would show the same value in continuous operation under hydrogen. Hence, it effectively shows no net drop caused by the biogas operation. On the other hand, even though it seems that the post-biogas reading showed better performance in Ni/YSZ cells, the drop due to biogas operation for Ni/YSZ was more with 0.343 W/cm^2 to 0.320 W/cm^2; considering there was no drop in performance in previous operation on hydrogen.

6.3 Carbon deposition-post test analysis

The cells were intact after cooling down in all tests as shown in Figure 6-15. Cooling down was done at the furnace's lowest rate possible; 1°C/minutes with 7 ml/minute of hydrogen to minimise cracks and prevent the Ni oxidation to NiO. No damage caused by delamination or cracks was observed. Figures 6-16a and 6-16b show the dismounted cells after SOFC cell

145

testing. As the silver paste became a dense structure at high temperature, dismounting destroyed the cells into small pieces. No obvious black carbon deposition covering the anode substrate surface was found on both cells. However, on the Ni/ScCeSZ's cell holder, black carbon deposited on the cell holder's wall as shown in Figure 6-16d. It was evidence that besides dry reforming reaction, there was methane cracking reaction took place during cell testing with biogas. In theory, the electrochemical reaction only happen at TPB. Hence, this observation shows that the cell's TPB reached out to the AS layer and not only limited to the AFL as the carbons deposited on the anode substrate were electrochemically converted to CO or CO_2. This was in agreement with observation by Sumi et al [65] that found less amount of carbon detected near the electrolyte.

Figure 6-15: After 48 hours testing with hydrogen and biogas.
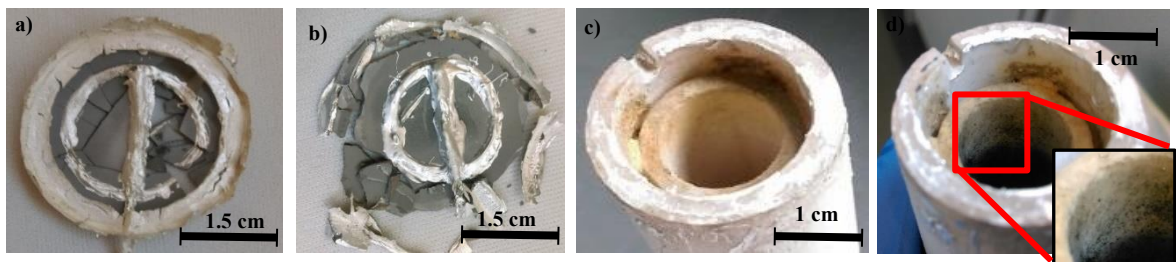
Figure 6-16: a) Ni/YSZ cell, b) Ni/ScCeSZ cell, c) Ni/ScCeSZ cell holder before test, and d) Ni/ScCeSZ cell holder after cell test.

6.3.1   Microstructural analysis (SEM-EDX)
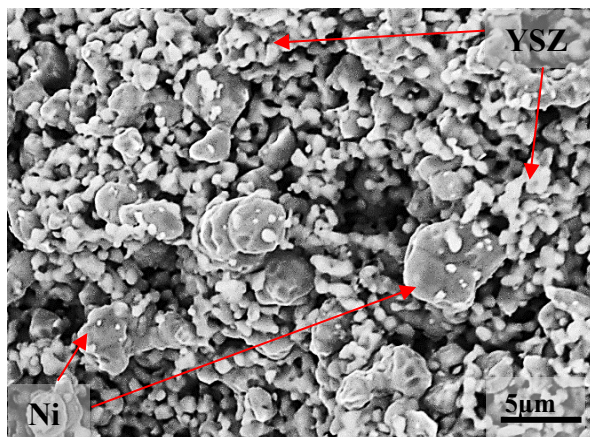
Figure 6-17: Anode substrate of Ni/YSZ after cell test. Coarse particles represents Ni while small circular particle represent YSZ.
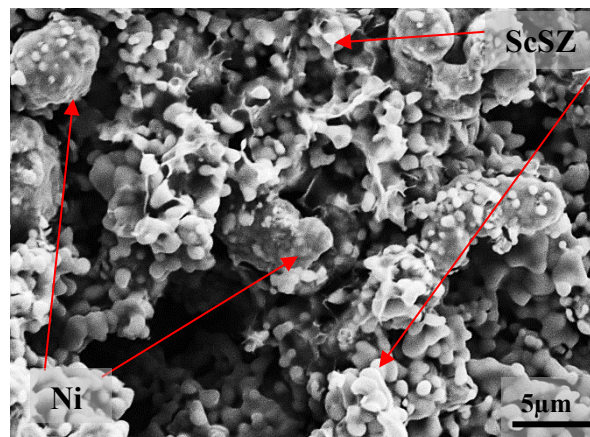
Figure 6-18: Anode substrate of Ni/ScCeSZ after cell test. Coarse particles represents Ni while small circular particle represent ScCeSZ.
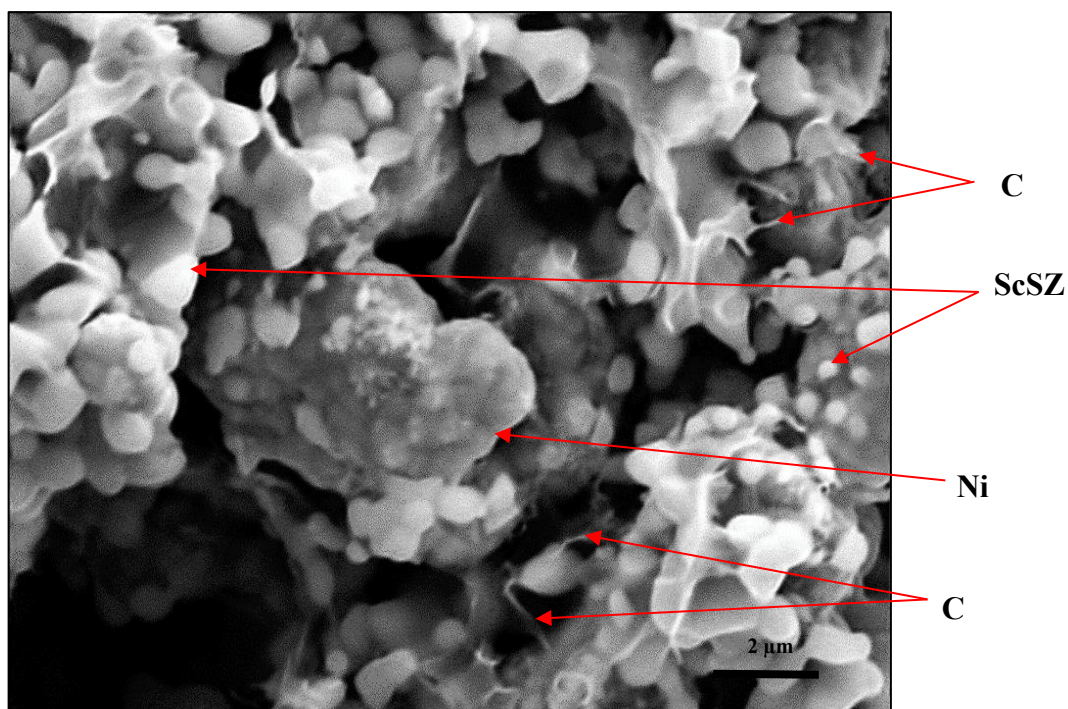
Figure 6-19: Ni/ScCeSZ at 10k magnification after 48 hours cell testing with hydrogen and biogas with carbon structure detected on anode surface. The sample coated with Pt prior to SEM.

To be able to detect carbon, the tested cells were coated with Pt prior to SEM observation. Figures 6-17 and 6-18 show the microstructure at the center of the anode substrate of Ni/YSZ and Ni/ScCeSZ cells after cell testing with 5.0k magnification using mixed mode of BSE and SE. The bright, smaller grains were the electrolyte materials while the darker, larger grains were Ni. Two differences that can be seen from the SEM images were the higher porosity volume and the growth structure on the Ni/ScCeSZ cells which can be seen in Figure 6-19 (enlarged image of Figure 6-18 at 10k magnification). The growth in Ni/ScCeSZ cells shows whisker-like structures with length of 0.5µm to 1µm. Along with the whiskers-like carbon structure, the larger surface area structure growth may originate from decomposed carbide. SEM images with higher magnification on the Ni/ScCeSZ sample are supplied in the Appendix IV.

Before elaborating the SEM-EDX result, a few points need to be addressed:

1) The samples coated with Pt to detect carbon structure (as in Figures 6-19, 6-18 and 6-19) cannot be used again to detect carbon using SEM-EDX function as Pt blocked all the signals below the Pt surface.

2) As anode is porous, quantification using SEM-EDX will not be accurate as the uneven structure will affect the electron signals.

3) The ability of SEM-EDX machine (Hitachi TM3030Plus) to detect carbon was confirmed by using a carbon tab and clean sample mount. The result shows high carbon peaks on carbon tab, but also with noise peaks at 2 on a clean sample mount. This observation is included in the Appendix IV.

4) SEM-EDX is a highly sensitive machine that can detect a small concentration of materials in the sample. Hence, small carbon contamination originates from the surrounding (fingerprints and dust) might gave some noise peak.

Considering points 2 to 4, SEM-EDX can represent only qualitative analysis. Surface scan analysis which shows carbon detection will be misleading because it is difficult to differentiate between noise peak and real peak of carbon. Line-scan function can still be used as it clearly indicates different intensity in the sample. Quantitative analysis carried out using temperature programme oxidation (TPO) on tested samples is a more accurate way to compare the amount of carbon, which will be discussed in Section 6.3.2.

EDX images in Figure 6-20 indicates no amount of carbon deposited on both cells near the anode functional layer area taken into account the background reading. The anode side that exposed more to fuel shows higher amount of carbon on both cells as in Figure 6-21. Slightly higher carbon peaks detected on Ni/ScCeSZ cells.
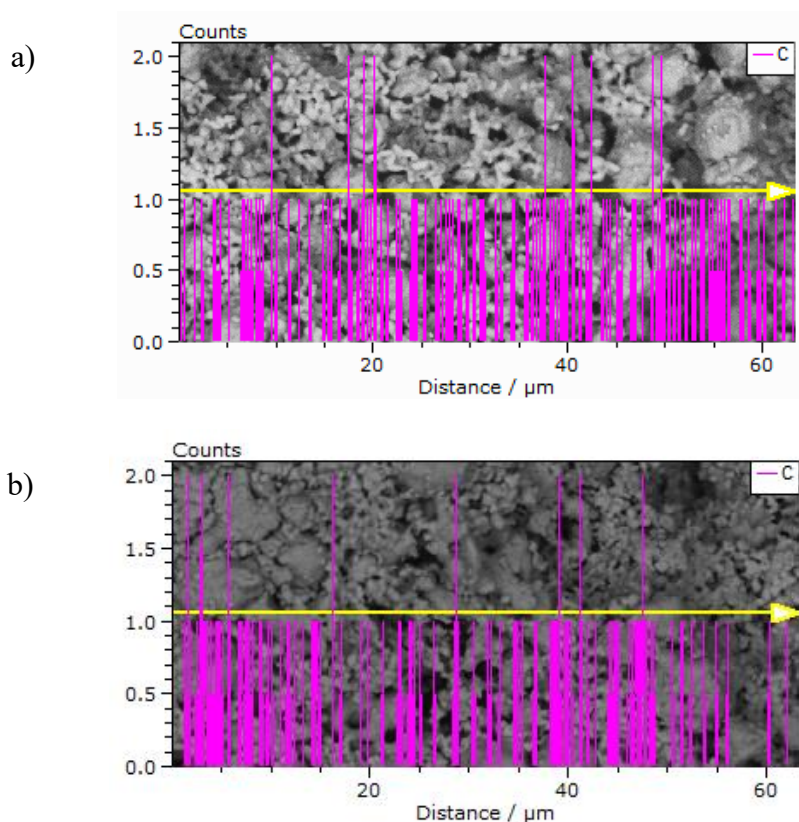
Figure 6-20: No carbon detected by SEM-EDX linescan analysis on a) Ni/YSZ and b) Ni/ScCeSZ near the anode functional layer area with using cross-sectional scan (with background/noise peak of 2 - refer appendix IV).**
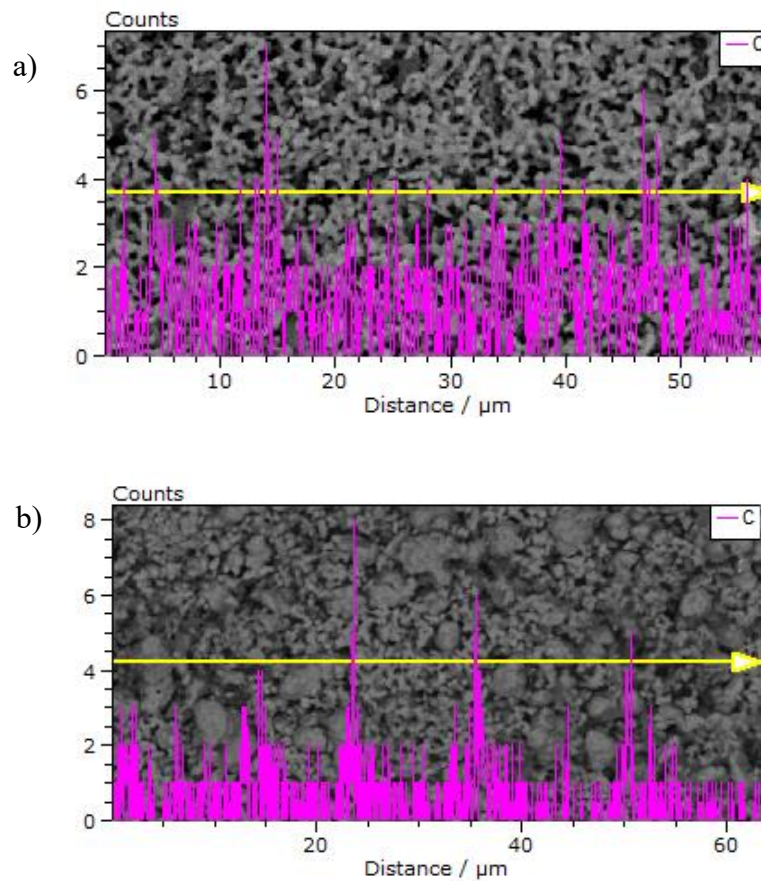
Figure 6-21: Higher amount of carbon detected on the anode surface facing the fuel of a) Ni/YSZ and b) Ni/ScCeSZ cell.

On Ni/YSZ cell, there were no clear carbon structure to be seen from the SEM even after coated with Pt, eventhough there are peaks detected using EDX (in uncoated sample). In the brief introduction to carbon growth in SOFC anodes from Chapter 2, it was explained that amorphous carbon can grow in different forms; films and filamentous. In Ni/YSZ, no specific carbon structure was visible which may indicate that amorphous carbon particles distributed on the Ni/YSZ surface, while in Ni/ScCeSZ, the whisker-like structure indicates the start of growth of carbon filaments [15]. It is assumed if the test was carried out for longer duration it would form carbon filament structures.

The growth of whisker-like structures on the Ni/ScCeSZ anodes was in agreement with the result from the post-test analysis on the tested Ni/ScCeSZ cells and Ni/ScCeSZ disc by Sumi et al. [15, 65]. While other researchers classify whisker-like structure as amorphous, Sumi et al suggest that the whisker-like filamentous structures were graphitic carbon in Ni/ScCeSZ; G-band (graphitic carbon) as opposed to D-band (amorphous carbon) detected by Raman spectroscopy. The Ni/ScCeSZ cells had a higher ratio of graphitic carbon compared to Ni/YSZ cells (92.4% vs 69.3%) as found by Sumi et al. [15]. This has been explained by Baker et al. [126]; filamentous carbon can have dual structure, graphitic at the skin and an amorphous core. Increases in electrochemical performance were reported previously with small amounts of graphitic carbon detected in the anode [15, 53, 54] as observed here in the Ni/ScCeSZ cells.

6.3.2   Temperature Programmed Oxidation (TPO)
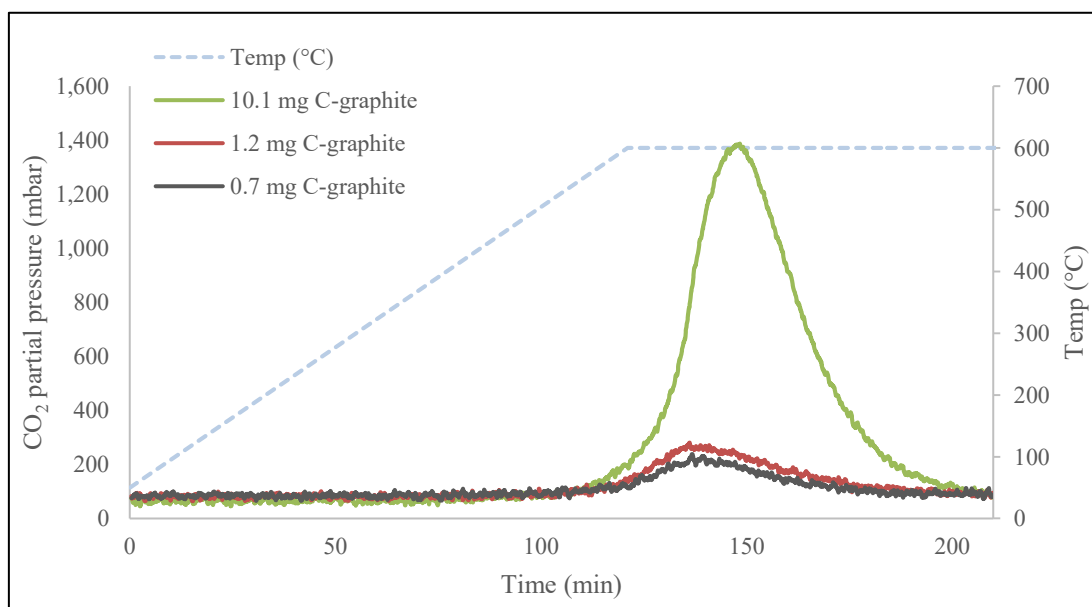
Figure 6-22: CO$_2$ peaks from TPO calibration of carbon graphite.

To quantify the amount of deposited carbon, temperature programmed oxidation (TPO) were carried out. TPO calibration using a known amount of carbon graphite was carried out prior to

actual sample to construct a calibration curve. Figure 6-22 represents the CO_2 peaks detected

by the mass spectrometer from the carbon graphite. Carbon graphite starts to oxidised at

520°C and complete the combustion at 600°C during the 1-hour dwelling stage. CO_2 peak

area used to construct a calibration curve, which follows a linear relationship with the amount

of carbon used. From the calibration curve, 1 mg of carbon correspond to 33.3 units of CO_2

peak area. The value obtained from the calibration curved was used as a factor to calculate the

quantity of carbon deposited in the tested cells. The calibration curve can be referred to

appendix

Carbon deposited in Ni/YSZ cells

From Figure 6-23, it was clear that the amount of CO_2 detected from the carbon burnt off

from Ni/YSZ cells were significantly lower than that of 0.7 mg graphitic carbon. Carbon on

tested Ni/YSZ samples started to burn off around 330-350°C with CO_2 peak at 450-500°C.

This temperature was lower than the burn-off temperature of the graphitic carbon powder. As

it is known that amorphous carbon oxidised at a lower temperature, hence this can deduce that

the type of carbon exists on Ni/YSZ cells was amorphous.
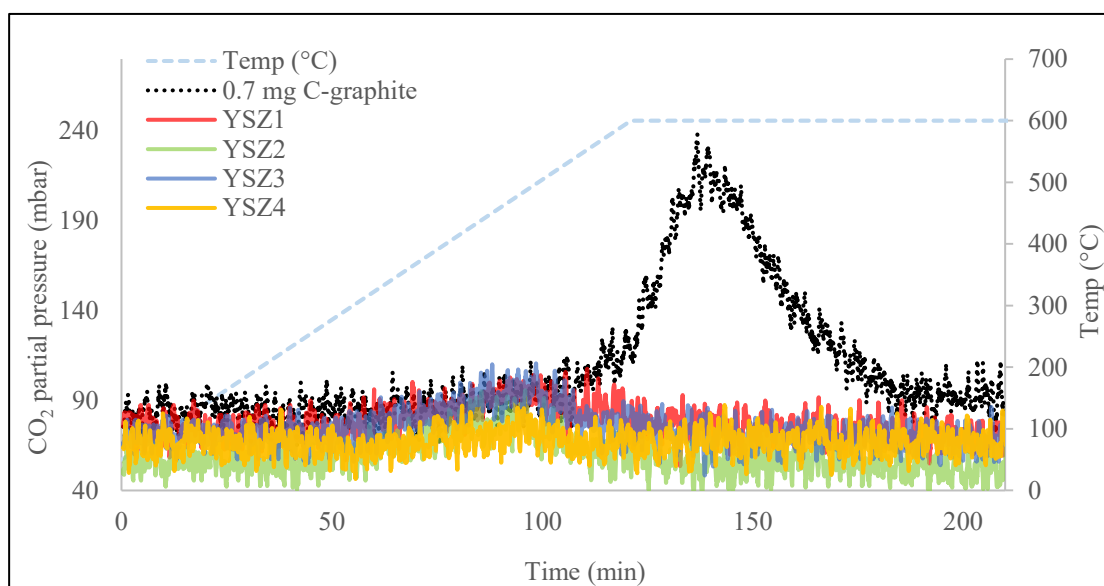
Figure 6-23: CO_2 peak from carbon burn off on Ni/YSZ cells with comparison to 0.7 mg of carbon graphite.
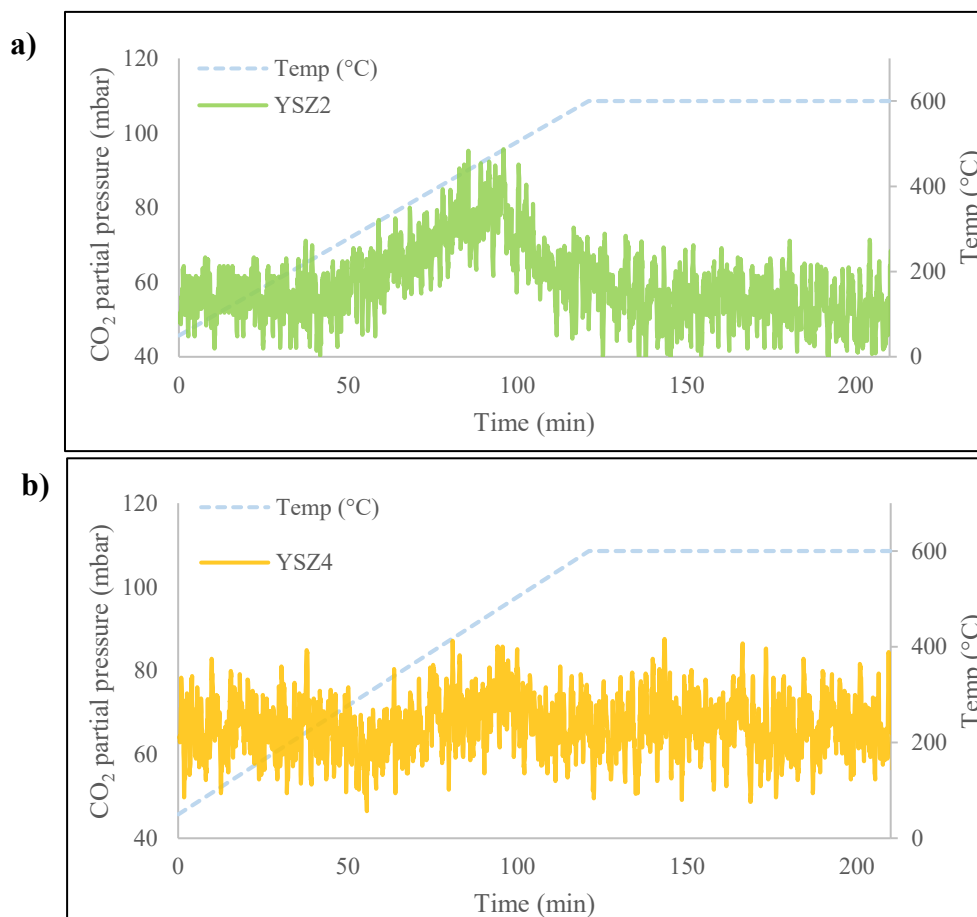
Figure 6-24: Highest and lowest CO$_2$ peaks on Ni/YSZ cells, a) YSZ2 (highest) and b) YSZ4 (lowest).

Figure 6-24a and b shows the highest and lowest CO$_2$ peaks from Ni/YSZ samples. Unlike

other samples, YSZ4 (Figure 6-24b) showed negligible CO$_2$ peak area. The slight difference

in amount of carbon deposited across the Ni/YSZ cells may cause by different batches of cell

fabrication. Although the same formulation and powder used, different cell batches inevitably

showed different homogeneity.

For carbon quantification, the same scale used as the plot in Figure 6-23. The units under the

CO$_2$ peaks for each sample were calculated and the exact amount of carbon deposited on each

sample was determined. With average sample weight of 0.202 gram, the amount of deposited

carbon on the samples was calculated as follow (based on YSZ01):

Carbon amount

CO_2 peak area/33.3 x 1mg = 30 units/33.3 units x 1mg = 0.09 mg C/sample.

0.09 mg C/ 202.00 mg catalyst *100 = 4.46 x 10^{-4} mg-C/ mg catalyst

Rate of carbon deposition

4.46 x 10^{-4} mg-C mg_{cat}^{-1}/ 24 hours = 1.86 x 10^{-5} mg-C mg_{cat}^{-1} h^{-1} or 1.86 x 10^{-3} mg-C g_{cat}^{-1} h^{-1}

Note that the carbon deposition rate calculated here is not the actual carbon deposition rate, but the net rate of the actual carbon deposited less the amount of carbon that has been oxidised to CO_2 or CO during SOFC electrochemical reaction. The rate calculated can be used as a future guideline to estimate the lifetime of the SOFC anode.

The amount of carbon detected on Ni/YSZ presented by Table 6-3 shows that only small amount of carbon deposited on Ni/YSZ cells after 24 hours test in biogas with an average of 5.68 x 10^{-4} mg-C/mg_{cat}. Similar observation was found in Troskialina [64] work which used similar testing condition. Troskialina [64] also found almost negligible amount of carbon deposited on Ni/YSZ cell despite of the 80% drop of performance in their work.

Comparing this value to the amount of carbon detected by Somalu et al. [14] and Eguji et al. [71] (ratio presented in %) in Section 2.2.2, the amount of carbon deposited on the Ni/YSZ anode cermet in this work was extremely low. The carbon deposited on Ni/YSZ cell in Ref [14] after 1 hour test was 0.32 % (mg C/mg cat), while in this work, the highest amount of carbon deposited on Ni/YSZ cell was 0.094%. As Somalu et al. [14] and Eguji et al. [71] tested the SOFC cermet in a quartz tube chamber (and not in SOFC mode), there were no

electrochemical reaction that oxidise the deposited carbon. Hence, more carbon found in their observation.

Table 6-3: Amount of carbon deposited on Ni/YSZ and Ni/ScCeSZ tested cells after 24 hours test in biogas.

	Amount of carbon deposited			Rate of carbon deposition $(mg\text{-}C/g_{cat}\ h)$
	per sample (mg)	**per unit catalyst $(mg\text{-}C/mg_{cat})$**	**per unit catalyst $(mg\text{-}C/mg_{cat})$ x 100%**	
YSZ1	0.090	4.46×10^{-4}	0.045	0.019
YSZ2	0.189	9.36×10^{-4}	0.094	0.039
YSZ3	0.150	7.43×10^{-4}	0.073	0.031
YSZ4	0.030	1.49×10^{-4}	0.015	0.006
ScSZ1	0.600	2.97×10^{-3}	0.297	0.124
ScSZ2	0.525	2.60×10^{-3}	0.260	0.108
ScSZ3	0.300	1.49×10^{-3}	0.149	0.062

Carbon deposited in Ni/ScCeSZ cells

Figure 6-25 shows that CO_2 peaks from Ni/ScCeSZ samples were detected at a higher temperature (600°C), similar to the burn off temperature of graphitic carbon. Hence, this is evidence that graphitic carbon existed in Ni/ScCeSZ. Figure 6-26 shows that there were two peaks detected in SC01. The first CO_2 peak was approximately at 400°C which was similar with the amorphous carbon peak detected from Ni/YSZ cells, and another one has peaks at 600°C which was where the graphitic carbon burnt off. SC2 and SC3 shows only one peak at 600°C. SC04 was slightly re-oxidise during cooling down as the supply of H_2 was interrupted. Hence, the result is not reported here as some of the carbon on SC4 sample has been converted to CO_2.

Opposite to our expectation based on sudden drop of performance in electrochemical test, the amount of carbon deposited on Ni/ScCeSZ samples were higher than that on Ni/YSZ cells as clearly shown by Figures 6-23, 6-25 and 6-27. Based on Table 6-3, the average amount of
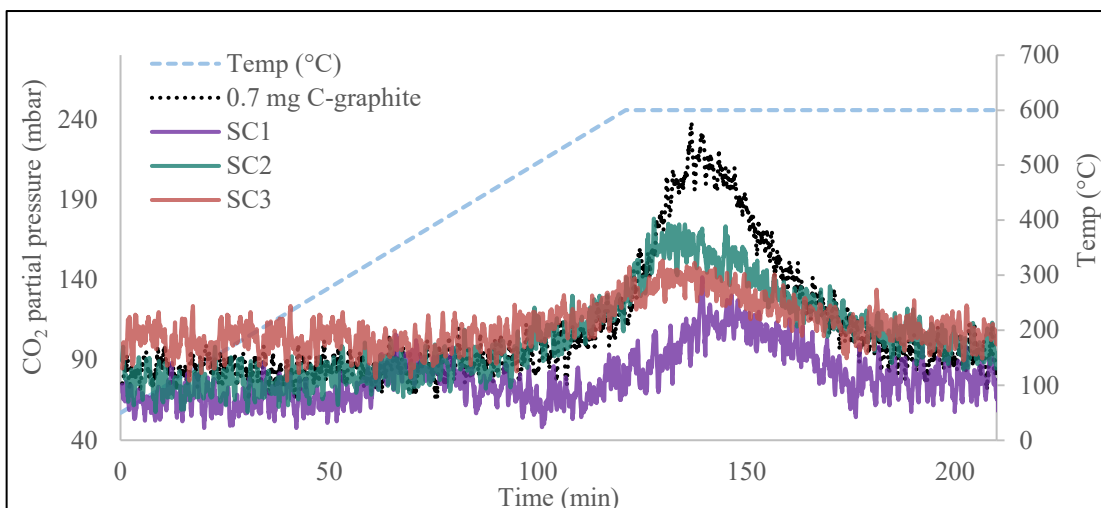
Figure 6-25: CO₂ peaks from Ni/ScCeSZ cells with comparison to 0.7 mg of carbon graphite.
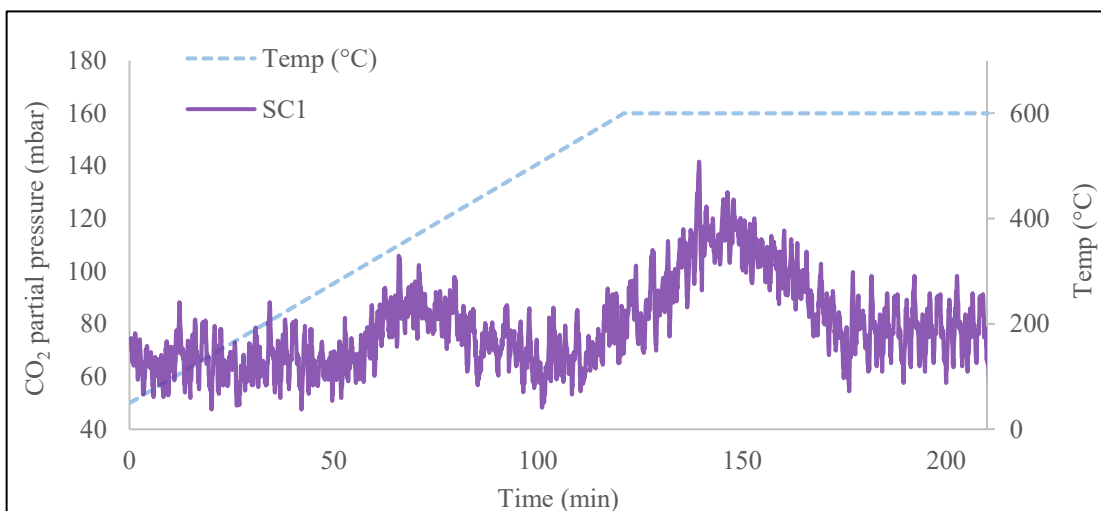
Figure 6-26: Two CO₂ peaks from Ni/ScCeSZ (SC1) sample from amorphous and graphitic carbon.
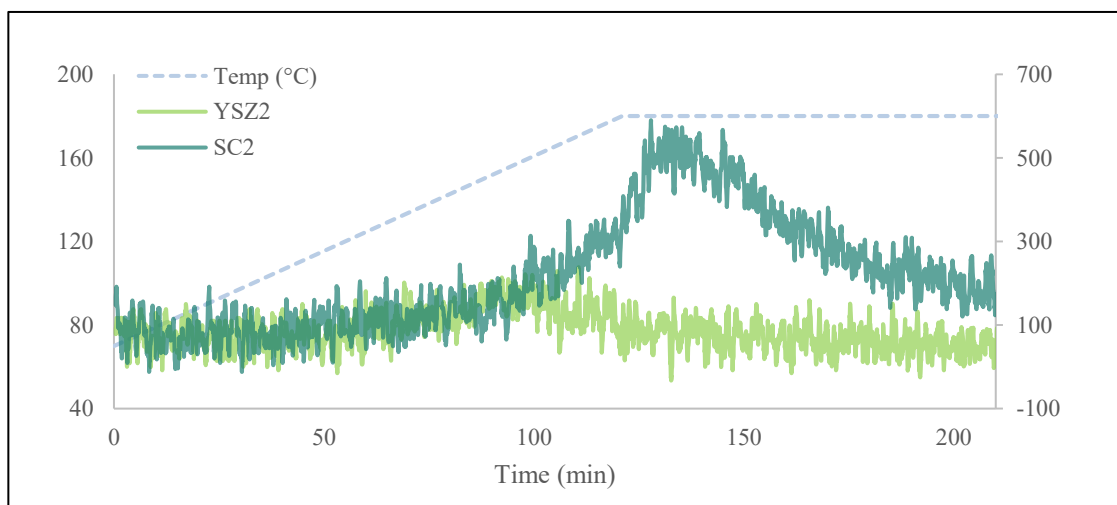
Figure 6-27: Comparison of CO₂ peaks from Ni/YSZ (YSZ2) and Ni/ScCeSZ (SC2).

carbon deposited on Ni/ScCeSZ samples were 2.35 x10^{-3} mg-C/mg$_{cat}$ opposed to the average amount of carbon on Ni/YSZ which was only 5.68 x10^{-4} mg-C/mg$_{cat}$. The highest amount of carbon deposited on Ni/ScCeSZ cell was 2.97 x 10^{-3} mg-C/mg$_{cat}$ after the 24 hours test in dry biogas with carbon deposition rate of 1.24 x 10^{-1} mg-C g$_{cat}^{-1}$ h^{-1}. Slightly different amount of carbon deposited across the Ni/ScCeSZ cells presented in Table 6-3 may originated from two different batch of 10ScCeSZ powder used.

The higher amount of carbon deposited on Ni/ScCeSZ cell compared to Ni/YSZ cell found in this work was in agreement with the observation by Ke et al. [72] and Sumi et al [20, 72]. Both works showed at intermediate operating temperature (800-850°C), more carbon deposited on Ni/ScCeSZ cells than that of Ni/YSZ and vice versa at higher temperature (900°C and above). Despite of higher amount of carbon detected in form of graphitic carbon, the electrochemical performance of Ni/ScCeSZ cells were higher.

6.4 Catalytic activity test

After the biogas test, the performance in hydrogen restored to 92% of the initial performance in Ni/YSZ and 83% for Ni/ScCeSZ cells. The restoration of the performance and the result from carbon quantification led to the test described here. This short catalytic reaction test was carried out to understand the response of the materials in terms of catalytic reaction by evaluating the gas purged from the outlet stream using a mass spectrometer. This test will not represent the overall reaction on the SOFC mode, as there were no electrochemical reaction in the quartz chamber, but will explain the catalytic activity on the anode surface.

6.4.1 Outlet gases evaluation

Figure 6-28a shows that the amount of hydrogen converted from simulated biogas in Ni/ScCeSZ pellets was higher than generated from a Ni/YSZ pellet. The identification of the species was by the molecular weight. Thus, for a plot of two different species with the same molecular weight would overlap, such as carbon monoxide and nitrogen. This explain the initally high reading of carbon monoxide as in Figure 6-28b. The measurements were started at the same time as the introduction of the simulated biogas. The delay in reading was caused by the lagging of the gas outlet to the mass spectrometer machine. Overall, Ni/ScCeSZ material show lower amount of reactant and higher amount of product gases in the outlet stream compared to Ni/YSZ. It shows that the catalytic activity of Ni/ScCeSZ was better; i.e a higher conversion of the reactant to product was achieved.
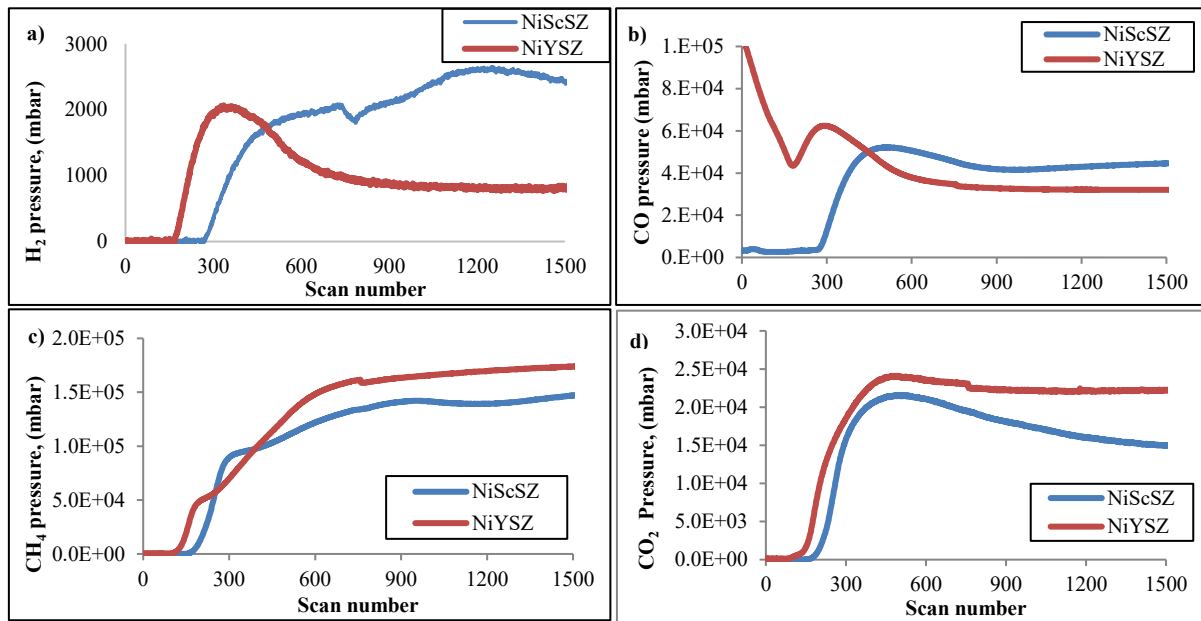
Figure 6-28: Individual partial pressures of exhaust gas from the catalytic reaction chamber, when Ni/YSZ and Ni/ScCeSZ exposed to biogas at 750°C.

6.4.2   SEM Microstructure analysis

After 1 hour exposure to biogas, Ni/YSZ cells remained intact while there was a deterioration of the Ni/ScCeSZ pellet. In 3 hours exposure to biogas, Ni/ScCeSZ pellet was completely damaged as in Figure 6-29. The Ni/YSZ pellet remained intact with small cracks at the edge while the Ni/ScCeSZ pellet size was increased to 1.39 cm from originally 1cm.
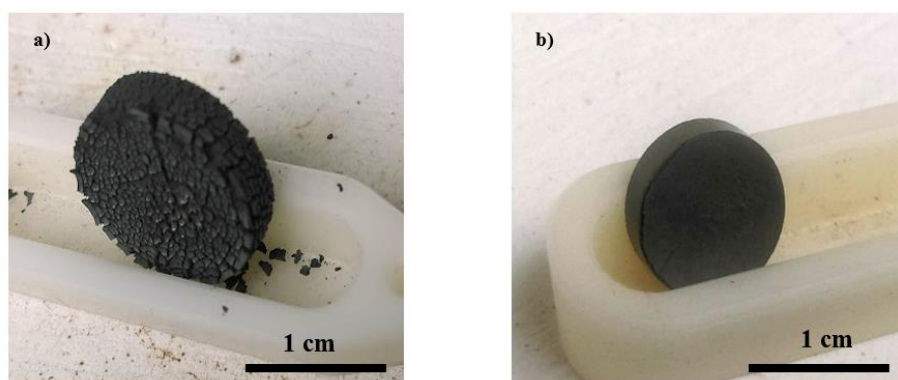
Figure 6-29: Pellets after 3 hours exposure to biogas a) Ni/ScCeSZ and b) Ni/YSZ.

The morphologies of carbon growth on the Ni/YSZ and Ni/ScCeSZ cells were distinct as shown in Figures 6-30 and 6-31. The Ni surface on Ni/YSZ materials shows rough, coral-like structures after exposure which may have been caused by the chemisorption or physical absorption of amorphous carbon. The excessive filamentous carbon growth caused stress and fracture in the Ni/ScCeSZ cells while increase in size indicates there was dissolution of carbon atoms into the metal structure causing volume expansion as described by Boldrin et al. [24]. All these effects were not observed in the SOFC as carbon might be electrochemically oxidised near the TPB area as found by Sumi et al [65]. This severe condition also caused by the excess of biogas fuel as the same flowrate was used, but the anode pellet size was three times smaller than the single SOFC cells.
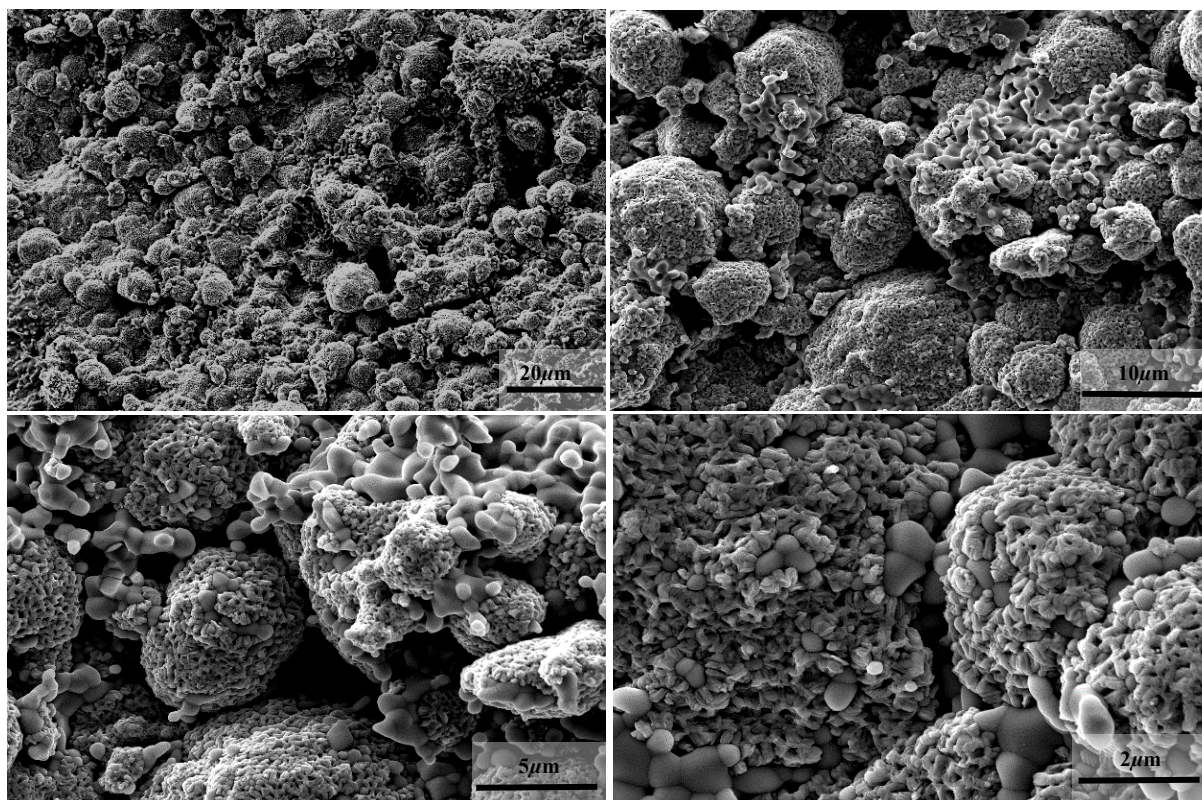
Figure 6-30: SEM on Ni/YSZ disc after 3 hours in simulated biogas at different magnification.
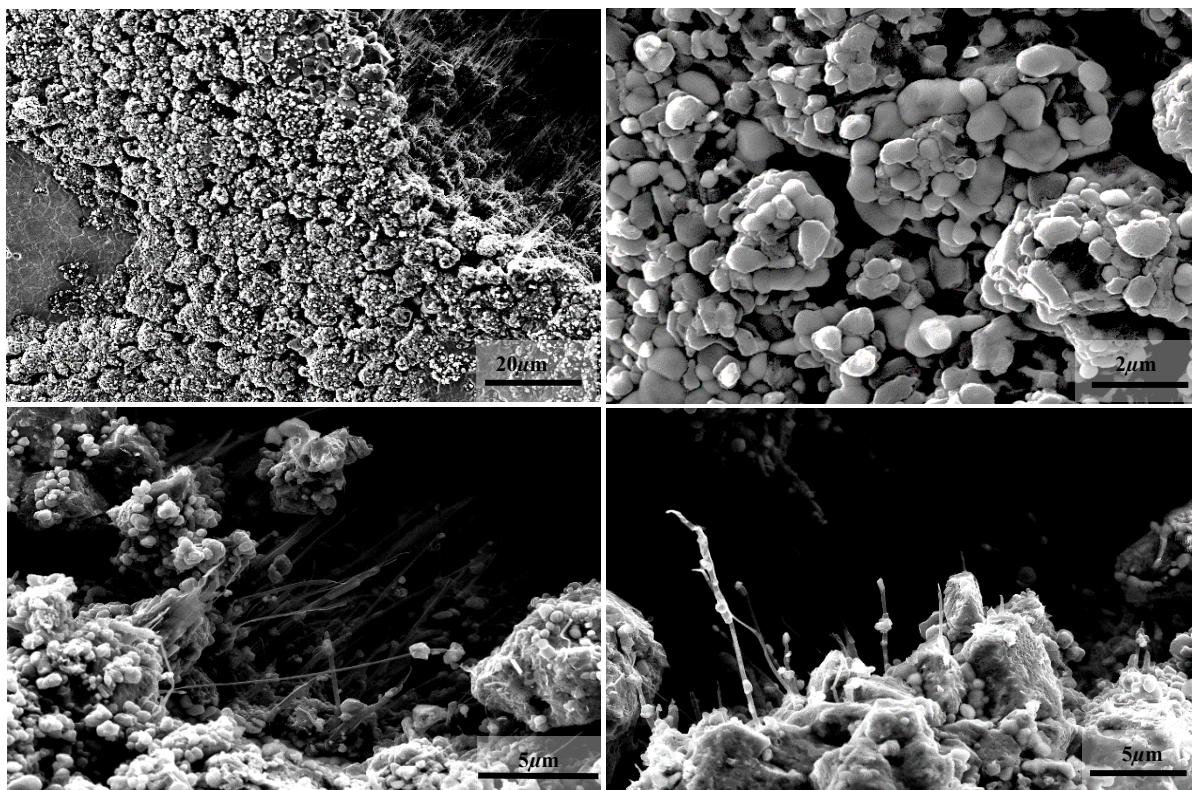
Figure 6-31: SEM on Ni/ScCeSZ disc after 3 hours in biogas with different magnification.

6.5 Additional discussion

The performance in both cells reduced right after the fuel swap despite having more reactant available with the same flow rate of biogas compared to hydrogen. In hydrogen, the fuel was readily available for the electrochemical reaction while in biogas, dry reforming reaction (Eq. 1-7) needed to take place before the fuel cell electrochemical reaction. Twofold amount of reactant will only be produced with 100% conversion of the biogas to H_2 and CO via dry reforming reaction, without any other reaction takes place. However, methane cracking might have taken place based on the carbon particles found on the cell holder and a small amount of carbon detected on the cells via SEM-EDX analysis. Assuming the catalytic activity in the anode was high enough, some of the carbon deposited had been electrochemically oxidised to CO and CO_2.

Furthermore, the assumption made for internal reforming was that the reforming reaction and all other side-reactions occurred at the anode substrate surface, while the electrochemical reaction occurred at the interface of electrolyte and anode functional layer; i.e. the TPB-region. However, if the reforming reaction also took place near the TPB, or the TPB sites originally reached out into the anode substrate region, less catalytic area was available for the electrochemical reaction. This might be the case, as only a small amount of carbon detected on the cell while visible carbon can be seen on the cell holder. For carbon to be electrochemically oxidized, the TPB length might originally extended to the anode substrate region.

The average drop of maximum power density (PD_{max}) from hydrogen to biogas was 79.7% in Ni/YSZ cells. Initially the significant drop of performance in Ni/YSZ cells with the fuel switch was suspected from carbon build up which blocked the reaction site for electrochemical

reaction. From visual observation of the tested cells, there were no obvious carbon deposition on the anode surface. The line-scan analysis (SEM-EDX) on the anode cross-section shows very small amount of carbon exists which was confirmed by the TPO. From the TPO, compared to Ni/ScCeSZ, small amount of amorphous carbon deposited on Ni/YSZ cells. This was in agreement with the restoration of the initial H_2 performance in the post-biogas analysis that showed that any effect of carbon build-up on the Ni/YSZ cells was limited. The additional catalytic activity test was evidence that the performance drop within the Ni/YSZ cells performance were inclined to the limitation of the catalytic ability to convert the biogas into H_2 and CO rather than the carbon build-up problem. The drop of OCV reflected the lower amount of reactant species because of this factor as elaborated in Section 6.4.1.

The average drop in PDmax in Ni/ScCeSZ cells (41.3%) with the fuel switch was smaller compared to Ni/YSZ cells. From TPO, the amount of carbon deposited in Ni/ScCeSZ was higher than that on Ni/YSZ cell at different carbon burn-off temperature. Similarity of carbon burn off temperature and filamentous carbon structure found in the microstructure deduced that the type of carbon formed on Ni/ScCeSZ was graphitic. Based on the argument in Section 6.2.5, the small amount of graphitic carbon build-up did not interfere with the electrochemical catalytic activity in the Ni/ScCeSZ. As mentioned briefly in Section 2.2.1, the carbon filaments may have an amorphous core, but surrounded by graphitic skin [75] in which enhance the metal network, hence enhancing the electrical conductivity.

Based on previous literature covered on Section 2.2.2, the different amount of carbon deposition and morphology was based on:

i – the crystalline structure of the oxides; that Ni/ScCeSZ cells promote filamentous carbon that has high graphitic carbon content, which has less blocking effect than amorphous carbon

ii - the solubility of Ni in ScSZ lattice was higher as suggested by Sumi et al. [20, 65, 72], and

iii – the SOFC test temperature, in which in IT-SOFC, higher amount of carbon formed on Ni/ScCeSZ cell than that on Ni/YSZ [20, 65, 72].

To conclude, Ni/ScCeSZ anodes shown better reforming activity for operation and less affected by the fuel switch as reflected by less performance drop compared to Ni/YSZ cell. Several factors caused the drop of performance in biogas for both cells; low reforming reaction on the anode surface and less electrochemical activity surface area available as some of the anode surface already used for the reforming reaction. Different carbon morphologies formed on the cells; with a mixture of filamentous (graphitic) and amorphous carbon found on Ni/ScCeSZ cells while only amorphous carbon formed on Ni/YSZ cells. Graphitic carbon in Ni/ScCeSZ cells may enhance the performance by providing more network in the anode. However, excessive graphitic carbon build-up will eventually lead to cell damage as shown by the sample in catalytic activity test.

CHAPTER 7: ELECTROCHEMICAL PERFORMANCE OF TIN DOPED NI/10SCCESZ IN HYDROGEN AND BIOGAS

7.1 Introduction

This chapter demonstrate how addition of tin improves the stability of the Ni/ScCeSZ and achieves better carbon tolerance in simulated biogas operation. This work is a continuation from previous work in the same research group which shows positive remarks of Sn addition using infiltration method (pipette drop) in commercial Ni/YSZ anode supported cells [50, 56, 64]. Brief review on surface alloying can be referred to Section 2.2.3. To date, no other work had been reported using tin doped Ni/ScCeSZ cells. Hence, it is interesting to see the electrochemical and carbon deposition behaviour under hydrogen and biogas for the Sn-Ni/ScCeSZ cells. The Sn-doped cells were characterised in hydrogen using Setup A; 21 ml/minute hydrogen and 7 ml/minute helium at 750°C. The tests were carried out at 750°C with dry simulated biogas at a flowrate of 14 ml/minute methane (CH_4), 7 ml/minute carbon dioxide (CO_2) and 7 ml/minute helium (He); which was the same volumetric flowrate used in setup A for hydrogen. The comparison was made using the OCV, polarisation curve, maximum power densities, constant current potential, electrochemical impedance spectroscopy and carbon deposition using SEM-EDX. The first part of this chapter reports the altered manufacturing steps used, while the second part reports the electrochemical results and the third part reveals the carbon and Sn distribution in the cell.

7.2 Tin doped Ni/ScCeSZ cell preparation

The fabrication of tin doped cells followed the previous multilayer aqueous tape casting method with some adjustment in the mixing stage. Tin chloride dihydrate ($SnCl_2.2H_2O$) was added to

the anode substrate layer while other layers were prepared following the previous manufacturing steps to produce standard SOFC cells. Discussion from this point onwards on manufacturing will focus on the anode substrate tape casting preparation.

Introducing $SnCl_2.2H_2O$ 0into the tape slurry during the first or second ball milling stage led to a very thick slurry, which cracked when completely dried, as shown in Figure 7-2. Addition of more plasticiser and binder may help to reduce the effect, but minimal changes in the composition were desired to compare the doped cells with the standard cells at the same parameters. The successful method of doping through mixing was by pre-dispersing $SnCl_2.2H_20$ (1 wt% of Sn:Ni) powders with one-hour ball milling at 120 rpm with water and dispersant. This pre-mixing was also beneficial as it may aid the adherence of Sn particles to the nickel surface, and not to the 10ScCeSZ surface. The amount of 1 wt% tin added was the optimum amount of tin used in previous work [64, 127]. As in previous cell fabrication in this thesis, the 10Sc1CeSZ powders (DKKK) were also pre-calcined at 900°C for the anode substrate to adjust the sintering behaviour and minimise the cell curvature. In this formulation, the pore former was substituted with same amount (wt%) of plasticisers and binders to the Ni/ScCeSZ cell sample TSC01 and TSC02 since an attempt at using pore formers resulted in a highly viscous slurry. However, sample TSC003 was successfully manufactured using 1 wt% of tapioca starch as the pore former. The multilayer tape casting process and full cell manufacturing followed the same procedure elaborated in Chapter 3 and the full cell manufacturing for tin doped cells is summarised in Figure 7.1.

Although the tape had been dried at 30°C, the moisture content was still high. Hence, further drying was carried out at 100°C with a dead weight placed on top carried out for 1 hour prior

to co-sintering. The role of the weight was to ensure the cell stayed flat during this stage. The cell was sandwiched between two pieces of 10 gram alumina plates and co-sintered at 1300°C following the heating profile in Figure 3-8. Figure 7-3 shows the sintered half-cells without the pre-drying at 100°C, sintering with too much weight on top, co-sintering with no weight, and a flat cell with the 10 gram weight placed on top and pre-dried at 100°C.
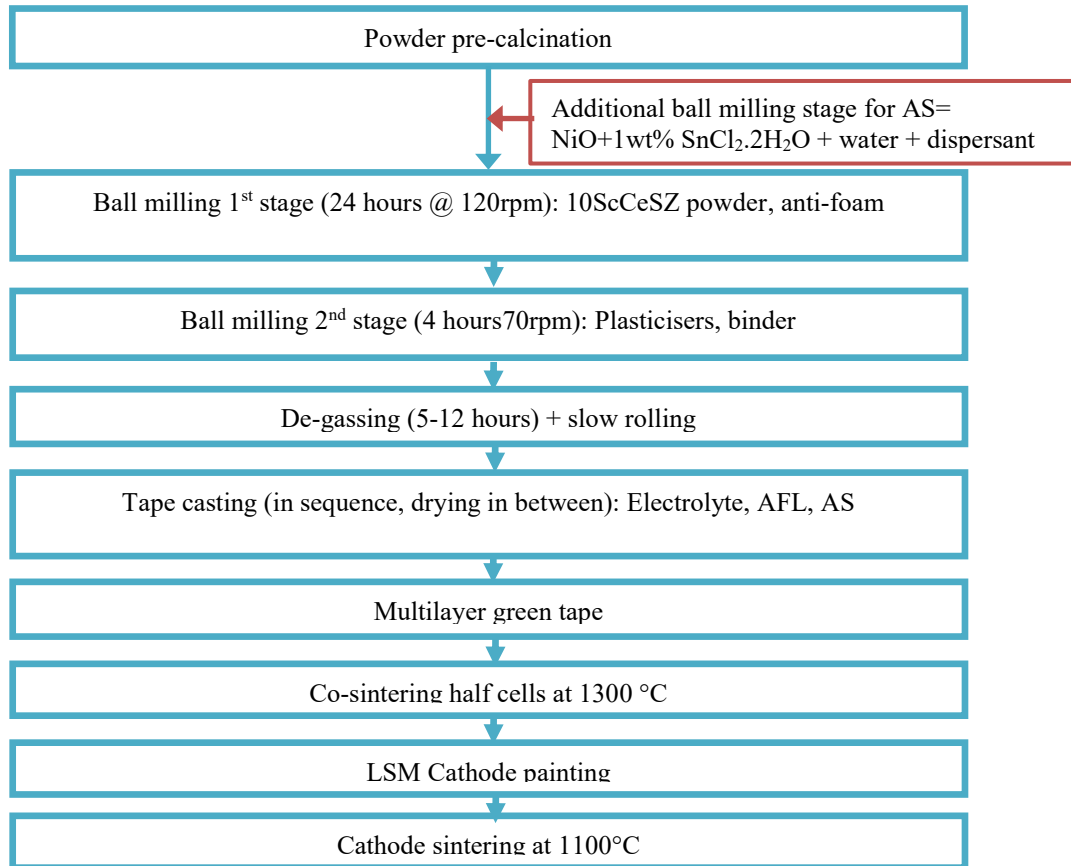
Figure 7-1: SOFC Full cell manufacturing with additional Sn as dopant.
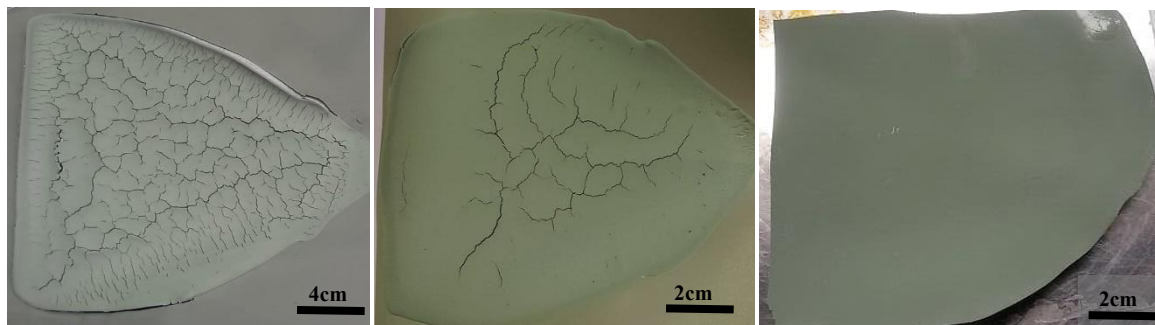
Figure 7-2: Ni/ScCeSZ green tape with blend in SnCl₂.2H₂O with different addition stage; a) after the first ball milling, b) after the second ball milling, c) pre-mix with NiO before mixing with 10ScCeSZ powder.
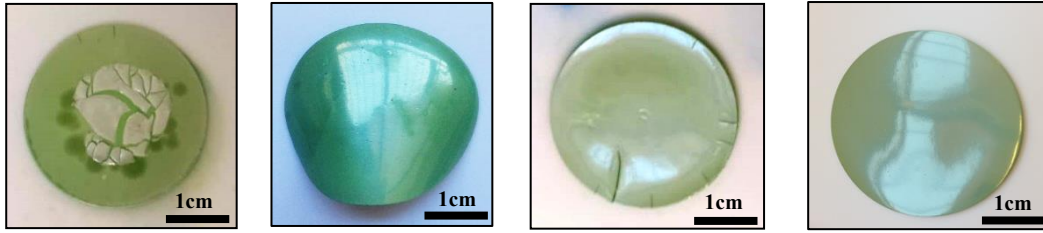
Figure 7-3: Tin doped Ni/ScCeSZ after co-sintering with, a) no pre-drying, b) no weight, c) 20g weight, d) 10g weight.
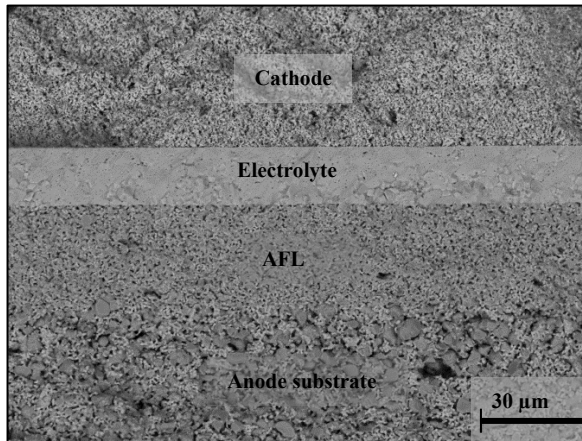
Figure 7-4: Cross section image of Sn-Ni/ScCeSZ. **Figure 7-5: Sn-Ni/ScCeSZ AS before cell test.**
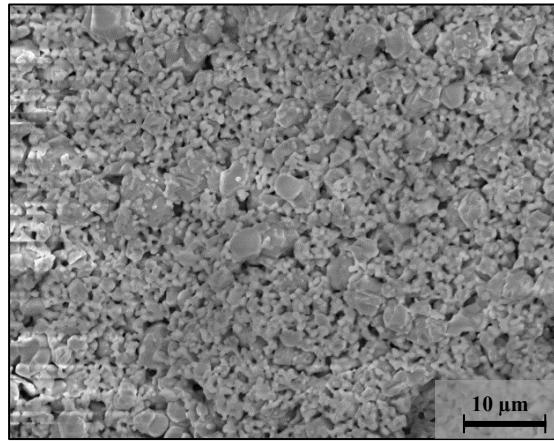
After optimisation, the Sn addition gave positive effect on cell manufacturing. The cells were flat with less curvature than Ni/ScCeSZ standard cell, which indicated that the co-sintering behaviour was influenced (via the coefficient of thermal expansion or CTE) by the introduction of the new dopant material. Figure 7-4 shows the microstructure of the Sn-Ni/ScCeSZ cells with dense electrolyte and porous anode substrate. Assuming the electrolyte layer sintering behaviour remained unchanged, the anode support layer sintered less; which les to less shrinkage of the half-cells, which also made the cell porous even with no additional pore former. It also shows that as less shrinkage was experienced by the whole cell, the electrolyte layer was slightly thicker; 20µm instead of 15µm. In contrast, Singh et al [128] reported that introduction of Sn led to higher shrinkage than with the undoped cells. The interaction of Sn to YSZ and ScCeSZ may be different, hence a different observation in shrinkage or the CTE.

7.3 Electrochemical performance

The Sn-doped cells performance will be compared to standard Ni/ScCeSZ cells. The overview of the cells used are presented in Table 7-1. Comparison with Ni/YSZ cells only made at the end of the chapter, comparing the overall behaviour between the cells with different materials.

Table 7-1: Overview of anode supported cells with different materials used.

Cell Identity	Material	Pore former
TSC01 and TSC02	Sn-Ni/ScCeSZ	Replaced with equal wt% organics (3wt%)
TSC03	Sn-Ni/ScCeSZ	1 wt% tapioca starch + 2wt% extra organics
SC04	Ni/ScCeSZ	Replaced with equal wt% organics (3wt%)
SC01, SC02 and SC03	Ni/ScCeSZ	3 wt% of tapioca starch
YSZ01, YSZ02, YSZ03, YSZ04	Ni/YSZ	3 wt% of tapioca starch

7.3.1   Open Circuit Voltage (OCV)

The OCV in hydrogen was stabilised at 1.00 V after 80 minutes of hydrogen introduction, and gradually dropped to 0.99 V during 24 hours of operation. Opposed to the result in Chapter 6, the OCV value after the fuel swap was higher than generated in hydrogen; 1.03 V. This result was consistent within all the cells tested shown by Figure 7-6. The increase of OCV was also observed in Sn-Ni/YSZ cells reported previously [50, 127, 128].

The increase of Gibbs free energy in the mixture of CO and H_2 fuel affected the OCV; which was not observed in the undoped Ni/ScCeSZ and Ni/YSZ cells. The Gibbs free energy for hydrogen and carbon monoxide obtained at 750°C were -191.457 kJ/mol and -193.549 kJ/mol [11], respectively which give the OCV value of 1.00V. The calculated OCV value were lower than obtained maybe due to difference in actual Gibbs energy value used.
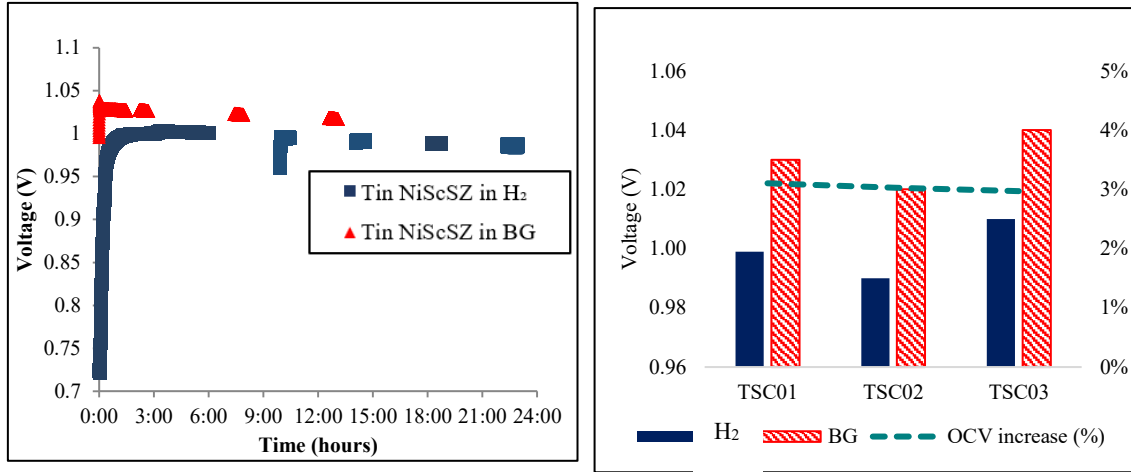
Figure 7-6: OCV under hydrogen and biogas (TSC01).

Figure 7-7: OCV increase with hydrogen to biogas fuel swap.

In addition the effect of higher Gibbs free energy, as the increase were not observed previously in Chapter 6, it is speculated that a higher amount of reactant available in response to better catalytic activity on the anode surface played a role.

7.3.2   *i*-V and Maximum power density curve

7.3.2.1   In hydrogen

Referring to Figure 7-8 and Figure 7-9, the highest current density (CDmax) and maximum power density (PDmax) obtained with the Sn-Sn-Ni/ScCeSZ (TSC02) was 0.783 A/cm^2 and 0.311 W/cm^2 respectively; which were higher than the undoped Ni/ScCeSZ cells with no pore former (SC04). The previous chapter showed the performance by undoped Ni/ScCeSZ cells with a porosity volume of 39% having a maximum power density ranging from 0.33 W/cm^2 to 0.44 W/cm^2. The absence of pore formers in the Sn-Ni/ScCeSZ cells led to reduced porosity which is speculated to cause a higher resistance for the fuel to diffuse through the anode substrate. Hence, comparison with Ni/ScCeSZ manufactured without pore former addition (SC04) will be made from this point onwards. All three Sn-Ni/ScCeSZ cells had better performance compared to the SC04 which had CDmax and PDmax of 0.608 A/cm^2 and 0.245 W/cm^2 respectively. In addition, comparing the performance at 6-hours and 22-hours *i*-V

169

measurements from Figure 7-8 and 7-9, Sn-Ni/ScCeSZ cells show less degradation compared the SC04 cells. However, if compared to other undoped Ni/ScCeSZ cells(refer to Figure 7-12), degradation within the initial hydrogen test was higher in the Sn-Ni/ScCeSZ cells.
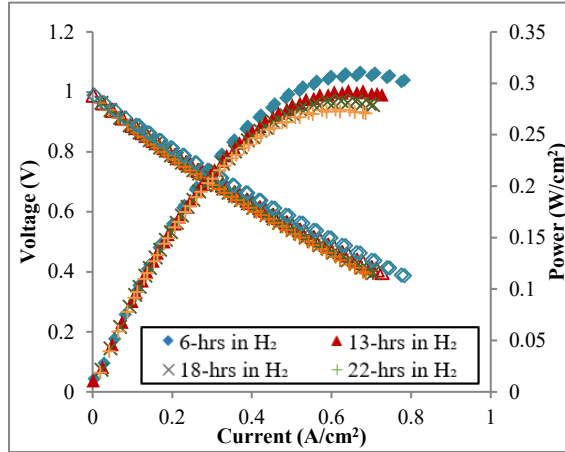
Figure 7-8: *i*V-PV curve of Sn-Ni/ScCeSZ in hydrogen (TSC02).
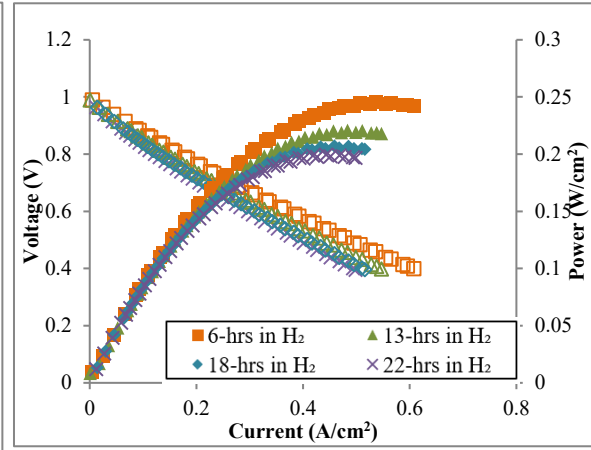
Figure 7-9: *i*V-PV curve of undoped Ni/ScCeSZ cell in hydrogen (SC04).

Table 7-2: Summary of OCV, current density and maximum power density for Sn-Ni/ScCeSZ in hydrogen and biogas

	OCV (V)		PD$_{max}$ (W/cm^2)				CD$_{max}$ (A/cm^2)		CD$_{0.7V}$ (A/cm^2)	
	H$_2$	BG	H$_2$ max	H$_2$ last	BG	Post BG	H$_2$	BG	H$_2$	BG
TSC01	0.999	1.04	0.277	0.245	0.228	0.226	0.687	0.574	0.275	0.200
TSC02	0.99	1.02	0.311	0.271	0.253	0.250	0.783	0.646	0.320	0.240
TSC03	1.01	1.04	0.404	0.350	0.314	0.254	1.014	0.802	0.34	0.280
SC04-0PF**	1.00	0.93	0.245	0.197	0.121	0.170	0.608	0.289	0.280	0.100

As no other work was found that looked into Sn-Ni/ScCeSZ cells, the closest comparison of performance in hydrogen could only be made with results on Sn-Ni/YSZ cells. Recent work reported by Farrell et. al [80] with Sn-Ni/YSZ cells showed power densities obtained were similar to the undoped Ni/YSZ cells in hydrogen operation; which was also observed by Troskialina [64] and Singh et al [127]. Both found that beyond the optimum Sn addition amount of 1wt% Sn, the electrochemical performance under hydrogen was observed to be

lower due to an increase of polarisation. In addition, Nikolla et al [79] found lower electronic

conductivity with a higher amount of Sn addition as a separate Sn oxide phase was formed.

Increasing the porosity content on the Sn-Ni/ScCeSZ with 1 wt% pore former led to

increasing performance with a maximum power density of 0.404 W/cm^2 in TSC03 as shown

by Table 7-1 and Figure 7-12. This value matched the performance of SC02 (Ni/ScCeSZ cells

with 39% porosity volume) which had the lowest electrochemical performance obtained with

Ni/ScCeSZ cells.

7.3.2.2   In simulated dry biogas

The maximum power density obtained directly after swapping to biogas in TSC02 was

0.253 W/cm^2 as depicted in Figure 7-10. This shows only a 0.018 W/cm^2 drop (7.4%)

compared to the last measurement when tested in hydrogen (0.271W/cm^2). There was also an

influence of the existing degradation of the cells as shown in Figure 7-8. If the same

consequent drop is assumed from the previous run (3.4%), the net percentage of drop by the

effect of swapping to biogas was only 4.0%. The drop with the fuel swap was significantly

lower than the Ni/YSZ cells and undoped Ni/ScCeSZ cells reported previously as summarised

by Figure 7-12 and Figure 7-13. The highest performance in biogas was shown in the Sn-

Ni/ScCeSZ cells (Figure 7-13). Note that TSC03 had a higher amount of porosity compared

to the other two Sn-Ni/ScCeSZ cells and Ni/ScCeSZ with no pore former(SC04), but lower

porosity value compared to Ni/ScCeSZ cells; SC01 to SC03.

Comparing with available literature, Kan et. al [8] did not observe any difference with

operation under methane between undoped and Sn-Ni/YSZ cells, but observed improvement

in long term stability in methane which extended from 27 hours to 137 hours. Troskialina [64]

and Andarini [56] observed same maximum power density under hydrogen and biogas in their

thesis work; which is also in agreement with observations of Farrell et. al [80] using ethanol as fuel. Slightly lower performance than hydrogen observed in this work maybe due to insufficient amount of Sn used as some of the Sn might have migrated to the other layers which will be discussed later in this chapter.
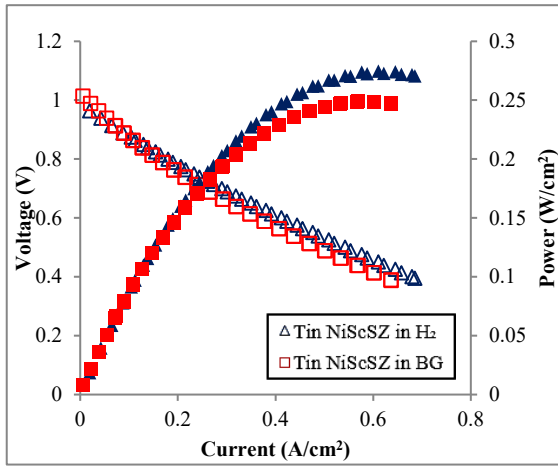
Figure 7-10: *i*V-PV curve of Sn-Ni/ScCeSZ cells in hydrogen and biogas (TSC02).
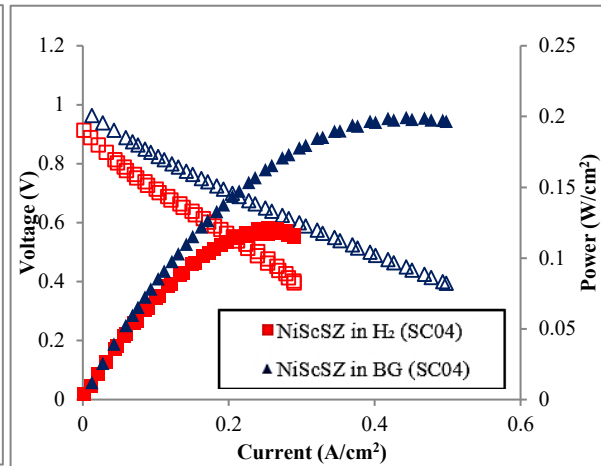
Figure 7-11: *i*V-PV curve of Ni/ScCeSZ cells with no pore former in hydrogen and biogas (SC04).
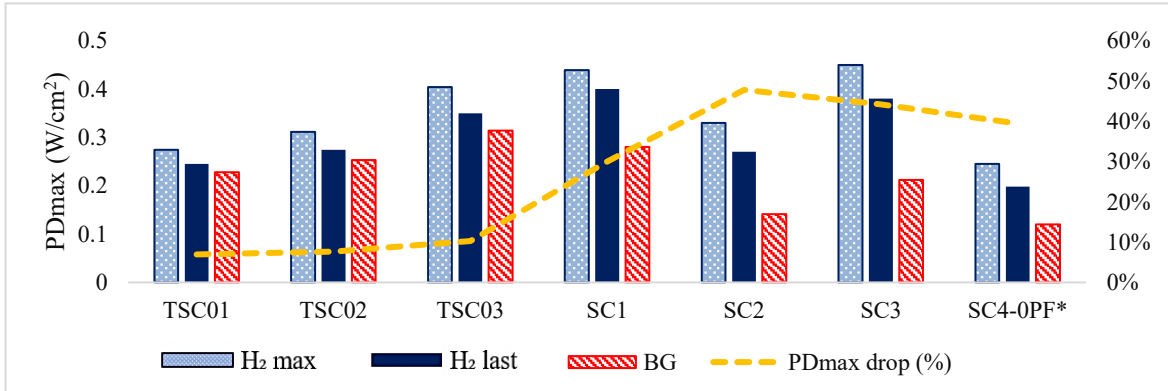
Figure 7-12: Comparison of maximum power density of Sn-Ni/ScCeSZ and undoped Ni/ScCeSZ cell.
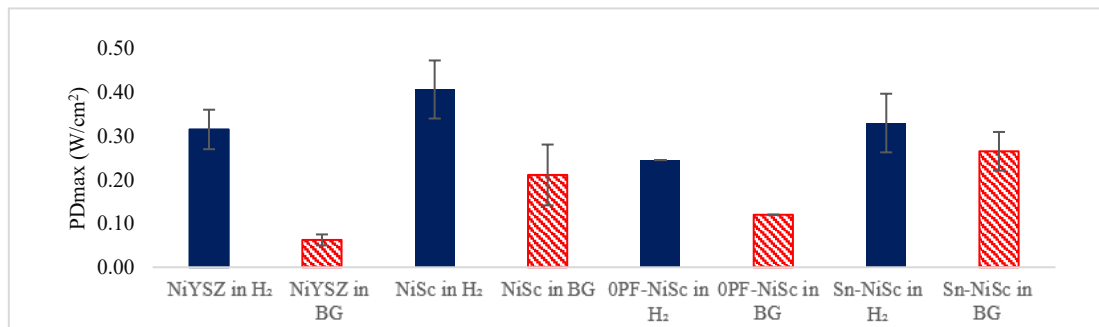
Figure 7-13: Average maximum power density in Ni/YSZ, Ni/ScCeSZ and Sn-Ni/ScCeSZ.

7.3.2.3   In hydrogen - Post biogas test

Figure 7-14 shows the *i*V-PV measurement of Sn-Ni/ScCeSZ (TSC02) before and after the fuel swap to biogas which shows maximum power density of 0.253 W/cm^2. As the drop in performance was small, the post-biogas test did not show a high degree of recovery, taking into account the existing 7.4% degradation in each *i*V measurement cycle. As previously, the carbon deposition was assumed to be low as not much deterioration was observed. The restoration of performance in hydrogen in post-ethanol fuel was also observed by Farrell et al. [80] in Sn-Ni/YSZ cells, while undoped Ni/YSZ cells showed 30% degradation in his work.
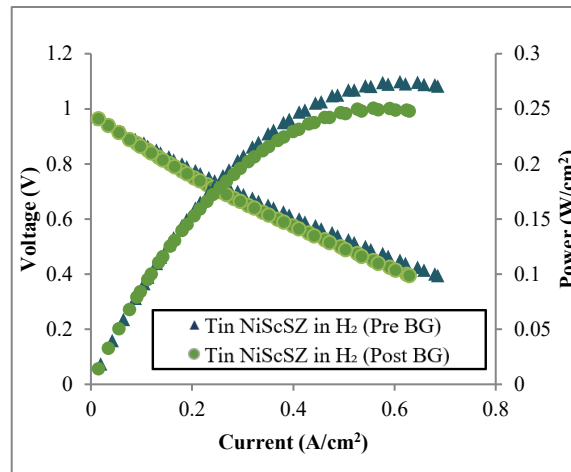
Figure 7-14: Post-biogas analysis in Sn-Ni/ScCeSZ cell (TSC02).

7.3.3   Durability test

Figure 7-15 shows the overall current density value at 0.7V for the cells for 49 hours of operation time. The plot shows the 24 hour test duration in hydrogen, followed by 24 hour test in biogas and 1 hour in hydrogen as post-biogas test. The first current density obtained at an operational voltage of 0.7 V in hydrogen was 0.352 A/cm^2 at the beginning and drop to 0.326 A/cm^2. This value gradually dropped by 6.1% at each cycle and gave the last current density of 0.29 A/cm^2 at 22-hours. In total, the decrease after 14 hours (from 7-hours to 22-hours) was 17.9%, which was 1.28% degradation per hour.
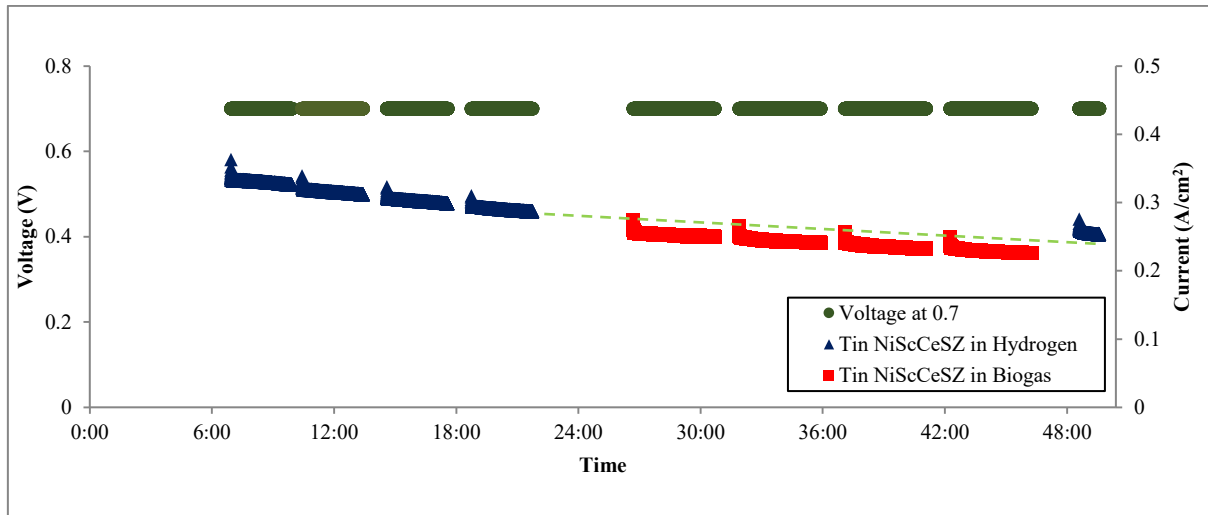
Figure 7-15: Potentiostatic measurement for 48 hours in hydrogen and biogas for Sn doped cells (TSC02).

Immediately when swapped to biogas, the current density value decreased to 0.25 A/cm^2 and slightly dropped to 0.23 A/cm^2 at 46 hours. The total drop from the last cycle in hydrogen and to biogas was 8.0%, which was similar to the drop in maximum power density covered in Section 7.3.2. By eliminating the gradual drop, the net drop caused by the swap was only 1.9%. The Sn-Ni/ScCeSZ cell found to be more stable in biogas setting, with a gradual decrease of 3%. Because of this lower degradation rate in biogas, the current density recovery of the cell's performance after the post biogas measurement was also higher than expected, if the system had run on hydrogen indicated by the green dotted line in Figure 7-15. This was not observed previously in the undoped Ni/ScCeSZ cells.

7.3.4 Electrochemical Impedance Spectroscopy (EIS)

Electrochemical Impedance Spectroscopy (EIS) measurements on Sn-Ni/ScCeSZ cell TSC03 under hydrogen, biogas, and post-biogas were carried out to understand the changes of resistance due to structural changes and carbon deposition. Previously, in other cells, the impedance measurement was only made once in post-biogas operation, while in cell TSC03 the measurement was recorded up to 22 hours after biogas operation.

174
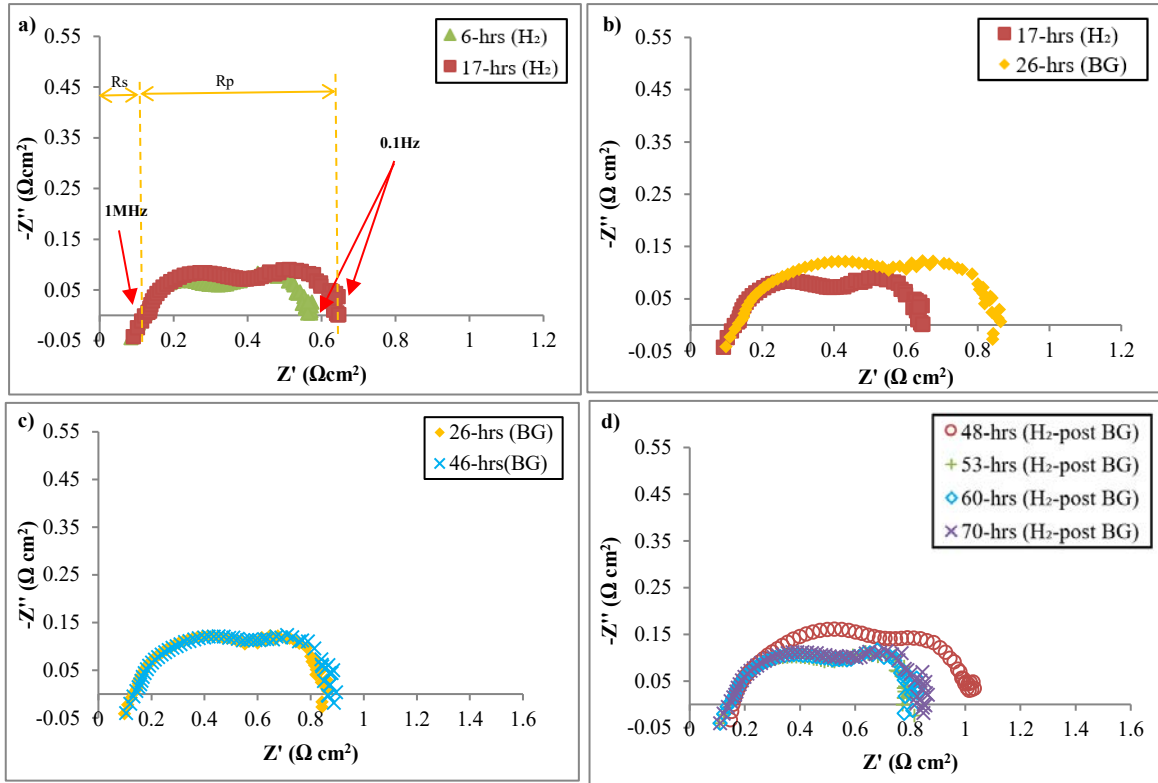
Figure 7-16: Nyquist plot for a Sn-Ni/ScCeSZ cell (TSC03) under a) hydrogen, b) hydrogen and biogas comparison, c) biogas, and d) hydrogen - post biogas.
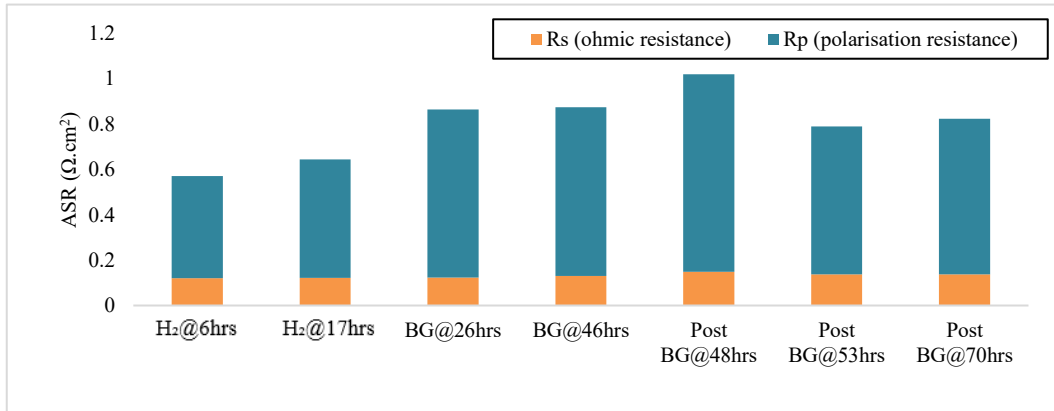
Figure 7-17: ASR contribution at different measured time under hydrogen and biogas.

Figure 7-16a shows the Nyquist plot under hydrogen operation at 6-hours and17 hours, while 7-16b shows the resistance before and after the fuel swap, Figure 7-16c shows the resistance changes during biogas operation while 7-16d shows impedance analysis in hydrogen after swapping back from biogas operation. Figure 7-17 shows the summary of ASR contributions by ohmic resistance and polarisation resistance from the impedance analysis in Figure 7-16.

The ohmic resistance in hydrogen was 0.120 Ωcm^2; higher than that measured in any Ni/ScCeSZ undoped cells in previous chapter with average value of 0.084 Ωcm^2. Regardless of the fact that the ohmic resistance were mainly dominated by the influence of interconnects and current collectors in the electrode supported cell [45], thicker electrolyte layer will have an impact to the ohmic resistance value. In Figure 7-26, the SEM-EDX analysis shows Sn detected in the electrolyte layer. Migration of Sn might happen during co-sintering stages. Hence, this may add another factor in high ohmic resistance value.

The total ASR in hydrogen measured at 6-hours was 0.571 Ω cm^2, which gradually increased to 0.644 Ω cm^2 at 17 hours as shown in Figures 7-16 and 7-17. This increase was due to the due to Ni coarsening in Ni/ScCeSZ as discussed in Section 5.5.2. When the fuel switched to biogas, the ASR increased from 0.644 Ωcm^2 to 0.864 Ωcm^2 which dominated by the increase in charge transfer resistance (R_{ct}) which presented by the semicircle in the high frequency range. R_{ct} might increase due to slow reaction, caused by the reduced amount of electron passes through as less reactant was available. In hydrogen, the reactant was readily available, while in biogas, the reactant for electrochemical reaction need to be produced from the reforming reaction. The lower frequency semi-circle which portrayed mass diffusion resistance also increased. This may have been caused by carbon deposition hindering the reaction or reducing reaction sites as these were also needed for the catalytic reaction in dry reforming or methane cracking.

Interestingly, during the 20 hours duration in biogas, there was no significant increase of polarisation, which was not expected. The increase in operation time in biogas fuel was expected to increase the resistance as more carbon buildup was expected on the anode. Recalling the current density measured in the stability test, lower degradation was observed compared to testing in hydrogen.

The increase of ASR in the beginning of the post-biogas measurement may have been due to anode re-arrangements when the fuel swap took place once more. In between the EIS measurement at 48 hours to 53 hours (Figure 7-16d), it is speculated that the carbons that was deposited near the reaction sites may have been preferentially oxidised, producing CO and reducing the polarisation resistance from 1.02 Ωcm^2 to 0.854 Ωcm^2. Although the ASR in post-biogas hydrogen was higher than in the pre-biogas hydrogen test, the ASR from 53 hours onwards was more stable compared to the pre-biogas hydrogen test. If the Sn-Ni/ScCeSZ cells had continued testing in hydrogen for 70 hours without any operation in biogas, assuming a constant rate of ASR increase in Figure 7-16a, the final ASR value in a hydrogen-only setting would have been higher than obtained in this test.

Table 7-3: ASR (with EIS) for Sn-Ni/ScCeSZ(TSC03), Ni/ScCeSZ with no pore former (SC04) and standard Ni/ScCeSZ (SC01) measured at first impedance measurement in each system

	TSC01		TSC02		TSC03		SC01		SC04	
	H_2	BG	H_2	BG	H_2	BG	H_2	BG	H_2	BG
R_{ohm} (Ω cm²)	0.203	0.221			0.120	0.123	0.084	0.084	0.084	0.087
R_p (Ωcm^2)	0.507	0.727			0.451	0.741	0.450	0.648	0.685	1.280
Total ASR (Ω/cm^2)	0.710	0.948	0.920	1.255	0.571	0.864	0.534	0.732	0.769	1.367

* No EIS data obtained for TSC02 due to machine error during measurement. Total ASR for TSC02 were calculated from iV curve at 0.7V
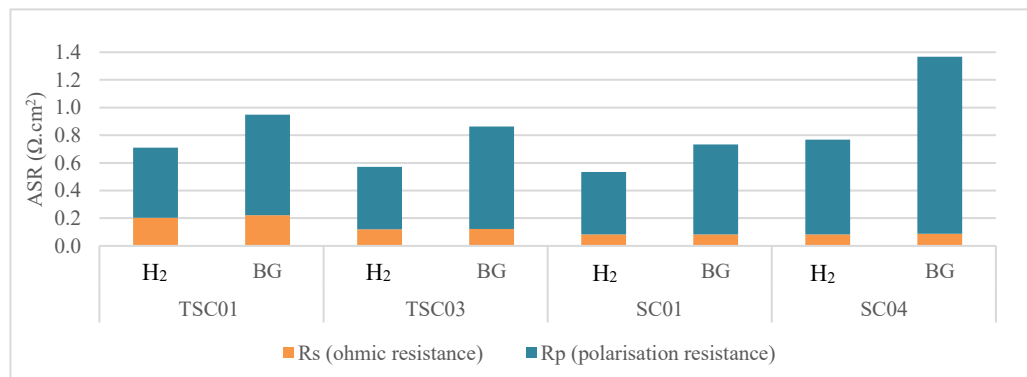
Figure 7-18: ASR comparison across several cells in Ni/ScCeSZ and Sn-Ni/ScCeSZ under hydrogen and biogas (from Table 7-3).

Table 7-3 and Figure 7-18 show the ASR comparison for standard undoped Ni/ScCeSZ cell (SC01), undoped Ni/ScCeSZ cell without pore former (SC04), Sn-Ni/ScCeSZ without pore former (TSC01), and Sn-Ni/ScCeSZ with 1wt% pore former (TSC03), obtained during the first impedance measurement in each setup. Even though the total ASR of the Sn-Ni/ScCeSZ were higher than SC01, the polarisation resistance were lower in both hydrogen and biogas test, while the increase of ohmic resistance in both Sn-Ni/ScCeSZ cells was mainly due to thicker electrolyte layer. Both Sn-Ni/ScCeSZ cells had lower ASR compared to cell SC04. With higher porosity, the Sn-Ni/ScCeSZ will have less polarisation, thus higher performance. There was no impedance measurement for TSC02 due to machine error during measurement. The ASR for TSC02 presented in Table 7-3 was calculated from the gradient of iV-curve at 0.7V.

7.4   Post test analysis

7.4.1   SEM-EDX analysis on anode layers

The microstructure of the Sn-Ni/ScCeSZ anode (TSC01 and TSC02) after cell testing as shown in Figure 7-19 and 7-20 showed a porous cell structure, even with absence of pore former. The pores were made up from reduction of NiO, and the burn-off of the increased amount of organics used. Filamentous growth structure and carbon films detected shown with the red arrow on Figure 7-19 and 7-20. However, more filamentous carbon was detected in the undoped Ni/ScCeSZ cells in the previous chapter shown in Section 6.3. Each filamentous carbon can have both structure, graphitic skin and amorphous head end [126]. As Sumi et al [65] revealed that the filamentous carbon growth on Ni/ScCeSZ had a higher graphitic-to-amorphous ratio, the existence of a small amount of filamentous carbon is speculated to be aiding the reaction as opposed to amorphous carbon.
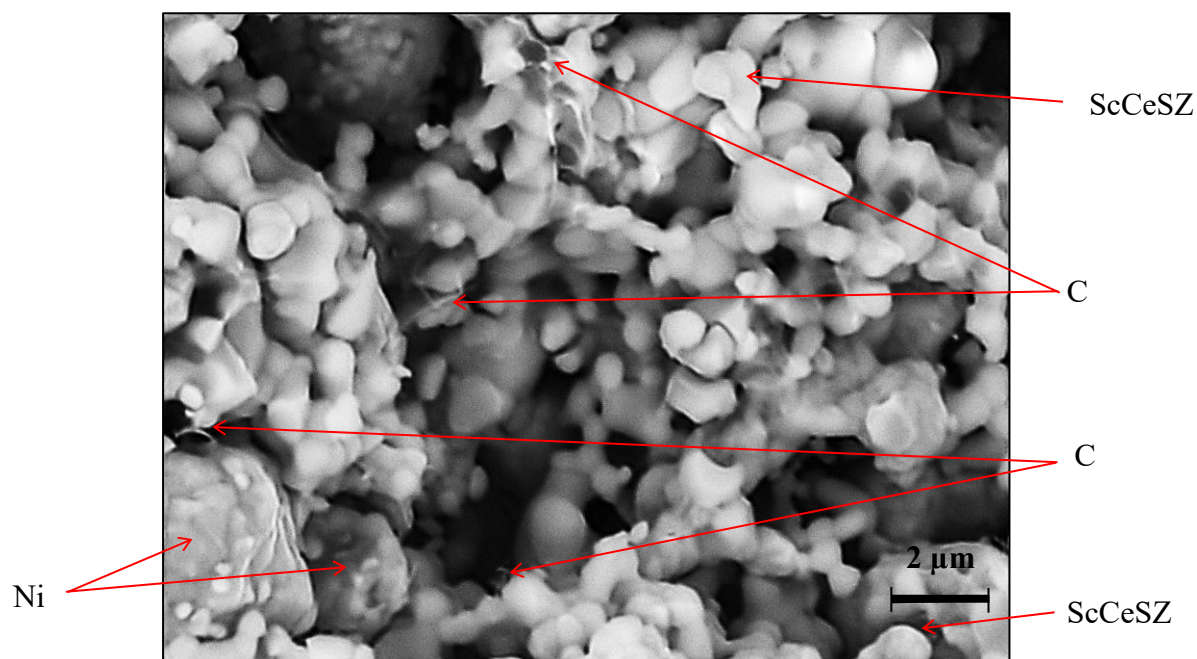
Figure 7-19: Anode substrate of Sn-Ni/ScCeSZ TSC01 after test in hydrogen and biogas.
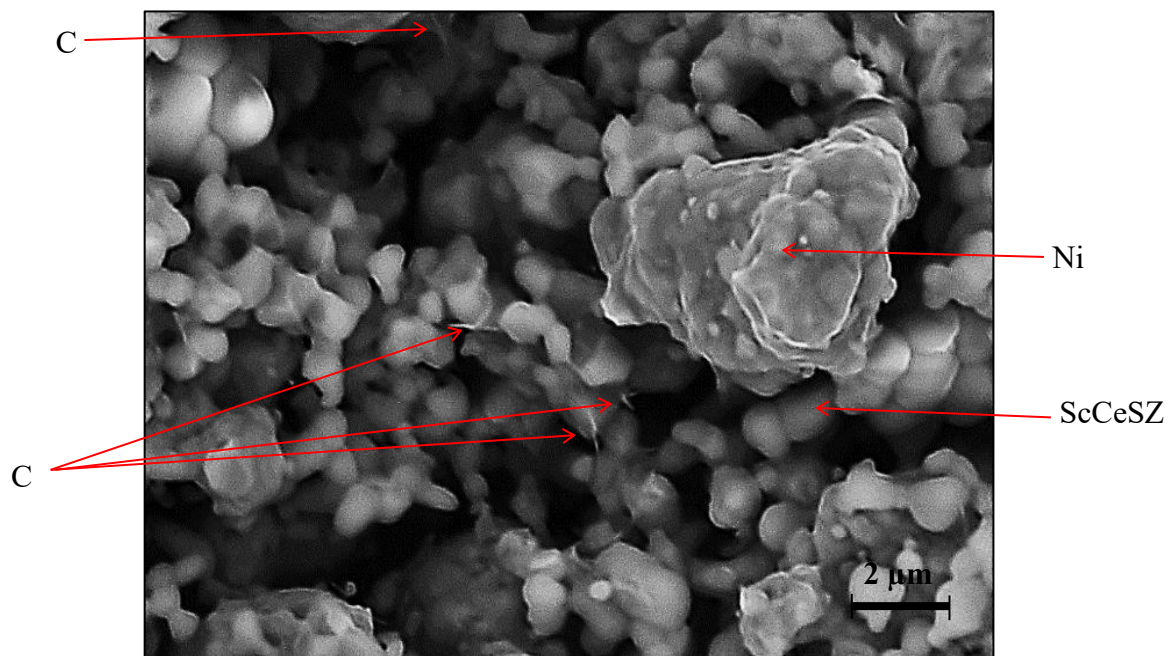
Figure 7-20: Anode substrate Sn-Ni/ScCeSZ TSC02 after test in hydrogen and biogas.

179

Figure 7-21 shows spectral and line-scan analysis of the anode substrate (AS) of cell TSC02. From the spectral analysis, Sn and Sc-rich region overlap more than Sn overlapping with Ni-rich regions. However, the line-scan analysis reveals that Ni exist in all region, only varied in term of concentration. XRD analysis by Andarini [56] revealed that Sn adheres to Ni surfaces forming a Sn/Ni alloy as has been assumed by other works on Sn dopant introduction [64, 80]. Another interesting point portrayed by Figure 7-21 was that; the carbon peaks coincide to Sc and Sn rather than to Ni peaks which complements the spectral analysis on the same site.

Another line-scan analysis at two different positions was carried out as shown in Figure 7-22. The highest carbon peaks up to 12 counts were detected at position-B, while constant frequency of carbon peaks ranging from 3 to 8 counts were detected at position A. Same frequency with lower peaks of carbon in the range 2 to 5 counts was detected in the anode functional layer (AFL) as shown in Figure 7-23.

Figure 7-24 shows the line scan analysis on the cross-sectional SEM image of TSC02 across AS and AFL at two different position. The result showed a lower peak of carbon detection in the range of 2 to 6 counts on AS layer and 1 to 3 counts in the AFL, respectively. Figure 7-25 shows the line scan analysis on the same cell with higher magnification focusing on the interface of the AS and AFL marked by red square box in Figure 7-24. At position A, Sn was detected in both AS and AFL even though the introduction of $SnCl_2.2H_2O$ was only to the AS slurry during manufacturing. Position B shows a lower amount of Sn detected on the AFL compared to position B. This can confirm the migration of Sn to the AFL that may happen during high temperature sintering (1300°C). As it is interesting to see the relationship between C and Sn, both C and Sn line-scans carried out at position A and C shows that C and Sn coincide supporting the surface analysis obtained earlier from Figure 7-21.
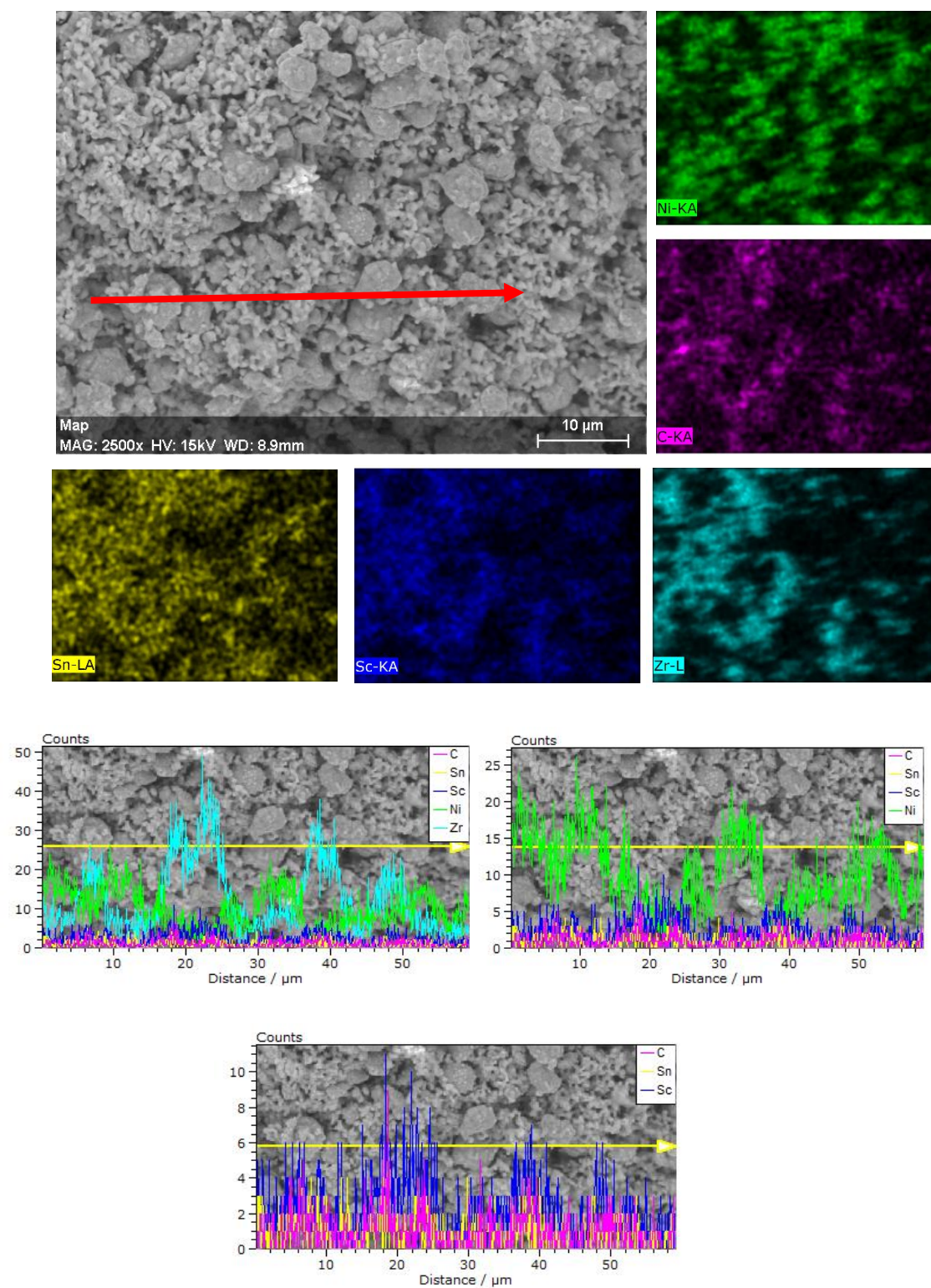
Figure 7-21: Spectrum and line-scan analysis(SEM-EDX) on Sn- Ni/ScCeSZ after cell testing.
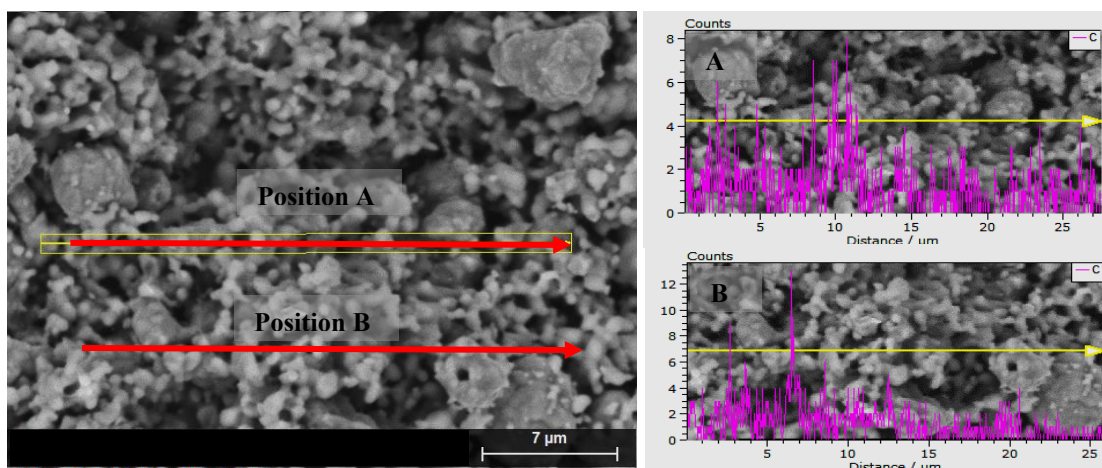
Figure 7-22: Carbon detection in anode substrate (AS) in Sn- Ni/ScCeSZ cell (SEM-EDX line scan analysis).
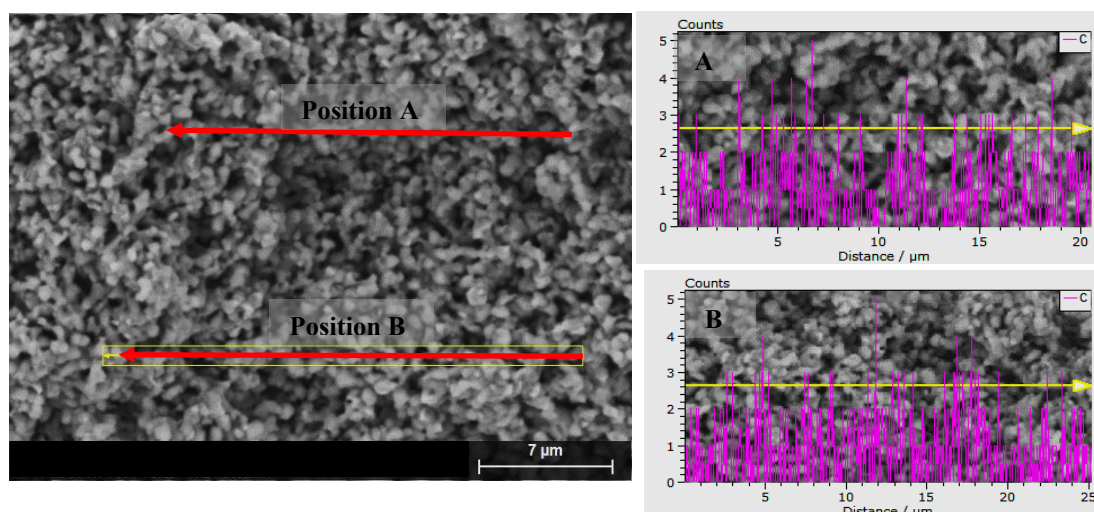
Figure 7-23: Carbon detection in anode functional layer (AFL) in Sn- Ni/ScCeSZ cell (SEM-EDX line scan analysis).
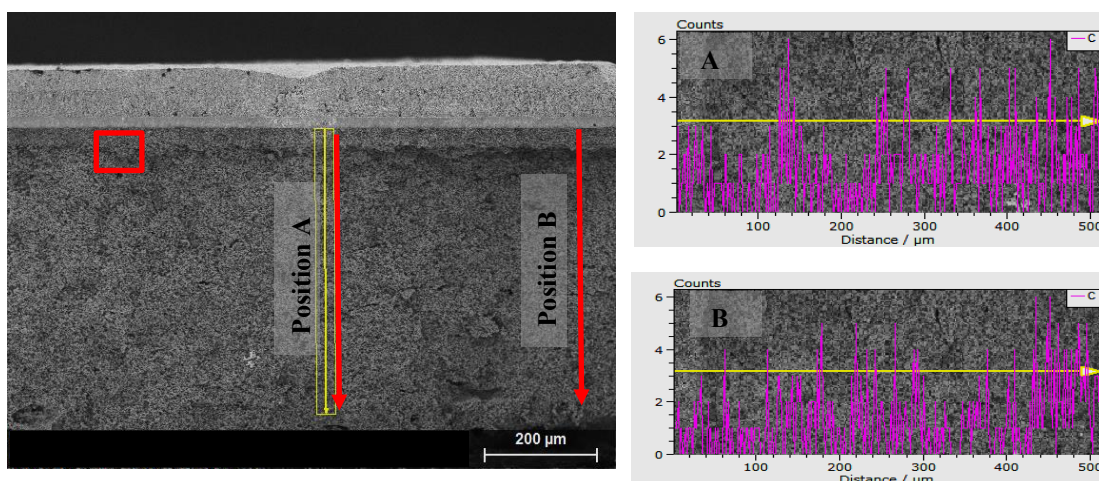
Figure 7-24: Carbon detection across AFL and AS layer in Sn- Ni/ScCeSZ cell (SEM-EDX line scan analysis).
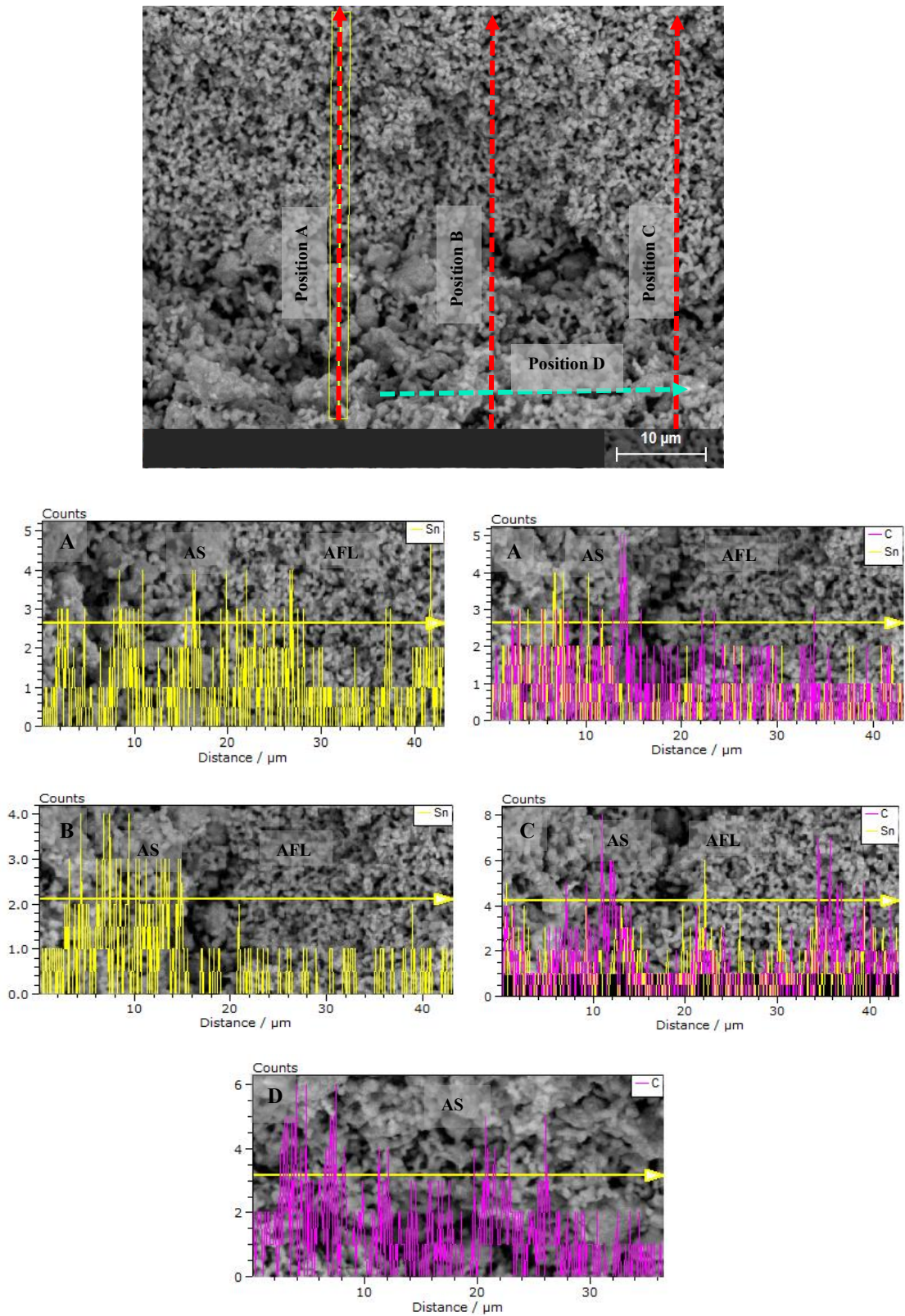
Figure 7-25: Carbon and tin detection using SEM-EDX line scan analysis on anode layers of Sn-Ni/ScCeSZ (TSC02).

Higher carbon detection on the AS compared to the AFL on position A agrees with the results from Figure 7-24. However, in position B, almost a similar pattern of carbon detection is shown by both AS and AFL. If a Sn/Ni alloy influence methane cracking reaction which produce carbon on-site; it is explainable as higher amount of Sn was detected as well in the AFL layer in position C.

From the detection of carbon at the AFL, it can be assumed that some methane cracking reaction also occurred near the TPB electrochemical reaction sites, although not as much as it took place in the anode substrate layer. For an internal dry-reforming SOFC, it was assumed that only electrochemical reactions take place in the AFL layer, with all reforming and cracking reaction takes place at the coarse Ni surface in the AS layer[LANZIINI]. If the methane cracking or dry reforming took place at the TPB, this would reduce the sites available for electrochemical reaction, hence this may be the reason why the performance was lower than in hydrogen. The carbon deposited near the TPB can be electrochemically oxidised and fuels the SOFC, depending on availability of the catalyst (Sn or Ni or Ce) to promote this.

Comparing the peak (amplitude) and the frequency of the carbon counts of AS layers of Sn-Ni/ScCeSZ with undoped Ni/ScCeSZ, there was more carbon detected in the Sn-doped cells. In undoped Ni/ScCeSZ, a lower frequency of carbon was detected with carbon peak range of 1 to 2 while in Ni/YSZ cells, the carbon peak range was 1 to 4. This result was in agreement with what had been reported by Singh et. Al [127] who tested Ni/YSZ and Sn-Ni/YSZ electrolyte supported cells operated with methane. Carbon detection in the AFL cannot be compared as no SEM-EDX analysis carried out on the AFL layer in undoped cells.

Spectral analysis on the cross-section of Sn-Ni/ScCeSZ cells as shown in Figure 7-26 evidences that a large amount of Sn detected on the cathode and electrolyte, which is

undesirable from the evidence of how it impacts on the ohmic resistance. Speculation can be made that Sn was inclined to adhere to Sc based on all of the SEM-EDX analysis so far. The adherence of Sn to Sc species needs to be further investigated to explain this observation.

Sn impregnation before sintering was attempted previously by Singh et al [128] who reported that the amount of Sn detected was 0.65% instead of 1% Sn impregnated in the anode substrate. However, this study did not show if any Sn species existed in the other parts of the cells. Kan et al [8] on the other hand showed that the amount of Sn in the cell was quite stable even after 300 hours but with different manufacturing techniques and working with nano-powder materials.
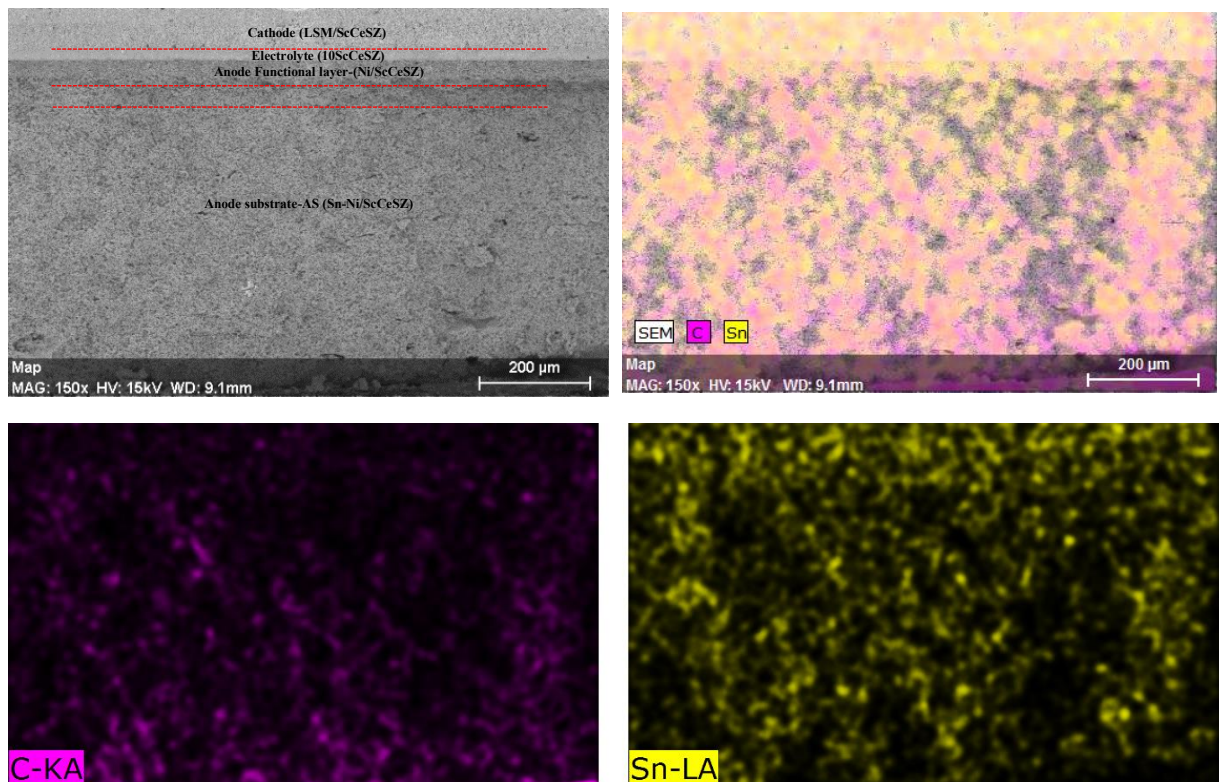
Figure 7-26: C and Sn detection on cross-sectional image of Sn-Ni/ScCeSZ (TSC02).

7.4.2 Temperature Programmed Oxidation (TPO)
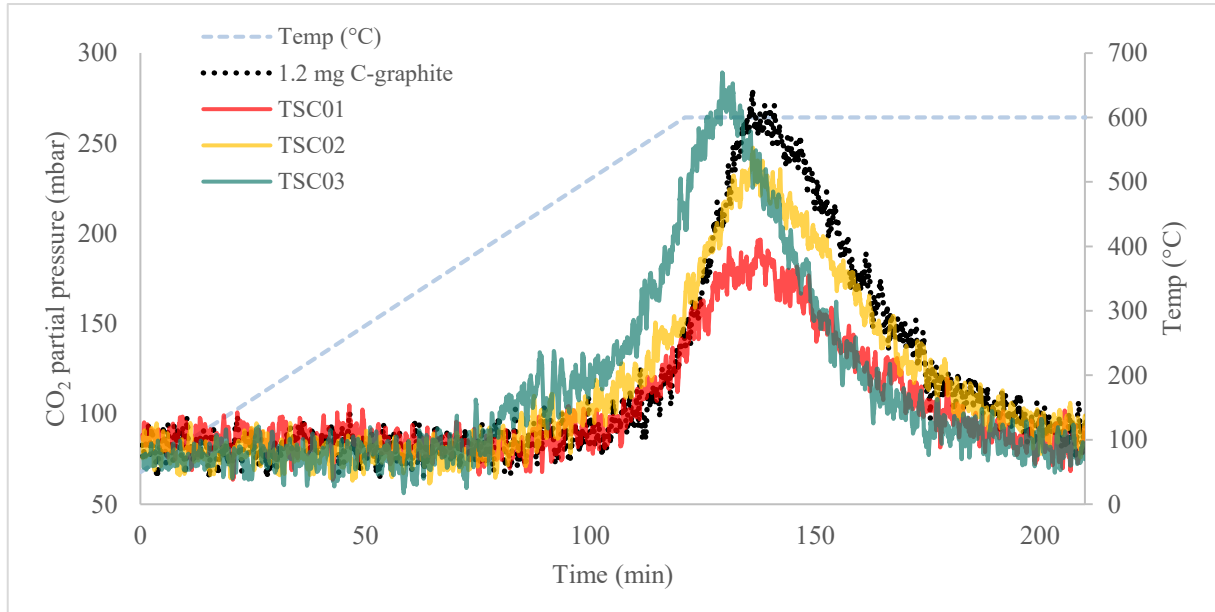
Figure 7-27: CO₂ peaks from carbon burn off on Sn-Ni/ScCeSZ cells with comparison with 1.2mg carbon graphite.

Table 7-4: Amount of carbon deposited on Sn-Ni/ScCeSZ calculated from TPO calibration.

	Amount of carbon deposited			Rate of carbon deposition (mg-C/g$_{cat}$ h)
	per sample (mg)	per unit catalyst (mg-C/mg$_{cat}$)	per unit catalyst (mg-C/mg$_{cat}$) x 100%	
TSC01	0.713	3.53×10^{-3}	0.353	0.147
TSC02	0.975	4.83×10^{-3}	0.483	0.201
TSC03	1.275	5.94×10^{-3}	0.631	0.248

Figure 7-27 shows that the amount of CO_2 released from the carbon burn off from the Sn-Ni/ScCeSZ samples were similar to that from 1.2 mg graphitic carbon powder. The CO_2 peaks found around 600°C, similar to the carbon burn-off temperature with those from undoped Ni/ScCeSZ and the carbon graphite powder. Hence, it was deduced that the carbon type formed on Sn-Ni/ScCeSZ was graphitic. The calculation method used was the same as in Section 6.3.2. The minimum amount of carbon deposited on the sample was 3.52×10^{-3} mg-C/mg$_{cat}$ which was higher than any undoped Ni/ScCeSZ cells elaborated in Section 6.3.2. The amount of

carbon deposited in the Sn-Ni/ScCeSZ samples for each cell is presented in Table 7-4 with an average of 4.89 x 10^{-3} mg-C/mg$_{cat}$.

In Sn-Ni/YS cell in Troskialina [64] and Singh et al [127] work, higher amount of carbon was also found in the Sn doped cell with no significant drop of performance. The carbon deposited in their work was also coincide with the graphitic carbon burn off temperature as found in this work. Apart from work by [64] and [127], there was no other literature that reported the same observation, high performance with higher graphitic carbon found in the tested sample.

7.5   Additional discussion

Sn addition during the mixing stage produced a flat cell with thicker individual layers. It is speculated that the coefficient of thermal expansion (CTE) mismatch of the layers was reduced because of Sn migration to the whole cell, which also increased the ohmic resistance in the Sn-Ni/ScCeSZ cells. This can be confirmed with dilatometer analysis which was not carried out due to limited time and space. Higher ohmic resistance and increase of anode polarisation due to an insufficient amount of porosity gave lower performance compared to the standard Ni/ScCeSZ cells, but when compared with the Ni/ScCeSZ cells with same porosity level (SC04), the performance in both hydrogen and biogas improved in Sn-Ni/ScCeSZ. Singh et al [128] demonstrated in their work that by incorporating Sn before the sintering stage influence the shrinkage of their cells, which was assumed to influence the operational stability of the Sn-doped cells.

A higher OCV value in biogas and higher amount of carbon detected in the post-analysis shows higher conversion of biogas in the Sn-Ni/ScCeSZ cells. Hence showing that the Sn-Ni/ScCeSZ can catalysed the dry reforming and methane cracking reaction to produce more reactant for the

electrochemical reaction. Nikolla et al [79] suggested that the improved performance in carbon-fuelled SOFC by the Sn-doped cells was due to: 1) the Sn/Ni catalyst is more efficient than Ni in forming C-O bonds rather than C-C bonds which means implies a higher rate of oxidation of carbon atoms rather than developing solid carbon, 2) Sn atoms displace low coordinated sites for nucleation and growth for carbon fibres 3) Sn/Ni active sites are more abundant, while the Ni (with no dopant) active sites were under-coordinated; i.e Sn atoms improved the Ni coordination sites, 4) weakens the binding of carbon atoms to low-coordinated sites.

Based on [79]'s points, before the post-test analysis carried out, initial assumption made was that less carbon deposition in biogas operation occurred in Sn-Ni/ScCeSZ cells since the performance in biogas showed relatively good value compared to undoped Ni/ScCeSZ cells. This proved to be wrong as more graphitic carbon was found on the Sn-doped Ni/ScCeSZ cells. More interestingly, from the line-scan analysis, the Sn and C detection coincided with each other; showing either 1) Sn was deposited on Ni and forming alloy; and carbon developed on the Ni surface, coincidently coincide with Sn, 2) the Ni-Sn alloy catalysed the methane cracking reaction, releasing H_2 and CO for the chemical reaction, hence a higher amount of fuel available. This produced a higher partial pressure from the reactants (on the anode side) and led to an increase the performance; but more carbon was also deposited on the anode.

In terms of the effect of Sn doping on the electrochemical performance, the Sn-Ni/ScCeSZ showed better performance in biogas compared to undoped cells, which agrees with the literature [8, 56, 64, 127]. The higher amount of carbon formed on Sn-doped cells opposed to what had been found by Farrell et al. [80] and the suggestion of Nikolla et al. [79] described above. On the other hand, it was in agreement with the observation from Singh et al. [127] and Troskialina [64]. Although a higher amount of carbon found in the Sn-doped cells than that on the undoped cells, the graphitic carbon did not block the reaction sites and may enhance the

electrochemical reaction. This speculation supported by the EIS analysis in the biogas (Section 7.3.4), where there was no significant increase in the polarisation resistance value opposed to the polarisation increase during the SOFC test in hydrogen. Mallon and Kendall [54] also suggested an increase in performance with a small amount of graphitic carbon.

The electrochemical performance with impregnation method practiced by Troskialina [64] and Singh et al. [127] shows no reduction of performance with Sn-Ni/YSZ when operated in biogas compared to the undoped Ni/YSZ cells. With impregnation-doping method, all dopant sits on the anode substrate surface (concentrating on Ni); which catalysed the dry reforming reaction. With the doping method practiced in this chapter (by slurry mixing), the Sn-dopant might sit in bulk and became inactive. Furthermore, the Sn migration to the electrolyte layer caused undesirable higher ohmic resistance. Hence, although the dopant introduction is easier with this method, impregnation method deemed to be more suitable.

CHAPTER 8: CONCLUSION AND FUTURE WORK

8.1 Conclusion

The fuel flexibility advantage of SOFC has been jeopardized by the low performance with carbonaceous fuels reported due to carbon deposition on the benchmark materials. Hence, driven the aim to develop an alternative material to replace Ni/YSZ anode for dry carbon fuels feed. Through the work in this thesis, the three main conclusions based on the objectives set in this thesis are:

1. Sn-Ni/ScCeSZ fit as replacement for Ni/YSZ cell for dry carbonaceous fuel SOFC based on higher electrochemical performance in dry biogas operation due to the improved reforming ability by the Sn introduction.

2. Ni/ScCeSZ surpassed Ni/YSZ electrochemical performances in both hydrogen and dry biogas in IT-SOFC regime. Better reforming ability, significantly higher electrochemical performance and the carbon morphology deposited on Ni/ScCeSZ during biogas operation makes Ni/ScCeSZ more suitable for biogas operation compared to Ni/YSZ.

3. Reverse tape casting method developed is suitable to produce quality SOFC cells with tailored parameter alterations to meet individual materials requirement. Manufacturing SOFC cells with different materials shows that the manufacturing parameters also constrained by the material's characteristic, and not only constrained by the microstructural and performance requirements.

To derive the conclusions above, several points from the results obtained in this thesis were carefully considered. In terms of electrochemical performance in dry biogas, Ni/ScCeSZ significantly outperformed Ni/YSZ, which was further enhanced by Sn introduction. The

primary reason of performance drop with the fuel switch from hydrogen to biogas on Ni/YSZ was the reforming ability of the anode and not caused by anode deactivation from carbon deposition. This point is crucial as most of the existing literature addressed carbon deposition as the reason behind the inability of Ni/YSZ operation in carbon fuels.

Different carbon morphology behavior found with the cells with different oxides; graphitic carbon deposited on Ni/ScCeSZ and amorphous carbon deposited on Ni/YSZ. The higher amount of graphitic carbon found in Ni/ScCeSZ and Sn-Ni/ScCeSZ did not block the reaction sites but also reduced the polarisation resistance during biogas operation in Sn-Ni/ScCeSZ. The accelerated gradual degradation throughout the electrochemical performance test in Ni/ScCeSZ cells (doped and undoped) was concluded to be due to Ni coarsening which impacted from incompatible starting material sizes and not caused by the phase changes in 10ScCeSZ. This is an important finding to safely lead to the conclusion on the suitability of Ni/ScCeSZ as promising anode materials.

In cell manufacturing, half-cells with different microstructure in each layer for different materials were successfully fabricated using reverse multilayer aqueous tape casting route. To meet the microstructural requirements for different materials, several parameter differences which were sintering temperature, pre-calcination temperature and the organics composition applied. This work also shows that with different materials and dopant introduction to the thick anode layer, the influence was not only on the electrochemical performance but also influence the manufacturing stage.

8.2 Further works

In term of development of SOFC cells, the most important suggestion for the future works is to use finer NiO starting size to avoid Ni coarsening. Long term degradation studies with focus of finding the critical size gap between Ni and electrolyte materials will be very beneficial in developing a stable SOFC cells. For developing Sn-Ni/ScCeSZ SOFC cells, although dopant introduction through slurry-incorporating method gave a good effect in term of manufacturing, the side effects on the ohmic resistance and the Sn occupancy in the inactive sites of the anode deemed to be undesirable. Hence, impregnation method on an SOFC anode deemed to be more suitable.

For continuation of this work, including the points above, it is suggested in the future work that additional work to be performed on the areas described in this section onwards. Note that the list is sorted by its priority and significance to this thesis. Hence, although the degradation study deemed to be the most important suggestion for the application of manufacturing to avoid degradation in the future work, it is the least relevance to this thesis original scope.

1. Carbon deposition and reforming ability test

   Duration: 3 months – MEng project

   a. Catalytic activity test for Sn-Ni/ScCeSZ

   b. Thermogravimetric reduction (TGR) test with dry biogas to identify the rate of carbon deposition without the influence of electrochemical reaction

2. Sn-NiScCeSZ cells development using Sn infiltration method

   Total duration: 6-12 months – MSc project level

   a. Attempt infiltration method on the ready-made Ni/ScCeSZ cells to observe the electrochemical performance of Sn doped cells with this method under dry biogas. Compare the result with Sn-Ni/YSZ cells. *(Duration: 6 months)*

   b. Complete ex-situ characterisation, SEM-EDX, XRD and XPS analysis to understand the behaviour of Sn on Ni/ScCeSZ cells. *(Duration: 6 months)*

3. Effect of manufacturing parameters to electrochemical performance.

   Duration: 3 months – MEng project

   c. Measure electrolyte conductivity value with sample prepared at different temperature to see the impact on conductivity value of using different co-sintering temperature.

4. Degradation study with focus to relationship of Ni coarsening and particle size.

   Total duration: 3 years - PhD level

   d. The relationship between the critical size gap of the electrolyte and NiO must be worked out by testing different pairs of sizes.

   e. Additional long stability test

   f. Raman Spectroscopy and more XRD analysis

REFERENCES

1. USDE, *Fuel Cell Handbook 7th Edition*, I. EG &G Technical Services, Editor. 2004.
2. University of Cambridge, *Fuel cells: SOFC Electrolytes*. 30 August 2018; Available from: https://www.doitpoms.ac.uk/tlplib/fuel-cells/printall.php.
3. Mistler, R.E. and E.R. Twiname, *Tape Casting: Theory and Practice*. 2000: Wiley.
4. Fergus, J.W., *Electrolytes for solid oxide fuel cells.* Journal of Power Sources, 2006. **162**(1): p. 30-40.
5. Cimenti, M. and J. Hill, *Direct Utilization of Liquid Fuels in SOFC for Portable Applications: Challenges for the Selection of Alternative Anodes.* Energies, 2009. **2**(2): p. 377.
6. Robert Timothy Leah, A.B., Mike Lankin, Ahmet Selcuk, Mahfujur Rahman, Andrew Clare, Lee Rees, Stephen Phillip, Subhasish Mukerjee, and Mark Selby, *Ceres Power Steel Cell Technology: Rapid Progress Towards a Truly Commercially Viable SOFC.* ECS transaction, 2015. **68**(1): p. 95-107.
7. Michálek, M., et al., *Comparison of aqueous and non-aqueous tape casting of fully stabilized ZrO_2 suspensions.* Powder Technology, 2015. **274**: p. 276-283.
8. Kan, H. and H. Lee, *Sn-doped Ni/YSZ anode catalysts with enhanced carbon deposition resistance for an intermediate temperature SOFC.* Applied Catalysis B: Environmental, 2010. **97**(1-2): p. 108-114.
9. Ishihara, T., N.M. Sammes, and O. Yamamoto, *Chapter 4 - Electrolytes*, in *High Temperature and Solid Oxide Fuel Cells*. 2003, Elsevier Science: Amsterdam. p. 83-117.
10. Badwal, S.P.S., *Zirconia-based solid electrolytes: microstructure, stability and ionic conductivity.* Solid State Ionics, 1992. **52**(1): p. 23-32.
11. *Appendix 1: Thermodynamic data of selected chemical reactions and substances*, in *Solid Oxide Fuel Cell Technology*, K. Huang and J.B. Goodenough, Editors. 2009, Woodhead Publishing. p. 278-279.
12. Wang, C., et al., *A novel multilayer aqueous tape casting method for anode-supported planar solid oxide fuel cell.* Materials Letters, 2011. **65**(14): p. 2251-2253.
13. Blum, L., et al., *Recent results in Jülich solid oxide fuel cell technology development.* Journal of Power Sources, 2013. **241**: p. 477-485.
14. Somalu, M.R., et al., *Fabrication and characterization of Ni/ScSZ cermet anodes for IT-SOFCs.* International Journal of Hydrogen Energy, 2011. **36**(9): p. 5557-5566.
15. Sumi, H., et al., *Performance of nickel scandia-stabilized zirconia cermet anodes for SOFCs in 3% H_2O-CH_4.* Solid State Ionics, 2004. **174**(1-4): p. 151-156.
16. Dees, D.W., et al., *Conductivity of Porous Ni / ZrO_2 - Y_2O_3 Cermets.* Journal of The Electrochemical Society, 1987. **134**(9): p. 2141-2146.
17. Spiridonov, F.M., L.N. Popova, and R.Y. Popil'skii, *On the phase relations and the electrical conductivity in the system ZrO_2-Sc_2O_3.* Journal of Solid State Chemistry, 1970. **2**(3): p. 430-438.
18. Jaworski, Z., B. Zakrzewska, and P. Pianko-Oprych, *On thermodynamic equilibrium of carbon deposition from gaseous C-H-O mixtures: updating for nanotubes*, in *Reviews in Chemical Engineering*. 2017. p. 217.
19. Menzler, N.H., et al. *Advanced manufacturing technology for solid oxide fuel cells*. in *Ceramic Engineering and Science Proceedings*. 2011.
20. Sumi, H., et al., *Comparison Between Internal Steam and CO_2 Reforming of Methane for Ni-YSZ and Ni-ScSZ SOFC Anodes.* Journal of The Electrochemical Society, 2010. **157**(8): p. B1118-B1125.
21. Yashima, M., M. Kakihana, and M. Yoshimura, *Metastable-stable phase diagrams in the zirconia-containing systems utilized in solid-oxide fuel cell application.* Solid State Ionics, 1996. **86-88**: p. 1131-1149.
22. Gorte, R.J. and J.M. Vohs, *Nanostructured anodes for solid oxide fuel cells.* Current Opinion in Colloid & Interface Science, 2009. **14**(4): p. 236-244.

23. Badwal, S.P.S., F.T. Ciacchi, and D. Milosevic, *Scandia–zirconia electrolytes for intermediate temperature solid oxide fuel cell operation.* Solid State Ionics, 2000. **136-137**: p. 91-99.

24. Boldrin, P., et al., *Strategies for Carbon and Sulfur Tolerant Solid Oxide Fuel Cell Materials, Incorporating Lessons from Heterogeneous Catalysis.* Chemical Reviews, 2016. **116**(22): p. 13633-13684.

25. Nikolla, E., J. Schwank, and S. Linic, *Promotion of the long-term stability of reforming Ni catalysts by surface alloying.* Journal of Catalysis, 2007. **250**(1): p. 85-93.

26. Fergus, J.W., *Solid oxide fuel cells: materials properties and performance*. 2009: CRC Press.

27. Shyam Kumar, C.N. and R. Bauri, *Enhancing the phase stability and ionic conductivity of scandia stabilized zirconia by rare earth co-doping.* Journal of Physics and Chemistry of Solids, 2014. **75**(5): p. 642-650.

28. Lanzini, A., et al., *Durability of anode supported Solid Oxides Fuel Cells (SOFC) under direct dry-reforming of methane.* Chemical Engineering Journal, 2013. **220**: p. 254-263.

29. Haering, C., et al., *Degradation of the electrical conductivity in stabilised zirconia system: Part II: Scandia-stabilised zirconia.* Solid State Ionics, 2005. **176**(3): p. 261-268.

30. Buccheri, M.A., A. Singh, and J.M. Hill, *Anode- versus electrolyte-supported Ni-YSZ/YSZ/Pt SOFCs: Effect of cell design on OCV, performance and carbon formation for the direct utilization of dry methane.* Journal of Power Sources, 2011. **196**(3): p. 968-976.

31. Hotza, D. and P. Greil, *Aqueous Tape Casting of Ceramic Powders.* Materials Science and Engineering a-Structural Materials Properties Microstructure and Processing, 1995. **202**(1-2): p. 206-217.

32. FuelCellWorks. *Kerosene-fueled 3-kW Solid Oxide Fuel Cell, successfully co-developed*. 2009 [cited 2018 15/02/2018]; Kerosene Fuel SOFC]. Available from: https://fuelcellsworks.com/archives/2009/12/14/kerosene-fueled-3-kw-solid-oxide-fuel-cell-successfully-co-developed/.

33. Shiratori, Y., et al., *Internal reforming SOFC running on biogas.* International Journal of Hydrogen Energy, 2010. **35**(15): p. 7905-7912.

34. RJ Braun, P.K., *Applications of SOFCs in Combined Heat, Cooling and Power Systems*, in *SOFC: From Materials to System Modeling*, T.S.Z. Meng Ni, Editor. 2013. p. 327-382.

35. Pecho, O.M., *Relationship between 3D Topology and Reaction Kinetics in SOFC Electrodes*. 2015, ETH Zurich: Zurich, Switzerland.

36. Irshad, M., et al., *A Brief Description of High Temperature Solid Oxide Fuel Cell's Operation, Materials, Design, Fabrication Technologies and Performance.* Applied Sciences, 2016. **6**(3).

37. Vasechko, V., *Thermo-Mechanical Investigations of Reoxidation-Stable Material Concepts for Solid Oxide Fuel Cells*, in *Mechanical Engineering Department*. 2014, RWTH Aachen University: Germany.

38. Menzler, N.H., et al., *Materials and manufacturing technologies for solid oxide fuel cells.* Journal of Materials Science, 2010. **45**(12): p. 3109-3135.

39. C Zuo, M.F.L., M L Liu, *Solid Oxide Fuel Cells* in *Sol-Gel Processing for Conventional and Alternative Energy*, M. Aparicio, Jitianu, A, Klein LC, Editor. 2012. p. 7-36.

40. Singhal, S.C. and K. Kendall, *Chapter 1 - Introduction to SOFCs*, in *High Temperature and Solid Oxide Fuel Cells*, S.C. Singhal and K. Kendall, Editors. 2003, Elsevier Science: Amsterdam. p. 1-22.

41. Koide, H., et al., *Properties of Ni/YSZ cermet as anode for SOFC.* Solid State Ionics, 2000. **132**(3): p. 253-260.

42. Huang, K. and J.B. Goodenough, *Chapter 5 - Oxide-ion electrolytes in solid oxide fuel cells (SOFCs)*, in *Solid Oxide Fuel Cell Technology*, K. Huang and J.B. Goodenough, Editors. 2009, Woodhead Publishing. p. 67-84.

43. Dicks, J.L.a.A., *Fuel Cell Systems Explained, Second Edition*. Second ed. 2003, West Sussex, England: John Wiley & Sons, Ltd.

44. Ivers-Tiffée, E. and A.V. Virkar, *Chapter 9 - Electrode Polarisations*, in *High Temperature and Solid Oxide Fuel Cells*, S.C. Singhal and K. Kendall, Editors. 2003, Elsevier Science: Amsterdam. p. 229-260.

45.   Huang, K. and J.B. Goodenough,Chapter *7 - Voltage losses in a solid oxide fuel cell (SOFC)*, in *Solid Oxide Fuel Cell Technology*, K. Huang and J.B. Goodenough, Editors. 2009, Woodhead Publishing. p. 98-140.

46.   Hauch, A. and M.B. Mogensen, *Testing of Electrodes, Cells, and Short Stacks*, in *Advances in Medium and High Temperature Solid Oxide Fuel Cell Technology*, M. Boaro and A.A. Salvatore, Editors. 2017, Springer International Publishing: Cham. p. 31-76.

47.   Huang, K. and J.B. Goodenough, *Chapter 9 - Performance characterization techniques for a solid oxide fuel cell (SOFC) and its components*, in *Solid Oxide Fuel Cell Technology*, K. Huang and J.B. Goodenough, Editors. 2009, Woodhead Publishing. p. 156-182.

48.   BloomEnergy. *BloomEnergyServer*, August 2018; Available from: https://www.bloomenergy.com/datasheets/energy-server-es5-200kw.

49.   Laycock, C.J., J.Z. Staniforth, and R.M. Ormerod, *Biogas as a fuel for solid oxide fuel cells and synthesis gas production: effects of ceria-doping and hydrogen sulfide on the performance of nickel-based anode materials.* Dalton Transactions, 2011. **40**(20): p. 5494-5504.

50.   Lina Troskialina, Aman Dhir, and R. Steinberger-Wiclkens, *Improved Performance and Durability of Anode Supported SOFC Operating on Biogas.* ECS transaction, 2015.

51.   Ye, X.-F., et al., *Preparation and performance of a Cu–CeO₂–ScSZ composite anode for SOFCs running on ethanol fuel.* Journal of Power Sources, 2007. **164**(1): p. 203-209.

52.   He, H. and J.M. Hill, *Carbon deposition on Ni/YSZ composites exposed to humidified methane.* Applied Catalysis A: General, 2007. **317**(2): p. 284-292.

53.   Dhir, A. and K. Kendall, *Microtubular SOFC anode optimisation for direct use on methane.* Journal of Power Sources, 2008. **181**(2): p. 297-303.

54.   Mallon, C. and K. Kendall, *Sensitivity of nickel cermet anodes to reduction conditions.* Journal of Power Sources, 2005. **145**(2): p. 154-160.

55.   Hagen, A., J.F.B. Rasmussen, and K. Thydén, *Durability of solid oxide fuel cells using sulfur containing fuels.* Journal of Power Sources, 2011. **196**(17): p. 7271-7276.

56.   Andarini, R.P., *Ex-situ characterisation of Solid Oxide Fuel Cell Operating on biogas using Tin Anode infiltration*, in *Chemical Engineering*. 2017, Univeristy of Birmingham: Birmingham.

57.   Wincewicz, K.C. and J.S. Cooper, *Taxonomies of SOFC material and manufacturing alternatives.* Journal of Power Sources, 2005. **140**(2): p. 280-296.

58.   Jiang, N. and E.D. Wachsman, *Structural Stability and Conductivity of Phase-Stabilized Cubic Bismuth Oxides.* Journal of the American Ceramic Society, 1999. **82**(11): p. 3057-3064.

59.   Ukai, K., et al., *Current Status of SOFC Development Using Scandia Doped Zirconia.* ECS Proceedings Volumes, 2001. **2001-16**: p. 375-383.

60.   Dasari, H.P., et al., *Synthesis, sintering and conductivity behavior of ceria-doped Scandia-stabilized zirconia.* Solid State Ionics, 2014. **263**: p. 103-109.

61.   Souza, J.P., et al., *Phase composition and ionic conductivity of zirconia stabilized with scandia and europia.* Materials Letters, 2018. **229**: p. 53-56.

62.   Grosso, R.L., S.L. Reis, and E.N.S. Muccillo, *Improved ionic conductivity of zirconia-scandia with niobia addition.* Ceramics International, 2017. **43**(14): p. 10934-10938.

63.   Yoon, K.J., et al., *Polarization measurements on single-step co-fired solid oxide fuel cells (SOFCs).* Journal of Power Sources, 2007. **172**(1): p. 39-49.

64.   Troskialina, L., *Improved Performance of Solid Oxide Fuel Cell Operating on Biogas using Tin Anode-infiltration*, in *Chemical Engineering*. 2015, University of Birmingham.

65.   Sumi, H., et al., *Effects of crystal Structure of yttria- and scandia-stabilized zirconia in nickel-based SOFC anodes on carbon deposition and oxidation behavior.* Journal of Power Sources, 2011. **196**(15): p. 6048-6054.

66.   Huang, B., et al., *Performance of Ni/ScSZ cermet anode modified by coating with Gd₀.₂Ce₀.₈O₂ for an SOFC running on methane fuel.* Journal of Power Sources, 2006. **162**(2): p. 1172-1181.

67.   Kishimoto, H., et al., *Feasibility of liquid hydrocarbon fuels for SOFC with Ni–ScSZ anode.* Journal of Power Sources, 2007. **172**(1): p. 67-71.

68. Zhou, J., et al., *A promising direct carbon fuel cell based on the cathode-supported tubular solid oxide fuel cell technology.* Electrochimica Acta, 2012. **74**: p. 267-270.

69. Huang, B., et al., *Characterization of the Ni-ScSZ anode with a LSCM–CeO$_2$ catalyst layer in thin film solid oxide fuel cell running on ethanol fuel.* Journal of Power Sources, 2010. **195**(10): p. 3053-3059.

70. Ye, X.-F., et al., *Use of La$_{0.75}$Sr$_{0.25}$Cr$_{0.5}$Mn$_{0.5}$O$_3$ materials in composite anodes for direct ethanol solid oxide fuel cells.* Journal of Power Sources, 2008. **183**(2): p. 512-517.

71. Eguchi, K., et al., *Reforming activity and carbon deposition on cermet catalysts for fuel electrodes of solid oxide fuel cells.* Catalysis Today, 2009. **146**(1-2): p. 154-159.

72. Ke, K., et al., *Effect of oxide on carbon deposition behavior of CH$_4$ fuel on Ni/ScSZ cermet anode in high temperature SOFCs.* Solid State Ionics, 2006. **177**(5-6): p. 541-547.

73. Puengjinda, P., et al., *Morphological evolution of NiO-ScSZ composite in a high-temperature reducing atmosphere.* Journal of the European Ceramic Society, 2012. **32**(1): p. 107-113.

74. Kishimoto, H., et al., *Rapid phase transformation of zirconia in the Ni-ScSZ cermet anode under reducing condition.* Solid State Ionics, 2008. **179**(35): p. 2037-2041.

75. Baker, R.T.K., *Catalytic growth of carbon filaments.* Carbon, 1989. **27**(3): p. 315-323.

76. Takeguchi, T., et al., *Effect of precious metal addition to Ni-YSZ cermet on reforming of CH$_4$ and electrochemical activity as SOFC anode.* Catalysis Today, 2003. **84**(3): p. 217-222.

77. Niakolas, D.K., et al., *Au-doped Ni/GDC as a new anode for SOFCs operating under rich CH4 internal steam reforming.* International Journal of Hydrogen Energy, 2010. **35**(15): p. 7898-7904.

78. Ioannidou, E., et al., *Au-doped Ni/GDC as an Improved Cathode Electrocatalyst for H2O Electrolysis in SOECs.* Applied Catalysis B: Environmental, 2018. **236**: p. 253-264.

79. Nikolla, E., J. Schwank, and S. Linic, *Comparative study of the kinetics of methane steam reforming on supported Ni and Sn/Ni alloy catalysts: The impact of the formation of Ni alloy on chemistry.* Journal of Catalysis, 2009. **263**(2): p. 220-227.

80. Farrell, B. and S. Linic, *Direct electrochemical oxidation of ethanol on SOFCs: Improved carbon tolerance of Ni anode by alloying.* Applied Catalysis B: Environmental, 2016. **183**: p. 386-393.

81. Schafbauer, W., N.H. Menzler, and H.P. Buchkremer, *Tape Casting of Anode Supports for Solid Oxide Fuel Cells at Forschungszentrum Jülich.* International Journal of Applied Ceramic Technology, 2014. **11**(1): p. 125-135.

82. Moon, H., et al., *Characteristics of SOFC single cells with anode active layer via tape casting and co-firing.* International Journal of Hydrogen Energy, 2008. **33**(11): p. 2826-2833.

83. Myung, J.-h., et al., *Development of solid oxide fuel cells (SOFCs) by tape-casting and single-step co-firing of monolithic laminates.* International Journal of Hydrogen Energy, 2014. **39**(5): p. 2313-2319.

84. Wang, Z.R., et al., *Improvement of anode-supported solid oxide fuel cells.* Solid State Ionics, 2008. **179**(27-32): p. 1593-1596.

85. P. Nahass, W.E.R., R.L. Pober, H.K. Bowen and W.L. Robbins,, *A comparison of aqueous and non-aqueous slurries for tape casting.* Ceramic Transactions, Vol. 15,Materials and Processes in Microelectronic Systems, 1990.

86. SolidPower, *DiscoverAboutSOFC*. 2016.

87. Nishihora, R.K., et al., *Manufacturing porous ceramic materials by tape casting—A review.* Journal of the European Ceramic Society, 2018. **38**(4): p. 988-1001.

88. Wesselmann, M., *Tape Casting Demo*. 2014, Polymer Innovations, Inc.: USA.

89. Wesselmann, M., *Useful Formulas for tape casting*. 2014, Polymer Innovations, Inc.: USA.

90. Fernández-González, R., et al., *Fabrication and electrical characterization of several YSZ tapes for SOFC applications.* Ceramics International, 2014. **40**(9, Part A): p. 14253-14259.

91. Baquero, T., et al., *Aqueous tape casting of micro and nano YSZ for SOFC electrolytes.* Ceramics International, 2013. **39**(7): p. 8279-8285.

92. Akbari-Fakhrabadi, A., et al., *Nanostructured Gd–CeO$_2$ electrolyte for solid oxide fuel cell by aqueous tape casting.* Journal of Power Sources, 2012. **218**: p. 307-312.

93. Fu, Y.-P., et al., *Aqueous tape casting and crystallization kinetics of $Ce_{0.8}La_{0.2}O_{1.9}$ powder.* Ceramics International, 2009. **35**(2): p. 609-615.

94. Luo, L.H., A.I.Y. Tok, and F.Y.C. Boey, *Aqueous tape casting of 10mol%-Gd_2O_3-doped CeO_2 nano-particles.* Materials Science and Engineering: A, 2006. **429**(1-2): p. 266-271.

95. Fu, C., et al., *Fabrication and evaluation of Ni-GDC composite anode prepared by aqueous-based tape casting method for low-temperature solid oxide fuel cell.* International Journal of Hydrogen Energy, 2010. **35**(1): p. 301-307.

96. Zhou, J., et al., *A Low Cost Large-Area Solid Oxide Cells Fabrication Technology based on Aqueous Co-Tape Casting and Co-Sintering.* Fuel Cells, 2014. **14**(4): p. 667-670.

97. Cai, G., et al., *Anode performance of Mn-doped ceria–ScSZ for solid oxide fuel cell.* Journal of Solid State Electrochemistry, 2010. **15**(1): p. 147-152.

98. Luo, X.-J., et al., *Effects of organic additives on viscosity of aqueous tape-casting aluminum nitride slurries.* Journal of Materials Science Letters. **22**(8): p. 589-590.

99. Stiernstedt, J, *Swerea IVF Manufacturing of porous nanocomposite SOFC anodes by aqueous tape casting.pdf.*

100. Moreno, V., et al., *Dense YSZ Laminates Obtained by Aqueous Tape Casting and Calendering.* Advanced Engineering Materials, 2013.

101. Moreno, V., R.M. Bernardino, and D. Hotza, *Mechanical Behavior of Yttria-Stabilized Zirconia Aqueous Cast Tapes and Laminates.* Journal of Ceramics, 2014. **2014**: p. 1-5.

102. Albano, M.P., et al., *Processing of porous yttria-stabilized zirconia by tape-casting.* Ceramics International, 2008. **34**(8): p. 1983-1988.

103. Wang, L., G. Tang, and Z.-K. Xu, *Comparison of Water-Based and Solvent-Based Tape Casting for Preparing Multilayer ZnO Varistors.* Journal of the American Ceramic Society, 2008. **91**(11): p. 3742-3745.

104. Wesselmann, M., *Defoamer Comments*. 2014, Polymer Innovations, Inc. USA.

105. Myung, J.-h., et al., *Fabrication and characterization of planar-type SOFC unit cells using the tape-casting/lamination/co-firing method.* International Journal of Hydrogen Energy, 2012. **37**(1): p. 498-504.

106. Park, H.-G., et al., *Performance improvement of anode-supported electrolytes for planar solid oxide fuel cells via a tape-casting/lamination/co-firing technique.* Journal of Power Sources, 2010. **195**(9): p. 2463-2469.

107. Zhou, J., et al., *A study of short stack with large area solid oxide fuel cells by aqueous tape casting.* International Journal of Hydrogen Energy, 2016. **41**(40): p. 18203-18206.

108. MALVERN. *Mastersizer 2000: User Manual.* [cited 2019 18February2019]; Chapter 2: How the mastersizer works.

109. Kiennemann, J., et al., *Drying mechanisms and stress development in aqueous alumina tape casting.* Journal of the European Ceramic Society, 2005. **25**(9): p. 1551-1564.

110. Kristoffersson, A. and E. Carlström, *Tape casting of alumina in water with an acrylic latex binder.* Journal of the European Ceramic Society, 1997. **17**(2): p. 289-297.

111. Wesselmen, M., *Tape Casting Thick Water Based Ceramic Tapes*. 2014, Polymer Innovations, Inc: USA.

112. McDonald, N., *The Manufacture and Testing of Anode Supported Ni-10Sc1CeSZ SOFCs for Intermediate Temperature Operation*, in *Chemical Engineering*. 2017, University of Birmingham: Birmingham, United Kingdom.

113. Wang, Z., et al., *A study of multilayer tape casting method for anode-supported planar type solid oxide fuel cells (SOFCs).* Journal of Alloys and Compounds, 2007. **437**(1-2): p. 264-268.

114. Haberko, K., et al., *Structural and electrical properties of Ni–YSZ cermet materials.* Journal of Power Sources, 2010. **195**(17): p. 5527-5533.

115. Hong, J.-E., *Anode supported SOFC using $LaGaO_3$ electrolyte film prepared by screen printing method*, in *Department of Automotive Science, Graduate School of Intergrated Frontier Science* 2012, Kyushu University: Japan.

116. Araki, W., et al., *Fracture mechanism of scandia-doped zirconia.* Acta Materialia, 2013. **61**(8): p. 3082-3089.

117. Orlovskaya, N., et al., *Mechanical properties of 10 mol% Sc₂O₃–1 mol% CeO₂–89 mol% ZrO₂ ceramics.* Journal of Power Sources, 2010. **195**(9): p. 2774-2781.

118. Kazlauskas, S., E. Kazakevičius, and A. Kežionis, *Electrical properties of scandia- and ceria-stabilized zirconia ceramics.* Solid State Ionics, 2017. **310**: p. 143-147.

119. Guo, C.X., et al., *Effect of alumina on the properties of ceria and scandia co-doped zirconia for electrolyte-supported SOFC.* Ceramics International, 2013. **39**(8): p. 9575-9582.

120. Zekri, A., et al., *Nickel Depletion and Agglomeration in SOFC Anodes During Long-Term Operation.* Fuel Cells, 2017. **17**(3): p. 359-366.

121. Mogensen, M. and P.V. Hendriksen, *Chapter 10 - Testing of Electrodes, Cells and Short Stacks*, in *High Temperature and Solid Oxide Fuel Cells*, S.C. Singhal and K. Kendall, Editors. 2003, Elsevier Science: Amsterdam. p. 261-289.

122. Yarmolenko, S., et al., *Phase Stability and Sintering Behavior of 10mol% Sc₂O₃–1mol% CeO₂–ZrO₂ Ceramics.* Journal of Fuel Cell Science and Technology, 2009. **6**(2): p. 021007-021007-8.

123. Chen, J., et al., *Characterization of Degradation in Nickel Impregnated Scandia-Stabilize Zirconia Electrodes during Isothermal Annealing.* Journal of The Electrochemical Society, 2017. **164**(9): p. F935-F943.

124. Yin, W. and S.S.C. Chuang, *CH₄ internal dry reforming over a Ni/YSZ/ScSZ anode catalyst in a SOFC: A transient kinetic study.* Catalysis Communications, 2017. **102**: p. 62-66.

125. Koh, J.-H., et al., *Carbon deposition and cell performance of Ni-YSZ anode support SOFC with methane fuel.* Solid State Ionics, 2002. **149**(3): p. 157-166.

126. Baker, R.T.K., et al., *Nucleation and growth of carbon deposits from the nickel catalyzed decomposition of acetylene.* Journal of Catalysis, 1972. **26**(1): p. 51-62.

127. Singh, A. and J.M. Hill, *Carbon tolerance, electrochemical performance and stability of solid oxide fuel cells with Ni/yttria stabilized zirconia anodes impregnated with Sn and operated with methane.* Journal of Power Sources, 2012. **214**: p. 185-194.

128. Singh, A. and J.M. Hill, *Evaluation of Sn-Modified Ni/YSZ SOFC Anodes for the Direct Utilization of Methane.* ECS Transactions, 2011. **35**(1): p. 1397-1406.

129. School of Crystallography, Birkbeck College, University of London (UCL), Advanced Certificate in Powder Diffraction on the Web, Structure refinement. *Tools: Phase transitions*. [cited on 17/02/2019]. Available from: http://pd.chem.ucl.ac.uk/pdnn/refine2/phase.htm

130. Jin, C., Mao, Y., Zhang, N., and Sun, K. *Fabrication and characterization of Ni-SSZ gradient anodes/SSZ electrolyte for anode-supported SOFCs by tape casting and co-sintering technique,* International Journal of Hydrogen Energy, 2015. **40** (26): p 8433-8441.

APPENDIX

APPENDIX 1: Slurry optimisation for 55 wt% solid loading for NiOYSZ and NiOScCeSZ.

	Wt%																		
	Vary dispersant			*Vary binder*				*Vary anti-foam*		*Vary PEG 400:PVA ratio*		*Vary pore former*			*Vary Wetting agent*	*Vary solid loading*	*Vary PEG 400:Glycerol ratio*		
	A1	**A2**	**A3**	**B1**	**B2**	**B3**	**B4**	**C1**	**C2**	**D1**	**D2**	**E1**	**E2**	**E3**	**F1**	**F2**	**G1**	**G2**	**G3**
Solid loading	55.0	55.0	55.0	55.0	55.0	55.0	55.0	55.0	55.0	55.0	55.0	55.0	55.0	55.0	55.0	50.0	55.0	55.0	55.0
BASF Dispex	2.0	1.5	1.0	1.0	1.0	1.0	1.0	1.0	1.0	1.0	1.0	1.0	1.0	1.0	1.0	1.0	1.0	1.0	1.0
PVA	4.5	4.5	4.5	4.5	5.0	6.0	5.4	5.4	5.4	5.4	5.4	5.4	5.4	5.4	5.4	5.4	5.4	5.4	5.4
PEG 400	1.4	1.4	1.4	1.4	1.4	1.4	1.4	1.4	1.4	2.7	4.1	4.1	4.1	4.1	4.0	4.1	0.0	5.4	2.7
Glycerol	1.4	1.4	1.4	1.4	1.4	1.4	1.4	1.4	1.4	1.4	1.4	1.4	1.4	1.4	1.4	1.4	5.5	0.0	2.7
Wetting agent	0.1	0.1	0.1	0.1	0.1	0.1	0.1	0.1	0.1	0.1	0.1	0.1	0.1	0.1	0.0	0.0	0.0	0.0	0.0
Anti-foam	0.1	0.1	0.1	0.1	0.1	0.1	0.1	0.2	0.5	0.2	0.2	0.2	0.2	0.2	0.2	0.2	0.2	0.2	0.2
Pore former	0.0	0.0	0.0	0.0	0.0	0.0	0.0	0.0	0.0	0.0	0.0	5.0	1.0	3.0	3.0	3.0	3.0	3.0	3.0
Water	-balance the 100% composition-																		

*Final composition used for AFL for both cells was composition D1 (without the wetting agent, for NiO/YSZ AS composition F1, while for NiO/ScCeSZ, composition G3.

APPENDIX II: FUEL UTILISATION CALCULATOR (HYDROGEN)

Courtesy by Oujen-Hodjati Pugh

Fuel Utilisation Calculation (100% F.U)		
Current density @ 0.7V	0.39	A/(cm^2)
Surface Area, based on cathode exposed area	1.68	cm^2
Total Current from Cell	0.655	A
N.B - 1 Coulomb of charge = 6.28E18 electons = 1Amp*second		
Therefore	0.655	A or [C/s]
N.B 1Coulomb = X electrons passed	6.25×10^{18}	electrons
N.B 1C/s = X electrons/second		
Number of electrons per second	4.10×10^{18}	Electrons/second
Number of electrons per min	2.46×10^{20}	Electrons/min

Hydrogen Consumption $H_2 \to 2H^+ + 2e^-$		
N.B We have 2 electrons per mole of H2		
Avogadro Number (number of atoms per mole)	6.02×10^{23}	1/mol
1mole equivalent of electrons per min --> (no electons per min/(Avogadro number)	4.08×10^{-4}	mole electrons eq./min
Number of moles H_2 needed to give above mole of electrons	2.04×10^{-4}	moles H_2/min
Mass flow rate of Hydrogen (H_2) per min (m = n/Ar)	4.12×10^{-4}	g/min
Hydrogen Density	0.002 P [Pa]/(8.314*T[K])	kg/m^3
101325Pa & 273K	0.089	kg/m^3
101325Pa & 1023K **(750°C)**	0.024	kg/m^3
"………………….." in [g/m^3]	23.831	g/m^3
Volumetric flow rate of hydrogen per min [m^3/min]	1.73×10^{-5}	m^3/min
Volumetric flow rate of hydrogen per min [ml/min]	17.30	ml/min

Oxygen Consumption $2H^+ + 2e^- + 0.5*O_2 \to H_2O$		
N.B We have 4 electrons eq per mole of O2		
Avogadro Number (number of atoms per mole)	6.02×10^{23}	1/mol
1mole equivalent of electrons per min --> (no electons per min/(Avogadro number)	4.08×10^{-4}	mole electrons eq./min
Number of moles H_2 needed to give above mole of electrons	1.02×10^{-4}	moles O_2/min

Mass flow rate of Oxygen (O_2) per min (m=n/Ar)	3.26×10^{-3}	g/min
Oxygen Density	0.032*P[Pa]/(8.314*T[K])	kg/m^3
101325Pa & 273K (STP)	1.429	kg/m^3
101325Pa & 1023K (750°C)	0.381	kg/m^3
"…………………….." in [g/m^3]	381.233	g/m^3
Volumetric flow rate of Oxygen per min [m^3/min]	8.56×10^{-6}	m^3/min
Volumetric flow rate of Oxygen per min [ml/min]	8.560	ml/min
Air flow rate required for stoichiometry	40.771	ml/min

Fuel Utilisation Calculation (X% F.U)

|		
Fuel flow rate provided - **Insert Here**	21	ml/min
Fuel Flow rate for 100% F.U	17.30	ml/min
Fuel Utilisation (theoretical required rate of reactant supplied/actual rate of reactant supplied)	**0.82**	

Simpler Way - Faradays equation

n$_{H2}$=(i*A)/(n*F)		mol H$_2$/ s C/(s*cm^2)
Current density - i	0.39	[A/cm^2]
Cell Area	1.68	cm^2
n= number of electron equivalent per mol H$_2$	2	e$^-$ eq/mole H$_2$
Faradays constant (F)	96485	C/eq
n$_{H2}$=	3.40×10^{-6}	mole H$_2$/second
n$_{H2}$=	2.04×10^{-4}	moles H$_2$/min
Mass flow rate of Hydrogen (H$_2$) per min (m=n/Ar)	4.12×10^{-4}	g/min
Hydrogen Density	0.002P[Pa]/ (8.314*T [K])	kg/m^3
101325Pa & 273K	0.0893	kg/m^3
101325Pa & 1023K (750°C)	0.0238	kg/m^3
"…………………….." in [g/m^3]	23.827	g/m^3
Volumetric flow rate of hydrogen per min [m^3/min]	1.73×10^{-5}	m^3/min
Volumetric flow rate of hydrogen per min [ml/min]	17.27	ml/min

Oxygen Consumption $2H^+ + 2e^- + 0.5*O_2 -> H_2O$		Units
N.B We have a 4 electron eq per mole O_2		
$n_{H2}=(i*A)/(n*F)$		mol H_2/ s
		$C/(s*cm^2)$
Current density - i	0.39	$[A/cm^2]$
Cell Area	1.68	cm^2
n= number of electron equivalent per mol H_2	4	e^- eq/mole O_2
Faradays constant (F)	96485	C/eq
$n_{H2}=$	1.69767×10^{-6}	mole O_2/second
$n_{H2}=$	1.02×10^{-4}	moles O_2/min
Mass flow rate of Oxygen (O_2) per min (m=n/Ar)	3.26×10^{-3}	g/min
Oxygen Density	$\underline{0.032*P[Pa}/(8.314*T[K])}$	kg/m^3
101325Pa & 273K	1.429	kg/m^3
101325Pa & 1023K (750°C)	0.381	kg/m^3
"…………………….." in $[g/m^3]$	381.225	g/m^3
Volumetric flow rate of oxygen per min $[m^3/min]$	8.55×10^{-6}	m^3/min
Volumetric flow rate of hydrogen per min [ml/min]	8.55	ml/min

APPENDIX III: POST TEST MICROSTRUCTURAL ANALYSIS ON NI/SCCESZ (WITH PHILIPS XL-30 FEG ENVIRONMENTAL-SEM)
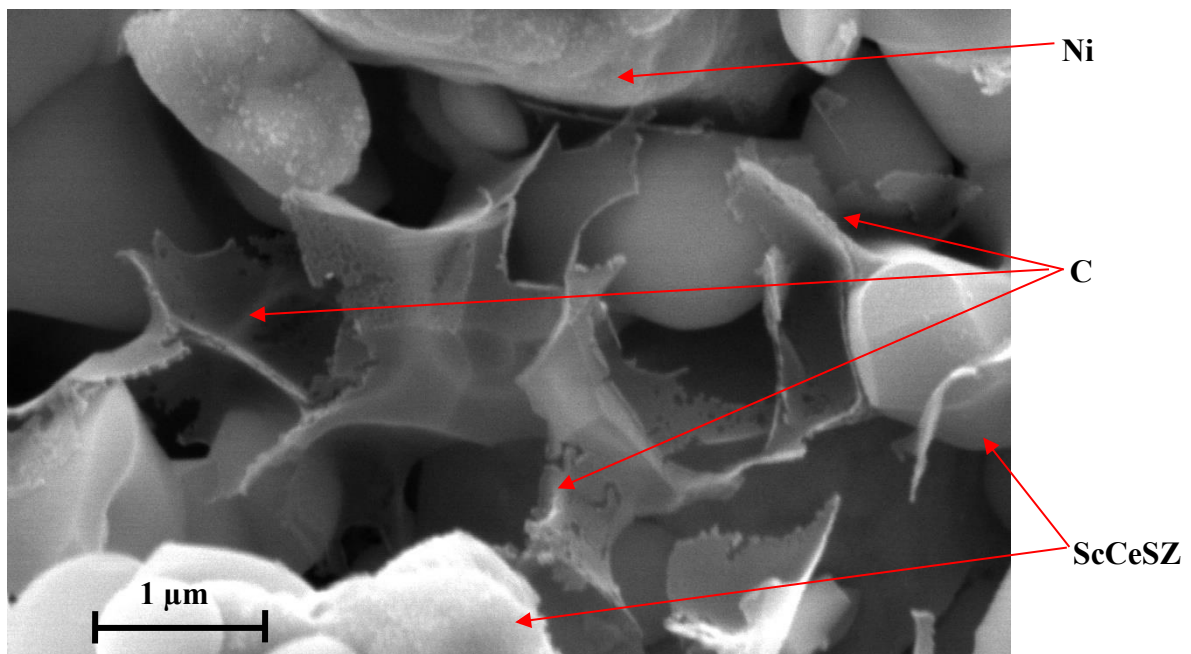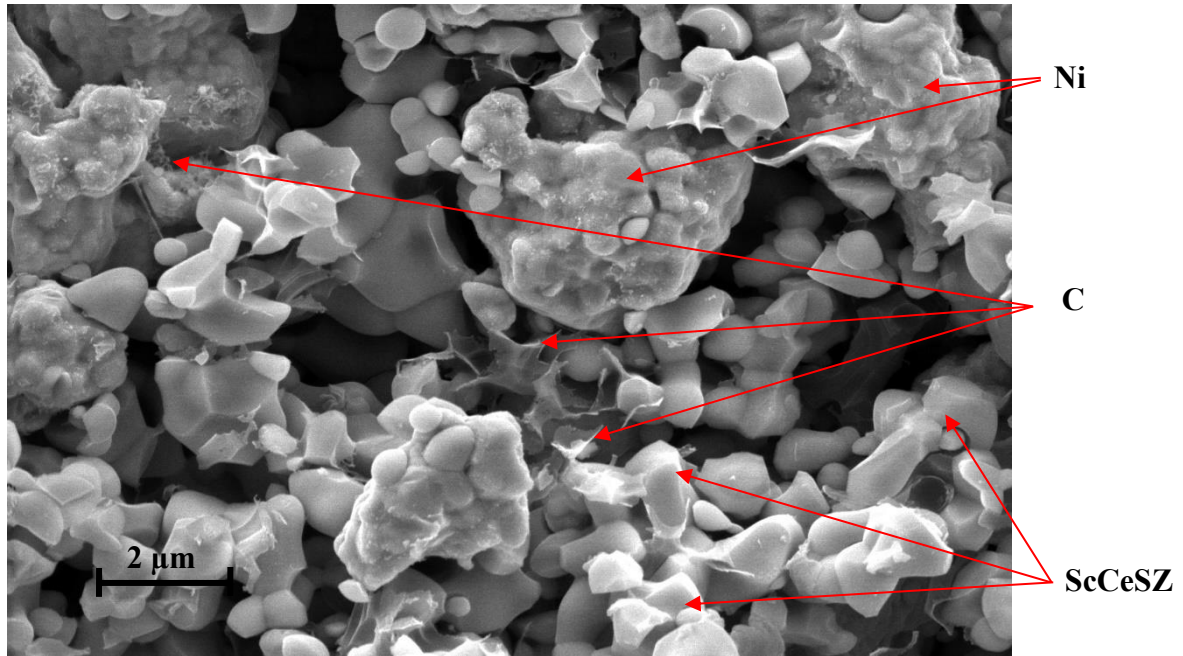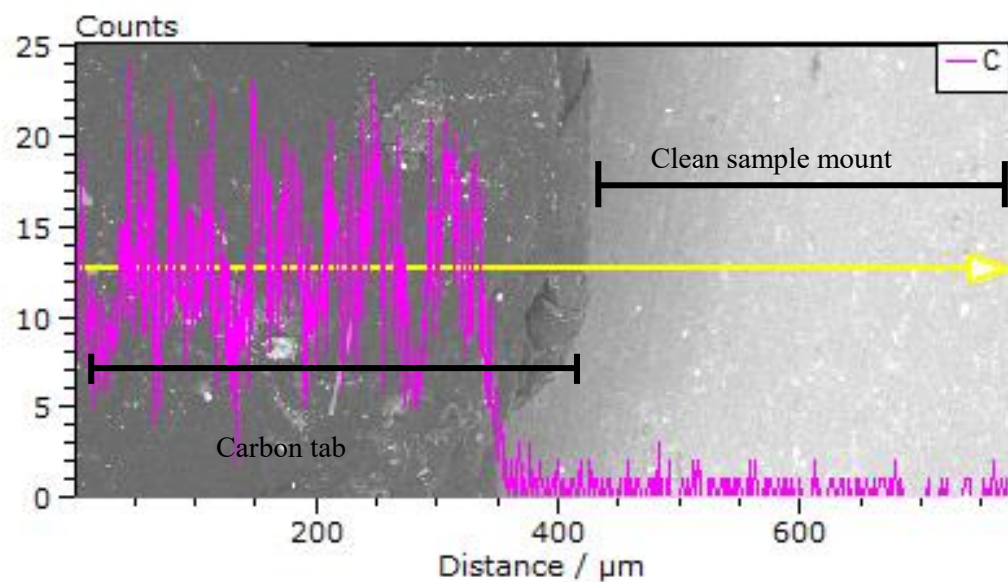

**SEM images displayed here instead as there were no comparison using the same machine for Ni/YSZ cells
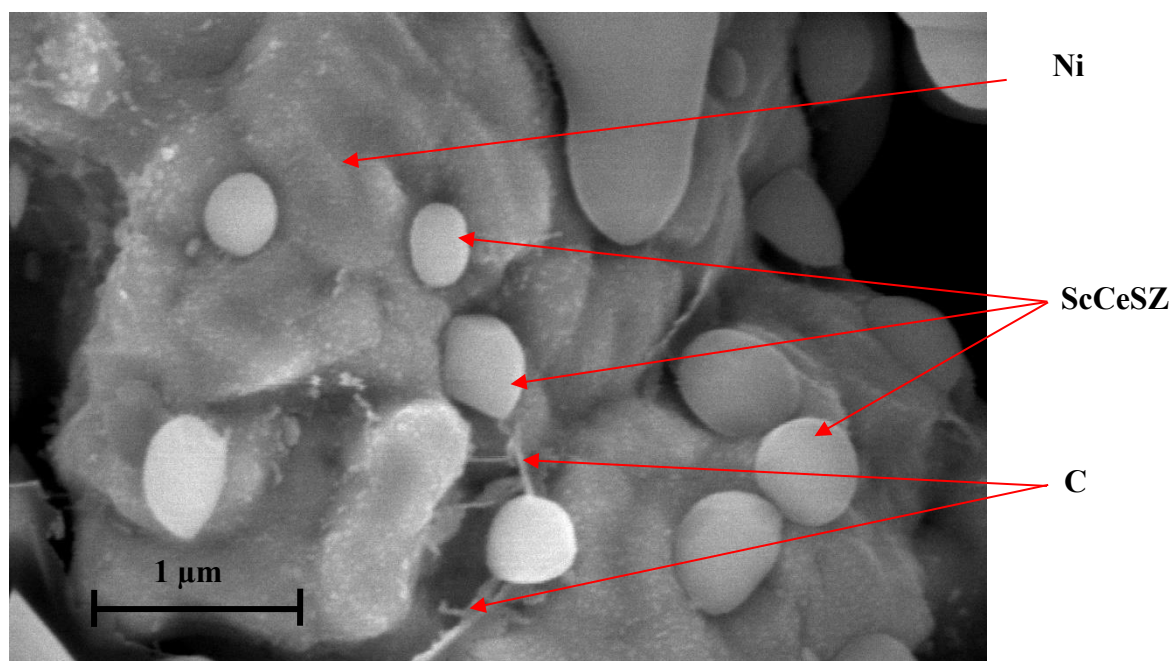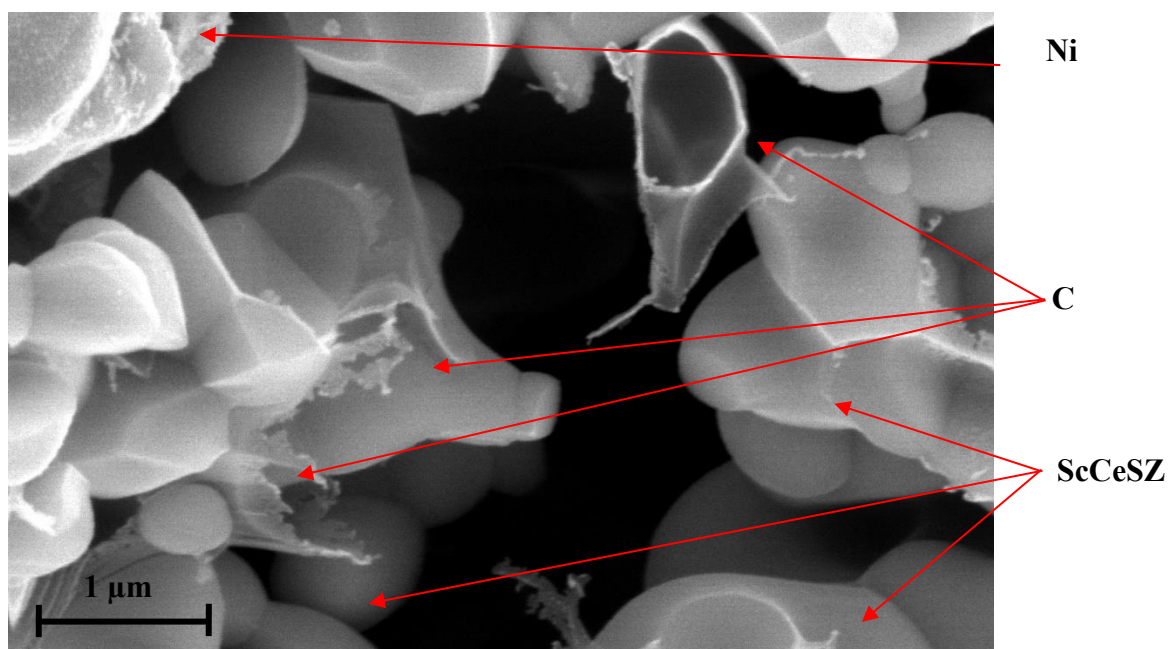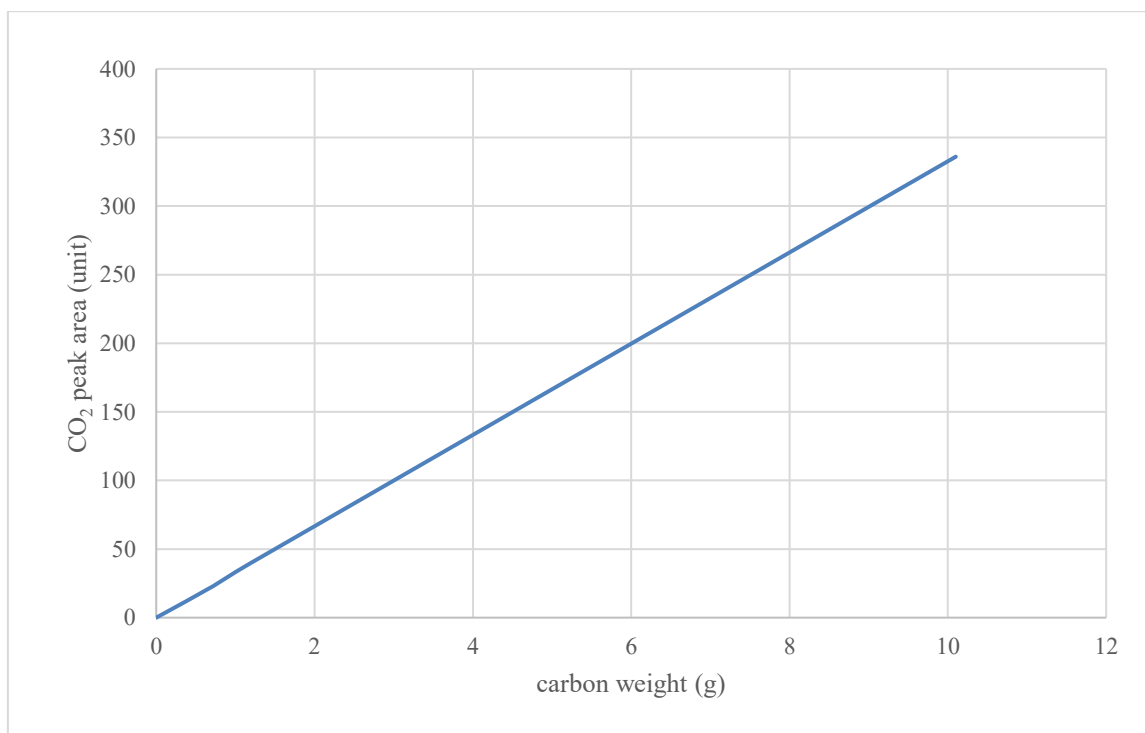
**SEM images displayed here instead as there were no comparison using the same machine for Ni/YSZ cells.
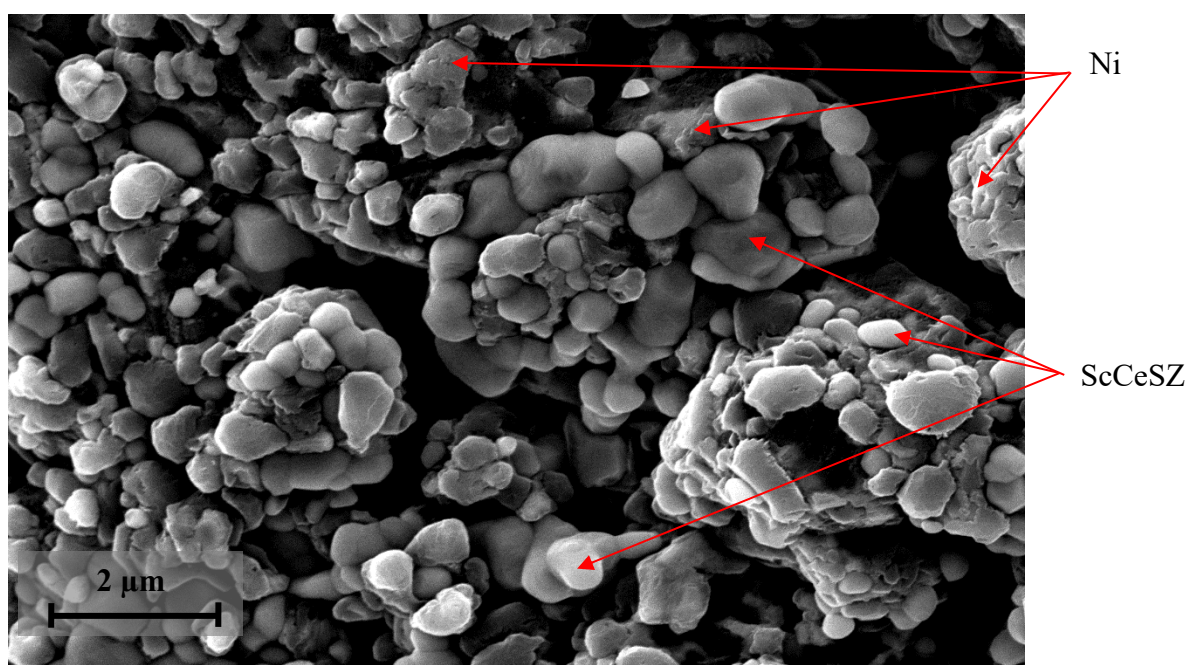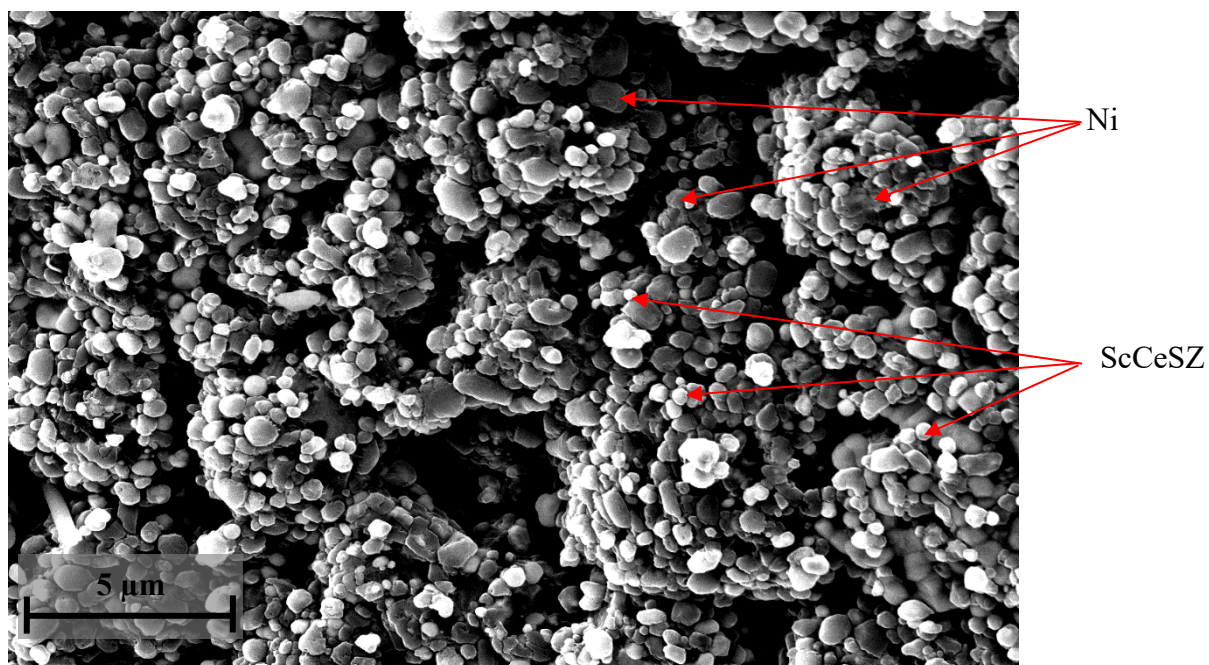
APPENDIX IV: CARBON TAB AND SAMPLE MOUNT TEST: TO CHECK THE ABILITY OF THE SEM-EDX MACHINE TO DETECT CARBON
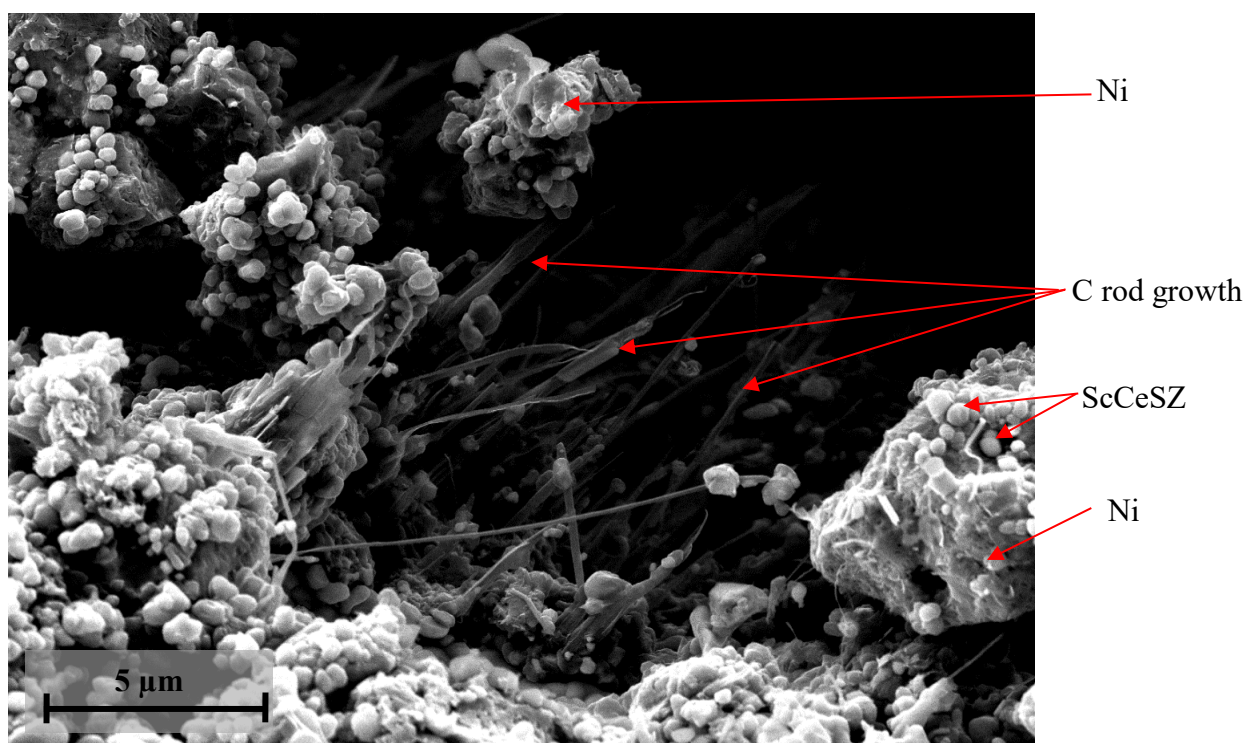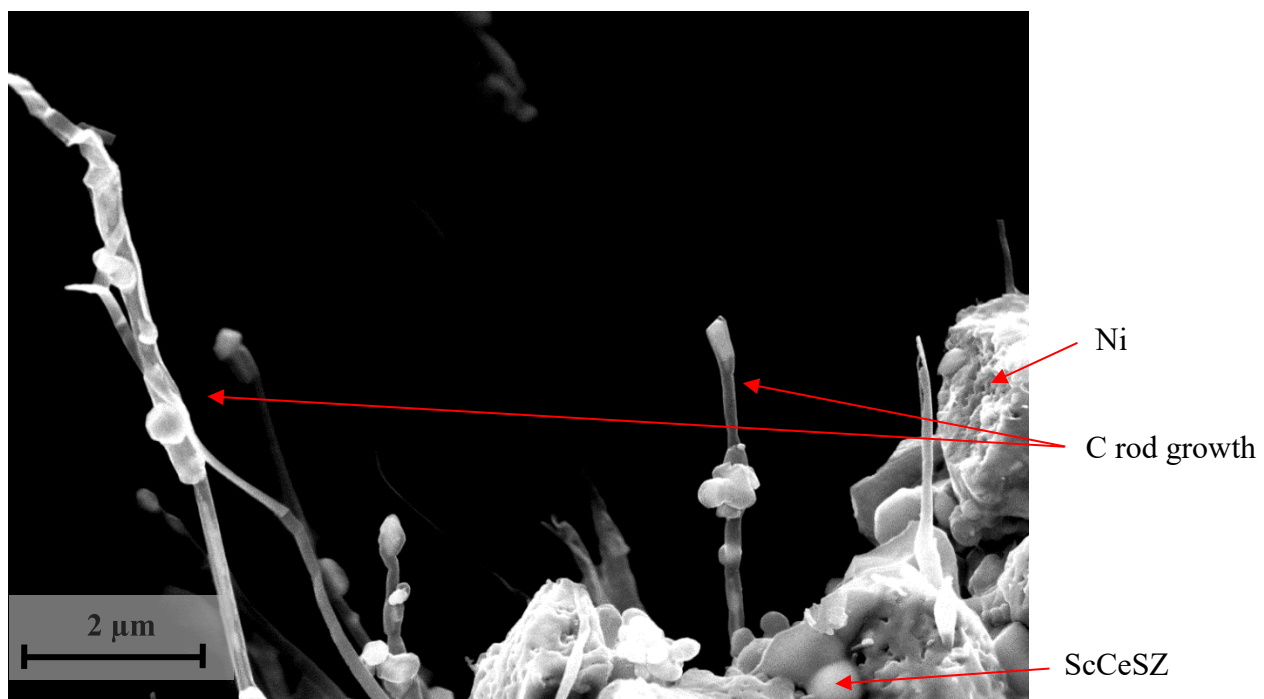

APPENDIX V: CALIBRATION CURVE FOR TPO (SECTION 6.3.2 AND 7.4.2)

APPENDIX VI: CARBON DEPOSITION IN NI/SCCESZ PELLET AFTER CATALYTIC ACTIVITY TEST

Ni

ScCeSZ

Ni

ScCeSZ

** SEM on the surface of the NiScCeSZ anode pellet after 3 hours exposure of biogas

** SEM on the cracks on the NiScCeSZ anode pellet after 3 hours exposure of biogas

APPENDIX VII: CARBON DEPOSITION IN NI/YSZ PELLET AFTER CATALYTIC ACTIVITY TEST